Development of Iron-Based Nanoparticles for Nitrate, Cesium and Strontium Removal from Contaminated Water

タメル, エス, アル, シュバイル

https://doi.org/10.15017/2534484

出版情報：Kyushu University, 2019, 博士（工学）, 課程博士
バージョン：
権利関係：

九州大学
KYUSHU UNIVERSITY

Development of Iron-Based Nanoparticles for Nitrate, Cesium and Strontium Removal from Contaminated Water

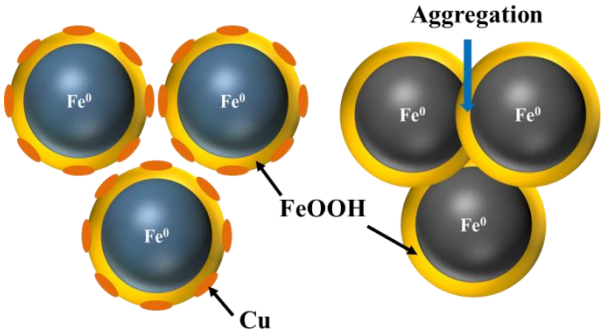

By

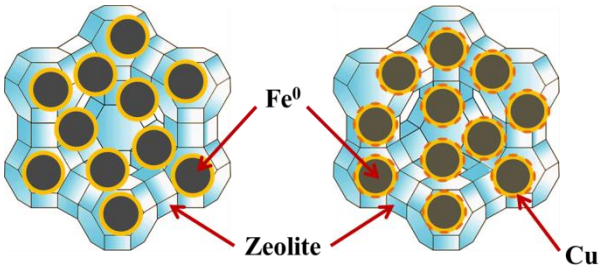

Tamer S R Shubair

KYUSHU UNIVERSITY

JAPAN

九州大学
KYUSHU UNIVERSITY

Development of Iron-Based Nanoparticles for Nitrate, Cesium and Strontium Removal from Contaminated Water

By

Tamer S R Shubair

Supervised by

Professor Osama Eljamal

A dissertation submitted in partial fulfillment of the requirements for the degree of

Doctor of Engineering (Dr. Eng.)

Department of Earth System Science and Technology

Interdisciplinary Graduate School of Engineering Sciences

KYUSHU UNIVERSITY

JAPAN

September 2019

Dedicated to

my beloved mother, father, brothers and sisters

and to my sweet elder brother's daughter Lama

PREFACE

This study is a doctoral dissertation that focuses on development a new treatment process for efficient removal of toxic/radioactive materials from contaminated waters. The experimental work of this study was conducted at Environmental Fluid Science Lab, Department of Earth System Science and Technology, Interdisciplinary Graduate School of Engineering Sciences, Kyushu University, Japan during the period from October 2016 to September 2019. The following list presents the articles which were published in international journals and conferences during this research study.

List of Articles in International Journals:

1. **Tamer Shubair**, Osama Eljamal, Atsushi Tahara, Yuji Sugihara and Nobuhiro Matsunaga, "Preparation of new magnetic zeolite nanocomposites for removal of strontium from polluted waters", Journal of Molecular Liquids, Vol. 288, pp. 1-11, 2019.
2. Osama Eljamal, **Tamer Shubair**, Atsushi Tahara, Yuji Sugihara and Nobuhiro Matsunaga, "Iron based nanoparticles–zeolite composites for the removal of cesium from aqueous solutions", Journal of Molecular Liquids, Vol. 277, pp. 613-623, 2019.
3. **Tamer Shubair**, Osama Eljamal and Nobuhiro Matsunaga, "Degradation of nitrate by modified surface of nano-zero valent iron in flow through permeable reactive barrier: different configurations", International Journal of Advances in Science, Engineering and Technology, Vol. 6, 2, pp. 69-72, 2018.
4. **Tamer Shubair**, Osama Eljamal, Ahmed M.E. Khalil, Atsushi Tahara and Nobuhiro Matsunaga, "Novel application of nanoscale zero valent iron and bimetallic nano-Fe/Cu particles for the treatment of cesium contaminated water", Journal of Environmental Chemical Engineering, Vol. 6, pp. 4253-4264, 2018.
5. **Tamer Shubair**, Osama Eljamal, Ahmed M.E. Khalil and Nobuhiro Matsunaga, "Multilayer system of nanoscale zero valent iron and nano-Fe/Cu particles for nitrate removal in porous media", Separation and Purification Technology, Vol. 193, pp. 242-254, 2018.

List of Articles in International Conference Proceedings:

1. **Tamer Shubair** and Osama Eljamal, "Fe/Cu nanoparticles–zeolite composite for efficient Sr^{2+} uptake from water", Oral, International Exchange and Innovation Conference on Engineering & Sciences (IEICES-2019), October 2019, Fukuoka, Japan.
2. **Tamer Shubair**, Osama Eljamal and Nobuhiro Matsunaga, "Removal of cesium from aqueous solutions by nanoscale zero valent iron–zeolite composite", Oral, International Symposium on Earth Science and Technology (ISEST-2018), November 2018, Fukuoka, Japan.
3. **Tamer Shubair**, Osama Eljamal and Nobuhiro Matsunaga, "Nano-Fe/Cu particles for the remediation of cesium contaminated solutions", Oral, International Exchange and Innovation Conference on Engineering & Sciences (IEICES-2018), October 2018, Fukuoka, Japan.
4. **Tamer Shubair**, Osama Eljamal and Nobuhiro Matsunaga, "Evaluation of nanoscale zero valent iron particles for the removal of cesium from aqueous solutions", Oral, International Conference on Materials Engineering & Science (IConMEAS-2018), IOP Conference Series Materials Science and Engineering, August 2018, Istanbul, Turkey.
5. **Tamer Shubair**, Osama Eljamal, Ahmed M.E. Khalil, Ibrahim Maamoun and Nobuhiro Matsunaga, "Enhancement of nitrate removal in porous media multilayer system using surface modified nanoscale zero-valent iron", Oral, Nano Today Conference (Nano Today-2017), December 2017, Hawaii, USA.
6. **Tamer Shubair**, Osama Eljamal, Ahmed M.E. Khalil and Nobuhiro Matsunaga, "Degradation of nitrate in porous media using multibarrier system of nano-Fe/Cu particles: column experiment", Oral, International Symposium on Earth Science and Technology (ISEST-2017), November 2017, Fukuoka, Japan.
7. **Tamer Shubair**, Osama Eljamal, Ahmed M.E. Khalil and Nobuhiro Matsunaga, "Nitrate removal in porous media using nanoscale zero valent iron: column experiment", Oral, International Exchange and Innovation Conference on Engineering & Sciences (IEICES-2017), October 2017, Fukuoka, Japan.

ACKNOWLEDGEMENTS

First of all I would like to express my deepest sense of gratitude and indebtedness to my dear supervisor **Prof. Osama Eljamal** for his precious guidance, advice, valuable assistance and endless support throughout this research work and during my life in Japan. **Prof. Eljamal** has provided me extensive personal and professional support and he has taught me a great deal about scientific research work and life in general.

I am also indebted to **Prof. Nobuhiro Matsunaga,** Head of Environmental Fluid Science Lab, for his kind support and motivation during this study.

I would like to thank **Prof. Atsushi Tahara** for his high cooperation, support and guidance during my research.

I am grateful to all the members of academic, support staff as well as Japanese and international students of the Environmental Fluid Science Lab for their encouragement, support and cooperation. I am especially indebted to **Dr. Ahmed Khalil,** Assistant Professor at Cairo University, Egypt, for his continuous support, inspiration and help.

I am also thankful to all my friends in Japan with whom I have had the pleasure during my stay in Japan, in particular, Muslims Community in Fukuoka.

A very special gratitude goes out to the Japanese Ministry of Education, Culture, Sports, Science and Technology (MEXT) for helping and providing the financial support required for my Ph.D. study at Kyushu University.

Nobody has been more important to me in the pursuit of this research than the members of my family. I would like to thank and express my high appreciation to my Father **Salah**, Mother **Wafaa**, Brothers **Ramadan**, **Mohammed**, **Bashar**, **Abdel-Hakeem** and Sisters **Lamia** and **Noor** for their love, support, encouragement, sacrifice and prayers for me.

Tamer S R Shubair

Fukuoka, Japan

ABSTRACT

Environmental contamination is one of the important issues that the world is facing today and it is widening with each passing year and leading to deadly and harmful effect to the earth. Water is one of the world's most abundant resources, but less than 1% of the global supply of water is available and adequate for human use. Owing to the rapid growth of urbanization, industrialization and modern agricultural practices, contamination of stream water or groundwater is on the rise. An increasing number of drinking water sources are showing evidence of pollution with organic and inorganic compounds. These environmental contaminants have a harmful effect on the human health; therefore, technologies for the removal of hazardous pollutants from waters are highly desired.

The Great East Japan Earthquake of magnitude 9 and resulting tsunami on March 11, 2011, triggered the Fukushima Daiichi Nuclear Power Plant disaster. A very large amount of radioactive materials was vented into the environment and subsequently caused serious radioactive contamination of the surrounding land, seawater and groundwater. In addition, with the rapidly increasing dependence on nuclear energy and the application of radionuclides in medicine, industry, agriculture and researches, treatment and disposal of radioactive wastewater has become one of the most significant challenges in nuclear waste management and nuclear industry to almost all countries. Some of the important radioactive isotopes in the liquid wastes are cesium (^{134}Cs and ^{137}Cs) and strontium (^{90}Sr). Cesium and strontium are considered as the most dangerous radionuclides to human health due to their long half-lives, high solubility, high transferability, high concentrations in the wastewaters and easy assimilation in living organisms. The reported materials for removal of radioisotopes, such as zeolites, activated carbon, kaolinite and biomaterials have limited application since separation the suspended fine solids of these adsorbents from the medium after use is very difficult, which may increase the risk of secondary environmental pollution in practice. Accordingly, there is an urgent need to develop new technologies that more efficient and economic for the treatment of toxic environmental pollutants. The application of nanotechnology in environmental fields gives a new solution for cleaning pollution and improving the performance of traditional water and wastewater treatment techniques.

Nanoscale zero valent iron (nZVI) has been shown to be effective for environmental remediation of a wide variety of contaminants present in water resources including nitroaromatic compounds, perchlorate, azo dyes, halogenated hydrocarbons, nitrate, phosphate, arsenic and heavy metal ions. Due to its large surface area and high number of active sites, nZVI enhances the removal efficiencies of those contaminants significantly via diverse mechanisms. Moreover, recent investigations demonstrated nZVI can be utilized as a promising technology in the clean-up of radionuclides contaminated waters. Nevertheless, nZVI exhibits strong tendency to agglomerate to micron size particles because of the high surface energy and intrinsic magnetic interaction, which decrease efficiency by reducing surface area for reaction and limit their field scale application. Modifying the surface of nZVI and supporting nZVI particles on a carrier have been proposed to improve the reactivity of these nanoparticles and resolve the aforementioned issues.

Therefore, in this study, nZVI-based materials were applied to examine their effectiveness for removal of radioactive isotopes such as cesium and strontium from contaminated waters. In addition, the performance of nZVI-based materials for removal of nitrate in porous media using an upflow packed sand column was tested. The nZVI-based materials were synthesized and their physicochemical characteristics were analyzed by transmission electron microscope (TEM), X-ray diffraction (XRD), scanning electron microscope-elemental analysis (SEM-EDS) and others. The effect of various operating variables such as initial metal ion concentration, contact time, initial solution pH, temperature, influence of competing ions and dosage of nZVI-based materials was investigated. The kinetic, thermodynamic and isotherm parameters of the removal process were also evaluated. Furthermore, the removal capacity was compared between synthesized nanomaterials and other reported adsorbents. Finally, nZVI-based materials were applied in simulated seawater or groundwater to demonstrate the reliability of the materials. The obtained results indicated that nZVI-based materials could be employed as promising methods for the removal of cesium and strontium from radioactive wastewaters. In addition, the results showed that nitrate removal in porous media could be enhanced effectively by using nZVI on the full length of porous media or using nano-Fe/Cu in multilayer porous media.

TABLE OF CONTENTS

LIST OF FIGURES

Chapter 4

Chapter 5

Chapter 6

LIST OF TABLES

CHAPTER 1

INTRODUCTION

CHAPETR 1- Introduction

This chapter gives a general background about the current situation of water pollution and presents an overview of the target contaminants for treatment in this research, nanotechnology for water treatment and the role of nZVI as a promising material in decontaminating a broad range of pollutants. The literature survey on nZVI involves recent advances in this technology, efficiency of nZVI in detoxification of a variety of common environmental pollutants, use of nZVI in filed scale application and toxicity assessment of nZVI on living organisms. It also contains aim and objectives of the research and describes the structure of the dissertation.

1.1. Problem statement

Water is one of the basic requirements for sustaining life. It is well known that the progress of life on this planet to its present form originated from water. Owing to the rapid growth of industrialization and urbanization, the global water utilization has doubled every 15 years. The water resources scarcity has created challenges for over 40% of the world population according to the World Health Organization (WHO), which means more than two billion people have no access to enough clean water [1]. Meanwhile, environmental pollution is becoming more and more severe in certain areas of the world. The presence of pollutants in the environment causes harm, discomfort, disorder and instability to the ecosystem. The natural resources have been exploited to fulfill the human needs, resulting in the degradation of water quality leading to ecological imbalance. The industrial and urban activities have led to increasing concentrations of a wide range of contaminants in water resources, which affect the health of millions of people around the world [2]. Hence, it is of critical importance to keep the different sources of drinking water free from toxic materials that pollute them.

In the United States, hundreds of thousands of sites have been identified with varied degrees of contamination. The U.S. Environmental Protection Agency (EPA) stated that it will take 30 to 35 years and cost up to $250 billion to clean up the hazardous contaminated sites [3]. Water quality and water pollution are also a highly complex problem in China. Both surface and groundwater supplies have deteriorated significantly during China’s rapid economic development. Large quantities of contaminants have been discharged into the

water-ways, overwhelming the self-purification capacity of water bodies. Currently, China's water supplies are undergoing severe challenge. In addition to the eutrophication of lakes, deterioration of river water, certain toxic substances such as pesticides, arsenic, and fluorin have been routinely detected in large quantities in many surface and ground waters, which threaten the safety of drinking water supplies and make water quality problems more complex [4].

The magnitude 9 Great East Japan Earthquake and resulting tsunami on March 11, 2011, seriously damaged Fukushima Daiichi Nuclear Power Plant. A substantial number of radioisotopes such as strontium (^{90}Sr) and cesium (^{134}Cs and ^{137}Cs) were released into the environment and subsequently caused serious radioactive contamination of surrounding soil, groundwater and seawater. The radioactivity depositions of the Sr and Cs directly released into the ocean was estimated to be 52 GBq for ^{90}Sr and 3.5 PBq for ^{134}Cs and ^{137}Cs, whereas that of the strontium and cesium released onto the land surface was estimated to be around 8.56 PBq for ^{90}Sr and 288 PBq for ^{134}Cs and ^{137}Cs [5]. The primary pathway of these radionuclides in food chain is waters; therefore, technologies for the removal of hazardous radioactive materials from waters are highly desired.

Present purification techniques, though efficient, cause several problems and have limited application under natural conditions that make treatment processes increasingly complex. Emerging technologies, such as nanotechnology, could be applied as an efficient cost-effective technology in the cleanup of contaminated waters. As demonstrated by a number of field-based and bench scale studies, the use of nanotechnology in drinking water treatment and pollution cleanup is promising. Nanoremediation have the potential not only to reduce the overall costs of cleaning up large-scale contaminated sites but also to reduce cleanup time and reduce some hazardous pollutant concentrations to near zero in situ . Nanotechnology-based methods offer more effective alternatives to conventional treatment techniques [6].

1.2. Background overview

This section presents an overview of the target contaminants for treatment in this study and the technology related to the used treatment method.

1.2.1. Nitrate

Nitrate contamination of groundwater has become a real environmental and public health alarm worldwide. Elevated concentrations of nitrate in drinking water can cause a significant risk to human health such as methemoglobinemia and blue baby syndrome in infants, and the development of cancer due to the potential reduction of nitrate (NO_3^-) to nitrite (NO_2^-) [7]. In this regard, the WHO and U.S. EPA have set the maximum contaminant level (MCL) of nitrate in drinking water at 50 mg NO_3^-/L and 10 mg NO_3^-–N/L, respectively [8]. The European Drinking Water Directive has set the standard limit for nitrate as 11.3 NO_3^-–N mg/L. In coastal waters, nitrate can also lead to severe environmental problems such as eutrophication and contribute to the formation of harmful algal blooms. The intensive use of nitrogen fertilizers for agriculture has been identified as the main source of groundwater contamination by nitrate. Additional sources of nitrate contamination include animal manure, landfill leachate, leaking septic tanks, municipal storm water runoff and industrial waste discharges [9].

1.2.2. Cesium

The Great East Japan Earthquake occurred in 2011 triggered the Fukushima Daiichi Nuclear Power Plant accident. Large amounts of radionuclides released into the environment following this severe incident [10]. Radioactive fallout led to contaminated seawater, groundwater and drinking water. Japanese soils were also contaminated with radionuclides. One of the various radionuclides produced by a nuclear accident, radioactive cesium (^{137}Cs) is the most hazardous element of radionuclides due to its abundance in nuclear fallout and radioactive wastewater and the hazards presented by its long half-life (about 30 years) and high emission of beta and gamma particles [11]. Exposure of humans to ^{137}Cs results in a wide variety of adverse health effects. Individuals subjected to large amounts of ^{137}Cs may display signs of acute radiation syndrome, such as nausea, diarrhea and vomiting [12]. Dermal injuries ranged from radiation dermatitis to severe radiation injuries resulting in amputation were also reported. In addition, high doses of ^{137}Cs can damage DNA and cells and increase the chances of cancer [13]. In food chain, radioactive liquid waste is the primary pathway of radionuclides; therefore, technologies for removing dangerous radioactive isotopes from liquid waste have received much attention.

1.2.3. Strontium

The disposal of radioactive wastewaters has received substantial concern from an environmental perspective since the accident at the Fukushima Daiichi nuclear power plant, which released enormous amounts of radioactive strontium (^{90}Sr) into the natural environment, thereby contaminating the groundwater, seawater and land surface. In addition, with the rapidly increasing dependence on nuclear energy, the treatment of radioactive waste solutions has become one of the most significant challenges in nuclear waste management and nuclear industry to almost all countries . One of the major contaminants is radioactive strontium (^{90}Sr). ^{90}Sr is a beta-gamma particles emitter with a respective half-life of 28.8 years [14]. Further, strontium is widely used in many industrial applications, such as ceramics, ferrite magnets, fireworks and optical materials [15]. ^{90}Sr poses a major threat to human health as it can replace Ca in bones, leading to bone cancer, tissue cancer, anemia and leukemia [16]. Thus, the demand for novel techniques to remove Sr from contaminated waters is increasing.

1.3. Nanotechnology

Nanotechnology pertain to the synthesis, characterization, exploration, exploitation, and utilization of nanostructured materials, which are characterized by having size ranging from 1 through 100 nm with a minimum of one dimension (1nm = 10^{-9} m). The chemical and physical properties of nanomaterials can significantly differ from both the single atom or the molecule and from the bulk matter of the same chemical composition. The unique structural characteristics, energetics, chemistry, dynamics and response of nanomaterials are novel and constitute the conceptual background for the field of nanoscience and nanotechnology [17]. A wide array of new devices and technologies for both domestic and industrial applications can be produced through suitable control of the properties and response of nanostructured materials. As particle size of material decreases, the proportion of atoms located at the surface raises, which increases its tendency to adsorb and react with other atoms, molecules and complexes to attain charge stabilisation. In addition, their tiny size allows nanomaterials to be integrated within aqueous suspensions and behave as a colloid. Today, engineered nanostructured materials are in many of the products that we utilize daily. For example, nano-silicon is employed to increase the efficiency and speed of

computer processors, whereas carbon nanotubes are applied to improve the strength of construction materials and sports equipment [18].

Two types of manufacturing methods can be considered in the field of nanotechnology; bottom up approach and top down approach. The bottom up approach constructs the nanoparticles from basic building blocks, such as atoms and molecules. This approach was pioneered by Richard Feynman, revealing that “there is plenty of room at the bottom”. On contrary, the top down approach involves methods of the diminution and processing of a bulk material, leading to the production of nanoscale particles. This approach was advanced by Jean-Marie Lehn, stating that “there is plenty of room at the top” [17].

Although industrial sectors including semiconductors; optical and photonic technologies; memory and storage technologies; biotechnology; and health care form the most products containing nanoparticles, the use of nanotechnology for the treatment of polluted waters and cleanup of hazardous waste sites has sparked a great deal of interest. The unique properties of nanomaterials, such as high specific surface area, high reactivity and strong sorption can make dramatic changes in water treatment processes. Many different nanoscale materials, such as nanoscale zero valent iron (nZVI), zeolites, metal oxides, carbon nanotubes, polymers, titanium dioxide, enzymes and various noble metals have been investigated for remediation of radionuclides, metal ions and organic and inorganic compounds [2, 3, 6, 19]. Increasing specific surface area has a direct effect on increasing the reactivity of those nanoparticles. For example, nZVI with surface areas in the range of 20–40 m^2/g can yield 10–1000 times greater reactivity compared with granular particles, which has a surface area less than 1 m^2/g [3]. Nanoscale particles may be able to spread in the subsurface and remain suspended in groundwater due to their small size and innovative surface coatings, allowing the particles to travel farther and achieve wider distribution than larger-sized particles. Nanosized particles can also be deployed via injection at almost any location and depth in terrestrial groundwater systems, thus providing a versatile remediation tool. Additionally, nanoparticles can easily penetrate into soil pores, a property that is particularly beneficial when contaminants are present underneath a building [18].

1.4. Zero valent iron as a promising material for water treatment

1.4.1. Zero valent iron

Iron is considered the fourth most abundant element in the earth's crust. During the last decade, numerous studies have been investigated the removal of various types of contaminants using zero valent iron (ZVI) because it is abundant, non-toxic, easy to produce and cheap. ZVI, with standard redox potential ($E^0 = -0.44$ V), is an effective reductant when reacting with contaminants such as Cr(VI) [1]. Thus, the electron transfer from ZVI to the contaminants is the main removal mechanism of contaminants by ZVI. ZVI can be obtained from various methods. Physical methods were used, such as lithography, grinding, abrasion, nucleation from homogeneous solutions or gas as well as annealing at elevated temperatures. Chemical methods have also been developed for the synthesis of ZVI [20]. The ZVI can be obtained using a reducing agent such as sodium borohydride ($NaBH_4$), according to the following reaction:

$$Fe(H_2O)_6^{3+} + 3BH_4^- + 3H_2O \rightarrow Fe^0 \downarrow + 3B(OH)_3^- + 10.5H_2 \quad (1.1)$$

In aqueous solutions, ZVI transfers two electrons to oxygen (O_2) to produce hydrogen peroxide (H_2O_2) (Eq. (1.2)). Another two electrons transfer from ZVI can reduce H_2O_2 to water (H_2O) (Eq. (1.3)). The combination of ferrous ions (Fe^{2+}) and H_2O_2 can produce hydroxyl radicals (•OH) which can oxidize a variety of organic compounds (Eq. (1.4)) [1].

$$Fe^0 + O_2 + 2H^+ \rightarrow Fe^{2+} + H_2O_2 \quad (1.2)$$

$$Fe^0 + H_2O_2 + 2H^+ \rightarrow Fe^{2+} + 2H_2O \quad (1.3)$$

$$Fe^{2+} + H_2O_2 \rightarrow Fe^{3+} + \bullet OH + OH^- \quad (1.4)$$

ZVI is also recognized as being highly liable to corrosion in aqueous media. The aqueous corrosion reactions of ZVI as follows [18]:

$$2Fe^0 + 4H^+ + O_2 \rightarrow 2Fe^{2+} + 2H_2O \quad (1.5)$$

$$2Fe^0 + 2H_2O \rightarrow 2Fe^{2+} + H_2 + 2OH^- \quad (1.6)$$

$$Fe^{2+} + 2H^+ + 1/2O_2 \rightarrow 2Fe^{3+} + H_2O \quad (1.7)$$

$$2Fe^{2+} + 2H_2O \rightarrow 2Fe^{3+} + H_2 + 2OH^- \quad (1.8)$$

In recent years, ZVI has been applied successfully to remediate contaminated waters with heavy metals, arsenic, nitrate, nitroaromatic compounds, chlorinated organic compounds, phenols and dyes [1, 18, 20, 21].

1.4.2. Nanoscale zero valent iron

The adaptation of nanoscale zero valent iron (nZVI) to remove many kinds of environmental contaminants has received a great attention in the last 10 years due to its very high surface area to volume ratio, higher reactivity rates and higher mobility than micron scale ZVI. In addition, its application does not require excavation as nZVI slurries can directly be injected underground, at or near the contaminant source zone [22]. nZVI is the most commonly utilized nanomaterial in Europe and in the United States for groundwater and soil remediation. nZVI was first tested by Wang and Zhang for contaminated water treatment [23]. Then, it has been adopted as highly effective material for degradation of a wide range of chemical contaminants, including azo dyes, halogenated compounds, heavy metals, polycyclic aromatic hydrocarbons, nitrate, phosphate, arsenic, selenium, uranium and plutonium [18]. The size of nZVI particles is typically less than 100 nm. The material can develop a core–shell structure when reacts with air or water (see Fig. 1.1). The thin outer iron (hydr)oxide layer facilitates electron transfer from the metal, thus maintaining reducing ability of the particles for containments. At the same time, the shell layer may also act as an efficient adsorbent for different pollutants. Because of the significant variation in contaminant chemistry, different contaminant removal mechanisms have been determined, including sorption, (co)precipitation, complexation and chemical reduction (Table 1.1) [24].

Fig. 1.1. Core–shell structure of nZVI.

The removal mechanism by nZVI for metal ions that have standard electrode potentials (E^0) that are very close to, or less than Fe^0 ($E^0 = -0.44$ V) like Cd^{2+} ($E^0 = -0.40$ V) and Zn^{2+} ($E^0 = -0.76$ V), occurs predominantly via sorption/surface complexation. In comparison, with metal ions that have E^0 much more positive than Fe^0 such as Hg^{2+} ($E^0 = 0.86$ V) and Cu^{2+} ($E^0 = 0.16$ V), removal occurs principally by surface mediated reductive precipitation.

Table 1.1: Possible contaminant removal pathways by nZVI.

Redox couple	Predominant removal mechanism using nZVI
$Cd^{2+} + Fe^0 \rightarrow Cd^0 + Fe^{2+}$	Sorption/surface complexation
$Zn^{2+} + Fe^0 \rightarrow Zn^0 + Fe^{2+}$	Sorption/surface complexation
$Hg^{2+} + Fe^0 \rightarrow Hg^0 + Fe^{2+}$	Reductive precipitation
$Cu^{2+} + Fe^0 \rightarrow Cu^0 + Fe^{2+}$	Reductive precipitation

1.4.3. Recent advances in nZVI

In spite of its effectiveness in the removal of contaminants, using nZVI in practical applications is limited due to its easy aggregation, lack of stability, limited mobility, rapid passivation and difficult separation from the treated medium. Many methods have been developed to overcome the weaknesses accompanying the use of nZVI and to increase effectiveness of nZVI, including doping of nZVI with other metals to form bimetallic iron nanoparticles, coating the surface of nZVI with stabilizers and deposition of nZVI onto solid porous supports.

1.4.3.1. Bimetallic nanoparticles

The deposition of a second transition noble metal such as copper (Cu), palladium (Pd), nickel (Ni), silver (Ag) or platinum (Pt) on the surface of iron to form bimetallic particles is a very well documented method of improving the remediation properties of nZVI. A small amount of those metals applied on the surface of nZVI greatly increases reactivity of the resultant particles. The noble metals enhance the reduction rates of nZVI significantly by serving as catalysts or reactive electron donors. Bimetallic iron nanoparticles play an important role in preventing oxide formation on the particle surface and provide good protection against passivation. In order to achieve the highest reactivity, Zhu and Lim [25]

recommend that metals be added to the nZVI at the time of use, rather than synthesizing bimetallic particles a priori and storing them. Pd is the most widely used catalyst with nZVI for remediation purposes. Fe/Pd bimetallic system shows extremely high removal efficiency for monochlorobenzene, tetrabromobisphenol A, 2,4-dichlorophenol and polychlorinated biphenyls. Tee et al. [26] reported the reaction rate of Fe/Ni particles to be much higher than bare nZVI for removal of Trichloroethylene (TCE). Similarly, Schrick et al. [27] inducated the degradation rate of TCE by Fe/Pd nanoparticles was over an order of magnitude faster than nZVI and nine times faster than Fe/Ni particles.

The disadvantages of bimetallic particles are their short lifetimes and the added environmental risk associated when injecting another metal into the subsurface [21].

1.4.3.2. nZVI surface coating

Numerous reports have shown that bare nZVI tends to agglomerate rapidly due to the high surface energy and strong intrinsic magnetic interaction between nZVI particles, decreasing nZVI dispersion in aqueous media and mobility in porous media. Therefore, researchers have focused on coating iron nanoparticles with stabilizers to minimize aggregation and settling, thereby increasing nZVI mobility to interact with target contaminants. These coatings/stabilizers include carboxymethyl cellulose (CMC), triblock copolymers, chitosan, xanthan gum, guar gum and cetyltrimethylammonium bromide (CTAB). Furthermore, Zhao et al. and Dong et al. adopted different stabilizers (polyacrylic acid (PAA), polyvinyl alcohol (PVA), Tween-20 and starch) to modify nZVI due to their availability, low cost and environmental safety [19, 21]. These surface modifiers cause a change of surface charge of nZVI to provide electrostatic repulsion and steric or electrosteric stabilization, which can improve its dispersion, stability and enhance its removal ability for various environmental contaminants in situ.

Emulsification of nZVI has also been applied to limit particle–particle and particle–soil interactions. In this approach, nZVI particles can be stabilized through their encapsulation in an oil phase utilizing viscosity to prevent particle settling. The nZVI emulsions are based on the formation of the type water-in oil-in water (W/O/W) [28] or oil-in water (O/W) [29]. A hydrophobic membrane is formed in W/O/W that separates nZVI particles contained in water droplets (10–20 μm) from the remaining medium. In the case

of O/W, iron nanoparticles are placed in oil droplets (1–2 μm) which cause a reduction of aggregation and preventing oxidation of the nanoparticles.

1.4.3.3. Immobilization of nZVI onto supports

The synthesis of nZVI immobilized on solid porous materials such as silica, activated carbon, zeolites, bentonite, kaolinite, palygorskite, resin, polystyrene resins, silica, carbon, green tea, multiwalled carbon nanotubes (MWCNTs), mesoporous carbon, mesoporous silica, graphene, reduced graphene oxide (rGO) and polymer membranes have attempted to remove different contaminants [18-20]. The use of such materials supporting nZVI can affect its physicochemical properties, prevents its oxidation and aggregation and provides an easy operation. Immobilizing nZVI particles on those supporting materials demonstrated high effectiveness in the removal of Pb(II), Cd(II), Cu(II), As(III), As(V), Cr(VI), nitrobenzene (NB), TCE, bisphenol A and dyes from waters [1, 20].

Among these complexes, graphene nanomaterials (GNs) supported nZVI have received a great research interest due to their superior physicochemical properties. Jabeen et al. [30] reported nZVI/G had a higher adsorption capacity for Cr(VI) ions (162 mg/g) compared with nZVI alone (148 mg/g). Li et al. [31] synthesized graphene oxide nanosheets supported nZVI (nZVI/GO) for in situ remediation of Cr(VI) polluted water, which achieved an effective adsorption ability (21.72 mg/g). The reduced graphene oxide supported nZVI (nZVI/rGO) was also developed to increase the reactivity and stability of nZVI. The nZVI/rGO showed excellent removal performance for Cr(VI) (187.16 mg/g) and Pb(II) (396.37 mg/g). Li et al. [32] also used nZVI/rGO to remove U(VI) ions under anoxic conditions and indicated that the removal capacity of U(VI) on nZVI/ rGO was similar to that on bare nZVI, achieving an adsorption capacity of 4174 mg/g.

1.4.4. Removal of hazardous contaminants by nZVI from waters

The use of nZVI for remediation of contaminated sites has received significant attention in recent years due to its ability to transform contaminates from toxic species to non-toxic or less toxic ones. nZVI is the most widely studied nanomaterial for water treatment. Numerous papers have been published in the last 10 years, summarizing the different aspects of science and technology for those nanoparticles. nZVI has shown to be an effective and versatile tool for the purification of contaminated waters and soils. It has

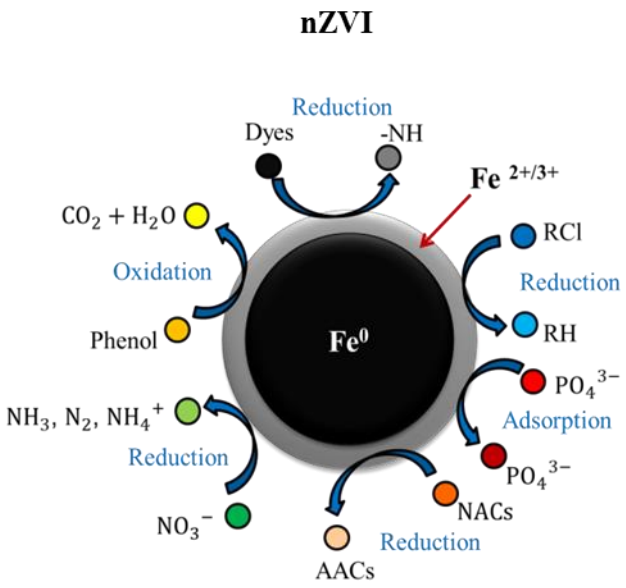

Fig. 1.2. Reaction mechanism of nZVI with different contaminants.

been proposed for use in the remediation of a wide range of priority pollutants, including heavy metals, arsenic, nitrates, nitro aromatic compounds (NACs), chlorinated organic compounds (COCs), dyes and phenols. nZVI enhance the removal efficiencies of those contaminants remarkably by diverse mechanisms as illustrated in Fig. 1.1. The application of nZVI in the treatment of the environment not only reduces the concentration of potential harmful substances, but also reduces the costs of large scale remediation and of the duration of the removal process.

1.4.4.1. Heavy metals removal by nZVI

Heavy metals are not biodegradable, toxic, carcinogenic and tend to accumulate in living organisms. During the last few years, nZVI has been widely investigated for the remediation of heavy metal ions and demonstrated effective removal and prosperous application for in situ purification of heavy metals. The carcinogenic, soluble and mobile Cr(VI) may be reduced by nZVI to less toxic Cr^{3+}, followed by subsequent precipitation as $Cr(OH)_3$ (Eqs. (1.3) and (1.4)) [33].

$$Cr_2O_7^{2-} + 2Fe + 14H^+ \rightarrow 2Cr^{3+} + 2Fe^{3+} + 7H_2O \quad (1.9)$$

$$Cr^{3+} + Fe^{3+} + 6OH^- \rightarrow Cr(OH)_3 \downarrow + Fe(OH)_3 \downarrow \quad (1.10)$$

nZVI was also applied to treat other heavy metals. Pb(II) and Ni(II) may be removed by nZVI through reduction, adsorption and surface precipitation [34]. nZVI also showed high uptake capacities and fast uptake kinetic toward Cu(II), Cd(II) and Zn(II). Üzüm et al. [35] demonstrated that nZVI was effective in the removal of Co(II) ions. Li et al. [36] indicated that nZVI/rGO revealed great removal capacity to Cd(II). Zhou et al. [37] found that more than 80% Sb(III) could be reduced into Sb(0) by nZVI/zeolite composite. Li et al. [38] reported that the combination of pillared bentonite with nZVI (nZVI/Al-bent) could enhance the reductive transformation of Se(VI) into less soluble Se(II).

1.4.4.2. Arsenic removal by nZVI

Hazardous arsenic is present in natural waters mostly in the forms of arsenate (As(V)) and arsenite (As(III)). Arsenic is classified by WHO as a first priority pollutant. Due to its toxic and carcinogenic effects, WHO has regulated the maximum arsenic concentration in drinking water to be less than 10 µg/L. As(III) is much more toxic and more mobile than As(V). Recent studies confirmed the potential use of nZVI for in situ treatment of arsenic contamination. The main removal mechanism of arsenic by nZVI involves reduction, adsorption, oxidation, precipitation and co-precipitation. Ramos et al. [39] investigated As(III) removal by nZVI and indicated 51% of the surface-bound arsenic remained as As(III) whereas 14% and 35% was transformed to As(V) and As(0). However, the common geochemical conditions may control the overall effectiveness of arsenic removal by nZVI. Biterna et al. [40] studied arsenic removal under different key parameters such as DO, pH, humic acid and hardness and results revealed that most of these variables affected negatively the removal of arsenic.

1.4.4.3. Uranium removal by nZVI

Uranium (U) is the most common radionuclides found at many nuclear waste sites. It is highly soluble and mobile in contaminated groundwater. Uranium pollution from related activities brings a higher health risk to human beings. Uranium contamination in water bodies can harm humans both chemically and radioactively. nZVI has been proven to be one of the most promising technologies for the removal of radioactive residuals from contaminated areas due to its large surface area and high number of active sites. Some studies demonstrated the effectiveness of nZVI in restoration of uranium contaminated

water resources [41]. The removal capacity of uranium by nZVI ranges from 0.43 mg/g to 8170 mg/g under a variety of conditions of remediation [42]. Different processes are involved in the removal of uranium by nZVI such as reduction, adsorption and minor precipitation. However, the removal capability of uranium by nZVI follows certain rules. At low concentrations of uranium (50–2500 µg/L), reaction equilibrium can be achieved within 24 h with a removal efficiency from 85% to 99% whereas in high concentrations of contaminated waters (20–1000 mg/L), it takes more than 10 days to remove on average 75% uranium [43].

1.5. Practical applications of nZVI

The use of nZVI for in situ environmental remediation has been applied in many countries, including the USA, Canada, Germany, the Czech Republic, Slovakia and Italy. The method of nZVI injection may be possible at almost any location and depth in a terrestrial groundwater system. The nZVI injection strategy can be tailored for the purification of mobile or immobile contamination. Injection of low mobile nZVI to form a reactive barrier is typically used for the treatment of mobile contaminant plumes. For the treatment of a static contaminant site, injection of mobile nZVI is typically selected for direct treatment. The National Institute of Environmental Health Sciences recorded 44 sites worldwide where nanomaterials were injected for remediation purposes [3]. Different pilot projects, in which nZVI was used for the treatment of waters, were conducted in real conditions. The achieved efficiency of contaminant removal varied from 40% to 100% depending on the kind of nZVI used and the type of contaminant to be removed [44].

The first pilot tests of the use of nZVI was carried out in 2000 in USA. 2.5 kg of nZVI/Pd was applied at a concentration of 1 g/L for the treatment of groundwater contaminated with PCE, TCE, VC and chloroform. A 96.5% removal of chloroorganic contaminants was obtained after 4 weeks of purification [45]. nZVI was also used at large scale application primarily for the elimination of chloroorganic contaminants from groundwater [46]. The US EPA listed 25 sites in the USA where nZVI was applied on a large scale for soil remediation. In Czech Republic, 300 kg of nZVI were injected over an area of several square kilometers and the removal of contamination varied from 60% to 90% [46].

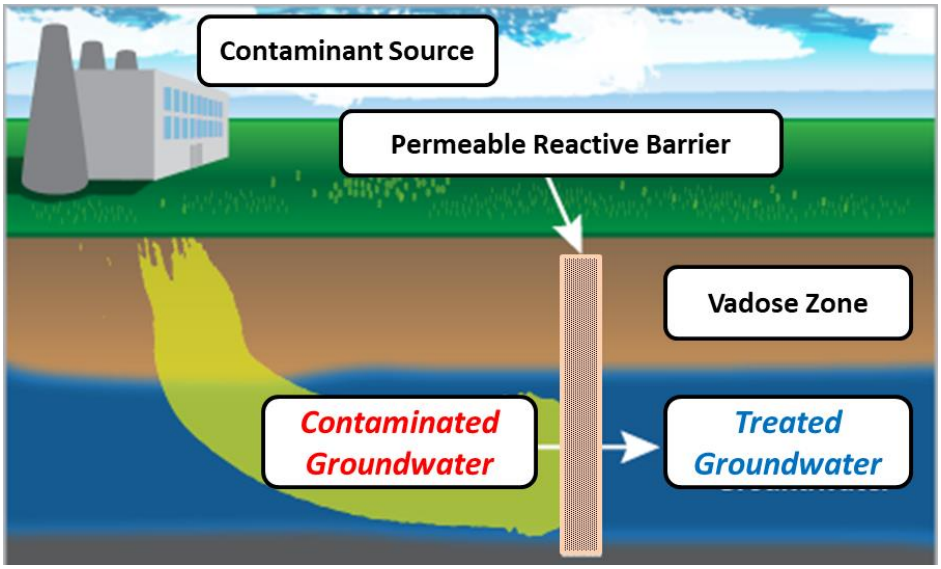

Fig. 1.3. Permeable reactive barriers (PRBs) technology.

Other in situ treatment technology is the permeable reactive barriers (PRBs). PRBs have been acknowledged as an innovative technology for sustainable in situ remediation of contaminated surface and subsurface waters due to their low cost, high efficiency and environmental friendly. A PRB is constructed perpendicular to the path of contaminated groundwater and down gradient as shown in Fig. 1.3. The reactive media within the PRB degrade or immobilize the contaminants as the water passes through the barrier [47]. ZVI PRBs have been successfully used to remediate groundwater contaminated by heavy metals, COCs [48], arsenic [49] and nitrate [50]. There are more than 200 ZVI PRBs developed at different contaminated sites since the first successful installation of the technology in 1995. In 2002, the US EPA classified the ZVI PRBs as a standard treatment technology. One drawback of PRBs is that they can only treat contaminant plumes that flow through them; they do not remediate contaminated waters that is beyond the barrier [3].

1.6. The environmental toxicology of nZVI

The concept of injecting engineered nanoparticles into environment, as a remedial method, has also attracted concern from both academic and environmental authorities. Consequently, the determination of the impact of nZVI on living organisms is of particular significance because of the increasingly popular use of those nanoparticles in the purification of waters and soils. The toxicity of nZVI particles towards living organisms can be caused specifically by their small size and high redox reactivity [51]. In the literature,

limited studies have reported demonstrable toxicity of nZVI to cells of different types and a majority of the reports focused mainly on its effect on microorganisms.

Studies revealed that nZVI can be adsorbed on cell membranes of bacteria which can cause structural changes to the membranes, block cellular ducts and inhibit mobility and nutrient intake leading to the death of bacteria [52]. The formation of reactive oxygen species (ROS), as a result of its oxidation, may arise peroxidation of lipids and damage to DNA and cells. It should be emphasized, however, that the strain of bacteria has a significant effect on their sensitivity to the presence of nZVI . For aquatic and soil organisms, the presence of CMC-nZVI proved to have high toxic effects on larvae of Oryzias latipes and Heterocypris incongruens in both soil andaquatic environments [53]. A high negative effect on the reproduction and mortality of soil organisms Folsomia candida was resulted from limited availability of oxygen and the effect of ROS formed during the oxidation of CMC-nZVI [54]. An inhibition of growth or an absence of mortality was noted in relation to earthworms (Eisenia fetida, Lumbricus rubellus) at a dose above 100 CMC-nZVI mg/kg of soil [55].

The toxic effect of nZVI on plants depends on the plant kind, the nZVI concentration and the properties of nanoparticles. An inhibiting effect of nZVI was observed on the growth and germination of Hordeum vulgare, Lolium perenne and Linum usitatissimum [56]. The direct deposition and accumulation of nZVI on roots surfaces resulted in the blocking of water and nutrient uptake by plant roots [56]. Due to its low solubility in water, nZVI can persist in biological systems causing a mutagenic effect on organisms [3]. It was also noticed an inhibition of growth of young leaves and decay of older ones in the presence of nZVI particles [57]. In case of mammalian cells, nZVI dissolved in physiological saline can cause the death of human bronchial epithelium cells. Some studies showed that nanoparticles of iron can lead to neurotoxic effects in rodent and neuron microglia [58]. The products of nZVI oxidation demonstrated to cause peroxidation of lipids and damage to DNA.

To sum up, it can be stated that nZVI can have a negative effect on microorganisms, animals, plants, and humans. However, it should be emphasized that the persistence of nZVI particles in subsurface environments will be limited due to their acute redox sensitivity. Even stabilized nZVI is likely to be immobilized in the subsurface through

aggregation, mineral sorption or degradation via oxidation. In addition, nanoparticles in real environments proved to be less toxic than indicated by laboratory experiments. Tong et al. [59] observed that C_{60} fullerenes, which destroyed microbes in the laboratory, did not cause serious damage to the microbial cultures present in the soil after several weeks of exposure. Moreover, the toxic effects of nZVI in most observed cases are below the level observed for other nanoparticles. The lower toxicity of nZVI may be because iron is a necessary element for all living organisms for correct development and a common element exist in soils [55]. Ma et al. noted a positive effect of nZVI on Typha latifolia growth [57]. As in the case of plant, a stimulation of the growth of Gram (+) bacteria in soils was observed [60]. It is worth mentioning that by applying a suitable modification, method of synthesis and dose, nZVI can be applied for the environmental treatment without any harmful effects on the surroundings.

1.7. Research aim and objectives

The main goal of the current research work was to develop a novel treatment process for efficient and selective removal of nitrate and radioactive isotopes (such as cesium and strontium) from contaminated waters. Therefore, this research introduces a new technology to deal with the environmental challenges in a manner that manages and conserves water resources, supports the economic growth requirements and sustainable regional development, provides a cleaner environment and ensures high quality of life for all citizens. This work supports the policies of waste treatment to create a healthy society and ensures sustainable development of drinking water resources for substantial population growth. The main objectives of this research study were:

- Study the effectiveness of nZVI and nano-Fe/Cu particles for the removal of nitrate in porous media using an upflow packed sand column. The effect of multilayer system and different thickness layers of nZVI/sand and (nano-Fe/Cu)/sand on the nitrate removal performance was investigated.
- Investigate the efficiency of nZVI and nano-Fe/Cu particles for cesium removal from aqueous solutions. The effect of several variables such as initial cesium concentration, contact time, pH, temperature, competing cations and dosage of the nanoparticles on the sorption behavior of cesium was studied using a batch

technique. The kinetic, thermodynamic and isotherm parameters of the removal process were investigated. The mechanism of cesium removal was discussed using different characterization approaches. The removal performance was also evaluated in simulated contaminated water after Fukushima accident.

- Fabricate nZVI–zeolite and nano-Fe/Cu–zeolite composites for the removal of cesium from aqueous solutions with the ability to separate the adsorbent magnetically. Batch sorption experiments were carried out to assess the effect of different parameters such as pH, initial concentration, contact time, adsorbent dosage and temperature. The kinetic, thermodynamic and isotherm parameters of the process were evaluated.
- Synthesize nanocomposites of nZVI–zeolite and nano-Fe/Cu–zeolite to determine their effectiveness in the sorptive removal of strontium from aqueous solutions and to enhance the separation of zeolite tiny particles from the environment after use magnetically. A variety of operating conditions such as initial strontium concentration, contact time, initial solution pH, temperature, presence of competing cations and dosage of nanocomposites were investigated. The strontium sorption behavior was assessed in terms of sorption isotherm, kinetic and thermodynamic studies. The nanocomposites were also applied in a real seawater medium.

1.8. Dissertation layout

This dissertation is consisted of seven chapters organized as follows:

Chapter 1 gives a general background about the current situation of water pollution and presents an overview of the target contaminants for treatment in this research, nanotechnology for water treatment and the role of nZVI as a promising material in decontaminating a broad range of pollutants. The literature survey on nZVI involves recent advances in this technology, efficiency of nZVI in detoxification of a variety of common environmental pollutants, use of nZVI in filed scale application and toxicity assessment of nZVI on living organisms. It also contains aim and objectives of the research and describes the structure of the dissertation.

Chapter 2 presents the materials and methods that were used in conducting the experimental works of this research involving chemicals preparation, synthesizing

procedure of pristine nZVI, bimetallic nano-Fe/Cu particles and composites with zeolite, characterization of the prepared nanomaterials and analytical investigations.

Chapter 3 introduces nitrate removal efficiency in porous media using nZVI and bimetallic nano-Fe/Cu particles in a multilayer system through an upflow packed sand column. The effect of multilayer and different thicknesses of nZVI/sand and nano-Fe/Cu particles on the nitrate removal performance was investigated. The distribution of nitrate trapped inside the column was evaluated by measuring nitrate concentrations, not only at the column inlet and outlet, but also at various intermediate sampling ports along the depth of the column.

Chapter 4 outlines the capability of nZVI and bimetallic nano-Fe/Cu particles for cesium removal from aqueous solutions. The effect of several variables such as initial cesium concentration, contact time, pH, temperature, competing cations and dosage of the nanoparticles on the sorption behavior of cesium was studied using a batch technique.

Chapter 5 displays synthesis of nZVI–zeolite and nano-Fe/Cu–zeolite composites through ion exchange process followed by liquid-phase reduction. The performance of the composites for the removal of cesium from aqueous solutions with the ability to separate the adsorbent magnetically was investigated. Batch sorption experiments were systematically carried out to assess the effect of different parameters such as pH, initial concentration, contact time, adsorbent dosage and temperature.

Chapter 6 shows the effectiveness of nZVI–zeolite and nano-Fe/Cu–zeolite composites in the sorptive removal of strontium from aqueous solutions. The sorption of strontium on both nanocomposites was studied in a batch sorption mode as a function of various environmental conditions such as initial strontium concentration, contact time, pH, temperature, dosage of sorbent and competing cations.

Chapter 7 includes the concluded remarks, main conclusions and recommendations drawn from this research.

CHAPTER 2

MATERIALS AND METHODS

CHAPETR 2- Materials and Methods

This chapter presents the materials and methods that were used in conducting the experimental works of this research involving chemicals preparation, synthesizing procedure of pristine nZVI, bimetallic nano-Fe/Cu particles and composites with zeolite, characterization of the prepared nanomaterials and analytical investigations.

2.1. Materials and chemicals

All chemicals and minerals utilized in this work were of analytical grade and used as received without further purification. All aqueous solutions and suspensions were prepared by deionized water and were purged with nitrogen for 20 min for deoxygenation process. To prepare the magnetic nanoparticles and nanocomposites, ferric chloride hexahydrate ($FeCl_3 \cdot 6H_2O$, 99%, Junsei Chemical Co., Japan), sodium borohydride ($NaBH_4$, 98%, Sigma–Aldrich Inc., USA), anhydrous copper chloride ($CuCl_2$, 99.9%, Aldrich Inc., USA) and ethanol (99.5%, Wako Co., Japan) were used. Commercially available zeolite powders (particle size <45 μm, surface area 900 m^2/g, pH_{pzc} 7.1) were supplied from Sigma Co., Germany. Potassium nitrate (KNO_3, 99.0%, Wako Co., Japan) was used to make the nitrate solution. Cesium was supplied as cesium chloride (CsCl, 99.9%), from Wako Co., Japan. Strontium chloride ($SrCl_2.6H_2O$, 99.9%, Wako Co., Japan) was applied as a source of strontium ions. To control solution pH, solutions of 0.01–1.0 M hydrochloric acid (HCl, 35–37%, Wako Co., Japan) and sodium hydroxide (NaOH, >93%, Wako Co., Japan) were used. Sodium sulfate (Na_2SO_4, 99%, Wako Co., Japan), magnesium chloride hexahydrate ($MgCl_2.6H_2O$, 97%, Wako Co., Japan), sodium bicarbonate ($NaHCO_3$, 99%, Wako Co., Japan) and calcium chloride dihydrate ($CaCl_2.2H_2O$, 70–79%, Junsei Chemical Co., Japan) were purchased to prepare simulated groundwater. Sodium chloride (NaCl, 99.5%, Wako Co., Japan), magnesium chloride hexahydrate ($MgCl_2 \cdot 6H_2O$, 97%, Wako Co., Japan), potassium chloride (KCl, 99%, Wako Co., Japan) and calcium chloride dihydrate ($CaCl_2 \cdot 2H_2O$, 70–79%, Junsei Chemical Co., Japan) were provided to simulate seawater concentration minerals and to evaluate the selectivity of the prepared samples. Standard sand (As One Co., Japan) was used as porous medium. Maximum and minimum diameter of sand particle was equal to 2 and 0.075 mm, respectively. The sand properties were estimated as bulk density (ρ_b = 1.3 g/cm^3) and average porosity (n = 0.35).

2.2. nZVI synthesis

nZVI was synthesized following the method first proposed by Wang and Zhang [23], based on chemical reduction of $FeCl_3 \cdot 6H_2O$ using $NaBH_4$ as depicted in the following reaction:

$$4Fe^{3+} + 3BH_4^- + 9H_2O \rightarrow 4Fe^0 + 3H_2BO_3^- + 12H^+ + 6H_2 \quad (2.1)$$

Briefly, $NaBH_4$ (98%, 0.74 M) was pumped slowly into $FeCl_3 \cdot 6H_2O$ (99%, 0.15 M) at a rate of 1.2 L/h using a roller pump in 500 mL four-neck glass flask as shown in Fig. 2.1. A continuous flow of nitrogen gas was maintained during synthesis to create an anaerobic condition. The synthesis was conducted with vigorous stirring at 400 rpm and kept under constant temperature 30 ± 0.5 ºC using a water bath. To complete the reaction, the synthesis was left 5 min as aging time. After reduction, the synthesized nanoparticles were washed with deionized deoxygenated water and ethanol at least three times, filtered by vacuum filtration and applied immediately in batch experiments.

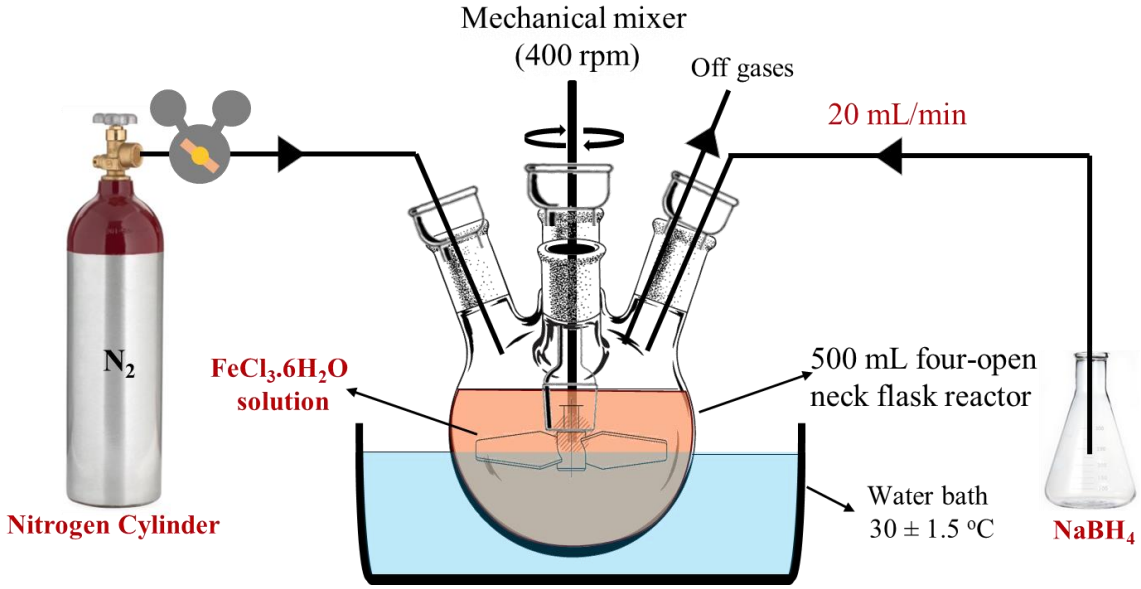

Fig. 2.1. Schematic of nZVI synthesis process.

2.3. Nano-Fe/Cu synthesis

Bimetallic nano-Fe/Cu particles were synthesized based on chemical reduction of ferric chloride hexahydrate using sodium borohydride as described in Eq. (2.1). In order to make 1 g of nano-Fe/Cu particles, sodium borohydride solution ($NaBH_4$, 98%, 0.74 M) was added slowly into ferric chloride hexahydrate ($FeCl_3.6H_2O$, 99%, 0.15 M) mixed with $CuCl_2$ in 500 mL four-neck glass flask at a rate of 1.2 L/h using a roller pump. The synthesis was processed under a continuous flow of nitrogen gas to create anaerobic condition. The synthesis was conducted with vigorous stirrer 400 rpm, under temperature 30 ± 0.5 ºC using water bath and left for 5 min as aging time to complete the reaction. The resulting black precipitates were filtered by vacuum filtration, washed with deoxygenated deionized water and ethanol three times and then applied immediately in batch experiments. According to Khalil et al. [61], the optimum coating rate in case of nano-Fe/Cu was 5% wt/wt of $CuCl_2/Fe^0$. The redox reaction between Cu^{2+} and nZVI occurred as follows:

$$Fe^0 + Cu^{2+} \rightarrow Fe^{2+} + Cu^0 \quad (2.2)$$

2.4. Preparation of nZVI–zeolite composite

The nZVI–zeolite composite was prepared by modifying the method first described by Wang et al. in our laboratory [62, 63]. The coating process consisted of a 1:1 mass ratio of nZVI and zeolite. Briefly, 2.5 g of $FeCl_3 \cdot 6H_2O$ and 0.5 g of zeolite were mixed in 100 mL of deoxygenated deionized water. The initial solution pH was monitored to be 4. The solution was treated with ultrasound for 10 min, and then vigorously stirred at room temperature for 30 min. To ensure a high degree of reduction of exchanged Fe(III), 50 mL of 0.58 M $NaBH_4$ solution was added at a rate of 1.2 L/h and agitated at 400 rpm in a 500 mL four-neck glass flask at 30 ºC as depicted in Fig. 2.2. The entire aqueous solution reduction process was carried out under anoxic condition by purging the system with a continuous flow of nitrogen. The resulting black solids were separated from the liquid phase using centrifugation at 5000 rpm (H-36, Sinoinstrument Co., Japan). The collected solids were then washed by centrifugation several times with deoxygenated deionized water and ethanol. Afterwards, the prepared nanocompiste materials were applied immediately in batch experiments.

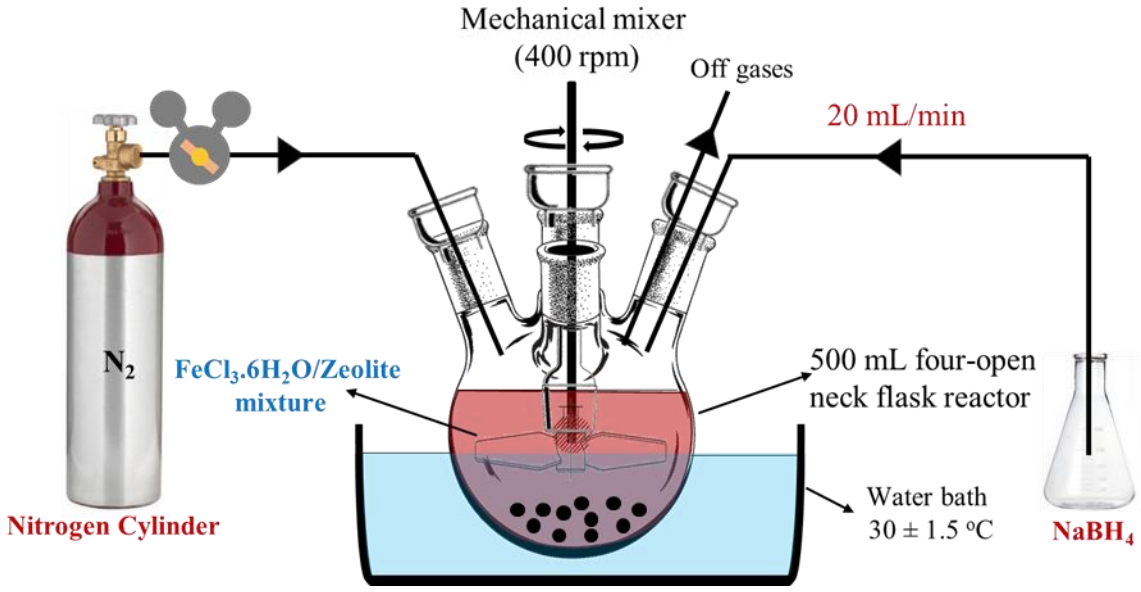

Fig. 2.2. Schematic description of nZVI–zeolite composite preparation.

2.5. Preparation of nano-Fe/Cu–zeolite composite

The nano-Fe/Cu–zeolite composite was prepared according to a procedure described by Wang et al. [63]. Briefly, 2.5 g of $FeCl_3.6H_2O$ were mixed with 0.5 g of zeolite in 100 mL of deoxygenated deionized water at a mass ratio of 1:1 (Fe^0:zeolite). The liquid-solid suspension was treated for 10 min using ultrasound, and then mixed vigorously at ambient temperature for 30 min. Subsequently, the mixture was placed in a four-necked flask and 50 mL of 0.58 M $NaBH_4$ solution was carefully pumped at a rate of 1.2 L/h with vigorous stirring (~400 rpm) and under constant temperature of 30 ºC. The $CuCl_2$ was added to $FeCl_3.6H_2O$ solution at a rate of 5% wt/wt of $CuCl_2/Fe^0$ before the launch of $NaBH_4$ reduction. The production of Fe^0 was the consequence of redox reaction in which electrons from $NaBH_4$ (reducing agent) were given to Fe^{3+} according to Eq. (2.1). Deposition of Cu on Fe^0 surfaces follows Eq. (2.2). The reduction reaction was performed under anaerobic conditions to avoid the rapid oxidation of Fe^0 particles. After the addition of $NaBH_4$, the resulting mixture was agitated for an additional 5 min as aging time. The black solid products were isolated from the aqueous phase through centrifugation at 3500 rpm for 60 min (H-36, Sinoinstrument Co., Japan) and then sequentially washed with deoxygenated deionized water to remove residual salts.

2.6. Material characterization

In order to determine the crystalline structure of the synthesized nanomaterials, X-ray diffraction patterns were obtained using Cu/Kα radiation operating at a tube voltage of 40 kV and current of 200 mA with scanning speed of 2° min–1 and scanning range between 3° and 90° (XRD, TTR, Rigaku, Tokyo, Japan) (see Fig. 2.3). The morphology of the prepared materials was examined using a transmission electron microscope (TEM, JEM−ARM 200F, JEOL Co., Japan) (Fig. 2.4). Scanning electron microscope coupled with energy dispersive X-ray spectrometry (SEM-EDS, JCM-6060LA/VI, JEOL Co., Japan) was also used to observe the morphological structure and to provide the elemental distribution of the samples (as depicted in Fig. 2.5). The Brunauter–Emmett–Teller (BET) specific surface area (SSA) was recorded for the nanoparticles using N_2 adsorption at 77 K on a specific surface area analyzer (Micromeritics 3Flex, USA) as shown in Fig. 2.6a, this BET SSA analysis was conducted after drying the nanomaterial samples in tubes at 150 C and degassed at 350 C for 2 h under N_2 stream. The particle size of the nanoparticles was measured using a laser diffraction particle size analyzer (SALD-2300, Shimadzu Co., Japan) (Fig. 2.6b).

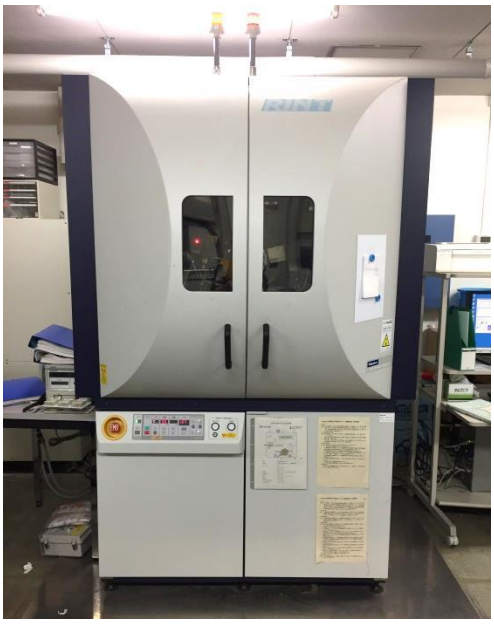

Fig. 2.3. X-Ray Diffraction (XRD, TTR, Rigaku, Tokyo, Japan).

Fig. 2.4. Transmission Electron Microscope (TEM, JEM−ARM 200F, JEOL Co., Japan).

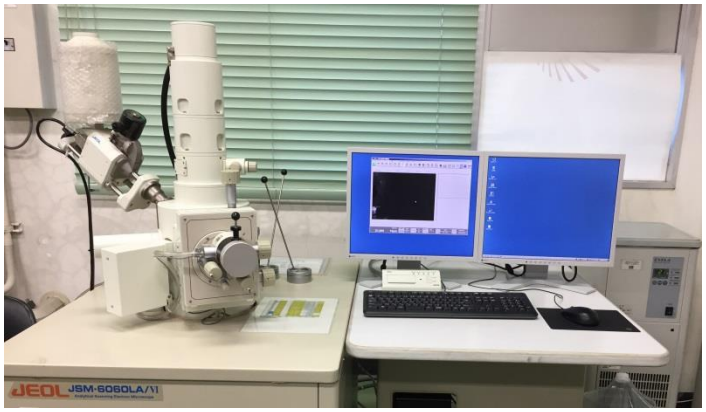

Fig. 2.5. Scanning Electron Microscope-Energy Dispersive X-Ray Spectrometry (SEM-EDS, JCM-6060LA/VI, JEOL Co., Japan).

(a) (b)

Fig. 2.6. (a) Specific Surface Area Analyzer (Micromeritics 3Flex, USA) and (b) Particle Size Analyzer (SALD-2300, Shimadzu Co., Japan).

2.7. Chemical analysis

Nitrate, nitrite, ammonium and dissolved total iron were determined using an UV–visible spectrophotometer (DR 3900, Hach Co., USA) as shown in Fig. 2.7, employing dimethylphenol method at 345 nm, USEPA diazotization method at 515 nm, salicylate meth od at 690 nm and TPTZ method (2,4,6-tri(2-pyridinyl)-1,3,5-triazine) at 590 nm, respectively. For cesium and strontium measurements, the liquid samples were analyzed using inductively coupled plasma mass spectrometry (ICP-MS, model: ICPM-8500, Shimadzu Co.) (see Fig. 2.8) by a 1000 times dilution in 1% nitric acid (HNO_3, 69%, Wako Co., Japan) [41]. Samples with elevated cesium or strontium concentrations were diluted by a 10000 factor. Besides, blanks, cesium and strontium standards at 0.1, 0.2, 0.5, 1, 5, 10, 50 and 100 ppb were prepared in 1% nitric acid [64]. pH and ORP were measured using a pH/ORP digital meter (D-72, Horiba Co., Japan).

Fig. 2.7. UV–Vis Spectrophotometer (DR 3900, Hach Co., USA).

Fig. 2.8. Inductively Coupled Plasma Mass Spectrometry (ICP-MS, model: ICPM-8500, Shimadzu Co.).

CHAPTER 3

MULTILAYER SYSTEM OF NZVI AND FE/CU NANOPARTICLES FOR NITRATE REMOVAL IN POROUS MEDIA

CHAPETR 3- Multilayer System of nZVI and Fe/Cu Nanoparticles for Nitrate Removal in Porous Media

In this chapter, nitrate removal efficiency in porous media was studied using nZVI and bimetallic nano-Fe/Cu particles in a multilayer system through an upflow packed sand column. The effect of multilayer and different thicknesses of nZVI/sand and nano-Fe/Cu particles on the nitrate removal performance was investigated. The distribution of nitrate trapped inside the column was evaluated by measuring nitrate concentrations, not only at the column inlet and outlet, but also at various intermediate sampling ports along the depth of the column. It was concluded that using nZVI in the full length of porous media or using nano-Fe/Cu particles in multilayer porous media could enhance nitrate removal effectively.

3.1. Introduction

Several physico-chemical and biological technologies have been proposed for removing nitrate from contaminated water like ion exchange, reverse osmosis, electrodialysis and biological denitrification [65]. However, these processes are relatively expensive and are often limited due to potential of side effect on water quality [66, 67]. Therefore, there is a need to explore attractive alternatives for resolving the problem of nitrate-contaminated sites. In recent years, zero valent iron (ZVI) has been employed intensively to remediate soil and groundwater contaminants such as As(III) [40], As(V) [68], Cr(VI) [69], Pb, Ni [70], Cu, Zn [71], PO_4^{3-} [72] and NO_3^- [73]. Nano-zero valent iron (nZVI) has shown higher reactivity compared with milli - or micro-sized iron for the effective removal of a wide range of contaminants [74]. The higher surface reactivity of nZVI is the result of larger surface area due to small size of particles [75]. In addition, these particles are nontoxic to aquatic organisms, available and cheap [50].

Recently, many efforts have been recorded to enhance the reactivity of nZVI. Doping the surface of nZVI using another metal (known as bimetallic nanoparticles), such as palladium (Pd), copper (Cu), platinum (Pt) or nickel (Ni) have been effective approach in degradation a variety of contaminants [76]. The advantages of bimetallic nanoparticles over nZVI alone are faster reaction kinetics and reduction of formation of toxic intermediates deposited on the surface of nZVI [77]. The increase in reactivity of bimetallic nanoparticles is related to catalytic hydrogenation and electrochemical effects [78].

For in situ nitrate removal from groundwater, permeable reactive barrier (PRB) is one of the well-known technologies owing to their effective operation and maintenance costs [79, 80]. ZVI PRB has been successfully used to remediate groundwater contaminated with nitrate [1, 81]. Several researches have focused on evaluating the behavior and efficiency of nitrate treatment by ZVI in laboratory scale column. Liu et al. [50] designed an anaerobic two-layer permeable reactive biobarrier to remediate nitrate contaminated groundwater in the presence of ZVI powder. Based on the results of their column experiment, the denitrification efficiency was estimated to be more than 94%. Similarly, Tehrani et al. [82] investigated nitrate removal using nZVI/Ni particles. They concluded that nitrate remediation was mostly influenced by seepage velocity, freshness and quantity of nZVI/Ni and particle size of porous media. Adding that the maximum nitrate removal did not exceed 85% in column experiment. Huang and Zhang [83] observed that adding certain selected cations (Fe(II), Fe(III), or Al(III)) in feed solution can greatly enhance nitrate removal and extending hydraulic retention time, increased nitrate reduction by Fe^0 packed columns. Gandhi et al. [66] studied degradation of nitrate by Fe^0 in columns under different microbial conditions and reported that reactive iron barriers can intercept and degrade nitrate effectively. Tang et al. [81] indicated that ZVI PRB is a potential technique for in situ remediation of soil and groundwater contaminated with nitrate in the alkaline conditions. Jeong et al. [84] investigated the removal efficiency of nitrate by ZVI in packed sand reactor bipolar electrolytic cell. The results showed that more than 99% of nitrate was removed and ammonia was the main final product of nitrate reduction. Hosseini and Tosco [85] assessed nitrate removal in a laboratory bench-scale aquifer system (60 cm length × 40 cm width × 50 cm height) using nZVI and carbon substrates. The results of their study demonstrated that the model has a great possibility for nitrate reduction in-situ contaminated groundwater. Araújo et al. [86] showed that the use of nZVI in PRBs is, indeed, a suitable technique for denitrification with high performance record but the long-term impact of nZVI on the environment and on the human health needs further work. Despite these studies, sufficient data cannot be found in the literature concerning the removal of nitrate using nanosized ZVI in packed sand column.

The main objective of this work was to study the effectiveness of nZVI and nano-Fe/Cu particles for the removal of nitrate in porous media using an upflow packed sand

column. To attain this goal, the effect of multilayer system and different thickness layers of nZVI/sand and (nano-Fe/Cu)/sand on the nitrate removal rate was investigated. Nine columns were operated using 10 g of nZVI or nano-Fe/Cu particles in each column under different configurations. Additionally, tenth column was filled with sand only and used as a control column. Nitrate concentration was monitored in the influent, effluent and at different sampling ports along the various depths of the column. To the best of our knowledge, this research is the first study that uses nZVI or nano-Fe/Cu particles in multilayer system in porous media along the length of packed sand column to remediate nitrate contamination.

3.2. Column experiment setup and operation

Column experiments were conducted using a Plexiglas column with a length of 25 cm and an internal diameter of 8.5 cm. The columns were pumped continuously with nitrate synthetic water in an upflow mode using a multiport peristaltic pump (RP-1000, As One, Japan). Four sampling ports were installed along the height of the column at 5 cm (S1), 10 cm (S2), 15 cm (S3) and 20 cm (S4) from the column inlet to allow for sample collection (Fig. 3.1a). 10 g of nZVI or nano-Fe/Cu particles were introduced in each column. The column experiments were comprised of ten columns. The first column (C1) was filled with sand only as a control column. The second column (C2) was first filled with a 5-cm high layer containing sieved sand; the second 10-cm high layer was filled with a homogenous nZVI/sand mixture (10 g of nZVI) while the third layer (10cm) contained just sand (see Fig. AI (1a) in Appendices Section). The third column (C3) was composed of a first layer at the bottom containing sand only (5-cm long); the second layer containing a homogenous mixture of nZVI/sand (5 g of nZVI) (5-cm long); the third layer was packed with 5 cm of sand; the fourth layer was filled with a mixture of nZVI/sand and the last layer contained only sand (5-cm long) (Fig. AI (1b)). The fourth column (C4) was packed with a 5-cm high layer of sand as a first layer; the second layer was packed with a 5-cm high layer of a homogenous mixture of nZVI/sand and the remaining of the column was filled with sand only (Fig. AI (1c)). C5, C6 and C7 were similar to C2, C3 and C4, respectively but with using nano-Fe/Cu particles instead of nZVI (Figs. AI (1d, e and f)). The eighth column (C8) was comprised of three layers of (nano-Fe/Cu)/sand in addition to a lower layer of 5 cm of

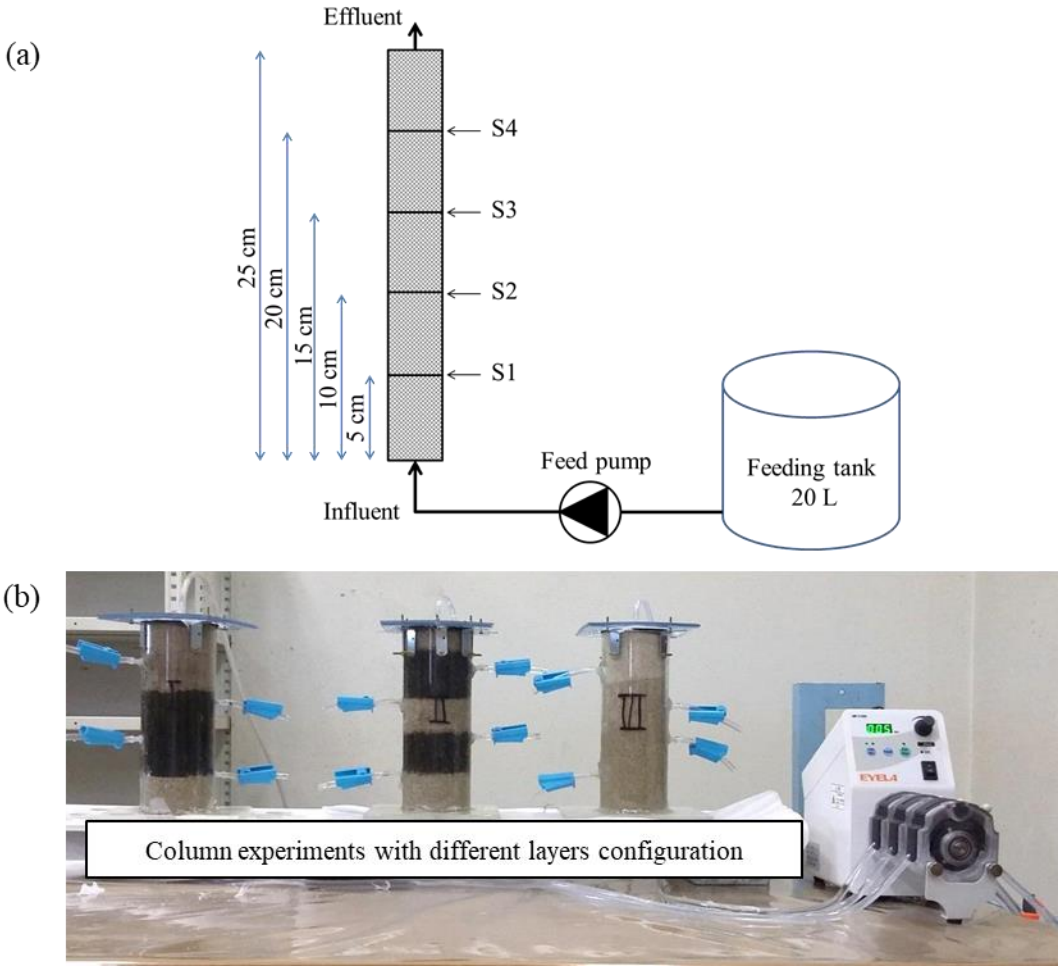

Fig. 3.1. (a) Schematic and (b) image of the continuous flow setup in the column experiments.

sand was placed at the bottom and a 5 cm sand layer was packed at the top (Fig. AI (1g)). C9 and C10 were similar to C2 and C6, respectively but the feed solution was simulated groundwater contaminated with nitrate (Figs. AI (1h and i)). The chemical compositions of the simulated ground water are provided in Table 3.1. The sand layers at the inlet and the outlet of C2–C10 were used to improve flow distribution and limit nanoparticles loss from each column. Table 3.2 summarizes the details of the column experiments in the present study. All column experiments above were repeated in triplicate.

During the whole experiments, each column was fed with 45 mg NO_3^--N /L from a 20 L tank. Flow rate was set to 5 mL/min and the residence time was thus 99 min. The pH of the influent solution in all experiments was nearly 7. The water samples were collected from influent, effluent and intermediate sampling ports and analyzed for pH, oxidation reduction potential (ORP), nitrate, nitrite, ammonium and total soluble iron.

Table 3.1: Chemical compositions of simulated groundwater used for C9 and C10.

Parameter	Ca^{2+}	Cl^{-}	Na^{+}	SO_4^{2-}	HCO_3^{-}	Mg^{2+}	pH
Concentration (mg/L)	31.36	79	131	203	89.58	8.07	7

Table 3.2: Experimental design in the present work.

Column No.	No. of layers	Layer length (cm)	Packing material	Feed solution
C1	1	25	sand	Nitrate solution
C2	1	10	nZVI	
C3	2	5		
C4	1	5		
C5	1	10	nZVI/Cu	
C6	2	5		
C7	1	5		
C8	3	3		
C9	1	10	nZVI	Simulated GW
C10	2	5	nZVI/Cu	contaminated with nitrate

3.3. Results and discussion

3.3.1. Characterization of synthesized nanoparticles

The nZVI particles were generally spherical in shape and aggregated in chain network structure as illustrated in Fig. AI (2a), while nano-Fe/Cu particles were irregular in form with chain like agglomeration as depicted in Fig. AI (2b). There was a shell structure on the surface of nZVI and nano-Fe/Cu particles in which the shell represented the oxidized part that surrounded the core of nZVI and nano-Fe/Cu particles. The peak at 2θ = 44.8° in the XRD spectrum of nZVI and nano-Fe/Cu particles (Figs. AI (3a and b)) confirmed the formation of zero valent iron while the weak peaks at 2θ=35°, 65° in the XRD spectrum indicate the presence of oxide in the synthesized nanoparticles. No Cu ions were detected in XRD spectrum of nano-Fe/Cu particles, which could be due to their relatively small concentrations. The particle size of nZVI and nano Fe/Cu particles was estimated using the particle size analyzer to be about 44 and 70 nm in average, respectively. The BET surface area of the synthesized nZVI and nano-Fe/Cu particles were 17 and 32 m^2/g, respectively.

3.3.2. Nitrate–nitrogen removal by nZVI/sand columns

The changes in NO_3^{-}–N, NH_4^{+}–N and NO_2^{-}–N concentrations in column experiments C1–C4 over time are presented in Figs. 3.2–3.5, respectively. Fig. 3.2 shows the temporal changes in nitrogen species in C1. No significant variations in NO_3^{-}–N, NH_4^{+}–N and NO_2^{-}–N were observed in control column filled with sand only (C1). Fig. 3.3 presents the

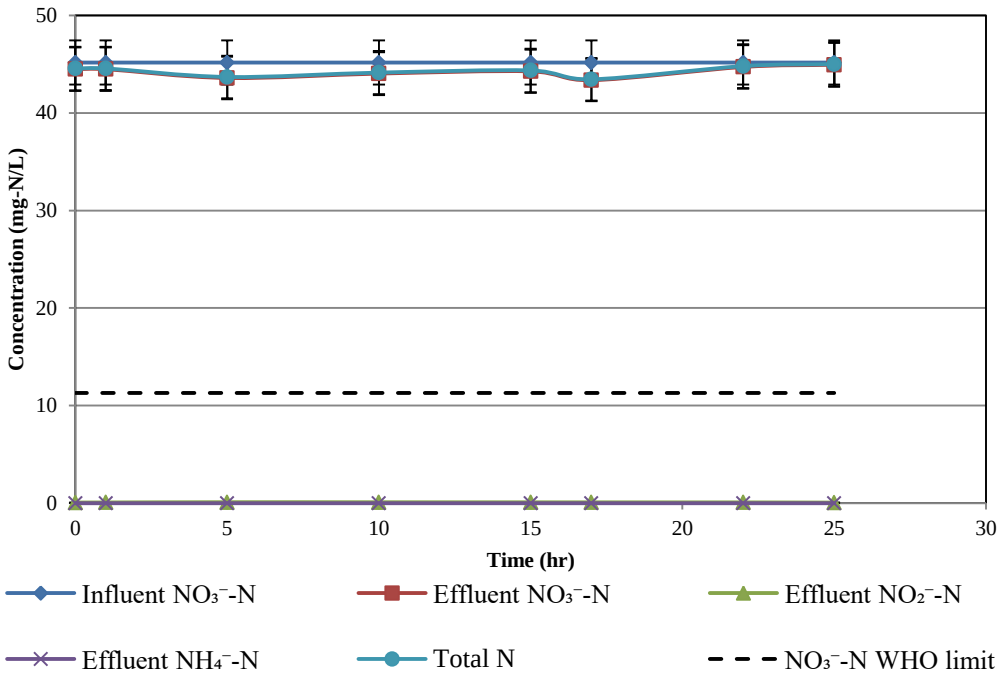

Fig. 3.2. Changes in nitrogen concentrations over time in C1 (control column).

temporal changes in nitrogen species in C2. NO_3^-–N concentration decreased quickly and more than 96% of NO_3^-–N was removed after 1 hr (Eqs. (3.1)–(3.3)). After this time, the concentration of NO_3^-–N relatively remained constant until 22 hr and then NO_3^-–N removal dropped from 93% after 22 hr to 70% after 25 hr. NH_4^+–N concentration increased gradually over the first 5 hr to reach 8.35 mg/L (as described in Eqs. (3.1) and (3.4)) and subsequently decreased slightly until 17 hr. At the end of experiment, approximately 35% of the added NO_3^-–N was recovered as NH_4^+–N. Low formation of NO_2^-–N was observed over time in C2 ($<$ 1.62 mg/L) (see Eqs. (3.4) and (3.5)). The nitrogen mass balance was about 69% in which nitrogen as NO_3^-–N, NH_4^+–N and NO_2^-–N. The incomplete nitrogen mass balance may be attributed to nitrate/ammonium sorption on iron surface [87], analytical standard errors in the determination of nitrogen species concentrations and nitrogen gas production [61]. Based on a literature survey, nitrate reduction by ZVI can take these following reaction pathways [67, 84, 88]:

$$4Fe^0 + NO_3^- + 10H^+ \rightarrow 4Fe^{2+} + NH_4^+ + 3H_2O \quad (3.1)$$

$$5Fe^0 + 2NO_3^- + 12H^+ \rightarrow 5Fe^{2+} + 6H_2O + N_{2(g)} \quad (3.2)$$

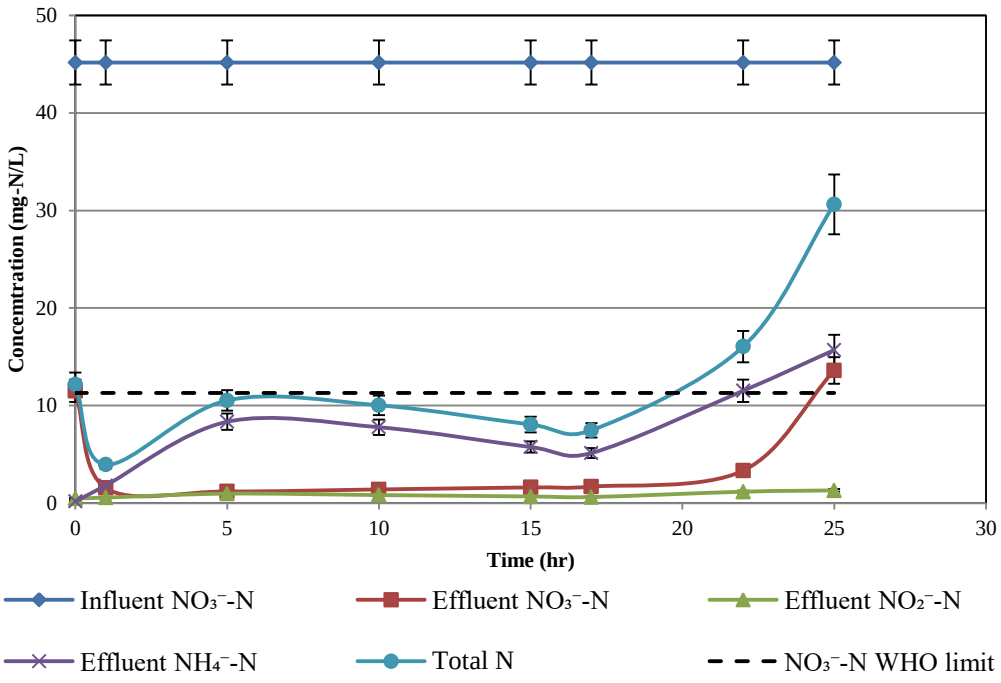

Fig. 3.3. Changes in nitrogen concentrations over time in C2 with a single 10-cm high layer of nZVI/sand.

$$Fe^0 + NO_3^- + 2H^+ \rightarrow Fe^{2+} + H_2O + NO_2^- \quad (3.3)$$

$$3Fe^0 + NO_2^- + 8H^+ \rightarrow 3Fe^{2+} + 2H_2O + NH_4^+ \quad (3.4)$$

$$3Fe^0 + 2NO_2^- + 8H^+ \rightarrow 3Fe^{2+} + 4H_2O + N_{2(g)} \quad (3.5)$$

NO_3^- is reduced in the presence of H^+ ions that are produced from reduction of H_2O and electrons that come from the core of ZVI. NO_2^- and NH_4^+ are produced and then NO_2^- participates in other reactions to produce NH_4^+ and N_2. Previous batch tests indicated that the predominant end product of nitrate reduction was ammonium [67, 87, 89]. However, Westerhoff and James [90] observed only 70% of the applied nitrate was recovered as ammonium during short-term column operations and about 20% of the influent nitrate was recovered during long-term column tests. These results are consistent with the results of our study.

Fig. 3.4 presents the temporal changes in nitrogen species in C3. The NO_3^-–N concentration decreased sharply and greater than 95% of the influent NO_3^-–N was removed after 5 hr. Afterwards, NO_3^-–N concentration increased steadily and reached 5.06 mg/L after 17 hr. After this time, NO_3^-–N removal dropped from 89% after 17 hr to 71% after 25

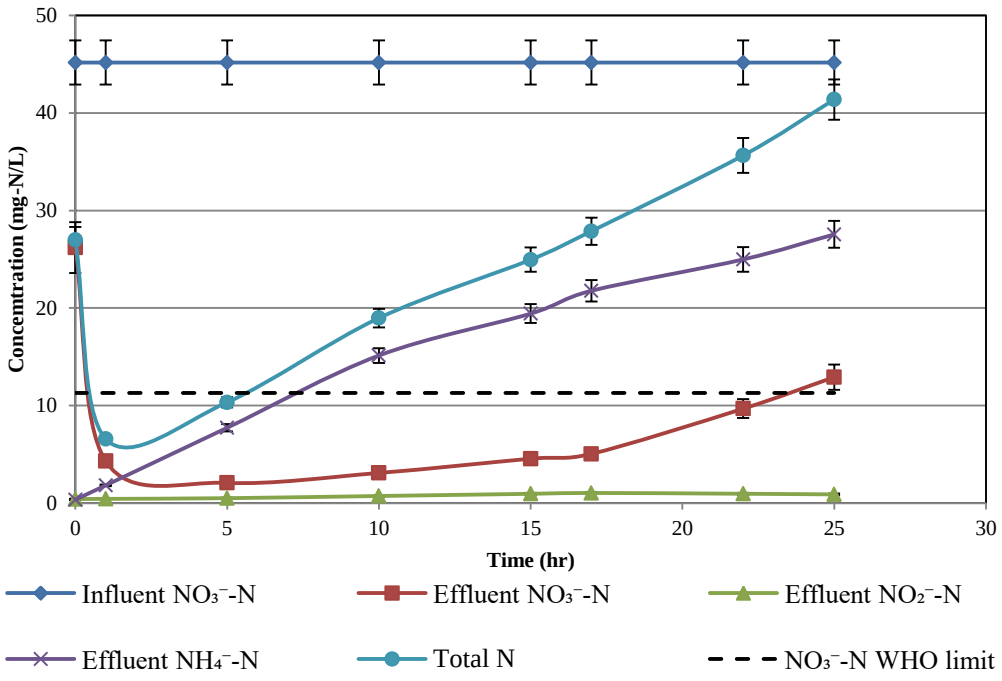

Fig. 3.4. Changes in nitrogen concentrations over time in C3 with double 5-cm high layers of nZVI/sand.

hr. The effluent NH_4^+–N concentration increased gradually and about 61% of the NO_3^-–N removed was recovered as NH_4^+–N. Little formation of NO_2^-–N was detected (< 1.05 mg/L) during C3 experiment. About 91% of total applied nitrogen was recovered as NO_3^-–N, NH_4^+–N and NO_2^-–N after 25 hr of operation. C3 with two 5-cm high layers of nZVI/sand removed less nitrate than C2 with one 10-cm high layer of nZVI/sand. This was likely due to iron oxides formed in the first layer of C3 precipitated on the surface of nZVI, which hinder the contact between the reactants.

Fig. 3.5 exhibits the temporal changes in nitrogen species in C4. The NO_3^-–N concentration at the outlet showed 98% of NO_3^-–N removal during the first hour and thereafter NO_3^-–N increased slowly to more than 4.02 mg/L after 17 hr. A gradual decrease in the rate of NO_3^-–N removal from 91% to 76% after 17 and 25 hr was observed, respectively. High accumulation of NH_4^+–N over time was noted in C4 and almost 70% of the influent NO_3^-–N was recovered as NH_4^+–N. Low NO_2^-–N formation was detected with a maximum of 0.91 mg/L after 25 hr. The final mass balance of nitrogen showed that 95 % of the initial nitrogen was recovered as NO_3^-–N, NH_4^+–N and NO_2^-–N. The removal efficiency of nitrate in C4 with one 5-cm high layer of nZVI/sand was less than C2 with

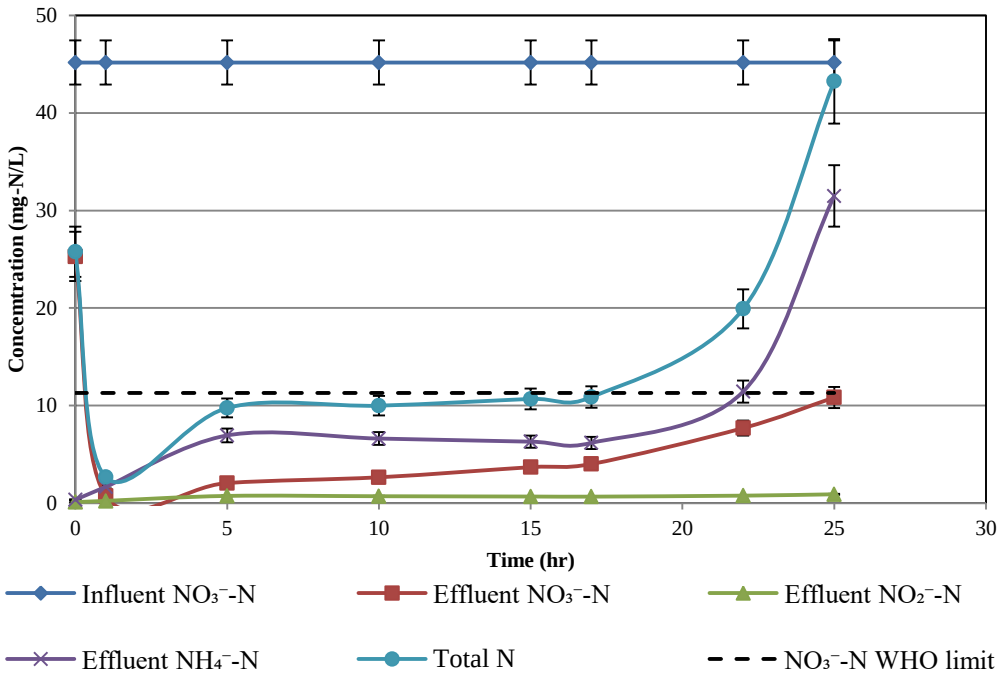

Fig. 3.5. Changes in nitrogen concentrations over time in C4 with a single 5-cm high layer of nZVI/sand.

one 10-cm high layer of nZVI/sand. This lower removal efficiency could be the result of insufficient contact time between nZVI and nitrate contaminant. Hosseini et al. [7] and Westerhoff and James [90] observed that nitrate reduction rate increased with longer retention time in packed sand columns.

3.3.3. Nitrate–nitrogen removal by (nano-Fe/Cu)/sand columns

The changes in NO_3^-–N, NH_4^+–N and NO_2^-–N concentrations in column experiments C5–C7 over time are presented in Figs. 3.6–3.8, respectively. Fig. 3.6 presents the temporal changes in nitrogen species in C5. NO_3^-–N concentration decreased significantly within the first 5 hr and more than 92% of NO_3^-–N was removed. After that, NO_3^-–N concentration increased gradually until the end of experiment. NH_4^+–N was produced remarkably in C5 with a maximum of 34.14 mg/L. NO_2^-–N formation was low during the first 10 hr and then increased steadily and reached a maximum of 6.64 mg/L after 22 hr. The nitrogen mass balance at the end of experiment was 98% as NO_3^-–N, NH_4^+–N and NO_2^-–N. On the basis of Khalil et al. [61] study, a complete removal of 100 mg/L as NO_3^- was obtained within 20 min by nano-Fe/Cu particles while it took about an hour using ordinary nZVI to remove the same amount of nitrate. Liou et al. [89] reported that ammonium was the primary end

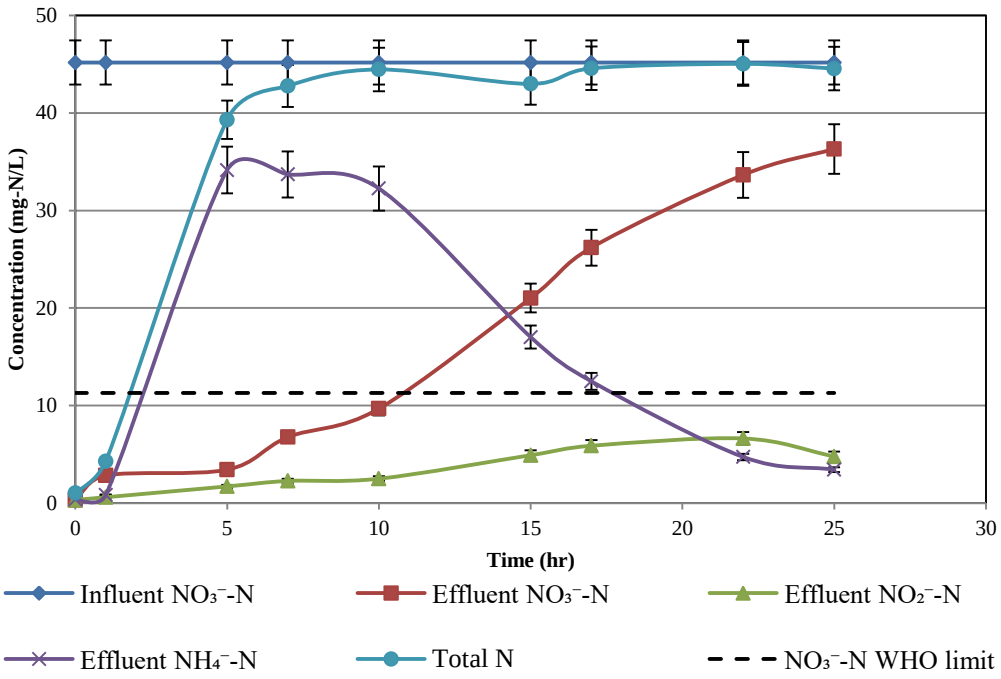

Fig. 3.6. Changes in nitrogen concentrations over time in C5 with a single 10-cm high layer of (nano-Fe/Cu)/sand.

product in nano-Fe/Cu systems. However, about 22–40% of the degraded nitrate was released as nitrite. They indicated the high accumulation of nitrite resulted from its less affinity to copper surface and its lower removal rate at alkaline conditions. Hosseini et al. [91] applied a modified surface of nZVI using Cu metal to remove 100 NO_3^-–N mg/L through packed sand column utilizing injection approach. The results revealed that 75% of influent nitrate was removed when nano-Fe/Cu concentration was 8 g/L and the pore water velocity through sand was 0.125 mm/s.

Fig. 3.7 shows the temporal changes in nitrogen species in C6. NO_3^-–N was removed rapidly and completely (~100%) after 1 hr and the removal efficiency of NO_3^-–N was maintained relatively constant until 10 hr. After this time, NO_3^-–N concentration increased sharply and the removal efficiency decreased to about 50% after 25 hr. NH_4^+–N generation was drastically increased in C6 with a maximum of 29.85 mg/L. Low effluent NO_2^-–N was formed during the first 10 hr and then NO_2^-–N increased slightly to 5.57 mg/L after 25 hr. Almost 94% of nitrogen mass recovery as NO_3^-–N, NH_4^+–N and NO_2^-–N was detected at the end of the experiment. Fig. 3.8 shows the temporal changes in nitrogen species in C7. About 100 % of NO_3^-–N was removed after 1 hr and subsequently NO_3^-–N concentration

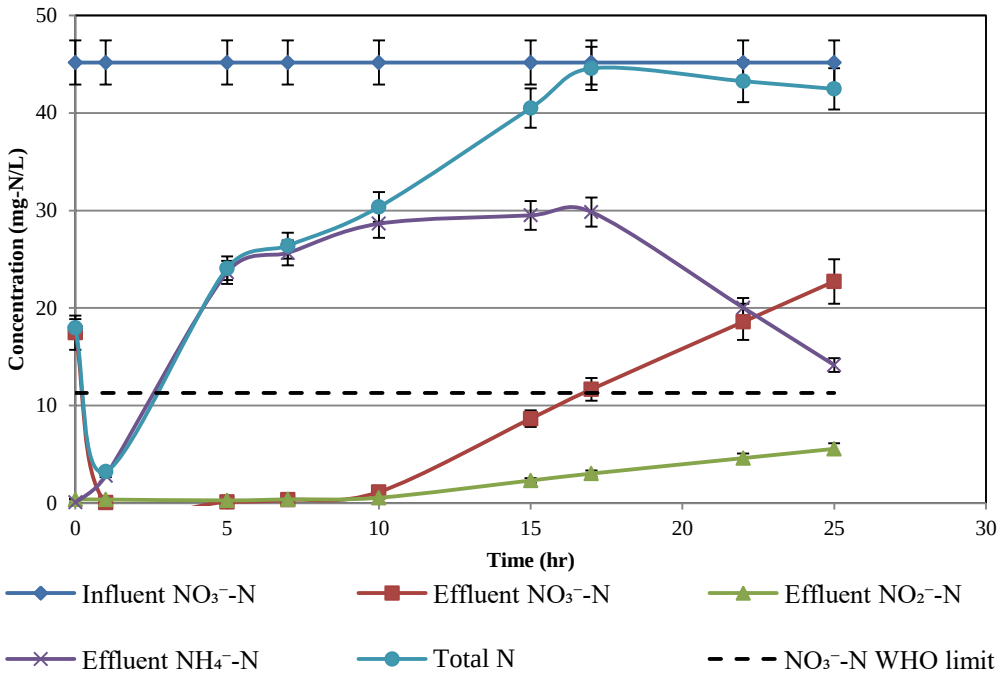

Fig. 3.7. Changes in nitrogen concentrations over time in C6 with double 5-cm high layers of (nano-Fe/Cu)/sand.

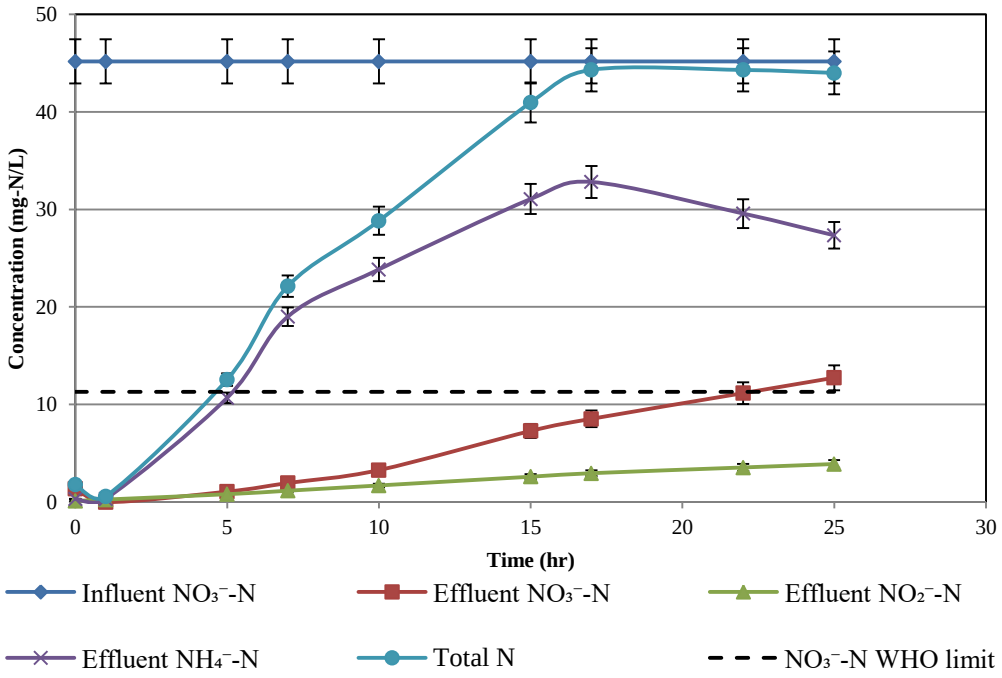

Fig. 3.8. Changes in nitrogen concentrations over time in C7 with a single 5-cm high layer of (nano-Fe/Cu)/sand.

increased slightly and reached to 1.07 mg/L after 5 hr. After this time, NO_3^-–N concentration rose up steadily and the removal efficiency decreased from about 97% after 5 hr to roughly 72% after 25 hr. The main nitrogen species remaining in the effluent of C7 was NH_4^+–N corresponding to about 61% of the total nitrogen introduced. Low production of NO_2^-–N was found during the first 5 hr and afterward NO_2^-–N concentration increased slowly to reach 3.9 mg/L after 25 hr. At the end of experiment, the nitrogen mass balance was more than 97% as NO_3^-–N, NH_4^+–N and NO_2^-–N. Fig. AI (4) shows the changes in NO_3^-–N concentration over time in C8 when the number of layers of (nano-Fe/Cu)/sand increased to 3 layers. Nearly 100 % of the NO_3^-–N was removed during the first 5 hr and then NO_3^-–N concentration increased slightly until 10 hr with an outlet NO_3^-–N of less than 1.74 mg/L. After that, the NO_3^-–N concentration increased almost constantly and the removal efficiency dropped to 45% after 25 hr.

3.3.4. Nitrate–nitrogen removal in simulated groundwater

Figs. 3.9 and 3.10 depict the temporal changes in nitrogen species in C9 and C10 when the simulated groundwater with 45 N mg/L of nitrate was injected into the columns. The maximum removal rate of 41% was obtained in C9 after 5 hr and NO_3^-–N concentration then increased gradually and a small amount of NO_3^-–N removal (about 15%) was observed after 25 hr (Fig. 3.9). The NH_4^+–N formation increased over time with a maximum of 6.65 mg/L was detected after 25 hr and no NO_2^-–N accumulation occurred in C9. For C10, above 89% of NO_3^-–N removal was observed during the first hour and remained relatively stable until 5 hr (Fig. 3.10). After this time, NO_3^-–N concentration increased steadily and NO_3^-–N removal dropped to 52% after 25 hr. High NH_4^+–N formation was found in C10 with a maximum of 27.65 mg/L and NO_2^-–N accumulated over time to reach 2.25 mg/L after 25 hr. The percentage of nitrate removal observed in C9 and C10 was significantly lower than those attained in C2 and C6, respectively. A possible explanation could be attributed to interference of other ions, which are frequently found in the natural groundwater. Ruangchainikom et al. [67] concluded that nitrate removal decreases significantly with increasing humic acid and calcium ions concentrations whereas increasing chloride concentration leads to the increase of nitrate removal rate.

To compare among columns (C1–C10), Figs. 3.11 and 3.12 present the maximum and overall nitrate removal in C1 to C10 during 25 hr of operation, respectively. Fig. 3.11

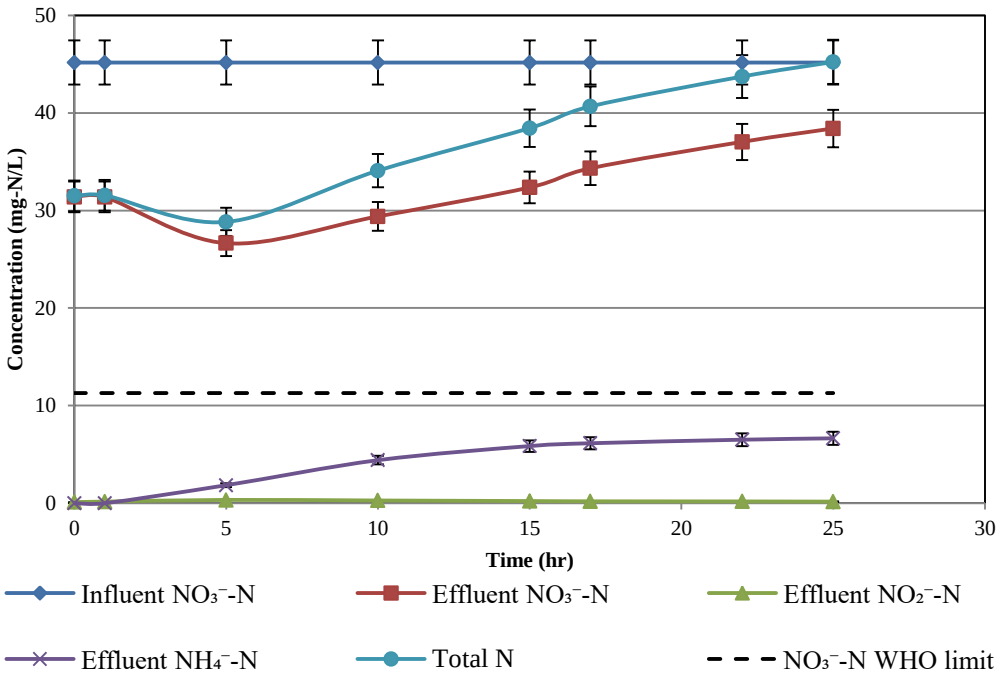

Fig. 3.9. Changes in nitrogen concentrations over time in C9 with a single 10-cm high layer of nZVI/sand when nitrate in simulated groundwater.

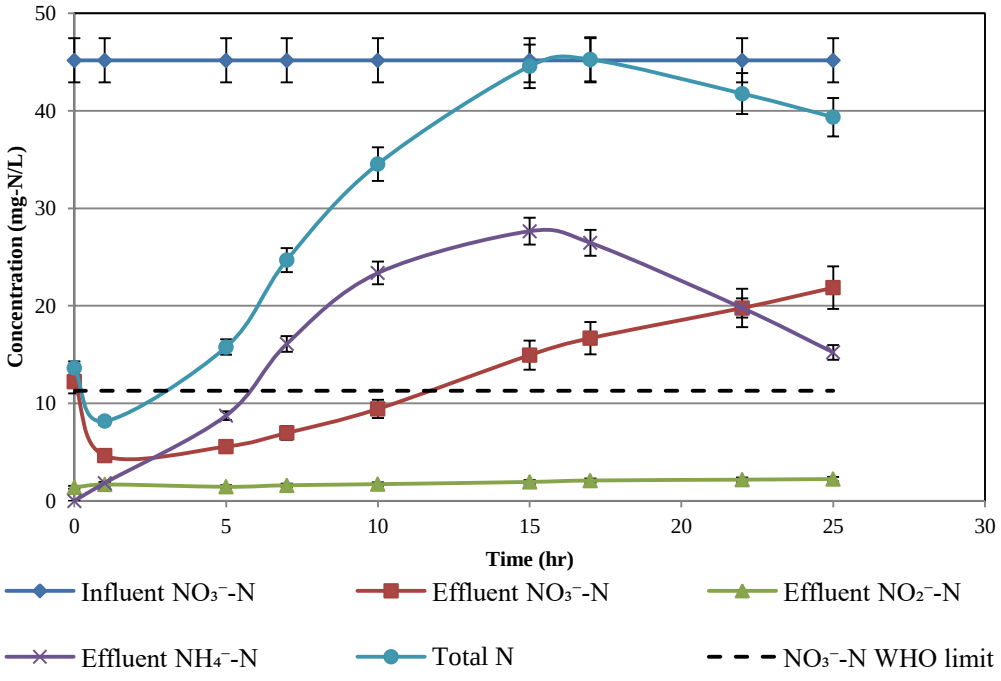

Fig. 3.10. Changes in nitrogen concentrations over time in C10 with double 5-cm high layers of (nano-Fe/Cu)/sand when nitrate in simulated groundwater.

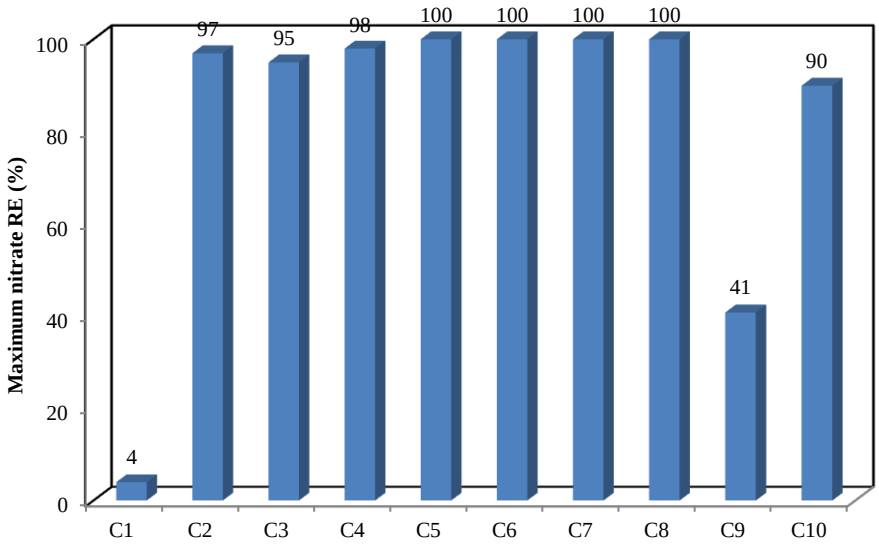

Fig. 3.11. Maximum nitrate removal efficiency in column experiments C1–C10 during 25 hr of operation.

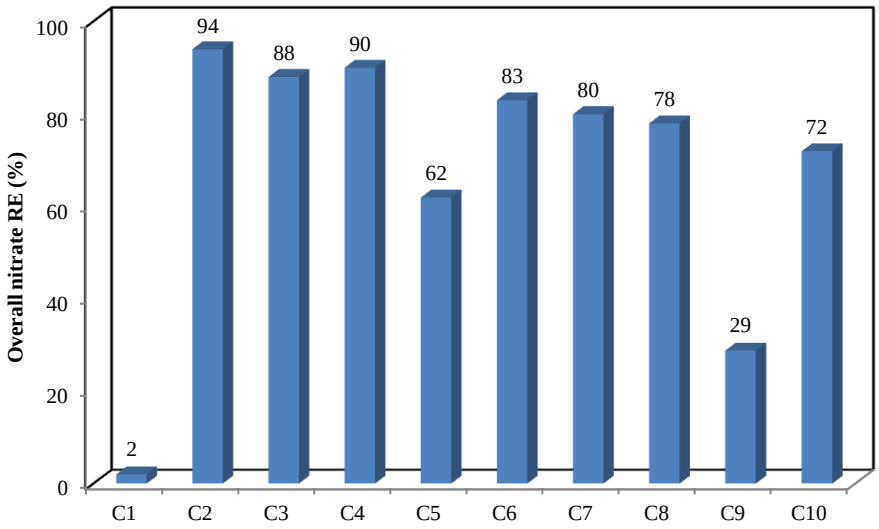

Fig. 3.12. Overall nitrate removal efficiency in column experiments C1–C10 after 25 hr of operation.

showed that the maximum percentage of nitrate removal in nZVI/sand columns (C2–C4) were 97%, 95% and 98%, respectively while in (nano-Fe/Cu)/sand columns (C5–C8), the maximum percentage of nitrate removal was 100%. These results indicated that (nano-Fe/Cu)/sand columns had higher percentage of nitrate removal than nZVI/sand columns. This was due to bimetallic nanoparticles have a higher reaction rate than those observed for bare nZVI. However, monitoring the nitrate concentrations in (nano-Fe/Cu)/sand columns showed a rapid saturation and faster than those of nZVI/sand columns. Furthermore, the overall nitrate removal efficiency in (nano-Fe/Cu)/sand columns was lower than those

obtained with nZVI alone. These results can be due to the formation of iron oxides which impede the exposure of copper to the reactants in the solution [89]. The maximum efficiency of nitrate removal dropped to 41% in C9 and 90% in C10 when the feed solution was simulated groundwater containing 45 N mg/L of nitrate which exhibited nano-Fe/Cu particles were more effective than nZVI for nitrate removal in simulated groundwater. These observations indicated that adding Cu ions decrease the interference effect of simulated groundwater compounds on nZVI reactivity. Fig. 3.12 indicated that the optimum condition to reduce nitrate among nZVI/sand columns (C2–C4) was C2 (overall nitrate removal efficiency = 94%) by a 10-cm high layer containing nZVI/sand whereas in (nano-Fe/Cu)/sand columns (C5–C8), C6 with two 5 cm (nano-Fe/Cu)/sand layers had the best performance to remove nitrate (overall nitrate removal efficiency = 83%). C2 exhibited the highest overall nitrate removal among C1–C10.

3.3.5. Total iron accumulation

Fig. AI (5) exhibits the changes in total Fe concentration in C1–C7 and C9–C10 over time. Results showed that the accumulation rate of total Fe in column experiments was highly variable. The total Fe concentration in the influent water was 0.62 mg/L. Negligible total Fe and always less than 0.62 mg/L was detected in C1. High accumulation of total Fe was found in C2 at the beginning of experiment which reached 36.26 mg/L and then this concentration decreased gradually to below 12 mg/L after 25 hr (Fig. AI (5a)). A considerable amount of total Fe was detected in C3 and C4 ranging between 18.27 mg/L and 35.23 mg/L (Fig. AI (5a)). The total Fe leaving C5 increased steadily from 5.7 mg/L at the start of the experiment to 12.11 mg/L after 25 hr (Fig. AI (5b)). In C6 and C7, the effluent total Fe increased rapidly during the initial operation to roughly 22.43 mg/L and then gradually decreased to less than 8.66 mg/L after 25 hr (Fig. AI (5b)). C9 and C10 showed lower total Fe formation with average of 5.2 mg/L when the feed solution was simulated groundwater contained nitrate of 45 N mg/L (Fig. AI (5c)). In general, higher release of iron achieves higher nitrate removal.

3.3.6. Temporal changes in pH and ORP

The pH and ORP monitoring in C2–C10 experiments appears in Figs. AI (6–8). The pH and ORP values varied slightly in control column (C1). A general increase in pH was

observed in C2–C10 due to the consumption of hydrogen ions as shown in Eqs. (3.1)–(3.5). The pH in nZVI/sand columns (C2–C4) increased rapidly from nearly 7.0 in the feed water to higher than 9 at the beginning of the experiment and then increased continuously to reach around 11 after 25 hr (Fig. AI (6)). In (nano-Fe/Cu)/sand columns (C5–C8), pH values were significantly high (9–10.55) but the final pH value was not as high as the pH in case of nZVI/sand columns (Fig. AI (7)). This slight decrease in pH was attributed to release of hydrogen ions in the presence of Cu ions as in Eqs. (3.6) and (3.7) [61].

$$2Cu + H_2O \rightarrow Cu_2O + 2H^+ \quad (3.6)$$

$$Cu_2O + H_2O \rightarrow 2CuO + 2H^+ \quad (3.7)$$

In regard to ORP, the initial values of ORP of about 20 mV dropped significantly at the start of operation to –140, –135 and –90 mV in C2–C4, respectively and then gradually decreased to less than –200 mV at the end of experiments (Fig. AI (6)). These high negative values of ORP indicating that Fe^0 creates strongly reductive environment. The ORP in C5–C8 decreased considerably to –203, –191, –206 and –201 mV at the end of experiments, respectively (Fig. AI (7)). It was also observed that the ORP in (nano-Fe/Cu)/sand columns decreased slowly and reached to a high negative value after quite a long reaction time. In case of using nitrate in simulated groundwater (C9 and C10), the increase in pH and the decrease in ORP values were not as high as in case of distilled water contaminated with nitrate (Fig. AI (8)). These results can be due to the interference effect of simulated groundwater compounds, which can retard the kinetic rate of nitrate removal by nZVI and nano-Fe/Cu particles.

3.3.7. Vertical profiles of nitrogen and total iron along nZVI/sand columns

Concentration profiles of NO_3^-–N, NO_2^-–N, NH_4^+–N and total Fe along the length of C2 (the best performance among nZVI/sand columns (C2–C4)) were obtained after 5 and 22 hr of operation (Fig. 3.13). The concentration profiles for C3 and C4 are presented in Appendices Section (Figs. AI (9 and 10)). No significant presence of NO_3^-–N, NH_4^+–N, NO_2^-–N and total Fe was detected along the control column (C1). The NO_3^-–N

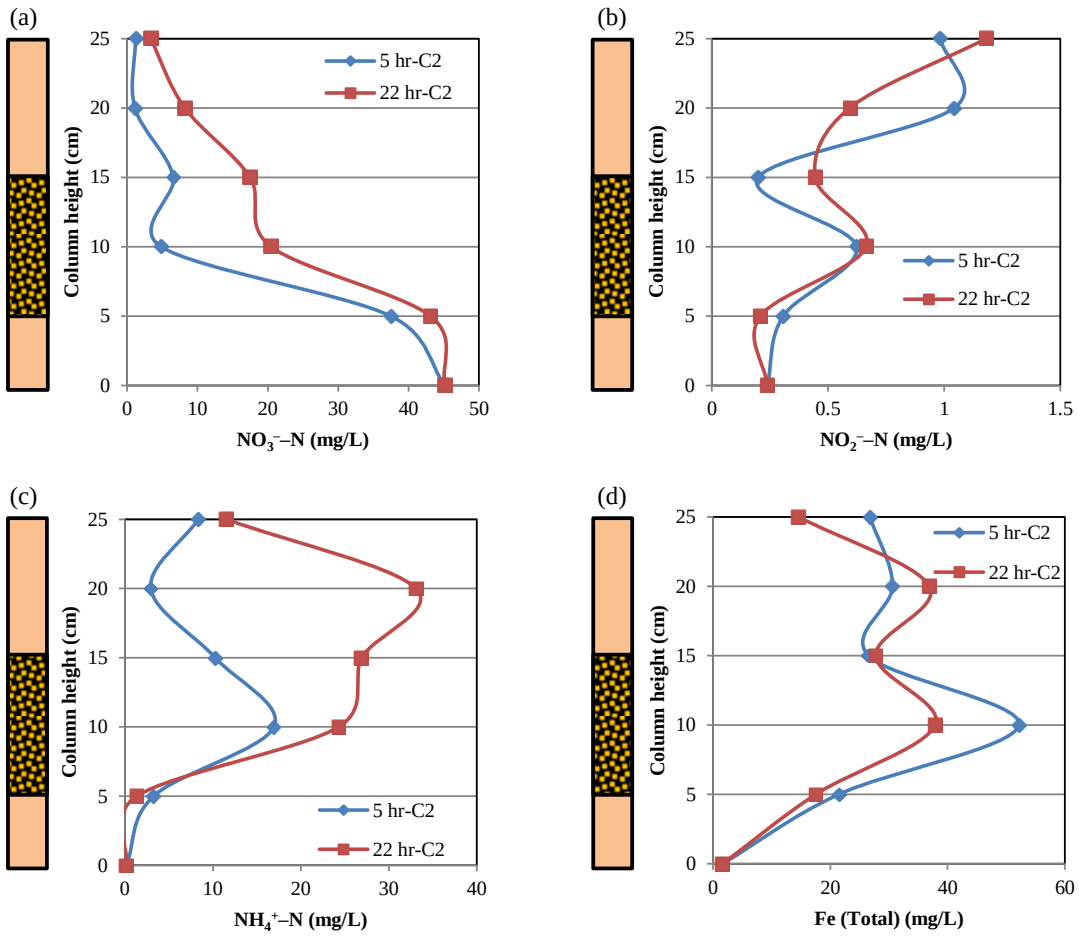

Fig. 3.13. Sample profiles of NO_3^-–N, NO_2^-–N, NH_4^+–N and total Fe concentrations along C2 after 5 and 22 hr feeding with 45 mg NO_3^-–N /L.

concentration rapidly descended within the first 10 cm to less than 4.83 mg/L after 5 hr and afterward slowly declined between 10 and 25 cm (Fig. 3.13a). The nitrate removal efficiencies at sampling ports of S1 to S4 were about 17%, 89%, 85% and 98% respectively. After 22 hr, almost 89% of the influent NO_3^-–N concentration was eliminated within the first 10 cm and the resultant NO_3^-–N (20.48 mg/L) steadily decreased between 10 and 25 cm. Fig. 3.13b shows a gradual increase in the NO_2^-–N accumulated along the column to 1.04 and 0.59 mg/L at 20 cm after 5 and 22 hr, respectively. The NH_4^+–N with a maximum of 16.94 mg/L was detected at 10 cm of C2 after 5 hr and then rapidly dropped to 2.93 mg/L at 20 cm (Fig. 3.13c). The formation of NH_4^+–N along C2 after 22 hr drastically increased throughout the column with a peak of 33.07 mg/L at 20 cm. The total Fe concentration along C2 quickly increased with a maximum of 52.18 and 37.88 mg/L up to

10 cm after 5 and 22 hr, respectively and relatively decreased thereafter between 10 and 25 cm (Fig. 3.13d). The mechanism of NO_3^-–N reduction by nZVI within C2 could be illustrated as the following. NO_3^-–N was highly reduced within nZVI/sand layer according to Eqs. (3.1)–(3.3). NO_2^-–N was initially produced between 5 and 10 cm as the main by product, but its concentration decreased rapidly between 10 and 15 cm due to the participation of NO_2^-–N in other reactions to produce NH_4^+–N (as in Eq. (3.4)). In the same time, NH_4^+–N production was observed between 5 and 10 cm (see Eq. (3.1)). The decrease in total Fe concentration between 10 and 25 cm could be because iron oxide shell inhibits the surface of nZVI core from rapid oxidation.

3.3.8. Vertical profiles of nitrogen and total iron along (nano-Fe/Cu)/sand columns

Concentration profiles of NO_3^-–N, NO_2^-–N, NH_4^+–N and total Fe along the length of C6 (the optimum condition among (nano-Fe/Cu)/sand columns (C5–C8)) are presented in Fig. 3.14. The concentration profiles for C5, C7 and C8 are depicted in Appendices Section (Figs. AI (11, 12 and 13)). As shown in Fig. 3.14, approximately 60% of NO_3^-–N was removed after 5 hr within the first layer of (nano-Fe/Cu)/sand and subsequently NO_3^-–N removal increased steadily and reached roughly 100 % at 20 cm of C6 (Fig. 3.14a). After 22 hr, NO_3^-–N concentration decreased slightly within the first 15 cm and afterward decreased quickly within the second (nano-Fe/Cu)/sand layer and was removed by 76% at 20 cm. High accumulation of NO_2^-–N was observed within the first layer of (nano-Fe/Cu)/sand after 5 hr with a maximum of 8.79 mg/L at 10 cm and afterward sharply declined to less than 0.27 mg/L between 10 and 25 cm (Fig. 3.14b). After 22 hr, NO_2^-–N was formed steadily along the column. NH_4^+–N drastically accumulated along C6 after 5 hr with a peak of 38.35 mg/L at 15 cm (Fig. 3.14c). No NH_4^+–N formation was detected over the first 15 cm of C6 after 22 hr. However, NH_4^+–N sharply accumulated within the second layer of (nano-Fe/Cu)/sand with a maximum of 30.32 mg/L at 20 cm. The total Fe concentration after 5 and 22 hr was detected along the column and ranged between 2.28 and 9.73 mg/L at sampling ports S1 to S2 (Fig. 3.14d). It was observed that NO_3^-–N reduction was high in the first layer of C6 because Cu ions can enhance better electron transformation from nZVI core. NO_2^-–N and NH_4^+–N were then produced between 5 and 10 cm (as

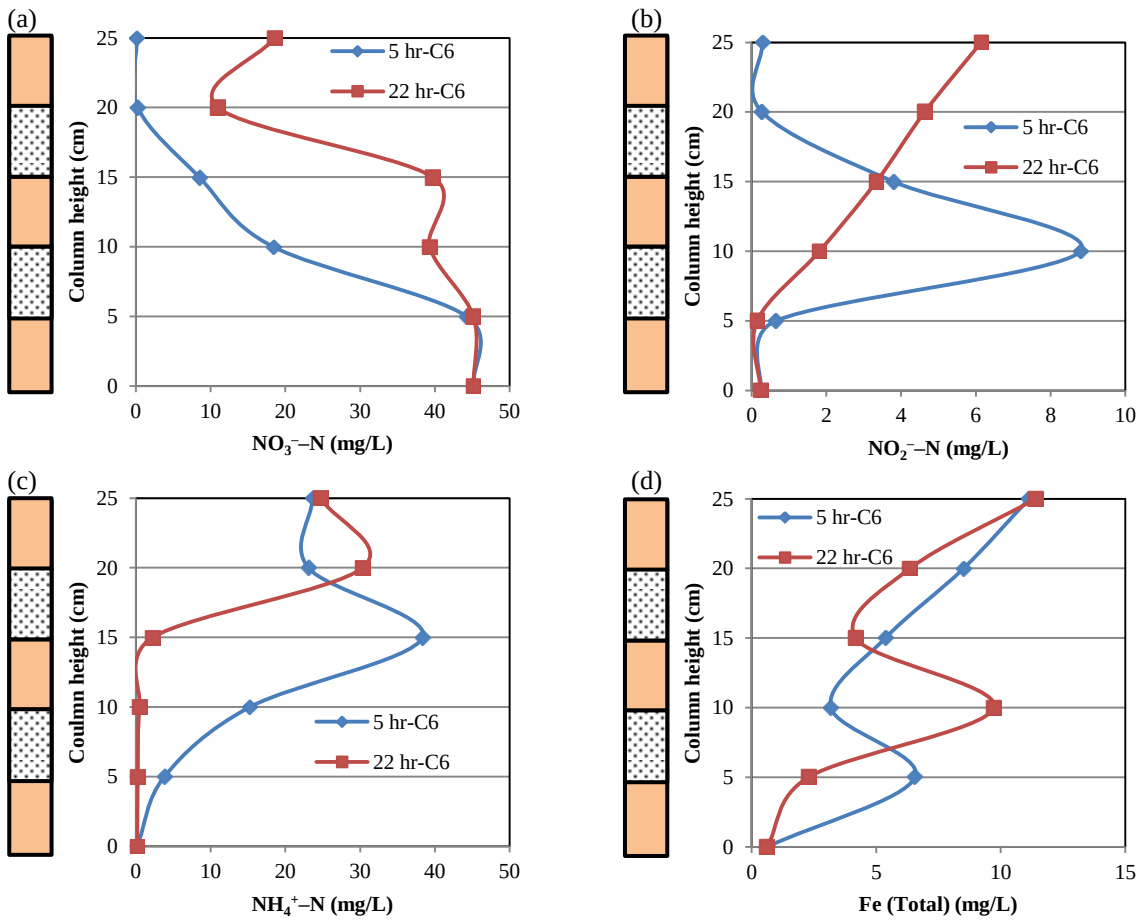

Fig. 3.14. Sample profiles of NO_3^-–N, NO_2^-–N, NH_4^+–N and total Fe concentrations along C6 after 5 and 22 hr feeding with 45 mg NO_3^-–N /L.

described in Eqs. (3.1) and (3.3)). NH_4^+–N increased but NO_2^-–N decreased between 10 and 20 cm according to Eq. (3.4). The formation of NO_2^-–N and NH_4^+–N along C6 after 22 hr was lower than those obtained after 5 hr. This was presumably due to the efficiency of Cu that was used in bimetallic nanoparticles decreases with time as a result of the formation of an iron oxide layer, which decreases the reduction rate of nano-Fe/Cu particles.

3.3.9. Vertical profiles of nitrogen and total iron when using simulated groundwater

Figs. AI (14 and 15) present the concentration profiles along C9 and C10 when the simulated groundwater containing 45 N mg/L of nitrate was used in the feed solution. 38% of NO_3^-–N was eliminated after 5hr within the 10-cm high layer of nZVI/sand along C9 while after 22 hr NO_3^-–N concentration decreased slowly and only 20% of the influent

NO_3^-–N was removed throughout the column (Fig. AI (14a)). Negligible NO_2^-–N formation and always less than 0.56 mg/L was detected along C9 (Fig. AI (14b)). High NH_4^+–N accumulation occurred along C9 with a maximum of 9.83 mg/L and the total Fe concentration averaged 3.34 mg/L (Figs. AI (14c and d)). Along C10, the NO_3^-–N concentration after 5 hr decreased rapidly within the first 10 cm and slowly declined thereafter to lower than 8.5 mg/L between 10 and 25 cm (Fig. AI (15a)). After 22 hr, only 40% of the influent NO_3^-–N was depleted along the column with a high NO_3^-–N of 27.32 mg/L at 20 cm. NO_2^-–N sharply accumulated along C10 with a peak of 3.88 mg/L (Fig. AI (15b)). NH_4^+–N was highly formed after 5 hr within the first 10 cm with a maximum of 27.7 mg/L and afterward descended rapidly between 10 and 25 cm (Fig. AI (15c)). After 22 hr, the NH_4^+–N accumulated steadily along the column and reached 15.29 mg/L at 20 cm. The formation of total Fe was detected along the column with average of 4.76 mg/L (Fig. AI (15d)). These results agree with the previously suggested mechanism in Eqs. (3.1)–(3.5).

3.3.10. Vertical profiles of pH and ORP

Concentration profiles of pH and ORP along the length of the columns C2–C10 were determined after 5 and 22 hr of operation (Figs. AI (16–18)). The variations in pH and ORP along the control column (C1) were not as high as those along C2–C10. The pH along C2 and C3 increased rapidly after 5 and 22 hr from 6.88 in the influent to 9.59–10.8 at sampling ports S1 to S4 (Figs. AI (16a and c)) while the ORP values decreased considerably along C2 and C3 after 5 (<-182 mV) and 22 hr ($<$ –218 mV) (Figs. AI (16b and d)). For C4, the pH was 9.17−9.78 after 5 hr at any sampling port, however, the pH was significantly higher (pH=10.76–11.11) after 22 hr (Fig. AI (16e)). High reductive environment was created along C4 and the ORP values dropped down to –235 mV after 22 hr (Fig. AI (16f)).

The pH increased steadily along C5 and C6 to 8.94–10.14 after 5 hr, but the pH values after 22 hr decreased with an average of 8.5 (Figs. AI (17a and c)). The ORP values decreased rapidly along C5 and C6 after 5hr ($<$ –180 mV) and lower than the ORP after 22 hr ($>$ –110 mV) (Figs. AI (17b and d)). The pH increased quickly within the (nano-Fe/Cu)/sand layer of C7 to around 8.7–10.47 and afterward remained relatively constant along the column (Fig. AI (17e)). The ORP dropped sharply along C7 with a minimum of –

228 mV was detected at 15 cm after 22 hr as shown in Fig. AI (17f). It is noticed that the pH values along nZVI/sand columns (C2–C4) after 22 hr were higher than those along (nano-Fe/Cu)/sand columns (C5–C8). In addition, the reduction in ORP values along nZVI/sand columns (C2–C4) after 22 hr was significantly higher than the corresponding values along (nano-Fe/Cu)/sand columns (C5–C8). The reason for these observations in pH and ORP is related to shorter life time of bimetallic nanoparticles compared to nZVI alone. Monitoring pH and ORP data has been commonly used as an indicator of successful emplacement of nZVI during field scale applications.

3.4. Conclusion

This study evaluates the application of nZVI and bimetallic nano-Fe/Cu particles in porous media in multilayer system to remove nitrate through an up flow packed sand column. The results indicated that using a single 10-cm high layer containing nZVI/sand demonstrated the best performance to remove nitrate among nZVI/sand columns and more than 97% of influent nitrate was removed while using double 5-cm high layer containing (nano-Fe/Cu)/sand achieved the optimum removal performance among (nano-Fe/Cu)/sand columns and nitrate removal was complete (100%). Furthermore, the nano-Fe/Cu particles exhibited more efficient and rapid nitrate removal than nZVI when the feed solution was simulated groundwater. Low formation of nitrite and always less than 1.32 NO_2^-–N mg/L was noted during nZVI/sand columns. Little formation of nitrite was detected during the initial stages of (nano-Fe/Cu)/ sand columns whereas comparatively high accumulation and greater than 3.9 NO_2^-–N mg/L was obtained at later stages. High generation of ammonium was found during nZVI/sand and (nano-Fe/Cu)/sand columns and more than 69% of applied nitrogen were recovered as nitrate, ammonium and nitrite at the end of experiments after 25 hr of operation. These observations suggest that nitrate removal in porous media could be enhanced effectively by using nZVI on the full length of porous media or using nano-Fe/Cu in multilayer porous media. Further study is necessary to investigate the performance of effective parameters like initial nitrate concentration, nanoparticles concentration and flow rate (retention time) through the packed column on nitrate reduction rate.

CHAPTER 4

TREATMENT OF CESIUM CONTAMINATED WATER BY NZVI AND FE/CU NANOPARTICLES

CHAPTER 4- Treatment of Cesium Contaminated Water by nZVI and Fe/Cu Nanoparticles

In this chapter, the capability of nZVI and bimetallic nano-Fe/Cu particles for cesium (Cs^+) removal from aqueous solutions was evaluated for the first time. The nanoparticles were characterized by TEM, XRD, SEM-EDS and BET-N_2 adsorption. The effect of several variables such as initial Cs^+ concentration, contact time, pH, temperature, competing cations and dosage of the nanoparticles on the sorption behavior of Cs^+ was studied using a batch technique. The obtained results demonstrated that nZVI and nano-Fe/Cu particles can be considered as promising materials for cesium removal from contaminated waters.

4.1. Introduction

To date, the recovery of hazardous cesium is an unsolved problem. Different cesium adsorbents, including zeolites [92], Prussian blue [93], calixarene [94], bentonite, sepiolite, kaolinite [95], pillared clay [96], sericite [97], and aluminum molybdophosphate [98], were intensively investigated to remove cesium from contaminated water. However, separation of these adsorbents from environment after use is very difficult. In recent decades, magnetic nanoparticles have been widely used in the fields of medicine, biotechnology, diagnostics and catalysis [99]. Magnetic nanoparticles compose of a magnetic based core and an outer functional shell that can sorb contaminants, which have been extensively studied for environmental remediation applications due to their quite small particle size and large surface area to volume ratio [100]. In addition, the magnetic nanoparticles can be recovered and separated easily from medium by applying an external magnetic field due to the intrinsic magnetic feature of the nanoparticles [101]. The magnetic separation of such tiny particles may be a more cost effective and an appropriate technique than sophisticated membrane filtration and centrifugation processes [102].

Several researchers investigated magnetic nanoparticles and magnetic nanocomposites to remediate a wide range of contaminants. Yang et al. [103] investigated arsenic adsorption to magnetite nanoparticles. Hu et al. [104] applied maghemite nanoparticles for the removal and recovery of Cr^{6+}. Tang et al. [105] modified the surfaces of Fe_3O_4 nanoparticles by gelatin coating for scavenging U^{6+}. Farghali et al. [106]

investigated graphene/Fe_3O_4 nanocomposite for the removal of ethylene blue dye from contaminated solutions. Liu et al. [107] coated the surface of Fe_3O_4 nanoparticles using humic acid for the removal of Cu^{2+}, Hg^{2+}, Cd^{2+} and Pb^{2+} from waters. Moamen et al. [102] examined the capability of preparing synthesized magnetic nano zeolite for elimination of Cs^{+} and Sr^{2+} from liquid radioactive waste stream. Hwang et al. [108] developed sodium-copper hexacyanoferrate using magnetic nanoparticles for the effective removal of radioactive Cs and enhanced magnetic adsorbent separation from water. Yang et al. [109] modified Prussian blue by magnetic nanoclusters for rapid magnetic separation of adsorbent from cesium contaminated water. Faghihian et al. [110] synthesized magnetic zeolite composite in the presence of Fe^{2+} and Fe^{3+} ions and the composite was tested for Cs^{+} and Sr^{2+} removal from aqueous solutions based on magnetically assisted separation.

To date, nanoscale zero valent iron (nZVI) has been shown to be efficient environmental remediator of a wide variety of contaminants involving chlorinated organics [111] and inorganic anions . In addition, nZVI has also been shown to considerably remediate solutions contaminated with a variety of transitions metals, such as: Cr [112], Co [113], Cu, Mo [114], Zn, Ni, Ag [115] and V [116]; post transition metals, such as: Pb, Cd [70] and metalloids, such as: As [117, 118] and Se [119]. However, studies for the treatment of radionuclides remain less widely examined and are limited to Ba [120], U [121], Pu [64] and TcO_4 [122].

To enhance the reactivity of nZVI, a number of coatings and stabilizers have been developed such as guar gum [123], carboxylmethyl cellulose (CMC) [124], starch [125] and many surfactants [126]. Coating nZVI using another metal such as Cu, Pd, Pt, Ni, and Ag to form bimetallic iron nanoparticles is another effective approach in the removal of a variety of contaminants [21]. A small amount of these metals deposited on the surface of nZVI enhances contaminant removal rates significantly [127]. Tratnyek et al. [78] showed that the improve in reactivity in the bimetallic system was attributed to catalytic hydrogenation and electrochemical effects.

In this present chapter, the efficiency of nZVI and nano-Fe/Cu particles for the removal of Cs^{+} from aqueous solutions was evaluated. The sorption of Cs^{+} was studied in a batch system with respect to initial cesium concentration, contact time, pH, temperature, competing cations and dosage of nanoparticles. The kinetic, thermodynamic and isotherm

parameters of the process were also investigated. In addition, the mechanism of Cs^+ removal by nZVI and nano-Fe/Cu particles was discussed using different characterization approaches.

4.2. Sorption batch studies

The sorption experiments were performed under kinetic and equilibrium conditions using a batch technique at 298 K. 1 g of nZVI and nano-Fe/Cu particles was contacted with 50 mL of 100 mg/L Cs^+ solution in different stoppered bottles and stirred on a magnetic stirrer at 1000 rpm (RSH-6DN, As One Co., Japan) for 2 h to attain equilibrium. After the experiments, the water samples were collected and filtered through 0.2 µm cellulose acetate filter. The obtained liquid were diluted with deionized water to an acceptable concentration range prior to analysis using inductively coupled plasma mass spectrometry (ICP-MS) technique. To investigate the effect of the solution pH on the Cs^+ uptake, the initial pH was adjusted at 3–12 using dilute solution of HCl or NaOH. To examine the effect of temperature on the Cs^+ removal, the experiments were conducted at four different temperatures ranging from 278 to 343 K. In order to investigate the effect of nanoparticles content on the sorption capacity, a series of dosage from 1 to 30 g/L was prepared. To evaluate the effect of competitive cation ions on the sorption process of Cs^+, different simulated waste solutions were prepared separately in the presence of Na^+, K^+, Mg^{2+} and Ca^{2+}. In addition, Cs^+ removal was tested in simulated contaminated water after Fukushima accident. All batch experiments were carried out in triplicate and the mean values were used to evaluate sorption parameters. The amount of sorbed Cs^+ by unit mass of the nanoparticles, q (mg/g), was calculated by the following equation:

$$q = \left(C_i - C_f\right) \times (V/m) \tag{4.1}$$

The distribution coefficient, K_d (L/g), was also calculated using the following formula:

$$K_d = (C_i - C_f)/C_f \times (V/m) \tag{4.2}$$

where C_i and C_f are the initial and final Cs^+ concentrations (mg/L) respectively, m is the amount of the sorbent (g) and V is the volume of the solution (L).

4.2.1. Kinetic experiments

Kinetic studies for sorption of Cs^+ onto nZVI and nano-Fe/Cu particles were performed at 298 K. 2 g of each sorbent were added to 100 mL of Cs^+ solution at pH 6 and the liquid samples were collected at different time interval (5–120 min). The experiments were also conducted at different initial concentrations of 1, 5, 50, 100, 150 and 200 mg/L. The uptake of Cs^+ as a function of time, q_t (mg/g), was calculated according to:

$$q_t = (C_i - C_t) \times (V/m) \quad (4.3)$$

where C_t is the concentration of Cs^+ at a time t.

4.2.2. Sorption equilibrium studies

The sorption isotherm measurements were conducted by mixing 1 g of nZVI and nano-Fe/Cu particles with 50 mL of Cs^+ solution at 298 K and initial pH of 6. Various concentrations of Cs^+ ranged from 1 to 1000 mg/L were investigated. After the equilibrium time was reached, the supernatants were filtered and the remaining Cs^+ concentrations were estimated using ICP-MS.

4.2.3. ICP-MS preparation and conditions

The liquid samples were analyzed using ICP-MS device by a 1000 times dilution in 1% nitric acid [64, 121]. Samples with elevated Cs^+ concentrations were diluted by a 10000 factor. Besides, blanks and Cs^+ standards at 0.1, 0.2, 0.5, 1, 5, 10, 50 and 100 ppb were prepared in 1% nitric acid. The ICP-MS instrument used was ICPM-8500 model (manufactured by Shimadzu Co.).

4.3. Results and discussion

4.3.1. Characterization of the synthesized nanoparticles

The XRD patterns (Fig. 4.1) of nZVI and nano-Fe/Cu particles revealed diffraction peaks at $2\theta = 44.8°$ and 82.53°, confirming that the synthesized nanoparticles consisted principally of highly crystalline metallic iron (Fe^0). The weak peaks at $2\theta = 35°$ and 65° in the XRD analysis suggested the presence of iron oxides in the synthesized nanoparticles [72]. TEM image of nZVI (Fig. 4.2a) showed that the synthesized nZVI particles were roughly spherical and aggregated into a chain-like structure owing to their magnetic

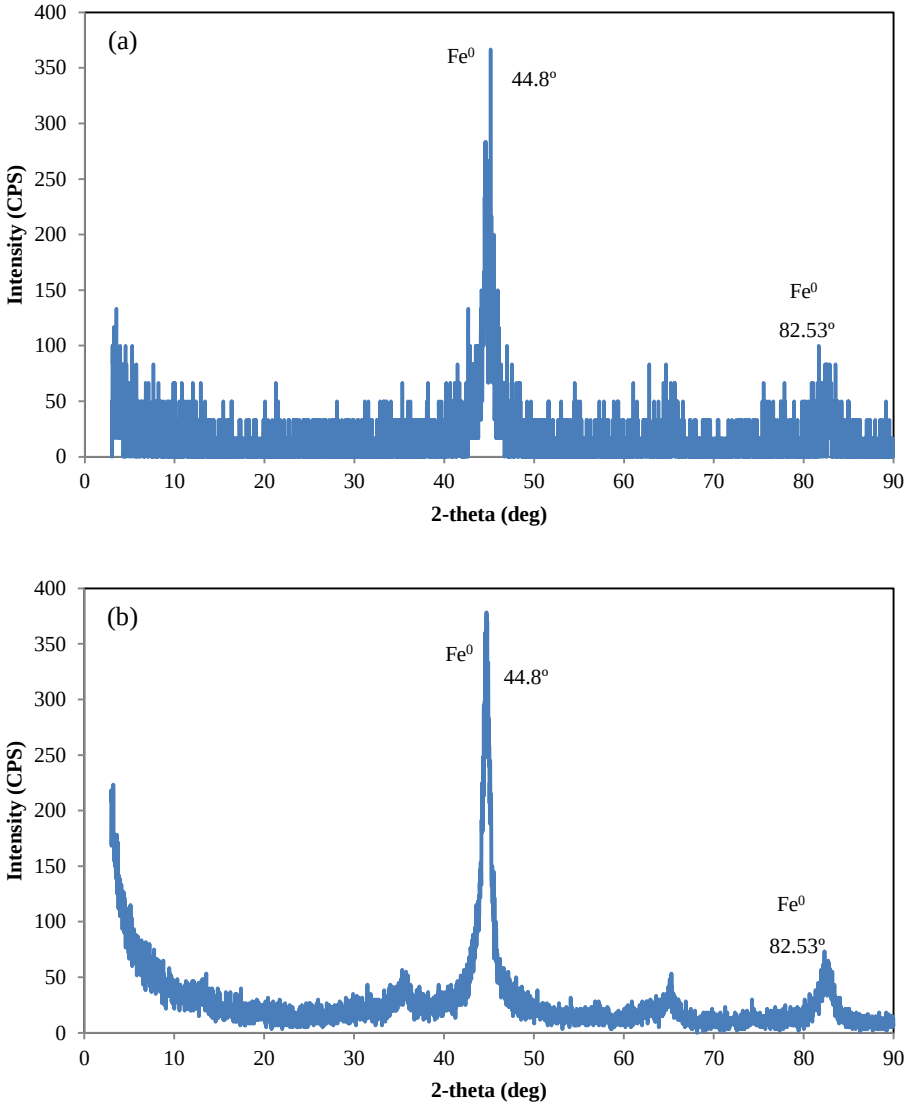

Fig. 4.1. XRD patterns of synthesized (a) nZVI and (b) nano-Fe/Cu particles.

attractions and high surface energies. In nano-Fe/Cu system (Fig. 4.2b), the chain-like morphology decreased and the particles were assembled together in bulks and mainly composed of irregular shaped particles. TEM images documented the presence of surface oxide layer that surrounded the nanoparticles core. The surface morphology of the synthesized nZVI and nano-Fe/Cu particles was also analyzed by SEM images (see Fig. AII (1) in Appendices Section). It was observed that the nZVI assembled together in chains (Fig. AII (1a)), while in case of nano-Fe/Cu particles, the chain-like conformation disappeared and replaced by irregular shapes as depicted in Fig. AII (1b). The elemental analysis of both nZVI and nano-Fe/Cu particles was studied by energy dispersive X-ray

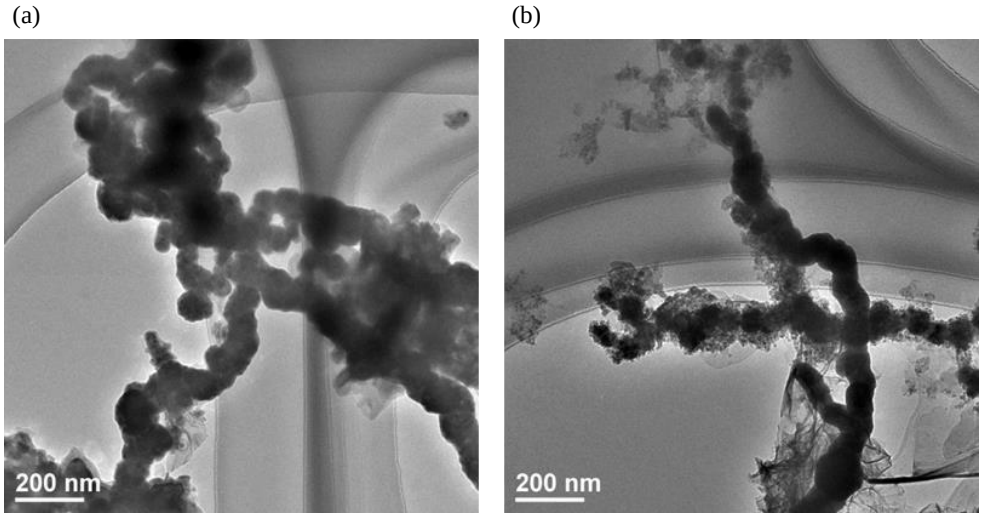

Fig. 4.2. TEM images of synthesized (a) nZVI and (b) nano-Fe/Cu particles.

spectroscopy (EDS) and its result is presented in Fig. AII (2). The presence of Fe in the synthesized nanoparticles was further confirmed by EDS. EDS analysis of nZVI showed peaks corresponding to Fe and O elements (Fig. AII (2a)). Cu, Fe and O were the main elements present in EDS spectrum of nano-Fe/Cu particles (Fig. AII (2b)). Traces of Na, Mg, Al and C were found in some samples. The BET specific surface area of nZVI was 17 m^2/g, compared to 32 m^2/g for nano-Fe/Cu particles. The mean particle size of nZVI and nano-Fe/Cu particles measured by the particle size analyzer was estimated to be about 44 and 70 nm, respectively.

4.3.2. Changes in pH and ORP

Fig. 4.3 shows the variations of solution pH and ORP with reaction time for nZVI and nano-Fe/Cu systems. For both systems, the pH and ORP were measured as 6 and 20 mV, respectively prior to addition of the nanoparticles. Immediately after the addition of the nanoparticles, the pH increased, reaching a maximum value of pH 9.44 and pH 9.34 in the nZVI and nano-Fe/Cu systems, respectively. Concurrently, a decrease in solution ORP was recorded, reaching a minimum value of –174 mV for nZVI system and –168 mV for nano-Fe/Cu system. These changes in pH and ORP can be attributed to the immediate oxidation of the iron nanoparticles surfaces (as shown in Eqs. (4.4)–(4.7)).

$$2Fe^0 + 4H^+ + O_2 \rightarrow 2Fe^{2+} + 2H_2O \quad (4.4)$$

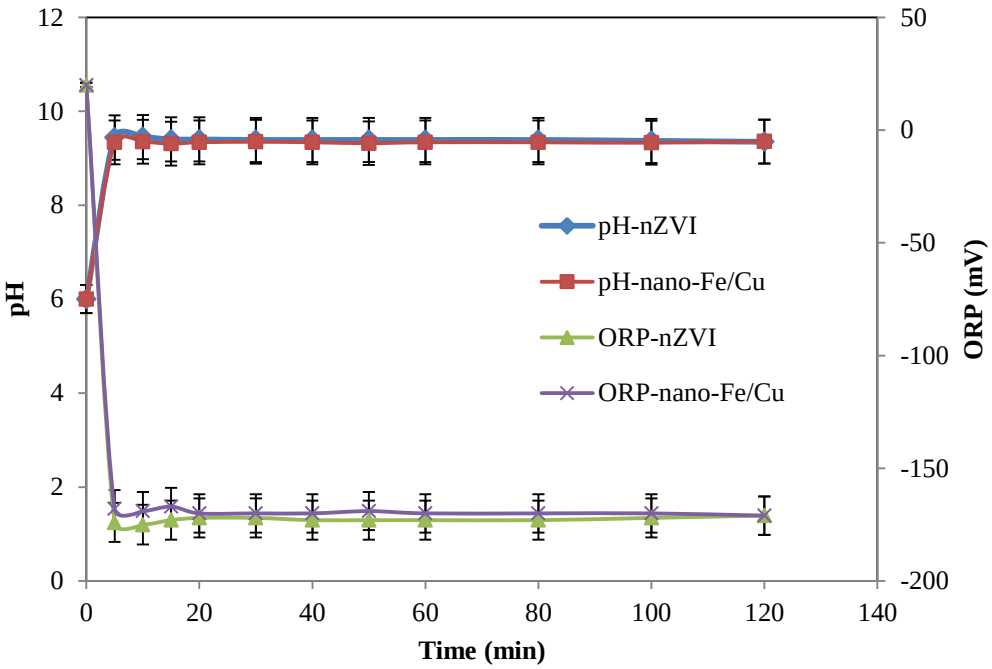

Fig. 4.3. Changes in pH and ORP over time during Cs^+ sorption by nZVI and nano-Fe/Cu particles. (Initial conditions: pH = 6, dosage = 20 g/L, initial Cs^+ concentration = 100 mg/L, temperature = 298 K).

$$2Fe^0 + 2H_2O \rightarrow 2Fe^{2+} + H_2 + 2OH^- \quad (4.5)$$

$$Fe^{2+} + 2H^+ + 1/2O_2 \rightarrow 2Fe^{3+} + H_2O \quad (4.6)$$

$$2Fe^{2+} + 2H_2O \rightarrow 2Fe^{3+} + H_2 + 2OH^- \quad (4.7)$$

According to these corrosion reactions, the nanoparticles would be as a dynamic and an active source for various types of corrosion products (Fe^{2+}/Fe^{3+}). It is presumed that these formed corrosion products would be responsible for the physical sorption of Cs^+ ions [64].

4.3.3. Effect of experimental condition on Cs^+ sorption process

4.3.3.1. Effect of pH

The effect of pH on the removal of Cs^+ by nZVI and nano-Fe/Cu particles was investigated over pH range from 3 to 12. As shown in Fig. 4.4, it is obvious that Cs^+ sorption process is a pH dependent process and the initial pH of the aqueous solution has high impact on Cs^+ removal by nZVI and nano-Fe/Cu particles. At initial pH 3, the sorption capacity of Cs^+ by nZVI and nano-Fe/Cu particles was 1.93 and 2.50 mg/g and the Cs^+

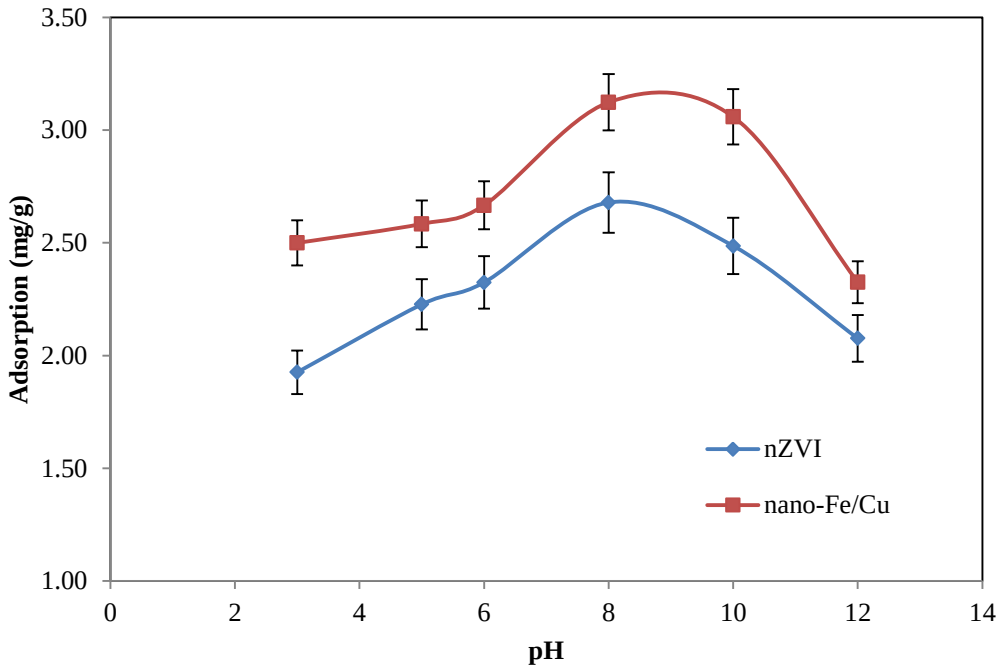

Fig. 4.4. Effect of pH on Cs^+ sorption by nZVI and nano-Fe/Cu particles. (Initial conditions: dosage = 20 g/L, initial Cs^+ concentration = 100 mg/L, temperature = 298 K).

removal was only 38.52% and 49.99%, respectively. The Cs^+ removal by nZVI and nano-Fe/Cu particles increased with the increase in the pH and the maximum removal was observed at pH 8 with Cs^+ removal of 53.58% and 62.46%, respectively. At higher pH values, Cs^+ removal by nZVI and nano-Fe/Cu particles decreased to only 41.52% and 46.50% and the sorption capacity was 2.08 and 2.33 mg/g, respectively. The Cs^+ removal was inhibited in the acidic medium because the H^+ ions compete with Cs^+ ions for the sorption sites. In addition, the degradation of some fraction of the nanoparticles may occur under acidic conditions. In the strong alkaline environment, the formed passive layer of iron hydroxide precipitates can hinder further oxidation of nZVI [112].

4.3.3.2. Effect of initial cesium concentration and contact time

The effect of contact time on sorption of Cs^+ ions onto nZVI and nano-Fe/Cu partilces was performed at 298 K and different initial concentrations of 1, 5, 50, 100, 150 and 200 mg/L and the results are presented in Fig. 4.5. It is clear that the Cs^+ sorption rate was initially very fast for both nanoparticles and the sorption amount of Cs^+ increased with increasing the initial Cs^+ concentration. The amount of sorbed Cs^+ onto nZVI increased

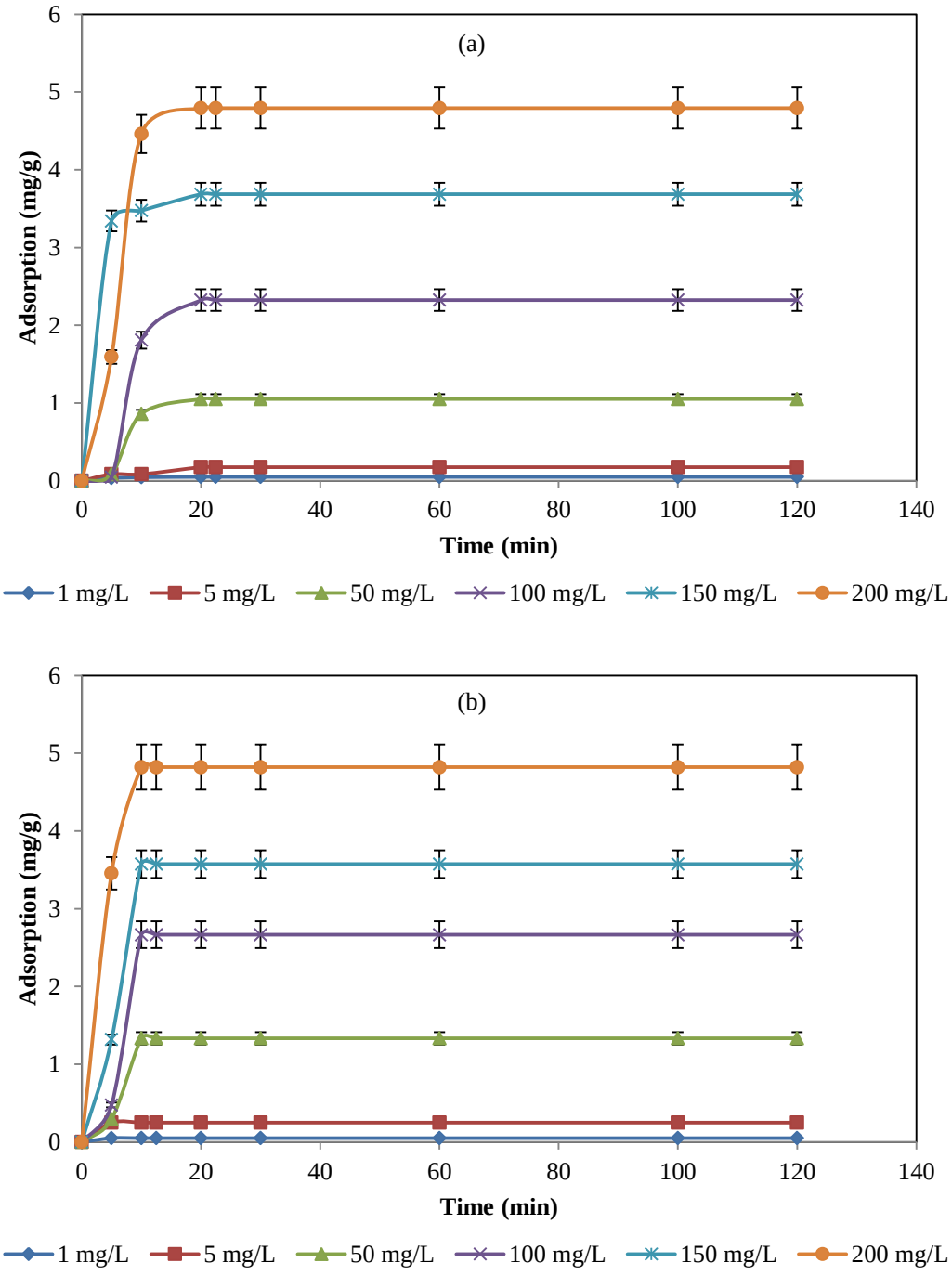

Fig. 4.5. Effect of initial Cs^+ concentration and contact time on cesium sorption by (a) nZVI and (b) nano-Fe/Cu particles. (Initial conditions: pH = 6, dosage = 20 g/L, temperature = 298 K).

with time attaining a maximum value after 20 min (Fig. 4.5a), while the equilibrium time in the case of nano-Fe/Cu particles was established after only 10 min (Fig. 4.5b). It was observed that the equilibrium time was independent on the initial Cs^+ concentrations

investigated in this study (1 to 200 mg/L). It can also be noted that the amount of Cs^+ sorbed onto nano-Fe/Cu particles was higher than that for nZVI. The removal of Cs^+ using nano-Fe/Cu particles varied than that of nZVI alone by 29.67%, 11.26% and 6.84% greater removal efficiency at initial concentrations of 5, 50 and 100 mg/L, respectively. This could be attributed to coating of nZVI by Cu^{2+} ions which decreases the aggregation and agglomeration of nZVI particles and increases the surface area of these nanoparticles [9]. In addition, Cu metal stimulates better electron transformation from nZVI core and thus increases the reactivity [100]. The presence of Cu in the bimetallic nanoparticles system at certain ratios can also prevent nZVI particles from being oxidized by O_2 [128]. The values of maximum removal of Cs^+ onto nZVI at 1, 5, 50, 100, 150 and 200 mg/L were 99.95%, 70.33%, 42.09%, 46.49%, 49.15% and 47.93%, while the values in the case of nano-Fe/Cu particles at the same initial concentrations were 99.99%, 99.98%, 53.36%, 53.33%, 47.67% and 48.22%, respectively. The higher sorption capacity of the nanoparticles at high Cs^+ concentrations could be attributed to higher possibility of collision between cesium ions and the nanoparticles. This behavior could also be related to the ratio of initial Cs^+ concentration to the available reactive sites on the surface of nanoparticles. It was concluded that the Cs^+ sorption process of nano-Fe/Cu particles was kinetically faster than that of nZVI. In addition, the difference in the Cs^+ sorption rates of nano-Fe/Cu particles and nZVI was greater at lower initial Cs^+ concentrations. Therefore, the rapid removal of cesium by nano-Fe/Cu particles could be even more evident under the actual conditions of an accident involving nuclear fallout.

4.3.3.3. Effect of contact time at different pH values

The effect of contact time on sorption of Cs^+ ions onto nZVI and nano-Fe/Cu particles at 298 K and different initial pH of 3, 6, 8 and 10 is illustrated in Fig. 4.6. The amount of Cs^+ sorbed onto nZVI sharply increased with time reaching an equilibrium value after about 20 min, and thereafter the sorption capacity remained constant (Fig. 4.6a). Whereas the time required for attaining equilibrium in case of nano-Fe/Cu particles was only 10 min (Fig. 4.6b). The equilibrium time remained practically unaffected by changing pH. Therefore, the sorption rate of Cs^+ on nZVI and nano-Fe/Cu particles was independent on initial pH.

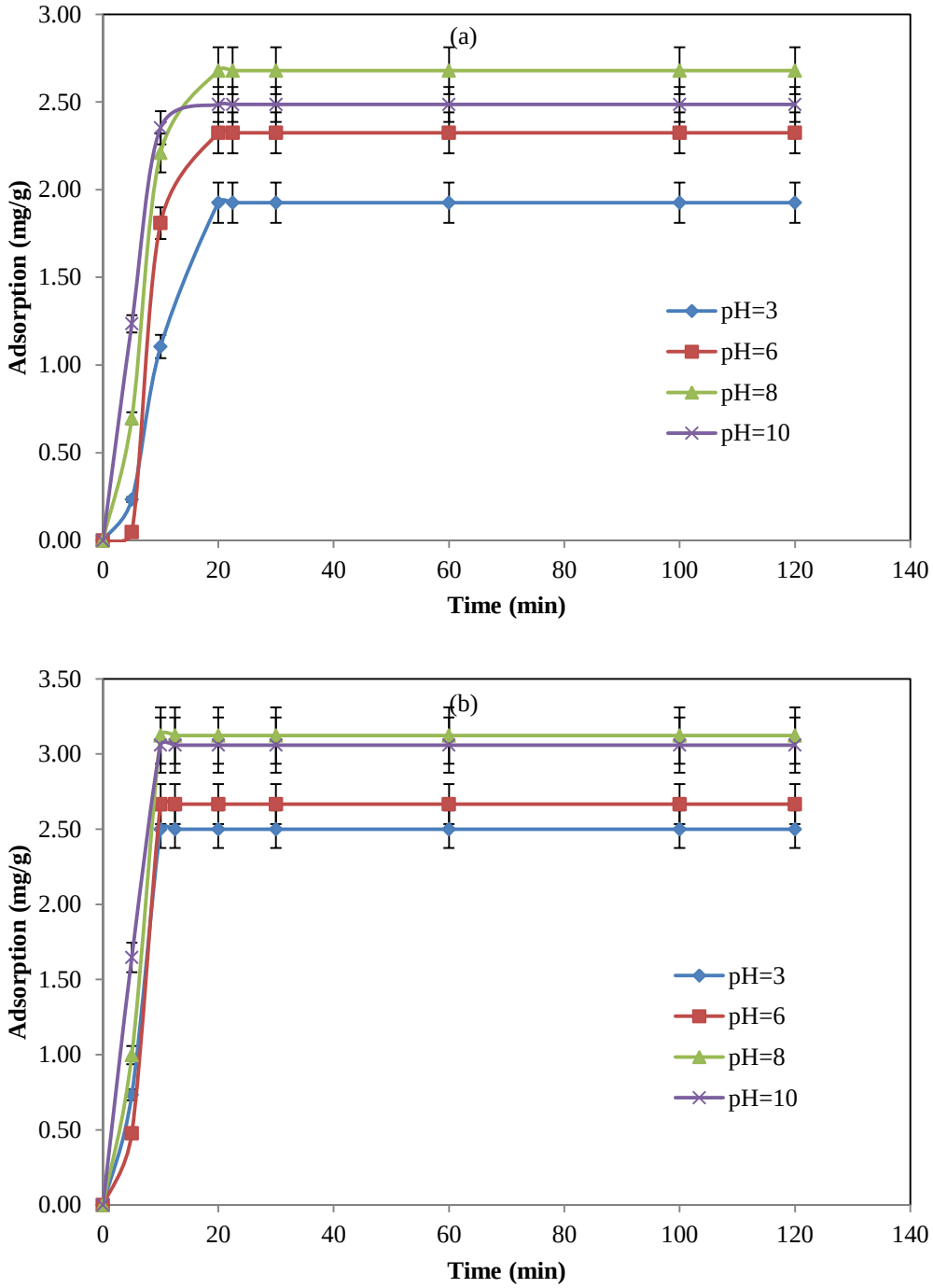

Fig. 4.6. Effect of contact time at different initial pH 3, 6, 8 and 10 on Cs^+ sorption by (a) nZVI and (b) nano-Fe/Cu particles. (Initial conditions: dosage = 20 g/L, initial Cs^+ concentration = 100 mg/L, temperature = 298 K).

4.3.3.4. Dosage effect

The removal of Cs^+ by nZVI and nano-Fe/Cu particles was studied by a series of nanoparticles dosage in the range from 1 to 30 g/L at initial Cs^+ concentration of 100 mg/L, initial pH of 6 and temperature of 298 K. The relation between dosage and removal of cesium is shown in Fig. 4.7. From Fig. 4.7, Cs^+ removal increased with increasing the amount of the nanoparticles that more active sites were available to sorb more Cs^+. With 1 g/L of nZVI, 29.54% of Cs^+ was removed and the sorption capacity attained its maximum which was 29.54 mg/g. The removal of Cs^+ was up to 33.43% when the dosage of nZVI increased to 2 g/L and the sorption capacity was 16.71 mg/g. These results proposed that the sorption capacity of nZVI was saturated when the dosage of nZVI was below 2 g/L in the treatment system. With 5 g/L of nZVI, the removal of Cs^+ achieved 36.76% with the sorption capacity of 7.35 mg/g. When the addition of nZVI increased to 10 g/L, the removal of Cs^+ achieved 47.27% and the sorption capacity was 4.73 mg/g. In the treatment system of 20 g/L of nZVI, 46.49% of Cs^+ was removed and the removal capacity was 2.32 mg/g. The removal of Cs^+ increased to 54.02% after the addition of 30 g/L of nZVI and the amount of Cs^+ sorbed onto the nanoparticles was 1.80 mg/g. In the nano-Fe/Cu treatment

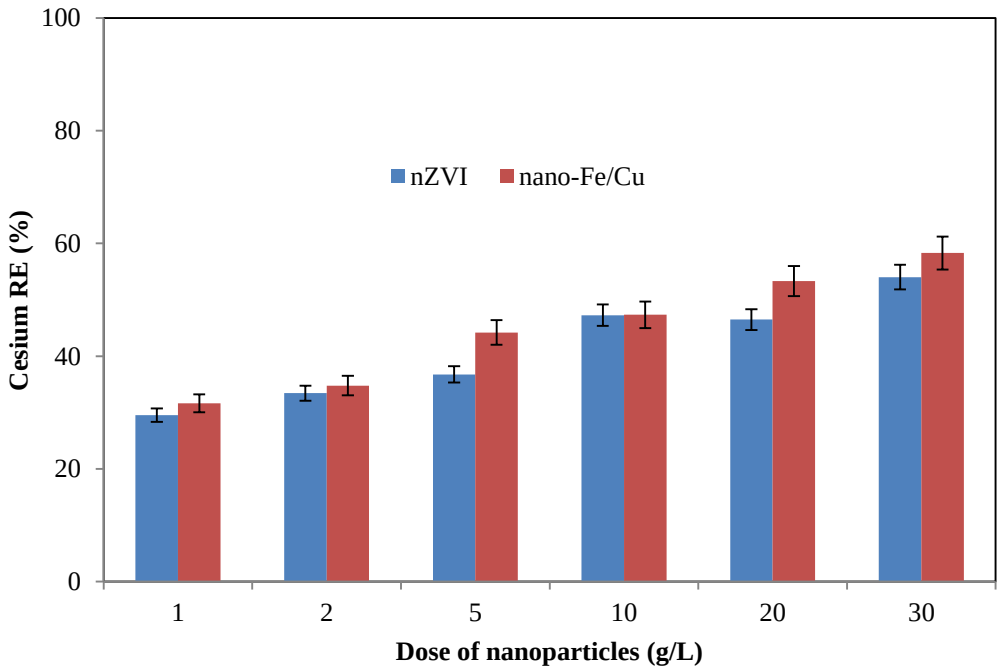

Fig. 4.7. Cs^+ removal by different dosage of nZVI and nano-Fe/Cu particles. (Initial conditions: pH = 6, initial cesium concentration = 100 mg/L, temperature = 298 K).

system, the values of maximum removal of Cs^+ at similar doses were 31.63%, 34.77%, 44.20%, 47.34%, 53.33% and 58.30% and the removal capacity was 31.63, 17.39, 8.84, 4.73, 2.67 and 1.94 mg/g, respectively. Comparison of Cs^+ removal by nZVI and nano-Fe/Cu particles indicated that Cs^+ removal was slightly larger for nano-Fe/Cu particles than for nZVI at similar dosage.

4.3.3.5. Matrix effect

The effect of competing cation ions on Cs^+ removal by nZVI and nano-Fe/Cu particles at 298 K and initial pH of 6 was examined and the results are presented in Table 4.1. Four simulated waste solutions were prepared separately in the presence of similar concentration (20 mg/L) of Na^+ (0.87 mM), K^+ (0.51 mM), Mg^{2+} (0.82 mM) and Ca^{2+} (0.50 mM) with initial Cs^+ concentration of 100 mg/L [129]. It is evident that the removal of Cs^+ were highly (decreased) affected in the presence of the competing cation. These findings confirmed that the cation ions can compete and lower the sorption of Cs^+ on the nanoparticles. It was noted that the effect of K^+ ions on Cs^+ removal was higher than Na^+ ions. This could be due to the close similarity in the hydration radii of K^+ and Cs^+ rather than to Na^+ [130]. In the presence of Mg^{2+} and Ca^{2+} ions, passivated precipitates such as $Mg(OH)_2$ and $CaCO_3$ formed on the nanoparticles surfaces resulting in blocking the electron transfer from the nanoparticles cores [131].

Table 4.1: Effect of different competing cation ions on Cs^+ removal by nZVI and nano-Fe/Cu particles at initial Cs^+ concentration = 100 mg/L, pH = 6, dosage = 20 g/L and temperature = 298 K.

Ions	nZVI	nano-Fe/Cu
	RE (%)	RE (%)
100 mg/L Cs^+ (without cations)	46.49	53.33
20 mg/L Na^+	44.91	31.39
20 mg/L K^+	42.06	29.92
20 mg/L Mg^{2+}	36.38	29.83
20 mg/L Ca^{2+}	36.25	33.83

4.3.3.6. Effect of temperature

The effect of temperature on Cs^+ sorption by nZVI and nano-Fe/Cu particles was investigated at four different temperatures of 298, 313, 328 and 343 K (Fig. 4.8). The sorption capacity decreased with increasing the temperature, suggesting that nZVI and nano-Fe/Cu particles were favorable for Cs^+ sorption at low temperatures. The values of

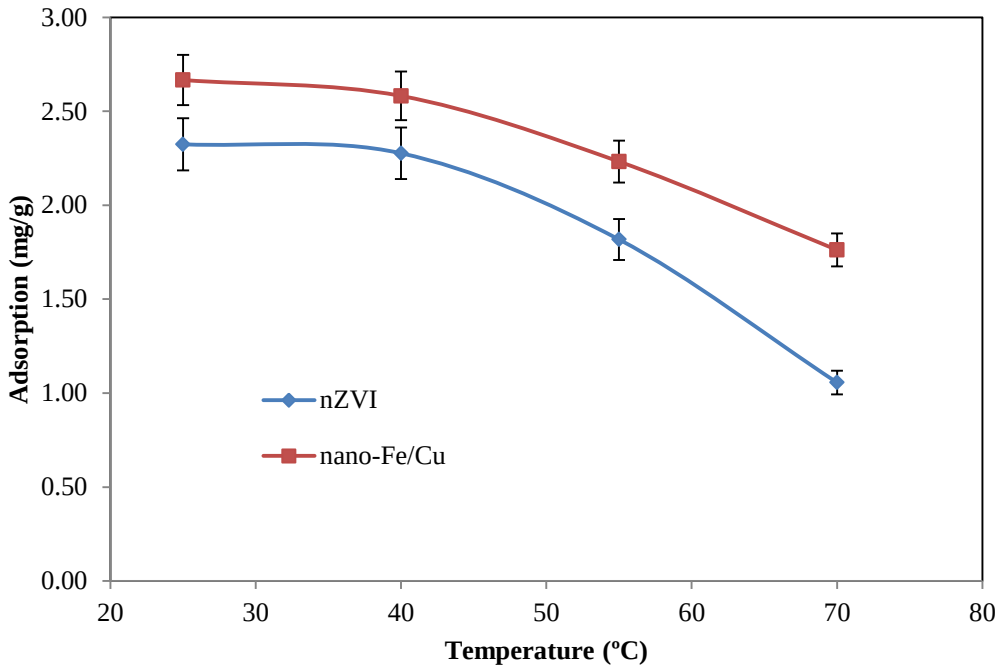

Fig. 4.8. Effect of temperature on Cs^+ sorption by nZVI and nano-Fe/Cu particles. (Initial conditions: pH = 6, dosage = 20 g/L, initial cesium concentration = 100 mg/L).

removal of Cs^+ onto nZVI at 298, 313, 328 and 343 K were 46.49%, 45.53%, 36.36% and 21.13% and the sorption capacity was 2.32, 2.28, 1.82 and 1.06 mg/g, respectively. In case of nano-Fe/Cu particles, the removal of Cs^+ at similar initial temperatures was 53.33%, 51.64%, 44.65% and 35.24% and the sorption capacity was 2.67, 2.58, 2.23 and 1.76 mg/g, respectively. These data were used to calculate the thermodynamic parameters. Results are consistent with the greater sorption of Cs^+ on natural clays [132] and Ba^{2+} on nZVI [120] with decreasing temperature.

4.3.4. Kinetic sorption modeling

Pseudo-first-order, pseudo-second-order, Elovich and intra-particle diffusion kinetic models were used for the evaluation of experimental data. The linear form of Lagergren pseudo-first-order model is written as:

$$\ln(q_e - q_t) = \ln q_e - k_1 t \qquad (4.8)$$

where q_e and q_t are the amount of Cs^+ ion sorbed per unit mass of the sorbents at equilibrium and at any time t (mg/g), respectively. k_1 is the pseudo-first-order rate constant (min^{-1}). The k_1 and q_e values were calculated from the slope and the intercept of plotting

of $\ln(q_e - q_t)$ against t. The obtained parameters are presented in Table 4.2. The calculated q_e are not in conformity with the experimental data, confirming that the sorption process of Cs^+ onto nZVI and nano-Fe/Cu particles could not follow a pseudo-first-order model.

The linear form of pseudo-second-order kinetic model and initial sorption rate (h) are expressed as:

$$t/q_t = 1/(k_2 q_e^2) + (1/q_e)\, t \tag{4.9}$$

$$h = k_2 q_e^2 \tag{4.10}$$

where k_2 is the rate constant of pseudo-second-order sorption (g/mg/min). The important parameters of k_2, q_e and h were obtained from the slope and the intercept of the plot of t/q_t versus t (Table 4.2). Comparing of k_2 values indicated that the sorption rate of Cs^+ onto nano-Fe/Cu particles is faster than that of the nZVI.

The intra-particle diffusion possibility was discussed by using the intra-particle diffusion model:

$$q_t = K_{\text{diff}} t^{1/2} + C \tag{4.11}$$

where q_t is the sorption capacity at time t, K_{diff} is the intra-particle diffusion rate constant (mg/g/min) and C is the intercept. It is clear from the results in Table 4.3, the intra-particle diffusion may not be a limiting step in the sorption process.

Elovich equation is written as follows:

$$q_t = \ln(\alpha\beta)/\beta + \ln t/\beta \tag{4.12}$$

where α and β are constants, α is the initial sorption rate of Elovich equation (mg/g/min) and β is adsorption constant (g/mg). The slope and the intercept of the plot of q_t versus $\ln t$ yielded the values of α and β. The results are listed in Table 4.3.

Comparison of the correlation coefficient (R^2) and calculated equilibrium sorption capacity (q_e) for four kinetic models revealed that the Cs^+ sorption process can be represented well by pseudo-second-order kinetics. It was reported that the rate of sorption process is controlled by chemisorption if the experimental data are successfully fitted to pseudo-second-order model [133]. Consequently, the overall rate constant of Cs^+ sorption

process onto nZVI and nano-Fe/Cu particles appeared to be controlled by the chemical sorption process.

Table 4.2: The calculated parameters of pseudo-first-order and pseudo-second-order kinetic models for cesium sorption onto nZVI and nano-Fe/Cu particles.

Sorbents	Initial concen. (mg/L)	$q_{e\ (exp.)}$ (mg/g)	Pseudo-first order model			Pseudo-second order model			
			k_1 (min^{-1})	$q_{e\ (theor.)}$ (mg/g)	R^2	k_2 (g/mg/min)	$q_{e\ (theor.)}$ (mg/g)	h (mg/g/min)	R^2
nZVI	1	0.05	0.0708	0.0031	0.4816	1.575	0.06	0.0050	0.9490
	5	0.18	0.0697	0.0098	0.4820	1.174	0.18	0.0399	0.9919
	50	1.05	0.0674	0.0464	0.4825	0.350	1.08	0.4104	0.9961
	100	2.32	0.0660	0.0900	0.4812	0.221	2.37	1.2414	0.9977
	150	3.69	0.0646	0.1238	0.4766	0.138	3.76	1.9540	0.9971
	200	4.79	0.0653	0.1724	0.4777	0.077	4.93	1.8768	0.9946
nano-Fe/Cu	1	0.05	0.0510	0.0004	0.3028	2.542	0.05	0.0074	0.9525
	5	0.25	0.0501	0.0020	0.3033	2.154	0.26	0.1400	0.9969
	50	1.33	0.0485	0.0094	0.3033	1.290	1.34	2.3248	0.9997
	100	2.67	0.0487	0.0191	0.3033	0.571	2.69	4.1158	0.9996
	150	3.57	0.0497	0.0281	0.3034	0.211	3.63	2.7792	0.9986
	200	4.82	0.0501	0.0392	0.3033	0.115	4.92	2.7664	0.9970

Table 4.3: The calculated parameters of Elovich and intra-particle diffusion kinetic models for cesium sorption onto nZVI and nano-Fe/Cu particles.

Sorbents	Initial concen. (mg/L)	Elovich model			Intra-particle diffusion model		
		α (mg/g/min)	β (g/mg)	R^2	K_{diff} (mg/g/min)	C (mg/g)	R^2
nZVI	1	0.011	81.73	0.8335	0.0047	0.009	0.6881
	5	0.052	25.23	0.8669	0.0151	0.046	0.6911
	50	0.427	4.45	0.8280	0.0822	0.360	0.6119
	100	1.120	2.08	0.8040	0.1733	0.880	0.5789
	150	1.818	1.32	0.7767	0.2730	1.422	0.5529
	200	2.084	0.98	0.7769	0.3673	1.731	0.5605
nano-Fe/Cu	1	0.018	89.70	0.7121	0.0040	0.016	0.5175
	5	0.130	19.56	0.7461	0.0182	0.099	0.5233
	50	1.160	4.07	0.7110	0.0855	0.642	0.4753
	100	2.193	2.01	0.7190	0.1733	1.262	0.4831
	150	2.142	1.41	0.7456	0.2513	1.512	0.5162
	200	2.540	1.02	0.7463	0.3505	1.931	0.5230

The k_2 values of pseudo-second-order model were used to calculate the activation energy of the sorption (E_a) (Fig. AII (3)) using the following Arrhenius equation:

$$\ln k_2 = \ln A - E_a/(RT) \tag{4.13}$$

where k_2 is the rate constant (g/mg/min), A is the temperature independent factor (g/mg/min), E_a is the activation energy of the sorption (kJ/mol), R is the gas constant

(8.314 J/mol/K) and T is the absolute temperature (K). The calculated value of E_a (Table 4.4) was less than 42 kJ/mol, indicating that Cs^+ sorbed onto nZVI and nano-Fe/Cu particles with low potential energy [134].

4.3.5. Evaluation of thermodynamic parameters

Thermodynamic parameters, including enthalpy change ($\Delta H°$) and entropy change ($\Delta S°$) were calculated using linear plot of Van't Hoff equation:

$$\ln K_d = (\Delta S°/R) - (\Delta H°/RT) \quad (4.14)$$

where K_d is the distribution coefficient (ml/g).

Fig. AII (4) shows the plot of $\ln K_d$ versus $1/T$. The Gibbs free energy change ($\Delta G°$) was determined from the following equation:

$$\Delta G° = \Delta H° - T\Delta S° \quad (4.15)$$

Table 4.4: Thermodynamic parameters for cesium sorption onto nZVI and nano-Fe/Cu particles.

Sorbent	E_a (kJ/mol)	A (g/mg/min)	$\Delta H°$ (kJ/mol)	$\Delta S°$ (kJ/mol/K)	$\Delta G°$ (kJ/mol)			
					298 K	313 K	328 K	343 K
nZVI	24.89	4404	−21.74	−0.0401	−9.80	−9.20	−8.60	−8.00
nano-Fe/Cu	16.14	341	−14.00	−0.0126	−10.25	−10.06	−9.88	−9.69

The calculated thermodynamic parameters are summarized in Table 4.4. Since the change in $\Delta H°$ values was found to be negative, the sorption process was exothermic in nature. This means that lower temperatures are favored for enhanced removal of cesium by nZVI and nano-Fe/Cu particles. Shahwan et al. [135] concluded that cations with low hydration enthalpies (low charge/size ratio like Cs^+) will demonstrate exothermic sorption behavior, while cations of higher charge/size ratio (like Sr^{2+}) will generally show endothermic sorption behavior. The negative values of $\Delta S°$ revealed a decrease in randomness at the solid/solution interface during the sorption process. The obtained negative values of $\Delta G°$ indicated the spontaneous nature of the sorption process. The increase in $\Delta G°$ values with increasing temperature, indicating that the sorption of Cs^+ ions was favored at lower temperatures.

4.3.6. Sorption isotherms

The relationship between the equilibrium amounts of Cs^+ sorbed onto the nZVI and nano-Fe/Cu particles prepared with different initial concentrations ranging from 1 to 1000 mg/L and the concentration of Cs^+ after equilibrium represented sorption isotherm (Fig. 4.9). Three sorption isotherm models including Langmuir, Freundlich and Redlich-Peterson models were considered to fit the experimental isotherm data. Langmuir isotherm is derived to model the monolayer sorption covered surfaces and proposes that sorption occurs at homogenous and energetically equivalent sites within the sorbent. The linear form of the Langmuir equation is expressed as:

$$1/q_e = 1/q_{max} + 1/(q_{max} b C_e) \quad (4.16)$$

where q_{max} is the maximum amount of Cs^+ ion sorbed per unit weight of the sorbents (mg/g), C_e is the equilibrium concentration of cesium ion in the solution (mg/L) and b is the Langmuir constant related to the free energy of sorption. The values of the constants of q_{max} and b were calculated from the slope and the intercept of the plot of C_e/q_e against C_e (Fig. AII (5)) and are given in Table 4.5. As it can be seen from Table 4.5, the maximum sorption capacity of nano-Fe/Cu particles for removal of Cs^+ was relatively higher than that for nZVI (q_{max} for nano-Fe/Cu particles was 37.62 mg/g compared to 32.51 mg/g for nZVI

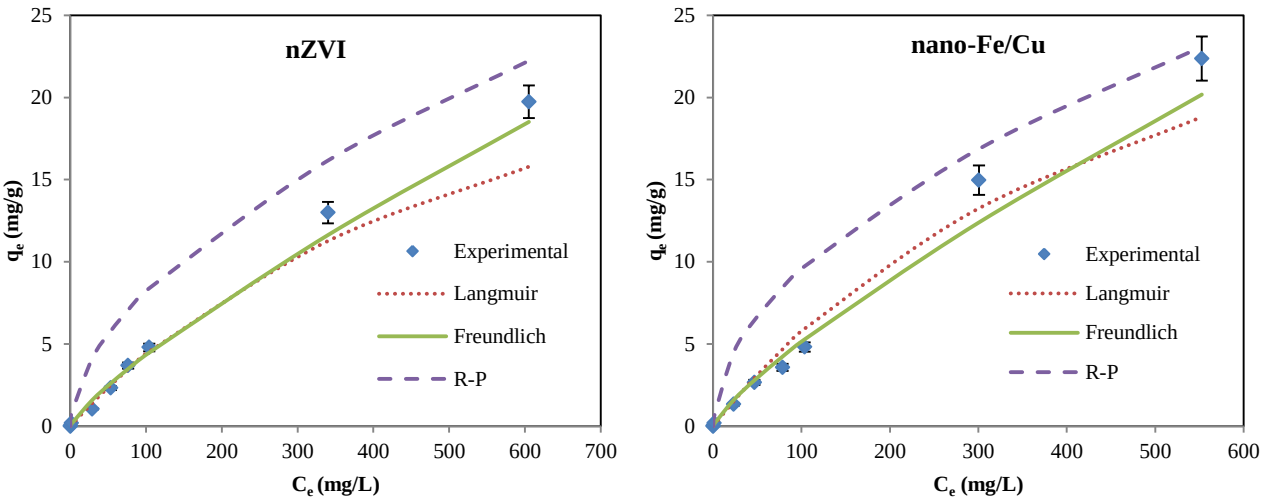

Fig. 4.9. Sorption isotherms of cesium onto nZVI and nano-Fe/Cu particles. (Initial conditions: pH = 6, dosage = 20 g/L, temperature = 298 K).

alone), confirming the higher sorption capacity of nano-Fe/Cu particles toward Cs^+. One of the important parameters of Langmuir model is the dimensionless constant (R_L) called separation factor, which can be defined as:

$$R_L = 1/(1 + bC_0) \tag{4.17}$$

where C_0 is the highest initial Cs^+ concentration (mg/L). The value of R_L indicated the type of isotherm to be favorable ($0 < R_L < 1$), unfavorable ($R_L > 1$), irreversible ($R_L = 0$) or linear ($R_L = 1$). The R_L values were found to be greater than 0 and less than 1 for both nanoparticles, indicating the sorption isotherms were favorable.

Freundlich isotherm model suggests that multilayer sorption occurs on heterogeneous surfaces. The linearized form of Freundlich model is given by:

$$\log q_e = \log K_f + 1/n \log C_e \tag{4.18}$$

where K_f the Freundlich constant related to the sorbent capacity and n the constant indicative to the intensity of the sorption process were calculated from the slope and the intercept of plotting of $\ln q_e$ versus $\ln C_e$ (Fig. AII (6)). The isotherm constants K_f and n are represented in Table 4.5. It can be observed that the Freundlich intensity constant (n) was greater than unity for both nanoparticles, suggesting that the tendency for sorption increases with increasing the Cs^+ concentration. Also the K_f value for nano-Fe/Cu particles was greater than for nZVI, confirming that nano-Fe/Cu particles had greater tendency for sorption of Cs^+.

Redlich-Peterson (R-P) isotherm suggests a three-parameter sorption isotherm model that integrates features from both the Langmuir and Freundlich isotherms which can be described as follows:

$$\ln(K_R\,(C_e/q_e) - 1) = g \ln C_e + \ln a_R \tag{4.19}$$

where K_R is the R-P sorption capacity constant calculated via trials and errors to obtain the maximum linear regression value of the isotherm. The parameters, a_R the R-P isotherm constant and g the exponent ($0 \leq g \leq 1$) were determined from the slope and the intercept of the plot of $\ln(K_R(C_e/q_e) - 1)$ against $\ln C_e$ (Fig. AII (7)). The calculated values of K_R,

a_R and g are listed in Table 4.5. When $g = 1$, the R-P equation reduces to the Langmuir equation and it implies a homogenous sorption process and when $g = 0$, the Freundlich equation forms and the heterogeneity predominates the surface sorption. The g values were found to be greater than 0 and less than 1, which indicated that the sorption of Cs^+ by nZVI and nano-Fe/Cu particles occurred on homogenous and heterogeneous surfaces.

Table 4.5: Sorption isotherm parameters for cesium sorption onto nZVI and nano-Fe/Cu particles.

Isotherm	Sorbents	Model parameters			
		q_{max} (mg/g)	$b \times 10^3$ (L/mg)	R_L	R^2
Langmuir	nZVI	32.51	1.56	0.391	0.9968
	nano-Fe/Cu	37.62	1.81	0.356	0.9981
Freundelich		n	K_f (mg/g)		R^2
	nZVI	1.80	0.33		0.9887
	nano-Fe/Cu	2.03	0.52		0.9923
Redlich-Peterson		K_R (L/g)	a_R (L/mg)	g	R^2
	nZVI	12	18.41	0.45	0.9023
	nano-Fe/Cu	22	24.47	0.49	0.9550

Comparison between the correlation coefficient (R^2) values for the three studied isotherms indicated that the equilibrium sorption data for both nanoparticles were satisfactory fitted to Langmuir and Freundlich models.

4.3.7. Cesium removal in simulated contaminated water after Fukushima accident

In 2011, a massive earthquake hit the Fukushima Daiichi nuclear plant located on the east coast of Japan. As a result of the earthquake, a tsunami occurred and disabled the Fukushima Daiichi reactors power supply and cooling system. To maintain cooling, seawater was pumped to the reactors, resulting in generation of large volumes of radioactive wastewater. The wastes contained a high TDS concentration, with the primary ions of Na^+, K^+, Mg^{2+} and Ca^{2+} [136]. In this study, Cs^+ removal in simulated contaminated water after Fukushima accident, which contained high concentrations of different cation ions, was investigated by nZVI and nano-Fe/Cu particles and the results are presented in Table 4.6. The dosage of the nanoparticles used was 1 g/L and the initial Cs^+ concentration was 1 mg/L. The Cs^+ concentration was chosen to simulate the actual level of cesium following a nuclear accident like Fukushima which is significantly lower than the concentrations of other cations (Note: the cesium concentration in a real scenario may be

less than 1 mg/L) [92, 93]. Both nanoparticles displayed excellent selective sorption toward Cs^+ (more than 99% removal) because the competing cation ions had no effects on the adsorption of low concentration of Cs^+ by nZVI or nano-Fe/Cu particles [129]. These results proved the potential utility of the nZVI and nano-Fe/Cu particles in the treatment of Cs^+ contaminated water generated after the Fukushima nuclear accident.

As we mentioned before, a wide variety of sorbent materials have been researched for Cs^+ removal from wastewater. A direct comparison with the previously reported sorbents cannot be drawn due to different experimental conditions between studies. However, the key advantage of nZVI and nano-Fe/Cu particles is their ability to be recovered and separated from the environment after the treatment process through magnetic attraction. This unique separation technique could prove of great benefit for the remediation of radioactive waste streams. In addition, some studies demonstrated the feasibility of regenerating magnetic nanoparticles and reusing in successive remediation cycles [137].

Table 4.6: Cesium removal by nZVI and nano-Fe/Cu particles in simulated contaminated water in Fukushima at initial Cs^+ concentration = 1 mg/L, pH = 6, dosage = 1 g/L and temperature = 298 K.

Ions	nZVI		nano-Fe/Cu	
	K_d (L/g)	RE (%)	K_d (L/g)	RE (%)
1 mg/L Cs^+ (without cations)	399.00	99.75	908.09	99.89
160 mg/L Na^+	321.58	99.69	433.78	99.77
200 mg/L K^+	113.94	99.13	184.19	99.46
100 mg/L Mg^{2+}	105.38	99.06	832.33	99.88
150 mg/L Ca^{2+}	127.21	99.22	101.04	99.02
Mix of competing cations	103.17	99.04	768.23	99.87

4.3.8. Analysis of reacted nanoparticulate solid

SEM images (Fig. AII (1)) implied that there was a remarkable change in the surface morphology of nZVI and nano-Fe/Cu particles after reaction with Cs^+. The surface of nZVI became flat and smooth (Fig. AII (1c)) while the nano-Fe/Cu particles had a crack-like structure (Fig. AII (1d)). Besides, nZVI and nano-Fe/Cu particles formed larger particles after reaction, which might be attributed to the deposition of iron corrosion products generated during the reactions occurred on the surface of the nanoparticles.

XRD analysis of the reacted nZVI and nano-Fe/Cu particles extracted at the end of the experiments is displayed in Fig. 4.10. Compared with the XRD pattern of unreacted nZVI and nano-Fe/Cu particles (Fig. 4.1), the reacted nanoparticles showed different

diffraction peaks, suggesting a significant change occurred in their composition. The XRD pattern of the reacted nanoparticles indicated the presence of metallic iron (Fe^0) at $2\theta =$ 44.8° and 82.53° [138]. The diffraction peaks of the fresh nanoparticles (Fig. 4.1) were higher and sharper than that of aged nanoparticles, which can be attributed to the fact that the nanoparticles were consumed during the removal of Cs^+ ions. Meanwhile, some new diffraction peaks were detected in Fig. 4.10, indicating that new components and compounds were generated on the surface of the nanoparticles. CsCl (the diffraction peaks at $2\theta = 22.22°$, 25.72°, 36.69°, 43.31°, 45.34°, 59.68° and 66.06°) can be found in the nZVI system (Fig. 4.10a) [139]. In nano-Fe/Cu system (Fig. 4.10b), CsCl (the diffraction peaks at $2\theta =$ 21.68°, 25.08°, 35.77°, 42.21°, 44.18°, 51.48°, 56.49°, 58.1° and 64.26°), Cu (the diffraction peaks at $2\theta = 43.35°$, 50.49° and 74.19°) and CuO (the diffraction peaks at $2\theta =$ 24.53°, 33.09°, 35.24°, 44.2° and 51.24°) can be observed [140-142]. Besides, some iron corrosion products such as lepidocrocite (γ-FeOOH), hematite (Fe_2O_3) and green rust can also be found [143].

EDS analysis in the SEM device was performed on the reacted nZVI and nano-Fe/Cu particles to confirm their composition. Large peaks of Fe and O appeared in the EDS spectra of both nanoparticles (Fig. AII (8)), confirming the results obtained from the XRD.

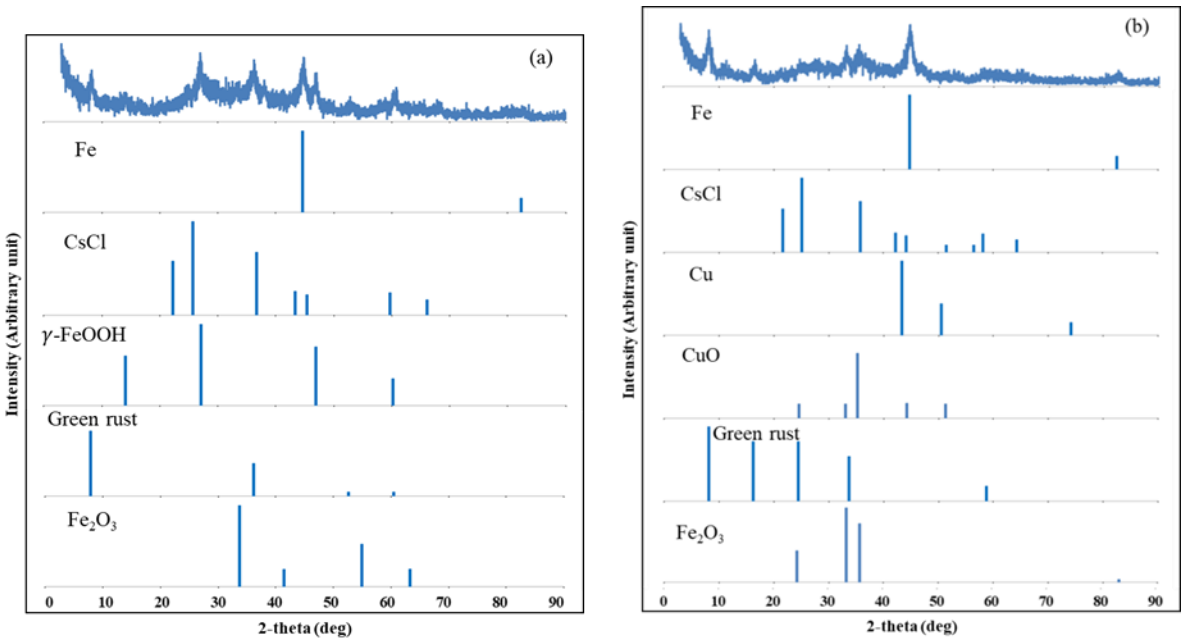

Fig. 4.10. XRD patterns acquired from the reacted nanoparticle solids at the end of experiments; (a) nZVI and (b) nano-Fe/Cu particles.

4.3.9. Schematic mechanism for cesium removal by nZVI and nano-Fe/Cu particles

The schematic mechanism of the Cs^+ ion removed by nZVI and nano-Fe/Cu particles is shown in Fig. 4.11. Based on the results obtained in this study and the confirmation data from XRD scanning for the reacted nZVI and nano-Fe/Cu particles, the adsorption mechanism plays a significant role in the removal of Cs^+ ion by nZVI and nano-Fe/Cu particles. Cesium cannot be reduced by nZVI or nano-Fe/Cu particles because the equilibrium reduction potential of Cs^+ (–3.026 V, Cs^+/Cs) is much lower than that of iron (–0.44 V, Fe^{2+}/Fe).

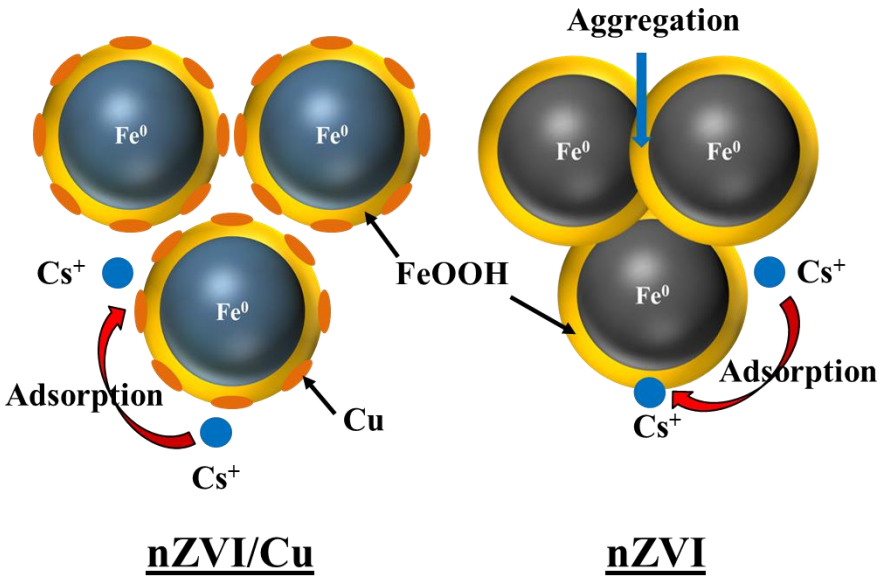

Fig. 4.11. Schematic mechanism of the Cs^+ removed by nZVI and nano-Fe/Cu particles.

4.4. Conclusion

This chapter evaluates the feasibility of using nZVI and nano-Fe/Cu particles for Cs^+ removal from aqueous solutions. nZVI and nano-Fe/Cu particles demonstrated desirable performance for Cs^+ removal. A minimum removal efficiency of 99% was reached for both nanoparticles at initial Cs^+ concentration of 1 mg/L and a dosage of 1 g-nanoparticles/L. Our results also showed that the Cs^+ sorption rate of nano-Fe/Cu particles was much faster than that of nZVI. Therefore, nano-Fe/Cu particles offer a much faster way in the treatment of radioactive Cs^+ wastes in emergencies after an incident at a nuclear power plant. Also the sorption capacity of the nano-Fe/Cu particles was higher than of nZVI. The kinetic

studies revealed that the experimental data were well fitted to the pseudo-second-order model, confirming that the chemical sorption process was the rate-controlling step. The equilibrium sorption data were successfully fitted to Langmuir and Freundlich isotherm models. Analysis of the thermodynamic parameters indicated that the sorption process was exothermic and spontaneous process. nZVI and nano-Fe/Cu partilces selectively sorbed Cs^+ in the presence of competing cation ions (Na^+, K^+, Mg^{2+} and Ca^{2+}) in the simulated contaminated water after Fukushima accident. The obtained results demonstrated that nZVI and nano-Fe/Cu particles can be used as efficient materials for Cs^+ removal from the contaminated solutions.

CHAPTER 5

REMOVAL OF CESIUM BY IRON BASED NANOPARTICLES ZEOLITE COMPOSITES

CHAPTER 5- Removal of Cesium by Iron Based Nanoparticles–Zeolite Composites

In this chapter, nZVI–zeolite and nano-Fe/Cu–zeolite composites for cesium (Cs^+) removal were fabricated through ion exchange process followed by liquid-phase reduction. The performance of the composites for the removal of Cs^+ from aqueous solutions with the ability to separate the adsorbent magnetically was investigated. Batch sorption experiments were systematically carried out to assess the effect of different parameters such as pH, initial concentration, contact time, adsorbent dosage and temperature. The obtained results suggested that both composites could be used as a promising technique for the treatment of waters containing cesium. To the best of our knowledge, there has been no study on the use of nZVI–zeolite and nano-Fe/Cu–zeolite composites in the treatment of cesium contaminated waters.

5.1. Introduction

Different decontamination techniques such as ion exchange, chemical precipitation, evaporation, adsorption and other technologies have been applied for eliminating radioisotopes from radioactive wastewaters [93, 144]. Ion exchange technique has become one of the most attractive treatment methods owing to its simplicity, efficiency and selectivity. Zeolites, as inorganic ion exchange materials, have extensively been studied for the treatment of radioactive waste because of their low cost, radiation and thermal stability, high ion exchange capacity and possible selectivity for certain radionuclides, such as cesium [145]. Zeolites have been characterized as microporous crystalline aluminosilicates, containing exchangeable cations such as Na^+, K^+, Ca^{2+} and Mg^{2+} [63, 146]. The cationic radioisotopes such as cesium can easily be removed by the ion exchange with the cationic ions of zeolites [147]. Natural zeolites have also been considered in a variety of environmental applications. Wang and Peng [148] reported that various natural zeolites showed a high sorption capacity for ammonium and heavy metal ions. Basaldella et al. [149] applied NaA zeolite to remove Cr from aqueous solutions. El-Kamash [145] used zeolite A for the removal of Cs and Sr from water. Zeng et al. [128] examined nitrate reduction by NaY zeolite and Inglezakis et al. [150] studied Pb, Cu, Mn, and Zn removal from aqueous solutions using natural zeolites. In spite of these benefits, zeolites have

limited application since after the adsorption of contaminants; separation of zeolites from the medium is very difficult due to their small particle size, leads to the inconvenient need for additional separation and may even result in secondary waste in practice. To resolve this problem, preparation of magnetic composites offers the advantage of easy, fast and efficient separation of such tiny particles by applying a magnetic field.

Several researchers have proceeded to use the magnetic separation technique for environmental remediation of a wide array of pollutants. Tang et al. [151] synthesized a magnetic gelatin-coated Fe_3O_4 composite for scavenging U^{6+}. Farghali et al. [106] prepared graphene/Fe_3O_4 nanocomposite for the removal of ethylene blue dye from polluted water. Liu et al. [107] modified the surface of Fe_3O_4 magnetic nanoparticles using humic acid for the removal of toxic Cd^{2+}, Cu^{2+}, Pb^{2+} and Hg^{2+} from water. Moamen et al. [102] developed magnetic nano zeolite for the sorptive removal of Cs^{+} and Sr^{2+} from liquid solutions. Yamaguchi et al. [152] reported a mesoporous carbon-γ-Fe_2O_3 nanoparticle composite to remove radioactive material emitted by the Fukushima Daiichi accident. Hwang et al. [129] fabricated sodium-copper hexacyanoferrate-modified magnetic nanoparticles for efficient removal of radioactive Cs followed by magnetic separation of the nanoparticles from the aqueous medium using an external magnet. Faghihian et al. [153] prepared a magnetic zeolite composite through the chemical co-precipitation of Fe^{2+} and Fe^{3+} in the presence of zeolite and the composite was evaluated for the adsorption of Cs^{+} and Sr^{2+}. Oliveira et al. [154] combined the adsorption features of zeolite Y with the magnetic properties of iron oxides in a composite to form a magnetic adsorbent for Cr^{3+}, Cu^{2+} and Zn^{2+} in contaminated water. Hong et al. [155] synthesized a magnetically separable alginate/Fe_3O_4 composite for Sr^{2+} removal from seawater.

In recent years, nanoscale zero valent iron (nZVI) has been widely utilized for the treatment of a broad range of contaminants including nitrate, azo dyes, heavy metal ions, nitroaromatic compounds, halogenated hydrocarbons and perchlorate [1, 21, 156, 157]. Due its large specific surface area and high number of active sites, nZVI enhances the removal efficiencies of those pollutants significantly [158, 159]. nZVI has also been proven to be one of the most promising techniques for the removal of radionuclides from liquid waste. Some studies demonstrated that nZVI effectively remediated solutions contaminated with Ba [160], Pu [64], U [42] and TcO_4 [122]. In addition, our previous work confirmed the

removal effectiveness of Cs by nZVI from contaminated areas [161, 162]. Because of Van der Waals and magnetic forces, nZVI often forms aggregates, resulting in the sharp decrease of reactivity, efficiency and durability, which could limit its application in practice [163]. Coating of nZVI using another metal such as Cu, Pd, Pt, Ag and Ni named bimetallic nanoparticles has shown to be effective approach in improving the performance of nZVI, which has been used in removal of a variety of contaminants [8, 164]. Tratnyek et al. [78] attributed the enhancement in the reactivity in the bimetallic system to catalytic hydrogenation and electrochemical effects.

In this chapter, we reported the synthesis of two composites, nZVI–zeolite (nZVI–Z) and nano-Fe/Cu–zeolite (nFe/Cu–Z). The efficiency of both composites for removal of cesium was evaluated under batch experiments. The effect of pH, contact time, initial concentration, composite amounts and temperature on the sorption process was investigated. The kinetic, thermodynamic and isotherm parameters of the process were also assessed. Furthermore, X-ray diffraction (XRD) and scanning electron microscope-elemental analysis (SEM-EDS) were used to characterize the prepared composites before and after Cs^+ adsorption.

5.2. Adsorption experiments

The adsorption behavior of nZVI–Z and nFe/Cu–Z composites was investigated using batch technique at 298 K. 1 g of each nanocomposite was mixed with 100 mL of Cs^+ solution (100 mg/L) and placed on a magnetic stirrer at 1000 rpm (RSH-6DN, As One Co., Japan) for 120 min. Preliminary investigations showed that the adsorption equilibrium time of each composite was less than 120 min. The Cs^+ solution was deoxygenated by nitrogen for 30 min before adding composite samples and kept sealed during the whole experiment. The initial solution pH in these experiments was monitored to be approximately 6. After adsorption, samples were collected and filtered using 0.22 µm syringe filters. The clear aqueous samples obtained were then diluted with deionized water and 1% HNO_3 to form appropriate Cs^+ concentrations prior to analysis using inductively coupled plasma mass spectrometry (ICP-MS, model: ICPM-8500, Shimadzu Co.) [92]. To determine the effect of pH on the adsorption process, the initial pH of the solutions was adjusted from 3 to 12

using a negligible volume of 0.1 HCl or 2 M NaOH. In order to investigate the effect of nanocomposites dosage on Cs^+ removal, a series of dosage from 1 to 10 g/L was assessed.

In the thermodynamic studies, the adsorption capacity of the nanocomposites was evaluated at four different temperatures of 298, 313, 328 and 343 K, respectively. The kinetic experiments were conducted at different initial pH values (3, 6 and 10) and different initial Cs^+ concentrations (50, 100, 150 and 200 mg/L). These experiments were also performed at different period of time (5–120 min). The adsorption isotherm measurements were carried out at various initial concentrations of Cs^+ (1–1000 mg/L). All experiments were carried out in triplicate and the average values were presented. The adsorbed amount of Cs^+ ions per unit mass of the nanocomposite, q (mg/g) was calculated from the mass balance equation as follows:

$$q = \left(C_i - C_f\right) \times (V/m) \tag{5.1}$$

To determine the selectivity of the nanocomposites to Cs, the distribution coefficient, K_d (L/g) was calculated by:

$$K_d = \left(C_i - C_f\right)/C_f \times (V/m) \tag{5.2}$$

where C_i and C_f are the initial and final Cs^+ concentrations (mg/L) respectively, m is the amount of the composite (g) and V is the volume of the solution (L).

5.3. Results and discussion

5.3.1. Characterization of the composites

Microscopic morphology of zeolite, nZVI–Z and nFe/Cu–Z samples was investigated by SEM and the images were shown in Fig. AIII (1) in Appendices Section. From the SEM image of zeolite, as illustrated in Fig. AIII (1a), the morphology of crystals with homogenous shapes was clearly visible. The average diameter of the single zeolite crystals was about 2−5 µm. In the SEM images of the nZVI–Z and nFe/Cu–Z composites (Fig. AIII (1b–d)), the presence of nZVI and nano-Fe/Cu particles on the surface of zeolite was observed. The iron nanoparticles dispersed evenly on the surface and edges of zeolite. On the other hand, the SEM micrographs revealed that there was a marked change in the morphology of zeolite after the nZVI and nano-Fe/Cu loading. The unique cubic structure

was lost and the particles were mainly aggregated into bulks and composed of irregular shaped particles. Similar findings were reported by Zeng et al. [128].

EDS was utilized to determine the elemental analysis of the zeolite and the composites, as shown in Fig. AIII (2). EDS analysis of zeolite showed peaks corresponding to Na, Si and Al elements with weight percentages of 15.20%, 34.54% and 50.27%, respectively. The Si/Al ratio of zeolite was 1.46 and close to that of reference [153]. EDS spectrums of nZVI–Z and nFe/Cu–Z (Fig. AIII (2b and c)) further confirmed the presence of Fe in the composites with weight percentages of 76.79% and 69.07%, respectively. As can be seen in Fig. AIII (3c), Cu (5.71 wt.%) was present in EDS spectrum of nFe/Cu–Z composite. These quantitative analysis revealed that nZVI and nano-Fe/Cu particles were successfully loaded onto the zeolite.

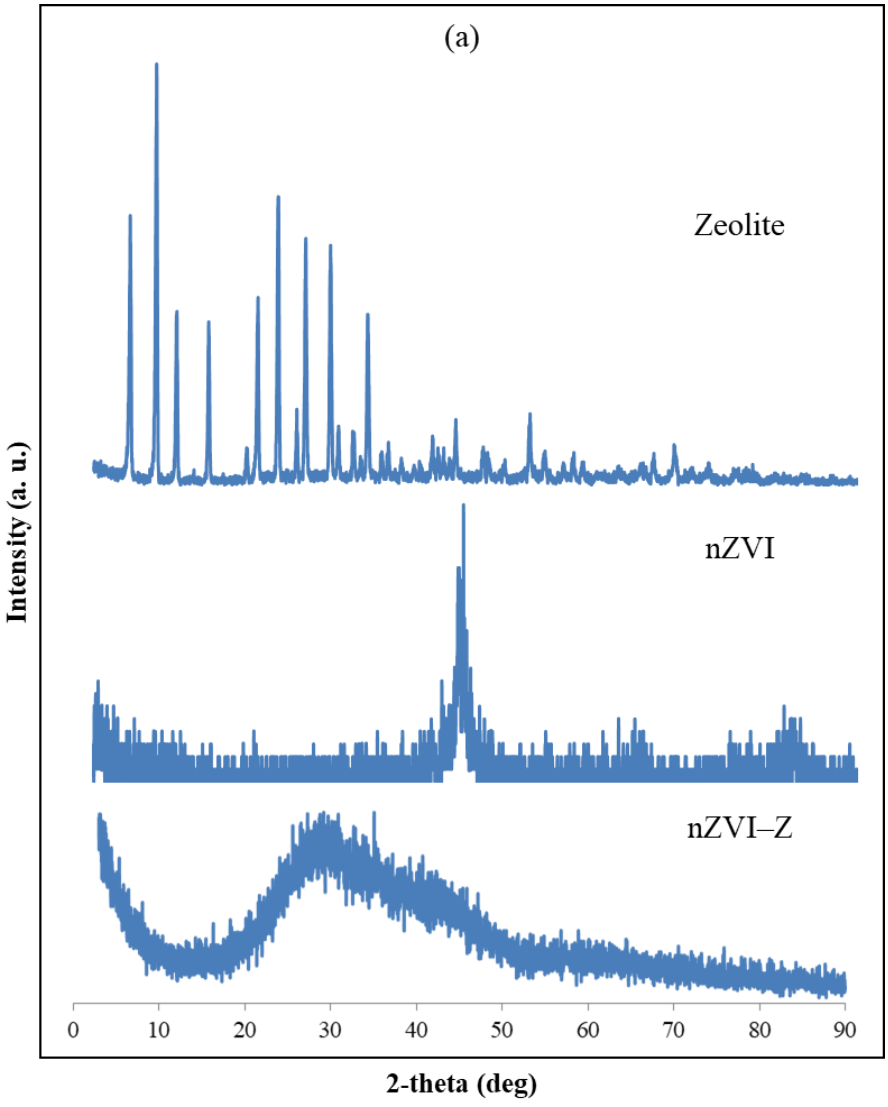

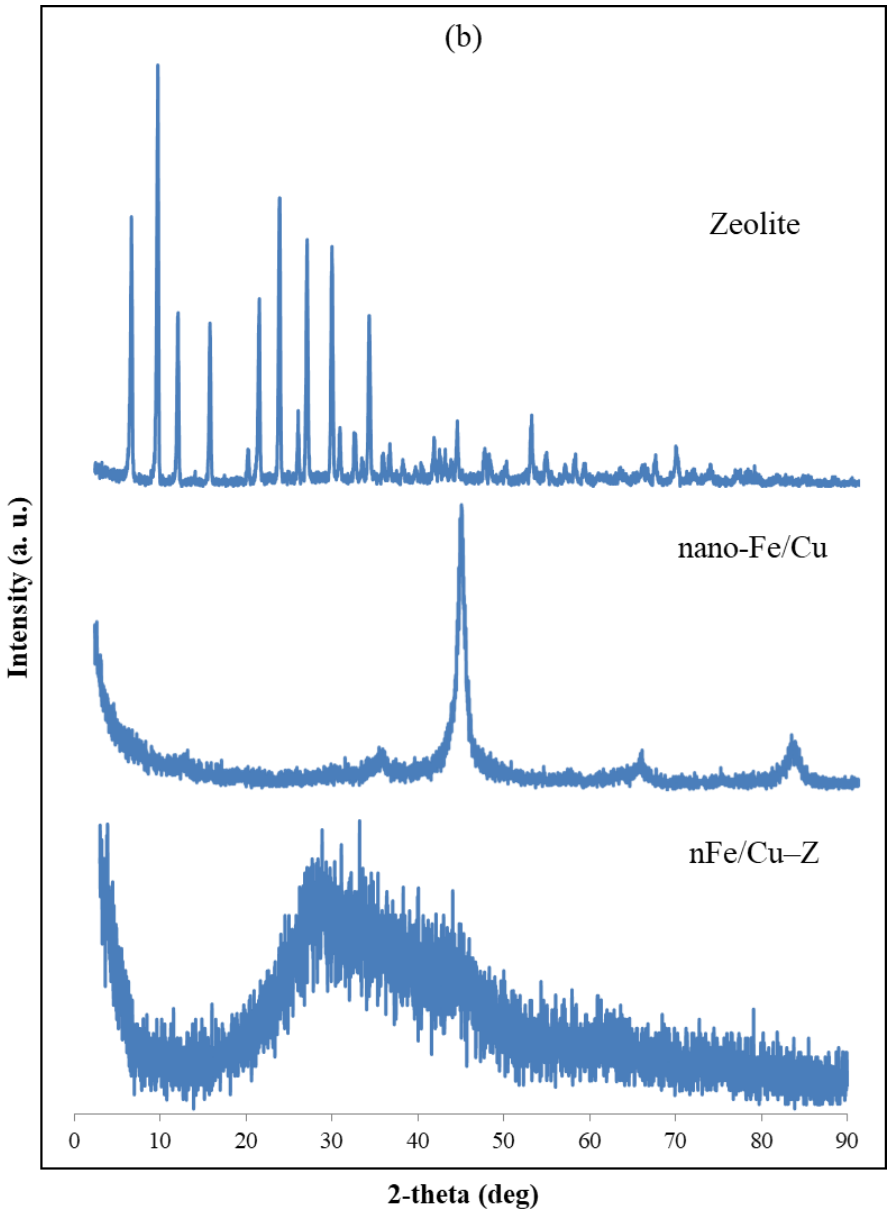

Fig. 5.1. XRD patterns of (a) zeolite, nZVI and nZVI–Z composite and (b) zeolite, nano-Fe/Cu particles and nFe/Cu–Z composite.

Fig. 5.1a and b show the XRD patterns of the commercial zeolite, nZVI, nano-Fe/Cu particles and composite samples. The sharp strong peaks in the XRD pattern of zeolite confirmed that the crystal structure of zeolite was in good agreement with that of the reference [128]. SiO_2 crystalline peaks at 2θ of 6.99°, 7.71°, 10.26°, 12.58°, 20.61° and 31.13° were well observed in the X-ray pattern of zeolite [165]. Moreover, the appearance of intense reflection peaks at 12.50°, 26.18°, 34.53°, 36.62°, 49.45° and 62.08° indicating the Al_2O_3 were detected [166]. The XRD measurements suggested the presence of a pure

cubic Fe^0 crystalline structure with its major reflection at 44.14° and 83.22°, which was observed on nZVI, nano-Fe/Cu particles and composite samples, although the Fe^0 peaks diminished significantly after the composites preparation (shown in Fig. 5.1a and b) [161, 167]. These results indicated that the zeolite was successfully loaded with nZVI. However, the XRD patterns of nZVI–Z and nFe/Cu–Z were not similar to zeolite, a phenomenon already described in the literature [128]. Further, the intensity of several characteristic diffraction peaks within the XRD spectra decreased for the composites compared with zeolite (Fig. 5.1a and b). Meanwhile, iron oxides (most likely Fe_2O_3 and Fe_3O_4) were observed in the XRD results of nZVI–Z and nFe/Cu–Z [166].

5.3.2. Effect of pH

The background pH of the aqueous solution can have a significant impact on the removal of Cs^+, due to surface charge, metal speciation and functional group chemistry of the adsorbents. Hence, the effect of pH on Cs^+ removal by nZVI–Z and nFe/Cu–Z composites was investigated over a pH range of 3 to 12 and the results are displayed in Fig. 5.2. It was observed that the amount of adsorbed Cs^+ ions onto both nanocomposites

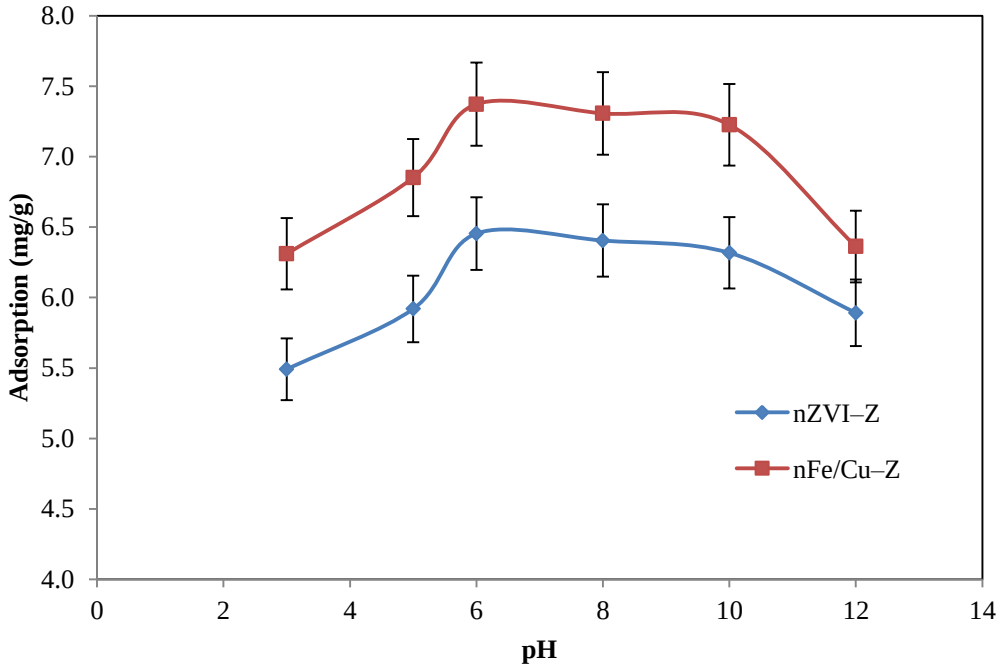

Fig. 5.2. Effect of pH on cesium adsorption by nZVI–Z and nFe/Cu–Z. (Initial conditions: dosage = 10 g/L, initial cesium concentration = 100 mg/L, temperature = 298 K).

increased with increase in the initial pH. The sorption amount of Cs^+ onto nZVI–Z and nFe/Cu–Z was 5.49 and 6.31 mg/g with background pH 3 and the Cs^+ removal was only 54.91% and 63.11%, respectively. When the initial pH was 6, the adsorption capacity of Cs^+ by nZVI–Z and nFe/Cu–Z increased to 6.45 and 7.37 mg/g with 64.54% and 73.72% removal were achieved, respectively. At lower pH values, the sorption process was inhibited in this acidic medium. This may be due to the presence of H^+ ions competing with Cs^+ ions for the exchange sites of the nanocomposites [102]. In addition, the dissolution of iron nanoparticles within the composites can occur under acidic conditions [129, 161]. The removal of Cs^+ decreased rapidly in strong alkaline environments due to the formation of Fe (oxy)hydroxide layers on the active sites of nZVI–Z and nFe/Cu–Z surfaces and as a result, the Cs^+ adsorption was inhibited at high pH values [112, 156]. These data indicated that Cs^+ removal by nZVI–Z and nFe/Cu–Z was strongly pH dependent. However, both nanocomposites could maintain efficient Cs^+ removal from the various radioactive liquid wastes having a wide range of pH because even the lowest adsorption capacity value was high enough for removal of Cs^+. The maximum Cs^+ adsorption was occurred at pH 6. So, all next adsorption experiments in this work were conducted at initial pH value of 6.

5.3.3. Effect of initial Cs^+ concentration and contact time

The effect of contact time on the amount of Cs^+ sorbed onto both nZVI–Z and nFe/Cu–Z was studied at 298 K and different initial concentrations of 50, 100, 150 and 200 mg/L and the results are presented in Fig. 5.3. It is clearly shown that the sorption process sharply increased with time for both nanocomposites and the sorption amount increased with the increase of the initial Cs^+ concentration. The uptake of Cs^+ increased with time reaching an equilibrium value in about 30 min for nZVI–Z (Fig. 5.3a), while in case of nFe/Cu–Z, the equilibrium was attained in approximately 20 min (Fig. 5.3b). As can be seen in Fig. 5.3, the equilibrium time was independent of the initial concentration. The increase in the adsorption capacity of the nanocomposites with increasing the initial Cs concentration could be related to the ratio of initial mole numbers of Cs^+ to the total available active sites. Meanwhile, it was found that the amount of Cs^+ ions sorbed onto nFe/Cu–Z was greater than that for nZVI–Z. The 59.43%, 64.54%, 66.12% and 64.23% of

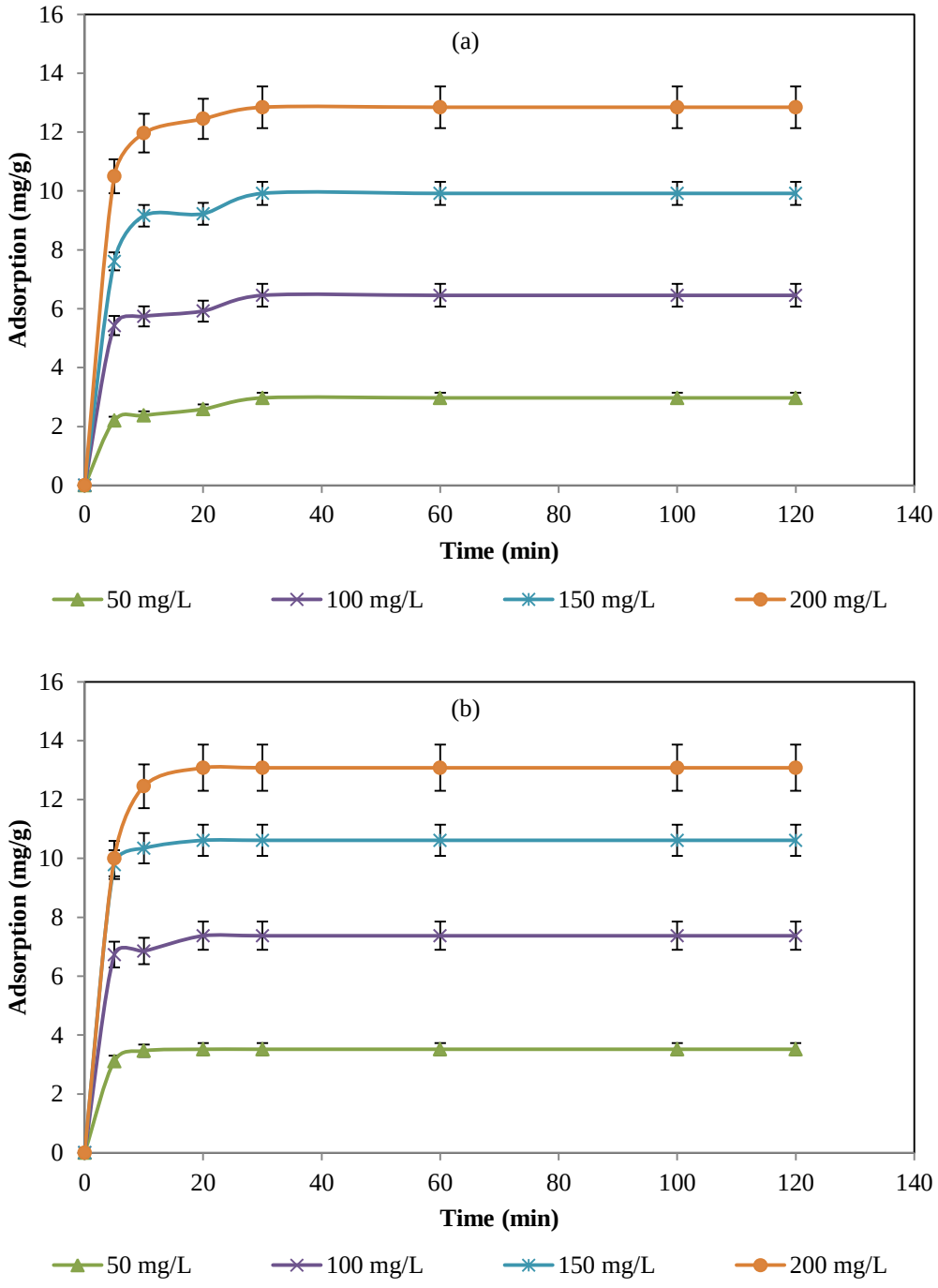

Fig. 5.3. Effect of initial cesium concentration and contact time on cesium adsorption by (a) nZVI–Z and (b) nFe/Cu–Z. (Initial conditions: pH = 6, dosage = 10 g/L, temperature = 298 K).

Cs^+ were removed by nZVI–Z at 50, 100, 150 and 200 mg/L, respectively, while the values in case of nFe/Cu–Z at similar initial concentrations were 70.35%, 73.72%, 70.77% and 65.39%, respectively. It can also be observed that the adsorption rate of Cs^+ using nFe/Cu–

Z was much higher than that of nZVI–Z. This behavior could be attributed to doping the surface of nZVI by Cu metal, which decreases the aggregation and agglomeration of nZVI particles within the composite [168]. In addition, the role of Fe in the bimetallic nanocomposite nFe/Cu–Z is as an electron donor while the second metal Cu acts as a promoter and thus enhances the reactivity. The presence of Cu in the bimetallic nanocomposite system can also prevent the oxidation of nZVI particles by O_2, which can also increase the adsorption of Cs^+ ions [161]. In emergencies, such as an incident at a nuclear power plant, it may be stated that nFe/Cu–Z offers a much faster way of removing Cs from the contaminated waters.

5.3.4. Effect of contact time at different pH values

The amount of Cs^+ sorbed onto both nZVI–Z and nFe/Cu–Z as a function of contact time and initial solution pH is illustrated in Fig. 5.4. The sorption process for both nanocomposites was quite rapid and between 85% and 95% of the maximal capacity was obtained within 10 min, indicating that nZVI–Z and nFe/Cu–Z had very fast adsorption kinetics towards Cs^+ ions. After this initial sharp sorption, the Cs^+ sorption increased at a slower rate and eventually reached a steady capacity. The time required for attaining a

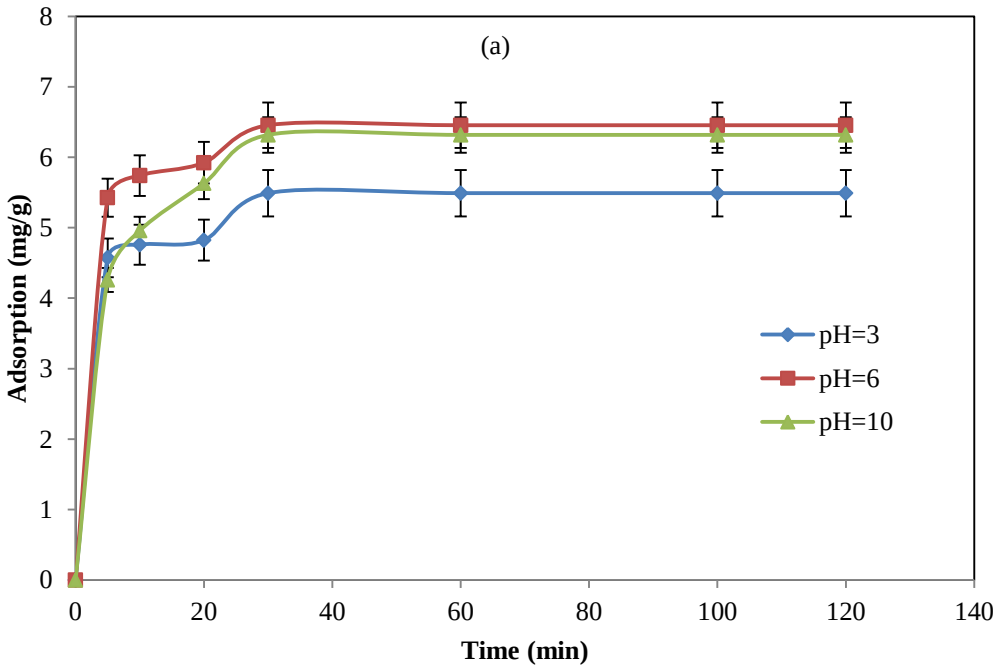

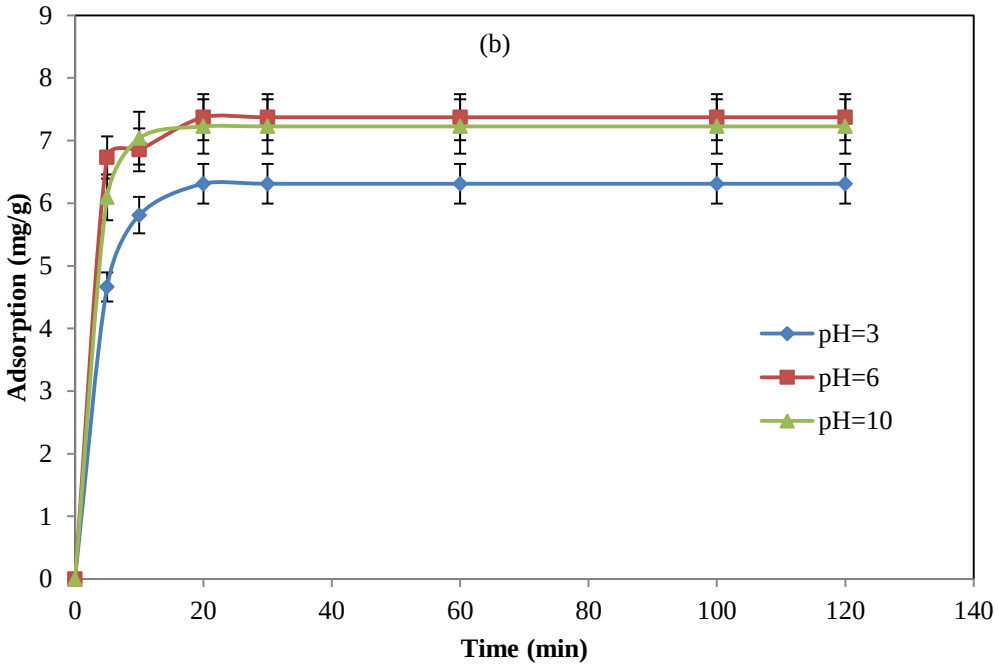

Fig. 5.4. Effect of contact time at different initial pH 3, 6 and 10 on cesium adsorption by (a) nZVI–Z and (b) nFe/Cu–Z. (Initial conditions: dosage = 10 g/L, initial cesium concentration = 100 mg/L, temperature = 298 K).

maximum value remained practically unaffected by initial pH (30 min for nZVI–Z (Fig. 5.4a) while 20 min for nFe/Cu–Z (Fig. 5.4b)). The equilibrium time was found to be independent of the initial pH.

5.3.5. Effect of dosage

The dosage of nZVI–Z and nFe/Cu–Z affects the Cs^+ sorption process. The removal of Cs^+ by the nanocomposites was investigated at different dosages (1–10 g/L) of nZVI–Z and nFe/Cu–Z at initial Cs^+ concentration of 100 mg/L. As shown in Fig. 5.5, Cs^+ removal increased with increasing amount of the nanocomposites from 1 g/L to 10 g/L and the maximum uptake was achieved at 10 g/L. The nZVI–Z composite attained Cs^+ removals of 7.82%, 26.87%, 37.82%, 44.21%, 59.28% and 64.54% at the dosages of 1, 2, 3, 5, 8, 10 g/L, respectively and the adsorption capacity of Cs^+ by nZVI–Z was 7.82, 13.44, 12.61, 8.84, 7.41 and 6.45 mg/g, respectively (Fig. 5.5a). Moreover, Cs^+ removal was much higher for nFe/Cu–Z than that for nZVI–Z, which showed removals of 19.91%, 27.19%, 39.62%, 56.07%, 66.07% and 73.72% at similar dosages, respectively, while the adsorption capacity

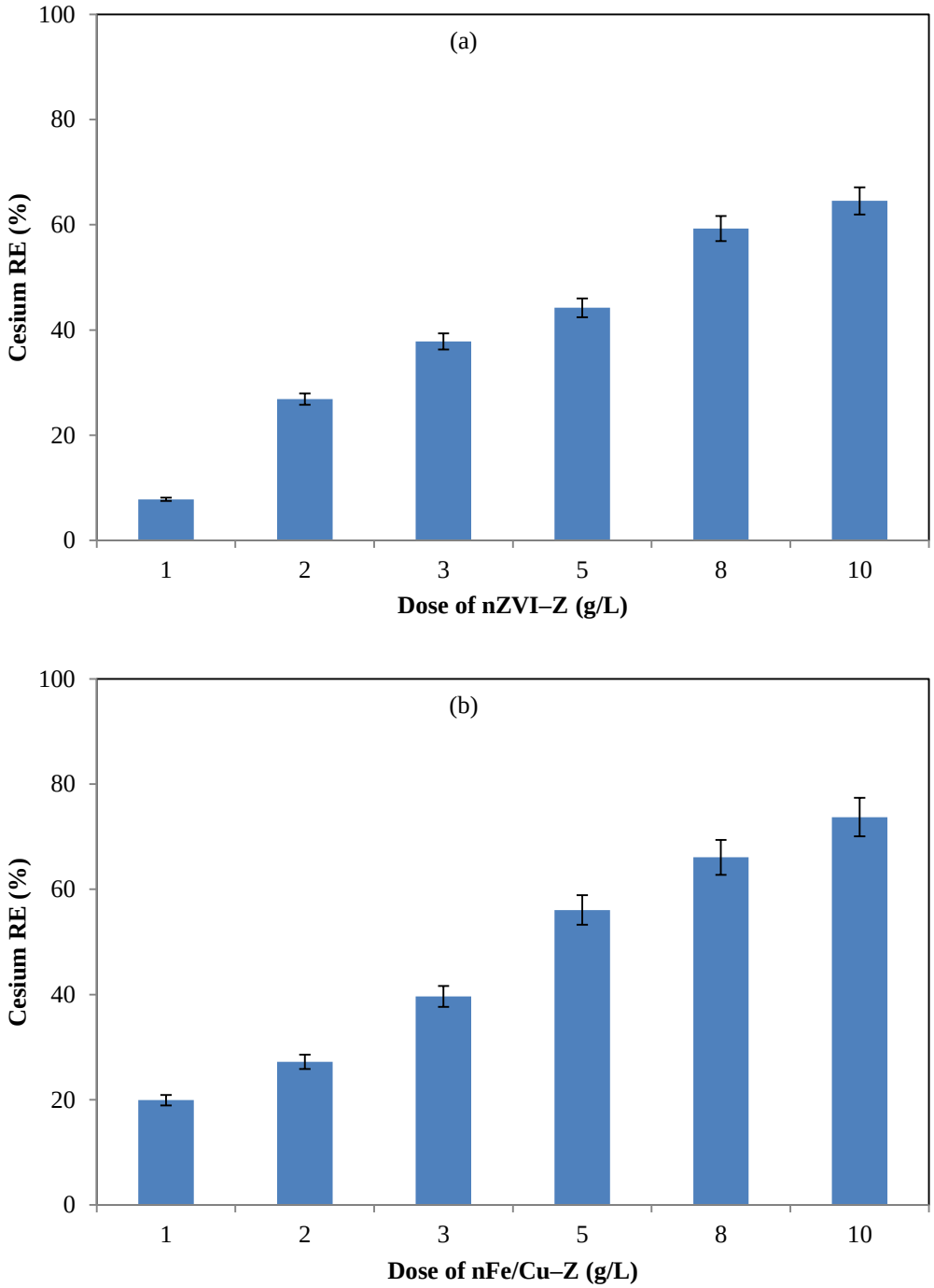

Fig. 5.5. Cesium removal by different dosage of (a) nZVI–Z and (b) nFe/Cu–Z. (Initial conditions: pH = 6, initial cesium concentration = 100 mg/L, temperature = 298 K).

was 19.91, 13.60, 13.21, 11.21, 8.26 and 7.37 mg/g, respectively (Fig. 5.5b). These results confirmed that nFe/Cu–Z is preferred for Cs^+ removal rather than nZVI–Z.

5.3.6. Kinetic sorption modeling

In this study, four kinetic models were used to describe the changes in the sorption of Cs^+ ions by the prepared nanocompesties with time: the pseudo-first-order, pseudo-second-order, Elovich and intraparticle diffusion model. The Lagergren pseudo-first-order model is written as [161]:

$$\ln(q_e - q_t) = \ln q_e - k_1 t \tag{5.3}$$

where q_e and q_t are the adsorption capacity of Cs^+ at equilibrium and at any time t (mg/g), respectively. k_1 is the adsorption rate constant of pseudo-first-order model (min^{-1}). The values of q_e and k_1 were determined from the slope and intercept of the plot of $\ln(q_e - q_t)$ versus t. The obtained parameters are presented in Table 5.1. As shown in Table 5.1, the calculated value of q_e was lower than the experimental result, indicating that the adsorption of Cs^+ onto nZVI–Z and nFe/Cu–Z is not well adjusted to the pseudo-first-order kinetics.

The pseudo-second-order kinetic model is expressed as [155]:

$$t/q_t = 1/(k_2 q_e^2) + (1/q_e)\, t \tag{5.4}$$

and initial sorption rate can be calculated by:

$$h = k_2 q_e^2 \tag{5.5}$$

where k_2 is the pseudo-second-order rate constant (g/mg/min). The slope and intercept of the linear plot of t/q_t against t were used to determine k_2 and q_e. The calculated values of k_2, q_e and h with the correlation coefficients (R^2) are summarized in Table 5.1. From Table 5.1, the reaction rate constant k_2 for nFe/Cu–Z was larger than that for nZVI–Z, confirming that the adsorption of Cs^+ onto nFe/Cu–Z is faster than on nZVI–Z. This can be illustrated by the fact that Cu metal is highly active when coupled with iron in zeolite [128]. The Cu helps to disperse the iron nanoparticles, thus the Cs^+ ions make more contact with the adsorptive sites of adsorbent and the adsorption rate increases. Similar performance was found by Wu et al. [169] in the removal of oxytetracycline using bimetallic Cu/nZVI nanoparticles.

The intraparticle diffusion model is given as [165]:

$$q_t = K_{\text{diff}} t^{1/2} + C \tag{5.6}$$

where K_{diff} is the intraparticle diffusion rate constant (mg/g/min) and C is a constant related to thickness of the boundary layer. As it is evident from the results in Table 5.2, the intraparticle diffusion model showed poor R^2 values, suggesting that the intraparticle diffusion was not the determining step in the sorption process.

Table 5.1: The calculated parameters of pseudo-first-order and pseudo-second-order kinetic models for cesium adsorption onto nZVI–Z and nFe/Cu–Z.

Adsorbents	Condition		$q_{e\ (\text{exp.})}$ (mg/g)	Pseudo-first order model			Pseudo-second order model			
				k_1 (min^{-1})	$q_{e\ (\text{theor.})}$ (mg/g)	R^2	k_2 (g/mg/min)	$q_{e\ (\text{theor.})}$ (mg/g)	h (mg/g/min)	R^2
nZVI–Z	pH	3	5.49	0.0744	0.650	0.6576	0.159	5.55	4.91	0.9996
		6	6.45	0.0733	0.672	0.6584	0.179	6.51	7.58	0.9998
		10	6.32	0.0771	0.955	0.6634	0.092	6.42	3.80	0.9994
	Initial	50	2.97	0.0766	0.432	0.6616	0.211	3.02	1.92	0.9994
	concen.	100	6.45	0.0733	0.672	0.6584	0.179	6.51	7.58	0.9998
	(mg/L)	150	9.92	0.0732	1.008	0.6582	0.119	10.00	11.87	0.9998
		200	12.85	0.0710	1.026	0.6557	0.139	12.92	23.23	0.9999
nFe/Cu–Z	pH	3	6.31	0.0631	0.187	0.4800	0.255	6.35	10.29	0.9998
		6	7.37	0.0600	0.164	0.4750	0.478	7.39	26.13	0.9999
		10	7.23	0.0593	0.148	0.4699	0.490	7.25	25.73	0.9999
	Initial	50	3.52	0.0572	0.059	0.4614	1.504	3.53	18.68	0.9999
	concen.	100	7.37	0.0600	0.164	0.4750	0.478	7.39	26.13	0.9999
	(mg/L)	150	10.62	0.0574	0.183	0.4668	0.592	10.63	66.91	0.9999
		200	13.08	0.0617	0.338	0.4766	0.158	13.15	27.28	0.9999

The Elovich equation can be defined as [153]:

$$q_t = \ln(\alpha\beta)/\beta + \ln t/\beta \tag{5.7}$$

where α is the initial sorption rate of Elovich equation (mg/g/min) and β is a constant related to surface coverage and activation energy for chemical sorption (g/mg). The slope and the intercept of plotting of q_t versus $\ln t$ were used to calculate α and β. The results are listed in Table 5.2.

Comparison of calculated q_e and the correlation coefficient R^2 for four kinetic models indicated that the sorption data were well fitted to pseudo-second-order model. These results explained that the sorption behavior followed the pseudo-second-order sorption mechanism and the rate-limiting step was chemisorption involving ion exchange. In addition, the observed pseudo-second-order reaction rate constant k_2 was dependent of

the initial pH and Cs concentration within the observed concentration range (Table 5.1). Similar behavior was reported for the adsorption of Cs^+ ions from aqueous solutions by other adsorbents [92, 144].

Table 5.2: The calculated parameters of Elovich and intra-particle diffusion kinetic models for cesium adsorption onto nZVI–Z and nFe/Cu–Z.

Adsorbents	Condition		Elovich model			Intra-particle diffusion model		
			α (mg/g/min)	β (g/mg)	R^2	K_{diff} (mg/g/min)	C (mg/g)	R^2
nZVI–Z	pH	3	5.12	1.027	0.7226	0.348	2.60	0.5092
		6	6.51	0.880	0.7045	0.401	3.15	0.4857
		10	3.86	0.824	0.8302	0.443	2.57	0.6121
	Initial concen. (mg/L)	50	2.08	1.804	0.7984	0.202	1.27	0.5838
		100	6.51	0.880	0.7045	0.401	3.15	0.4857
		150	9.01	0.559	0.7281	0.631	4.73	0.5013
		200	13.55	0.442	0.6915	0.789	6.44	0.4641
nFe/Cu–Z	pH	3	5.63	0.868	0.7267	0.403	3.03	0.4921
		6	9.96	0.801	0.6293	0.429	3.95	0.4095
		10	8.82	0.800	0.6518	0.429	3.80	0.4242
	Initial concen. (mg/L)	50	4.84	1.678	0.6233	0.203	1.90	0.4002
		100	9.96	0.801	0.6293	0.429	3.95	0.4095
		150	15.79)	0.564	0.6055	0.603	5.83	0.3868
		200	12.89	0.426	0.7013	0.816	6.49	0.4676

The goodness of fit was also discussed using Akaike Information Criterion (AIC). The AIC is a well-established statistical method that can be used for model selection in a situation where more than one model has been fitted to data [170]. Having a lower AIC value shows better fit to experimental data. For a small sample size, AIC is calculated from the equation [171]:

$$AIC = N\,ln\left(\frac{SSE}{N}\right) + 2k + \frac{2k(k+1)}{N-k-1} \tag{5.8}$$

where N is the number of observations, k is the number of parameters in the model and SSE (squared sum of errors) can be defined as:

$$SSE = \sum (q_{t,e} - q_{t,m})^2 \tag{5.9}$$

where $q_{t,e}$ and $q_{t,m}$ are the experimental adsorption capacity of Cs^+ (mg/g) at time t and the corresponding value which is obtained from the kinetic models. The AIC values of all the kinetic models are presented in Table 5.3. Smaller AIC values were observed for pseudo-

second-order kinetics. This implied that the pseudo-second-order model is significant in defining the Cs^+ adsorption process onto nZVI–Z and nFe/Cu–Z and fits the experimental data better than other kinetic models.

Table 5.3: AIC values of kinetic models employed for cesium adsorption onto nZVI–Z and nFe/Cu–Z.

Adsorbents	Condition		Kinetic models			
			Pseudo-first order	Pseudo-second order	Elovich	Intra-particle diffusion
nZVI–Z	pH	3	11.004	−16.037	3.323	4.914
		6	13.992	−17.908	6.046	7.515
		10	8.169	−8.809	2.367	6.074
	Initial concen. (mg/L)	50	−0.629	−21.631	−7.335	−4.492
		100	13.992	−17.908	6.046	7.515
		150	19.341	−6.071	11.731	13.676
		200	24.362	−4.307	16.195	17.689
nFe/Cu–Z	pH	3	14.685	−6.313	5.815	7.927
		6	19.566	−18.107	9.708	10.502
		10	19.002	−10.202	9.138	10.260
	Initial concen. (mg/L)	50	9.784	−24.146	−0.429	0.380
		100	19.566	−18.107	9.708	10.502
		150	25.522	−15.343	15.313	15.921
		200	25.798	3.206	16.590	18.356

5.3.7. Sorption thermodynamics

In order to gain insight into the thermodynamic properties of the adsorption process, the adsorption removal of Cs^+ onto nZVI–Z and nFe/Cu–Z composites was examined at four different temperatures of 298, 313, 328 and 343 K (Fig. 5.6). The adsorption amount of Cs^+ increased with increasing temperature. The thermodynamic parameters, including enthalpy change ($\Delta H°$), entropy difference ($\Delta S°$) and Gibbs free energy change ($\Delta G°$) of Cs adsorption on the composites were derived from the experimental results. The values of enthalpy ($\Delta H°$) and entropy ($\Delta S°$) changes can be obtained from the slope and intercept of the linear plot of Van't Hoff equation [92]:

$$\ln K_d = (\Delta S°/R) - (\Delta H°/RT) \quad (5.10)$$

where K_d is the distribution coefficient (ml/g). The plot of $\ln K_d$ against $1/T$ is shown in Fig. AIII (3). The value of free energy of the sorption reaction ($\Delta G°$) was calculated by the following [160]:

$$\Delta G° = \Delta H° - T\Delta S° \quad (5.11)$$

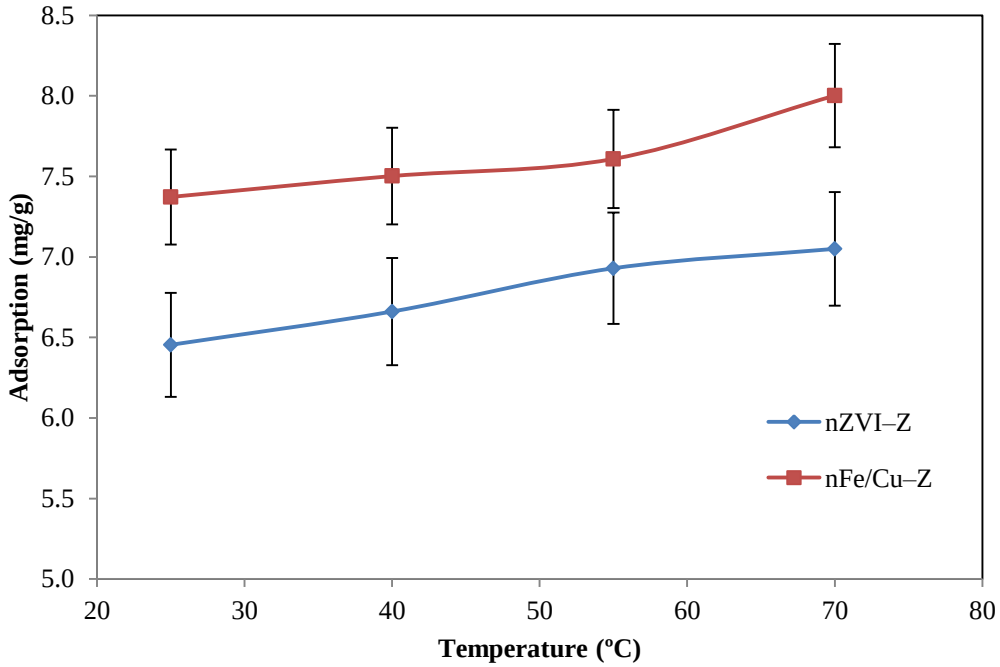

Fig. 5.6. Effect of temperature on cesium adsorption by nZVI–Z and nFe/Cu–Z. (Initial conditions: pH = 6, dosage = 10 g/L, initial cesium concentration = 100 mg/L).

The values of $\Delta H°$, $\Delta S°$ and $\Delta G°$ calculated using the above equations are provided in Table 5.4. The positive value of $\Delta H°$ revealed that the Cs adsorption reaction was endothermic, which implied that higher temperatures were favored for enhanced removal of Cs^+ ions by nZVI–Z and nFe/Cu–Z. The change in $\Delta S°$ was found to be positive suggesting that more disorder at the solid–solution interface was generated as a result of Cs^+ adsorption. Negative $\Delta G°$ values indicated that Cs adsorption occurred spontaneously. The decrease in $\Delta G°$ values with increasing temperature confirmed the improvement of Cs adsorption at high temperature. The higher absolute values of $\Delta G°$ for nFe/Cu–Z than that for nZVI–Z confirming that the sorption of Cs^+ on nFe/Cu–Z was more favorable than on nZVI–Z. The endothermic nature and positive entropy change of Cs^+ adsorption by other adsorbents have previously been reported [93, 145].

Table 5.4: Thermodynamic parameters for cesium adsorption onto nZVI–Z and nFe/Cu–Z.

Adsorbents	E_a (kJ/mol)	A (g/mg/min)	$\Delta H°$ (kJ/mol)	$\Delta S°$ (kJ/mol/K)	$\Delta G°$ (kJ/mol)			
					298 K	313 K	328 K	343 K
nZVI–Z	15.57	94.72	5.34	0.0612	−12.89	−13.81	−14.73	−15.64
nFe/Cu–Z	13.94	131.71	6.28	0.0677	−13.88	−14.90	−15.91	−16.93

5.3.8. Activation energy for Cs adsorption

The activation energy (E_a) of Cs adsorption onto nZVI–Z and nFe/Cu–Z was determined using Arrhenius equation [172]:

$$\ln k_2 = \ln A - E_a/(RT) \tag{5.12}$$

where k_2 is the rate constant obtained from the pseudo second-order equation (g/mg/min), A is the Arrhenius factor, E_a is the activation energy of the adsorption (kJ/mol), which represents the minimum energy for the adsorption reaction, R is the gas constant (8.314 J/mol/K) and T is the absolute temperature (K). E_a can be estimated through the linear plot of $\ln k_2$ versus $1/T$ (Fig. AIII (4)). The values of E_a were 15.57 and 13.94 kJ/mol for nZVI–Z and nFe/Cu–Z, respectively (see Table 5.4). The positive sign of E_a revealed that the adsorption rate will increase as the temperature increases. Since the E_a values was less than 42 kJ/mol, physical sorption may affect the reaction mechanism. Also, the obtained values of E_a implied that the adsorption of Cs^+ followed with a low potential energy [173].

5.3.9. Sorption isotherm

In order to determine the maximum adsorption capacity as well as understand the adsorption behavior and mechanism, Cs removal performance of the nZVI–Z and nFe/Cu–Z was evaluated by measuring sorption isotherm. Fig. 5.7 describes the relationship between the equilibrium amounts of Cs^+ ions adsorbed onto the nanocomposites prepared with different initial concentrations and the concentration of Cs^+ in the liquid at equilibrium, while maintaining a constant amount of the adsorbents. The initial Cs^+ concentration range was 1–1000 mg/L. As can be seen in Fig. 5.7, the quantitiy of Cs^+ ions sorbed at equilibrium, q_e, increased with the increase of the initial Cs^+ concentration in the aqueous phase and the initial rapid sorption was followed by a slow approach to equilibrium at higher concentration.

Two theoretical isotherm models, including Langmuir and Freundlich isotherms were employed to fit the obtained equilibrium data. Langmuir sorption isotherm model assumes monolayer coverage of the sorption surfaces, the sorption occurs on homogenous sites within the adsorbent and all the sorption sites have the same energy. The Langmuir model equation can be written as [165]:

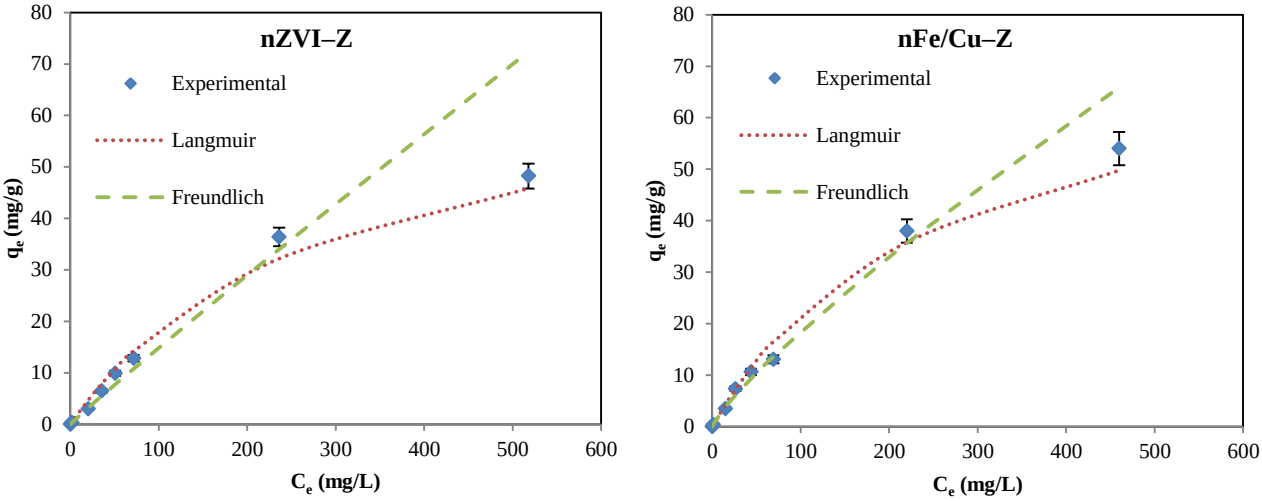

Fig. 5.7. Adsorption isotherms of cesium onto nZVI–Z and nFe/Cu–Z. (Initial conditions: pH = 6, dosage = 10 g/L, temperature = 298 K).

$$q_e = q_m K_L C_e/(1 + K_L C_e) \quad (5.13)$$

where q_m is the maximum monolayer adsorption capacity (mg/g), C_e is the equilibrium Cs^+ concentration (mg/L) and K_L is the Langmuir constant related to the energy of adsorption (L/mg). The values of q_m and K_L were calculated from the slope and the intercept of the linear plot of $1/q_e$ against $1/C_e$ (Fig. AIII (5)) and are summarized in Table 5.5. The R^2 values of 0.9999 and 0.9963 indicated that the Cs^+ adsorption onto nZVI–Z and nFe/Cu–Z was properly described by the Langmuir isotherm, where a larger sorption was obtained with the nFe/Cu–Z rather than with nZVI–Z (The sorption capacity of Cs^+ increased from 71.12 mg/g onto nZVI–Z to 77.51 mg/g onto nFe/Cu–Z). The K_L values related to sorption energy confirmed that nFe/Cu–Z had higher affinity for Cs^+ ions. The excellent fit between the experimental data and the theory behind the Langmuir model suggested that sorption process of Cs^+ onto nZVI–Z and nFe/Cu–Z occurred by the formation of monolayer chemisorption.

One of the important characteristics of the Langmuir model is the dimensionless constant called equilibrium parameter (R_L), which could be calculated from [174]:

$$R_L = 1/(1 + K_L C_0) \quad (5.14)$$

where C_0 is the highest initial Cs^+ concentration (mg/L). The value of R_L indicated the type of Langmuir isotherm. The sorption process may be irreversible $(R_L = 0)$, favorable $(0 < R_L < 1)$, linear $(R_L = 1)$ or unfavorable $(R_L > 1)$. The obtained data (Table 5.5) confirming the favorable adsorption of Cs^+.

Freundlich isotherm model is widely used to describe the multilayer sorption and assumes that sorption occurs on heterogeneous surfaces of the adsorbent. The equation describing the Freundlich isotherm can be represented by [144]:

$$q_e = K_f C_e^{1/n} \tag{5.15}$$

where K_f is the Freundlich constant indicative of the adsorption capacity and n is the constant indicative of the adsorption intensity. The linear plot of $\ln q_e$ versus $\ln C_e$ is shown in Fig. AIII (6), which suggested that the sorption of Cs^+ agreed well with the Freundlich isotherm. The values of the constants K_f and n were calculated from the slope and the intercepts of the plot and given in Table 5.5. As it can be seen from Table 5.5, the Freundlich constant (n) was greater than unity, indicating that the nZVI–Z and nFe/Cu–Z showed higher tendency for adsorption with increasing solid phase concentration. It can also be observed that the K_f value for nFe/Cu–Z was greater than for nZVI–Z, confirming the higher adsorption capacity of nFe/Cu–Z towards Cs^+.

Table 5.5: Sorption isotherm parameters for cesium adsorption onto nZVI–Z and nFe/Cu–Z.

Isotherm	Adsorbents	Model parameters			
		q_{max} (mg/g)	$K_L \times 10^3$ (L/mg)	R_L	R^2
Langmuir	nZVI–Z	71.12	3.50	0.222	0.9999
	nFe/Cu–Z	77.51	3.90	0.204	0.9963
Freundelich		n	K_f (mg/g)		R^2
	nZVI–Z	1.04	0.18		0.9917
	nFe/Cu–Z	1.20	0.40		0.9968

5.3.10. Analysis of the composites after Cs^+ adsorption

The samples were also characterized by SEM microscopy to observe the morphological changes after Cs^+ adsorption. Typical SEM images of the microstructure of zeolite, nZVI–Z and nFe/Cu–Z after the removal of Cs^+ are shown in Fig. AIII (7a–d). The rectangular crystallinity of zeolite particles was maintained after Cs^+ sorption with a similar

size distribution (Fig. AIII (7a)). On the other hand, nZVI–Z and nFe/Cu–Z exhibited larger particle size after Cs^+ adsorption, which may be attributed to the formation of iron oxide/ hydroxide precipitates (Fig. AIII (7b–d)). A similar conclusion has been drawn in recent sorption experiments of Pb^{2+} using montmorillonite–nZVI and zeolite–nZVI composites [165].

In order to further explain the change in the tested samples due to the removal of Cs^+, the chemical composition of the zeolite, nZVI–Z and nFe/Cu–Z obtained by EDS method after Cs^+ adsorption is shown in Fig. AIII (8a–c). It was clear that new peaks can be found in the EDS spectrum of the samples after the removal of Cs^+, which indicated significant changes occurred in their composition. Cs was detected in the EDS analysis of zeolite, nZVI–Z and nFe/Cu–Z with weight percentages of 1.86%, 3.09% and 2.66%, respectively. The decrease in the weight ratio of Na in zeolite, nZVI–Z and nFe/Cu–Z (from 15.20%, 5.05% and 4.68% to 15.01%, 1.67% and 0.83%, respectively), confirming that the Cs^+ ions were successfully removed by the samples. The presence of O in the nZVI–Z and nFe/Cu–Z after Cs^+ adsorption (Fig. AIII (8b and c)) suggested that significant iron corrosion took place in the composites during Cs^+ removal, as verified by subsequent XRD analysis [169].

The XRD patterns of the zeolite and the composites were recorded after Cs^+ adsorption (Fig. 5.8a–c). The XRD patterns showed that zeolite maintained good crystallinity while significant differences can be observed in the XRD spectra of nZVI–Z and nFe/Cu–Z after the removal of Cs^+. The nZVI–Z and nFe/Cu–Z clearly displayed weak crystallinity and the main peaks of both composites exhibited lower intensities compared with the initial samples. The diffraction peaks of Fe^0 can be detected at 44.14° and 83.22°, and associated to the nZVI immobilized on the composite surfaces [165]. The peaks at 18.87°, 24.03°, 30.17°, 33.03°, 35.45°, 49.21°, 57.56° and 62.26°, can be attributed to the formation of amorphous phases of iron oxides, primarily Fe_2O_3 and Fe_3O_4 from Fe^0 oxidation [175]. Meanwhile, the XRD patterns of nZVI–Z and nFe/Cu–Z suggested the presence of some new diffraction peaks after Cs^+ adsorption, which indicated that some new components were generated on the surfaces of the composites. The characteristic diffraction peaks of CsCl appeared in Fig. 5.8b and c at 25.28°, 29.86°, 30.70°, 36.04°, 54.58°, 63.69°, 68.42°, 72.67° and 76.81° [161]. Besides, Cu (the diffraction peaks at 43.47°, 50.67° and 74.68°) and CuO (the diffraction peaks at 32.41°, 35.60°, 39.13°, 49.21°,

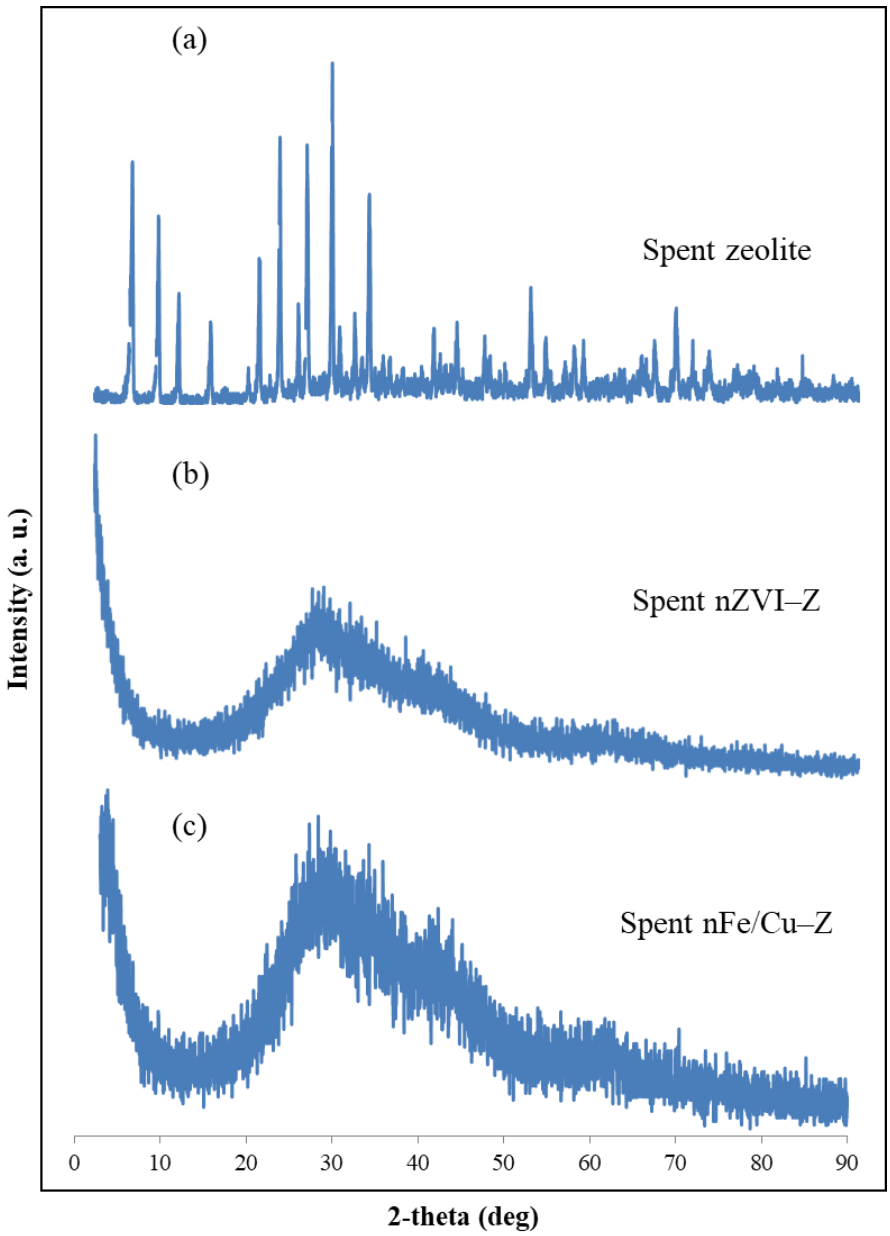

Fig. 5.8. XRD patterns of (a) zeolite, (b) nZVI–Z and (c) nFe/Cu–Z acquired at the end of experiments after Cs^+ adsorption.

61.80° and 68.42°) can also be found in Fig. 5.8c [161]. The XRD results supported the formation and immobilization of nZVI and nano-Fe/Cu particles, as well as sorption of Cs^+ ions on the composites. On the other hand, the composite can be efficiently separated by a fast and simple magnetic attraction process as the change of its optical absorbance (I_t) with time monitored at 320 nm was rapidly achieved in the presence of an external magnetic force, as shown in Fig. 5.9. Further, the homogenously mixed nanocomposite solution was

rapidly collected on the side of a bottle in the presence of a permanent magnet (see Fig. 5.10).

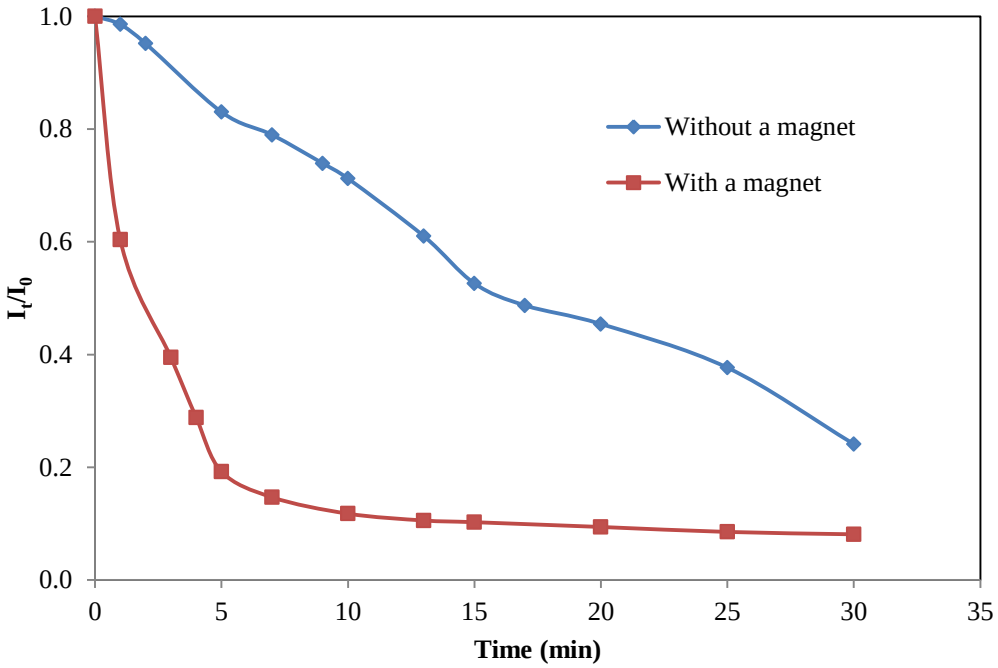

Fig. 5.9. The normalized absorbance (I_t/I_0) as a function of time monitored at 320 nm in the absence of an external magnet and after placing a permanent magnet.

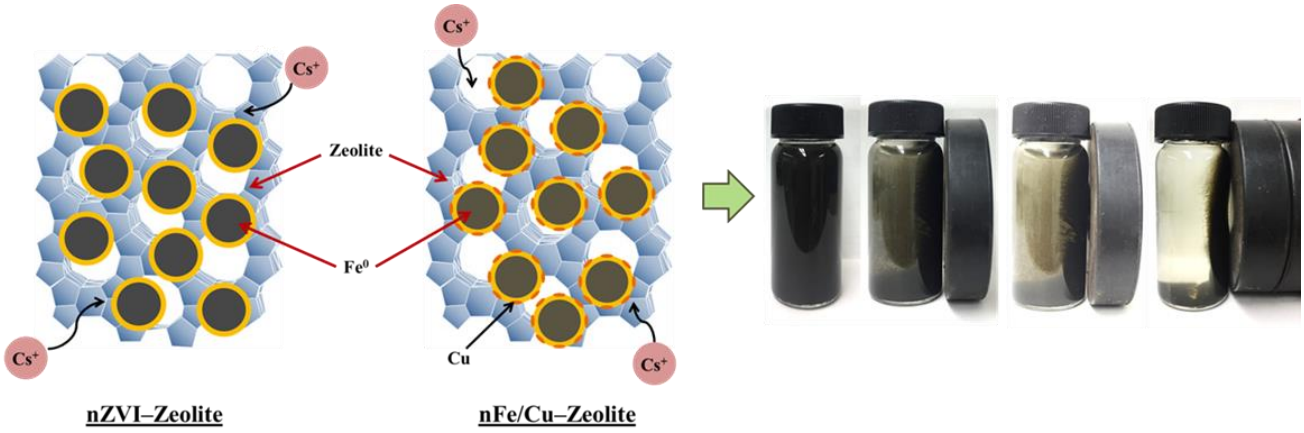

Fig. 5.10. Separation of the composites from solution after Cs^+ adsorption by applying an external magnet.

5.3.11. Comparison of adsorption capacity of Cs^+ onto various adsorbents

The maximum adsorption capacity of the nZVI–Z and nFe/Cu–Z composites for removal of Cs^+ were compared with various adsorbents reported in the literature, the data are summarized in Table 5.6. From these data, it can be seen that the nZVI–Z and nFe/Cu–Z possessed a much higher adsorption capacity value than many other adsorbents [176-179], confirming the high adsorption capacity of prepared nanocomposites toward Cs^+ ions. Furthermore, it can be noted that the Cs adsorption capacity onto the nanocomposites was much higher than other magnetic adsorbents, such as Prussian blue-modified magnetite [180], magnetite [181], magnetic chitosan [182] and magnetic Prussian blue/graphene oxide nanocomposites [183]. Although the adsorption capacity value of the nZVI–Z and nFe/Cu–Z was lower than these obtained from zeolite [144] or mesoporous silica [184], the nanocomposites can be easily collected from the solution using an external magnet after their application, whereas others cannot be readily separated.

Table 5.6: Adsorption capacity of Cs^+ by various adsorbents.

Adsorbents	Capacity (mg/g)	References
nZVI–Zeolite	71.12	Present work
nano-Fe/Cu–Zeolite	77.51	Present work
Clinoptiloite	49.26	[179]
Montmorillonite	57.04	[178]
Marble	2.373	[177]
Nanocrystalline mordenite	37.3	[176]
Prussian blue-modified magnetite	16.2	[180]
Magnetite	70.77	[181]
Magnetic chitosan	3.86	[182]
Magnetic Prussian blue/graphene oxide nanocomposites	55.55	[183]
Zeolite	102	[144]
Mesoporous silica	151.5	[184]

5.4. Conclusion

nZVI–Z and nFe/Cu–Z composites were synthesized, characterized and evaluated for the removal of Cs^+ based on the magnetic separation of the adsorbent from water after treatment. The XRD and SEM-EDS results confirmed the formation of Fe^0 on both nZVI–Z and nFe/Cu–Z composites. Both nanocomposites demonstrated effective performance for Cs^+ removal from contaminated water. The kinetic data showed a good fit to the pseudo-second-order kinetic model, which means that the chemical sorption was the rate-limiting

step. Comparing of k_2 values confirmed that the adsorption process onto nFe/Cu–Z was faster than on nZVI–Z. Also nFe/Cu–Z exhibited higher sorption capacities than for nZVI–Z. The Langmuir and Freundlich isotherm approaches successfully modeled the equilibrium sorption data. The values of thermodynamic parameters (positive $\Delta H°$ and negative $\Delta G°$) were indicative of the endothermic and spontaneous nature of Cs^+ sorption process. Separation of the nanocomposites from solution after treatment was rapidly achieved via applying an external magnet. These results supported the potential use of both composites in many environmental applications such as those involving remediation of nuclear wastewaters.

CHAPTER 6

REMOVAL OF STRONTIUM USING MAGNETIC ZEOLITE NANOCOMPOSITES

CHAPTER 6- Removal of Strontium Using Magnetic Zeolite Nanocomposites

In the present chapter, nanocomposites of nZVI–zeolite and nano-Fe/Cu–zeolite were synthesized via a simple liquid-phase reduction approach and tested to determine their effectiveness in the sorptive removal of strontium (Sr^{2+}) from aqueous solutions. The sorption of Sr^{2+} on both nanocomposites was studied in a batch sorption mode as a function of various environmental conditions such as initial Sr^{2+} concentration, contact time, pH, temperature, dosage of sorbent and competing cations (Na^{+}, K^{+}, Mg^{2+} and Ca^{2+}). The present study confirmed that the prepared nanocomposites could be employed as promising methods for the removal of Sr^{2+} from wastewater streams. To the authors' knowledge, this is the first study reporting Sr^{2+} removal from contaminated waters by nZVI–zeolite and nano-Fe/Cu–zeolite composites.

6.1. Introduction

During the last decades, a variety of treatment technologies and processes, for example, conventional coagulation, chemical precipitation and flocculation, membrane filtration, ion exchange, adsorption and reverse osmosis, have been developed for removing Sr from waste streams [178]. Among the reported techniques, adsorption is the most favorable method because it is simple, low cost and effective for water purification [174]. Various adsorbents have been applied for the removal of strontium ions including clay mineral, activated carbon, clinoptilolite, kaolinite, montmorillonite and biomaterials [5]. Zeolites are one of the most effective adsorptive materials, which have been widely used for disposal of low and medium radioactive wastes due to their high thermal, radiation and mechanical stability, high sorption capacity and selectivity. Zeolites are microporous, aluminosilicate minerals with three dimensional framework structures. The presence of aluminum in the structure of zeolites, a negatively charged framework appears which is neutralized by exchangeable cation ions, mostly sodium. The cationic radionuclides such as strontium can readily replace sodium ions from the crystals, thus giving important sorption features to zeolites. However, zeolites cannot be used in an open environment since upon radioisotopes being removed; separating the suspended fine solids from aqueous solutions is not an easy task and may even lead to secondary pollution under real conditions [185].

Another essential factor to be considered in the adsorption technique is the effectiveness with which the sorbent materials can be recovered and reused. The rapid separation and efficient regeneration are very crucial to face the environmental treatment challenges. Accordingly, it is necessary to develop a new method of remediation that does not generate secondary harmful substances in practice, and involves candidates that can be recycled and easily applied on an industrial scale.

Nowadays, researchers have paid much attention towards magnetic materials for use in environmental remediation applications, which have shown promising performance in contaminants removal or toxicity mitigation. The magnetic based materials provide an effective way to rapid separation, fast reaction rate and easily regenerable. The magnetic separation process has been widely utilized as an efficient, easy and economic method for reliable capture of metal ions from liquid waste. In order to improve their applicability for the remediation of contaminated waters, several magnetic composite materials have been reported. Hong et al. [155] synthesized a magnetically separable alginate/Fe_3O_4 composite for the practical application of Sr removal from complex media. Periyasamy et al. [186] fabricated magnetic nano-hydroxyapatite encapsulated alginate beads for selective Cr^{6+} removal from water. Niu et al. [187] prepared humic acid coated Fe_3O_4 magnetic nanoparticles for efficient sulfathiazole uptake from aqueous media. Thanh et al. [185] reported a nanocomposite of magnetic hydroxyapatite nanorods for the removal of Cu^{2+} and Ni^{2+} from aqueous solutions. Banerjee et al. [188] developed a novel magnetic nano-adsorbent by modifying Fe_3O_4 nanoparticles with gum arabic to treat Cu^{2+} from liquid waste. Sasaki et al. [180] synthesized Prussian-blue-modified magnetite (PB-Fe_3O_4) for the treatment of Cs^{+} from wastewater.

Recently, nanoscale zero valent iron particles (nZVI) have received much attraction for their possible application to the remediation of contaminated waters and soils [189]. nZVI have an extremely high surface area to volume ratio, resulting in significantly higher reactivity rates than micron size particles for purification purposes in permeable reactive barriers [190]. nZVI have been successfully used for the detoxification of a wide range of pollutants involving chlorinated organic compounds, nitroaromatic compounds, dyes, phenol and nitrate [1]. In addition, nZVI have been recognized to be effective in the immobilization of an array of metal and metalloid contaminant species comprising As [191],

Cr [192], Cd [172], Cu, Zn [71], Ni [112], Pb [70], Co [35] and Ag [193]. Recent investigations demonstrated nZVI can be utilized as a promising technology in the clean-up of radionuclides contaminated waters . However, studies are limited to radioisotopes of U, Pu [64], Ba [160], TcO_4 [122] and our group's Cs-sorption investigations [161, 162, 164].

Nevertheless, nZVI exhibit strong tendency to agglomerate to micro ZVI because of the high surface energy and magnetic forces of particles, which decrease the effective surface area and limit the removal performance [167]. To overcome this problem, a number of techniques have been applied to enhance the efficiency of nZVI, such as synthesis of bimetallic nanoparticles, immobilization onto solid supports or polymers and use of surfactants modification [18]. In the bimetallic system, deposition of a thin layer of a second metal such as Cu, Ni, Pd or Pt on the surface of nZVI particles has shown to be effective in increasing the reactivity. Doping nZVI surface with other metals is supposed to improve the contaminant removal rates by serving as reactive electron donors or hydrogen catalysts [78].

In this chapter, Sr^{2+} removal and recovery from aqueous solutions was investigated using composites of nZVI–zeolite (nZVI–Z) and nano-Fe/Cu–zeolite (nFe/Cu–Z). The two nanocomposites were synthesized and their physicochemical characteristics were systematically analyzed by transmission electron microscope (TEM), X-ray diffraction (XRD) and scanning electron microscope-elemental analysis (SEM-EDS) before and after Sr^{2+} sorption. The effectiveness of the prepared nanocomposites was studied in batch sorption mode under a variety of operating conditions such as initial Sr^{2+} concentration, contact time, initial solution pH, temperature, presence of competing cations and dosage of nanocomposites. The Sr sorption behavior was evaluated in terms of sorption isotherm, kinetic and thermodynamic studies. The Sr^{2+} removal capacity was compared between synthesized materials and other reported sorbents. Finally, nZVI–Z and nFe/Cu–Z were applied in a real seawater medium for the removal of Sr^{2+} to demonstrate the reliability of the materials.

6.2. Sr^{2+} uptake experiments

The sorption experiments were conducted at 298 K by using batch technique. The sorption capacities of nZVI–Z and nFe/Cu–Z composites for Sr^{2+} were studied using

aqueous solutions of this metal ion. The stock solution of Sr^{2+} was prepared by dissolving $SrCl_2.6H_2O$ in deoxygenated deionized water. In brief, 0.2 g of each nanocomposite was added into 100 mL of 100 mg/L initial Sr^{2+} concentration in several conical flasks. The mixture was then sealed and placed on a magnetic stirrer with a rotation speed of 1000 rpm (RSH-6DN, As One Co., Japan). The initial solution pH was monitored to be approximately 6 in these experiments. After the suspensions were agitated for 1 h to attain equilibrium, the supernatants were filtered through a 0.2 μm PVDF syringe filter. The Sr^{2+} concentration in the filtrate was measured via inductively coupled plasma mass analysis (ICPM-8500, Shimadzu Co.). The influence of pH on the Sr^{2+} sorption capacity was studied at different initial pH within the range of 3–12. The pH was adjusted using negligible volumes of 0.01–1.0 M HCl or NaOH. The dosage effect experiments were carried out with various dosage from 1 to 10 g/L of prepared nanocomposites. In the co-existing ions effect experiments, the initial concentration of Sr^{2+} was fixed at 100 mg/L and 200 mg/L of Na^+, K^+, Mg^{2+} and Ca^{2+} concentration was added. Double competitive systems (Sr/Na, Sr/K, Sr/Mg and Sr/Ca) were prepared to obtain the influence of different cations. In addition, the selectivity of nanocomposites for Sr sorption was evaluated in seawater for which the concentrations of cations (Na^+ (10000 mg/L), K^+ (400 mg/L), Mg^{2+} (1200 mg/L) and Ca^{2+} (400 mg/L)) are much higher than that of Sr^{2+}. In the equilibrium temperature studies, the experiments were also conducted at different temperature conditions like 298, 313, 328 and 343 K. The kinetic of Sr^{2+} sorption on nZVI–Z and nFe/Cu–Z was examined at different initial Sr^{2+} concentrations (1, 5, 50, 100, 150 and 200 mg/L). The concentration of Sr^{2+} was measured after various time intervals ranging from 5 to 60 min. The experiments aiming to determine the equilibrium sorption isotherm were performed with initial concentration of Sr^{2+} in the range of 1–1000 mg/L. All experiments were conducted in triplicate and the outcomes recorded here in the average values.

The Sr^{2+} sorption capacity was calculated according to the following equation:

$$q_e = (C_0 - C_e) \times (V/m) \tag{6.1}$$

The removal efficiency of Sr^{2+} ions was calculated using the difference of Sr^{2+} concentrations in aqueous solution as follows:

$$R\% = (C_0 - C_e)/C_0 \times 100 \quad (6.2)$$

where q_e (mg/g) is the amount of Sr^{2+} ions sorbed onto the unit amount of the sorbent, C_0 (mg/L) is the initial concentration of Sr^{2+}, C_e (mg/L) is the equilibrium Sr^{2+} concentration, V (L) is the aqueous solution volume and m (g) is the mass of sorbent in dry form.

For the nanocomposites selectivity towards Sr^{2+} ions, the distribution coefficient, K_d (L/g), was determined using the equation expressed as follows:

$$K_d = (C_0 - C_e)/C_e \times (V/m) \quad (6.3)$$

A high K_d value suggests high uptake capacity and selectivity of the Sr^{2+} onto the sorbent.

6.3. Results and discussion

6.3.1. Characterization of the nanocomposites

The XRD diffraction patterns of zeolite, nZVI, nano-Fe/Cu particles, nZVI–Z and nFe/Cu–Z are shown in Fig. 6.1. In Fig. 6.1a, the XRD spectra of zeolite matched well with that of the known crystal structure [144]. A series of characteristic peaks were observed in the XRD pattern of zeolite within the range of 3 to 90°, which revealed important characteristic 2θ peaks at 28.74°, 29.35°, 29.48°, 31.63°, 36.60°, 36.66°, 43.53° and 47.57° belonging to SiO_2 [165]. Additionally, 2θ peaks at 12.50°, 26.18°, 29.33°, 31.89°, 34.53°, 34.81° and 36.62° were found in zeolite which corresponded to the presence of Al_2O_3 [138]. In Fig. 6.1b and c, nZVI and nano-Fe/Cu particles showed significant diffraction peaks at 2θ = 44.60°, 64.68° and 82.35°, indicating the presence of pure Fe^0 [127]. The above-mentioned characteristic peaks of zeolite and Fe^0 were also found in nZVI–Z and nFe/Cu–Z samples. However, for both nanocomposites, crystal structure changes were observed in their XRD patterns (Fig. 6.1d and e). Obviously, several diffraction peaks within the XRD spectra exhibited a lower intensity after the iron loading compared with the initial samples; the results are in accordance with a previous report [128]. This indicated that the crystallinity of zeolite and Fe^0 was influenced during the synthetic procedure of the nanocomposites. Signals of the iron oxides (primarily Fe_2O_3 and Fe_3O_4 generated from Fe^0 oxidation) were also detected in the XRD patterns of freshly synthesised nZVI–Z and

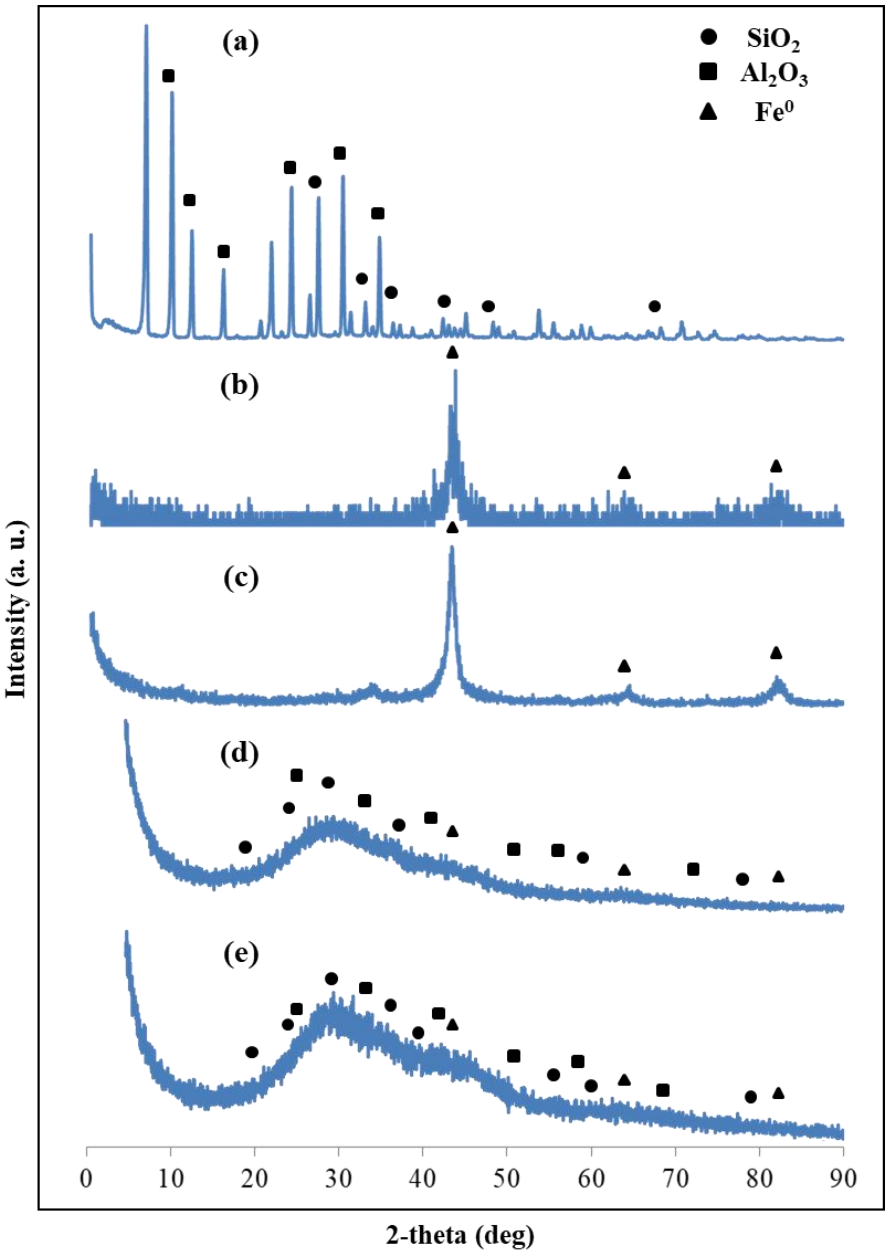

Fig. 6.1. XRD spectra of (a) zeolite, (b) nZVI, (c) nano-Fe/Cu particles, (d) nZVI–Z and (e) nFe/Cu–Z.

nFe/Cu–Z [166]. The XRD measurements confirmed the formation and immobilization of Fe^0 on both nanocomposites.

The surface morphology of zeolite, nZVI–Z and nFe/Cu–Z were identified using SEM and TEM and the images are demonstrated in Fig. AIV (1) in Appendices Section. The SEM micrograph of zeolite particles (Fig. AIV (1a)) indicated that the material was composed of individual, cubic particles ranging in size from 2 to 5µm. On the other hand, significant differences can be observed in the morphology of nZVI–Z and nFe/Cu–Z when

Fe and Fe/Cu loaded on the surface of zeolite, as shown in Fig. AIV (1b-f). The images detected the porous, irregular and aggregated structure of nZVI–Z and nFe/Cu–Z. The SEM images clearly showed that the iron nanoparticles were well immobilized and dispersed on the outer surface and within the pores of zeolite. It was also found that nZVI–Z and nFe/Cu–Z displayed the stacked layers. These findings are in good agreement with the microscopic observations reported by Wang et al. [63].

The EDS analysis was conducted to determine the chemical composition of zeolite, nZVI–Z and nFe/Cu–Z samples, as shown in Fig. AIV (2). The EDS spectrum for zeolite indicated the presence of Na (15.21 wt%), Si (50.48 wt%) and Al (34.30 wt%) in the structure (Fig. AIV (2a)). The EDS spectra of nZVI–Z (Fig. AIV (2b)) exhibited peaks corresponding to Fe element with a weight percentage of 76.73%. Cu (4.70 wt%) and Fe (68.45 wt%) were the main elements present in the EDS spectrum of nFe/Cu–Z (Fig. AIV (2c)). According to EDS quantification, Fe and Fe/Cu were loaded onto zeolite cages successfully. The EDS results were in agreement with those of XRD analysis.

6.3.2. Effect of iron content

The loading content of iron in the nanocomposites is an important factor influencing the particle properties of nZVI–Z and nFe/Cu–Z. Fig. 6.2 shows the Sr removal efficiency of the both nanocomposites as a function of the iron content. It was shown that the Sr removal decreased when the loading content of iron was changed from 25% to 75%, the nZVI–Z and nFe/Cu–Z composites with 25% of iron loading content resulted in the highest Sr removal of 86.82% and 89.73%, respectively. This observation was owing to the decrease in the amount of zeolite (which is responsible for Sr^{2+} removal) with increasing the iron content in the nanocomposites. On the other hand, the recovery efficiency of the nanocomposite via magnetic separation was obtained by plotting the normalized absorbance (I_t/I_0) monitored at 560 nm as a function of time (see Fig. 6.3) [194]. As shown in Fig. 6.3, the change of I_t/I_0 was well correlated to the change of the iron content (i.e., the I_t/I_0 of the suspension rapidly decreased as the iron content increasing from 25% to 75% in the presence of an external magnetic field). In addition, it can be seen from Fig. 6.4 that the nanocomposite particles were easily separated from aqueous solution after applying an external magnet. Taking into account two aspects of maximizing the Sr^{2+} removal

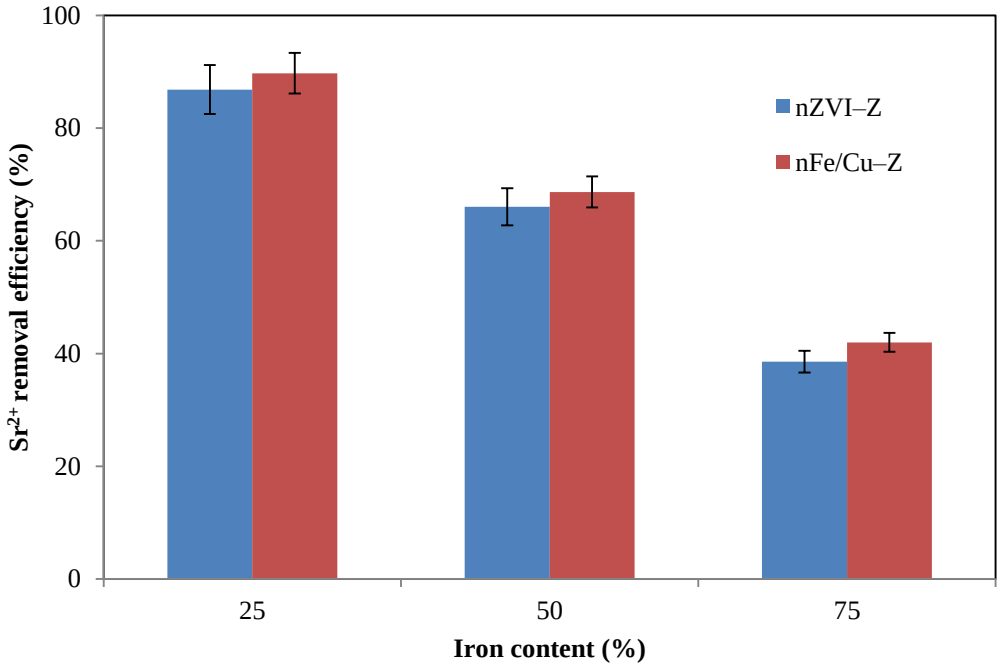

Fig. 6.2. Removal efficiency of Sr^{2+} by nZVI–Z and nFe/Cu–Z with different iron contents. (Initial conditions: pH = 6, initial Sr^{2+} concentration = 100 mg/L dosage = 2 g/L, temperature = 298 K).

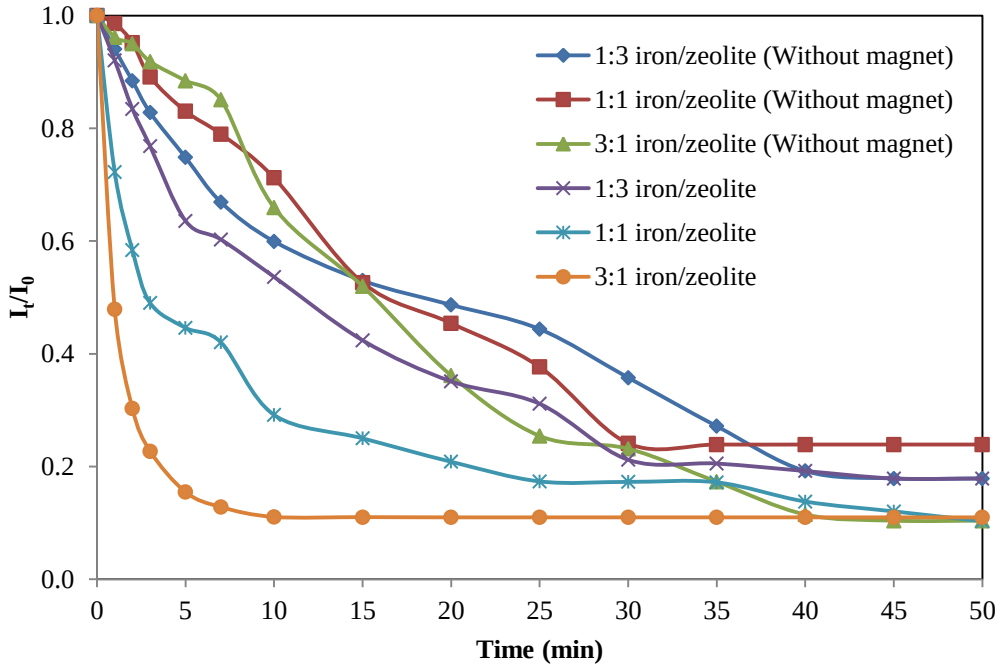

Fig. 6.3. Variations of normalized absorbance (I_t/I_0) of nZVI–Z with different iron contents as a function of time in the absence and presence of an external magnetic force.

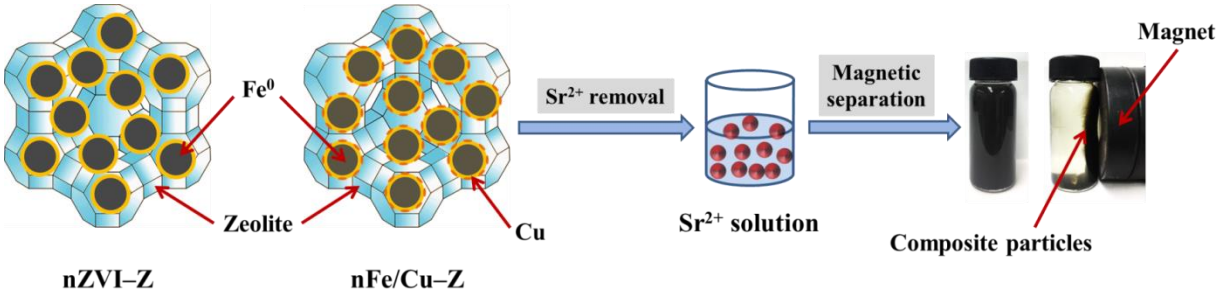

Fig. 6.4. Separation of the Sr^{2+} sorbed nanocomposite particles from aqueous solution via an external magnet.

performance and simultaneously realizing a desirable magnetic separation, the nZVI–Z and nFe/Cu–Z composites with iron content of 50% (the iron/zeolite ratio is 1:1) were used for all Sr^{2+} sorption experiments in this study.

6.3.3. Effect of initial Sr^{2+} concentration and contact time

The effect of initial concentration and contact time on Sr^{2+} sorption on nZVI–Z and nFe/Cu–Z composites were examined using different concentrations of Sr^{2+} within 1–200 mg/L with different period of contact time in the range of 5–60 min at initial solution pH 6 and the results are shown in Fig. 6.5. As it is evident from Fig. 6.5, that Sr^{2+} sorption capacity increased with increase in reaction time and attained rapid saturation for both nanocomposites. Nevertheless, the time to reach sorption equilibrium and the maximum sorption amount were different. The equilibrium time was reached after 30 min for nZVI–Z (Fig. 6.5a), whereas shorter time was obtained for nFe/Cu–Z, being 20 min (Fig. 6.5b). The equilibrium times were found to be the same for different concentrations of 50, 100, 150 and 200 mg/L. Similar behavior was also obtained in our previous investigation [194]. For next sorption experiments, the fixed time of 60 min was chosen to assure that the equilibrium sorption was achieved. It was observed that both the efficiency and rate of Sr^{2+} removal decreased corresponding to increased initial concentration. At a fixed dosage of the nanocmposites, the total available reactive sites are limited, thus the ratio of available sorption sites to Sr ions is less at higher initial concentrations. However, the larger initial concentration resulted in a larger Sr sorption. Therefore, the removal of Sr^{2+} by nZVI–Z and nFe/Cu–Z is concentration dependent. The maximum sorption capacities of nZVI–Z at initial concentrations of 1, 5, 50, 100, 150 and 200 mg/L were found to be 0.18, 0.94, 9.08, 17.83, 26.17 and 32.83 mg/g, respectively while the capacities for nFe/Cu–Z at similar

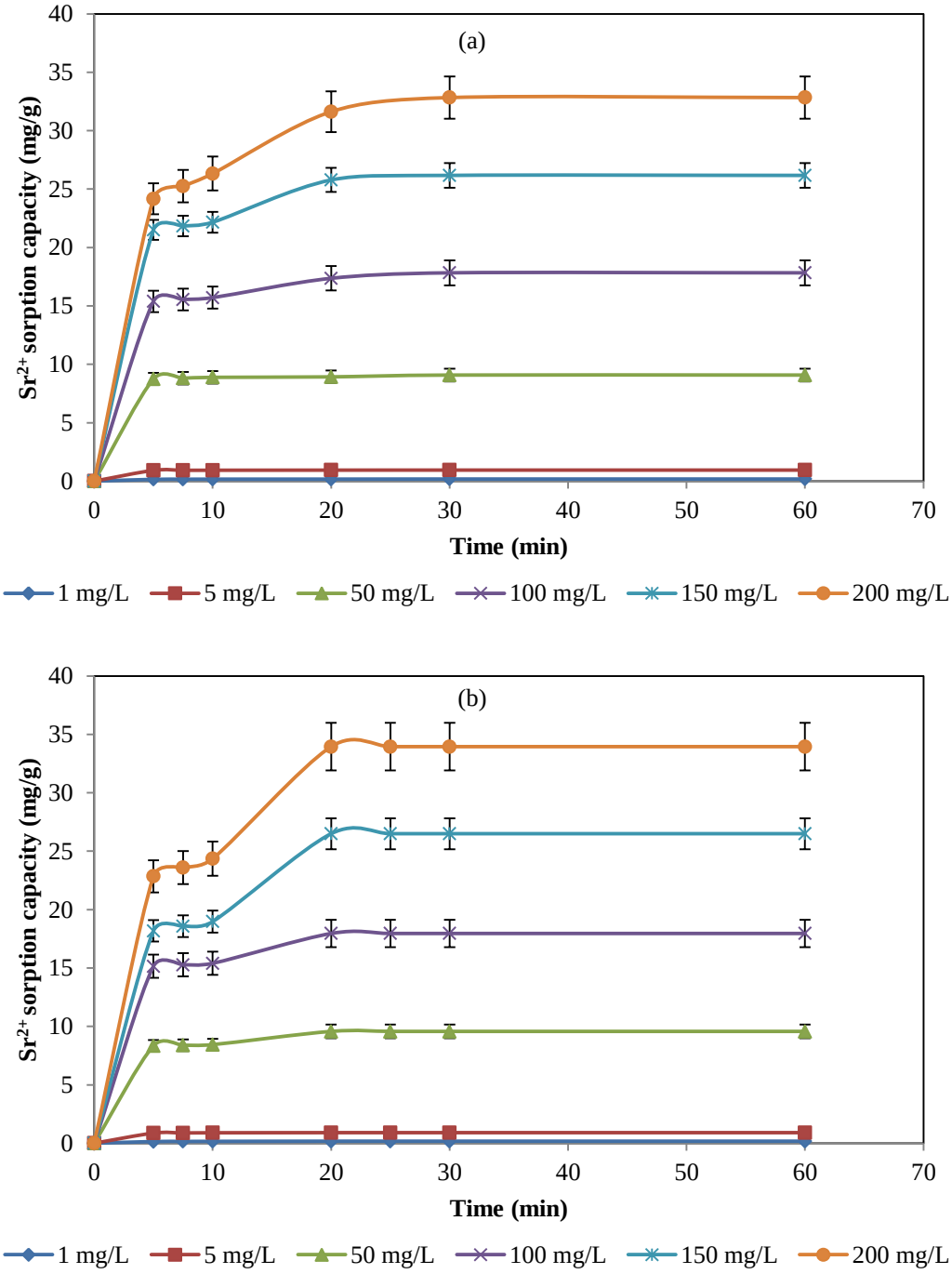

Fig. 6.5. Effect of initial concentration and contact time on Sr^{2+} sorption by (a) nZVI–Z and (b) nFe/Cu–Z. (Initial conditions: pH = 6, dosage = 5 g/L, temperature = 298 K).

concentrations were 0.17, 0.91, 9.57, 17.96, 26.50 and 33.95 mg/g, respectively. nFe/Cu–Z composite possessed higher sorption rate than nZVI–Z composite because the presence of Cu^0 promotes corrosion rate of Fe^0 and acts as a good conductor of charge transfer during the reaction [128].

6.3.4. Effect of pH

The initial solution pH is one of the significant factors controlling the sorption of Sr^{2+} since it influences not only the speciation of Sr in aqueous medium but also the surface charge of the sorbents. Experiments examining Sr^{2+} sorption by nZVI–Z and nFe/Cu–Z composites were carried out at initial pH 3–12, and the results are plotted in Fig. 6.6. The sorption of Sr^{2+} onto the nanocomposites sharply increased with increasing initial solution pH from 3 to 12, indicating that Sr sorption on nZVI–Z and nFe/Cu–Z is strongly pH-dependent. It was reported that the dominant species of Sr at pH 3–11 is Sr^{2+} species [195]. At low pH, the dissolution of nZVI–Z and nFe/Cu–Z and deconstruction of sorption sites on composites surfaces hinder the sorption reaction in acidic environment [178]. In addition, the excess protons compete for the available sorption sites with Sr^{2+} ions [196]. Therefore, the sorption of Sr^{2+} onto nanocomposites was unfavorable at low pH and the ion exchange between Sr^{2+} and nanocomposites surfaces can lead to the sorption of Sr^{2+}. At high pH, the surface of nanocomposites was negatively charged as the number of protons decreased with increasing pH therefore, it attracted the positive Sr ions towards itself electrostatically, thus resulting in an increase of Sr^{2+} sorption. At pH values of above 11, the clear increase in Sr^{2+}

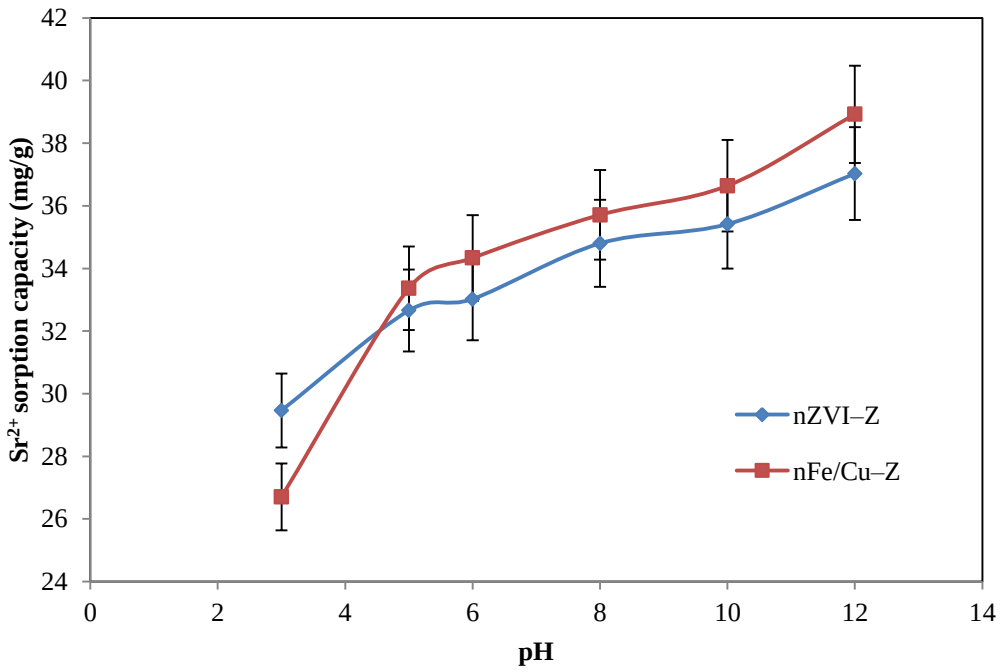

Fig. 6.6. Effect of pH on Sr^{2+} sorption by nZVI–Z and nFe/Cu–Z. (Initial conditions: dosage = 2 g/L, initial Sr^{2+} concentration = 100 mg/L, temperature = 298 K).

sorption may be caused by the precipitation of $Sr(OH)_2$. The formation of $Sr(OH)^+$ is another possible mechanism for enhancing Sr sorption onto the nanocomposites [178]. At pH 12, a high Sr sorption capacity of 37.03 and 38.92 mg/g was observed for nZVI–Z and nFe/Cu–Z, respectively. Hence, the optimal pH, at which the capacity of nZVI–Z and nFe/Cu–Z to sorb and remove Sr^{2+} is maximal, was 12. This result is similar to that reported in previous studies of the sorption behavior of Sr^{2+} on montmorillonite [16], phosphate-modified montmorillonite [178], sericite [197] and iron oxide [198].

6.3.5. Effect of solid content

The dependence of Sr^{2+} sorption on nZVI–Z and nFe/Cu–Z at different solid contents was carried out at 298 K and initial pH of 6 within the nanocomposite dosage range of 1–10 g/L. Experiments were based on 100 mL solution with 100 mg/L of initial Sr^{2+} concentration. The sorption efficiency of Sr^{2+} as a function of sorbent dosage is illustrated in Fig. 6.7. It was found that the removal efficacy increased as the dosage of nanocomposites was raised. With increasing the solid content, the number of active sites on nanocomposite surface increased which led to high Sr^{2+} removal. It is clear from Fig. 7 that the dose of sorbent was more crucial and it had greater effect on the sorption percentage for high metal concentration. The removal efficiency reached almost 90% for both nanocomposites when a dosage of 5 g/L was used, indicating that the nZVI–Z and nFe/Cu–Z revealed strong affinity to Sr^{2+} ions. Further, the nanocomposites possessed no significant change in their sorption efficiency when the dosage was increased to above 5 g/L. As a result, a sorption dosage of 5 g/L was selected for kinetic and isotherm studies.

It was also observed that the sorption capacity of Sr^{2+} on nZVI–Z and nFe/Cu–Z decreased with increasing solid contents. This may be because Sr^{2+} can easily access the sorption sites of nanocomposites at low solid content and thereby the sorption capacity is high. In contrast, a large amount of sorbent decreases the unsaturated sites of sorption highly and leads in overcrowding of solid particles, which reduces the Sr^{2+} sorption on the nanocomposites [199]. Moreover, the possibility of collision between solid particles enhances at higher solid content that causes a reduction in the total surface area and an increase in the length of diffusion path [16].

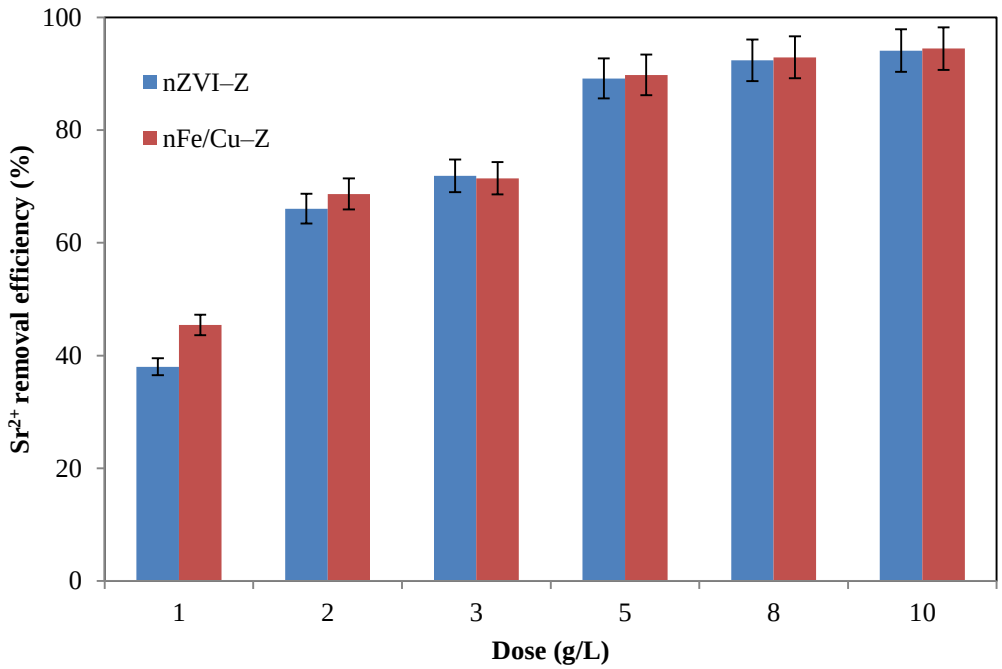

Fig. 6.7. Sr^{2+} removal by different dosage of nZVI–Z and nFe/Cu–Z. (Initial conditions: pH = 6, initial Sr^{2+} concentration = 100 mg/L, temperature = 298 K).

6.3.6. Effect of temperature

Temperature is an important factor affecting Sr^{2+} removal. Sorption studies were carried out at four different temperatures viz., 298, 313, 328 and 343 K at initial concentration of 100 mg/L and pH of 6. The effect of temperature on the sorption of Sr^{2+} onto nZVI–Z and nFe/Cu–Z is presented in Fig. 6.8. The sorption capacity of Sr^{2+} enhanced as temperature increases from 298 K to 343 K suggesting an endothermic nature of Sr^{2+} sorption. The increase in the sorption capacity with the increase of temperature is likely due to more rapid diffusion of Sr^{2+} ions into the internal pores of the nanocomposite particles [166] and the increase in the number of active sorption sites created on the sorbent surface [186]. The results revealed that high temperature is advantageous for Sr^{2+} sorption on nZVI–Z and nFe/Cu–Z. The similar temperature dependent sorption behaviors of Sr^{2+} on various types of sorbents were obtained by other researchers [197].

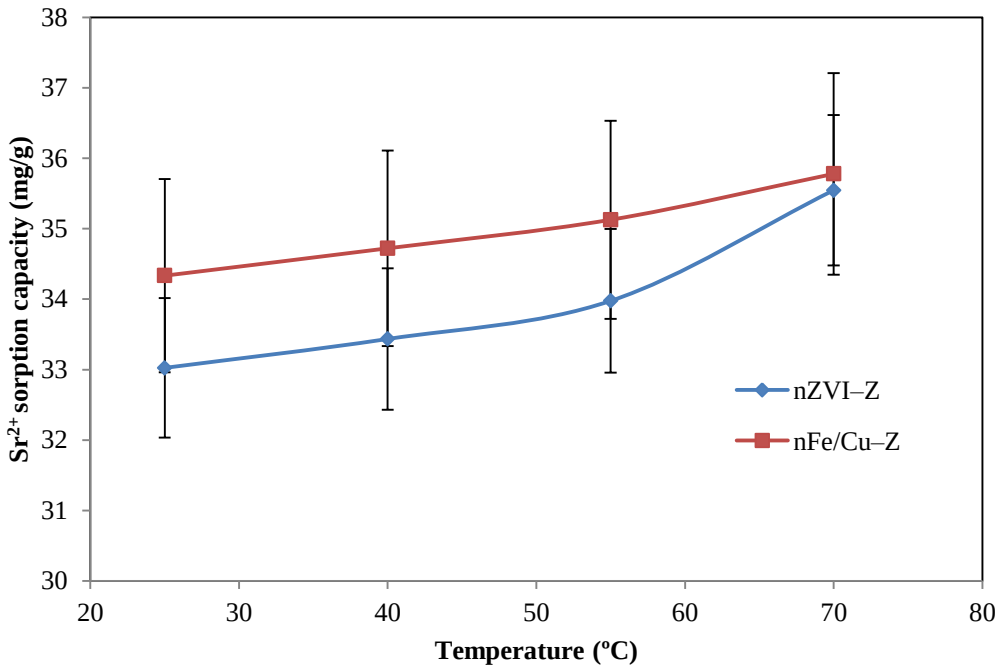

Fig. 6.8. Effect of temperature on Sr^{2+} sorption by nZVI–Z and nFe/Cu–Z. (Initial conditions: pH = 6, dosage = 2 g/L, initial Sr^{2+} concentration = 100 mg/L).

6.3.7. Effect of solution chemistry on Sr^{2+} sorption

Alkali and alkali-earth metal ions like Na^{+}, K^{+}, Mg^{2+} and Ca^{2+}, which exist broadly in seawater and Nuclear Power Plant wastewater, may compete with Sr^{2+} ions for the available sorptive sites; thus, it is highly required to investigate the sorption performance of nZVI–Z and nFe/Cu–Z composites under various solution chemistry conditions prior to the practical application. Accordingly, the Sr sorption capacity of the nanocomposites was evaluated in the presence of co-existing cations and the selectivity for Sr sorption was examined. The Sr^{2+} sorption experiments were conducted in the presence of Na^{+}, K^{+}, Mg^{2+} and Ca^{2+} at a 200 mg/L of co-ions concentration with initial Sr^{2+} concentration as 100 mg/L [186] and the results are shown in Fig. 6.9. It is evident that the Sr sorption capacity was inhibited in the presence of co-existing various types of cations by affecting the sorption behavior of Sr. However, the nanocomposites still exhibited high Sr uptake, implying that the nZVI–Z and nFe/Cu–Z have the ability of selectively and efficiently in removing Sr^{2+} from aqueous solutions under the above competing cation ions conditions. The results are in good consistency with that reported by Hong et al. [155] for Sr^{2+} sorption on alginate/Fe_3O_4 composite.

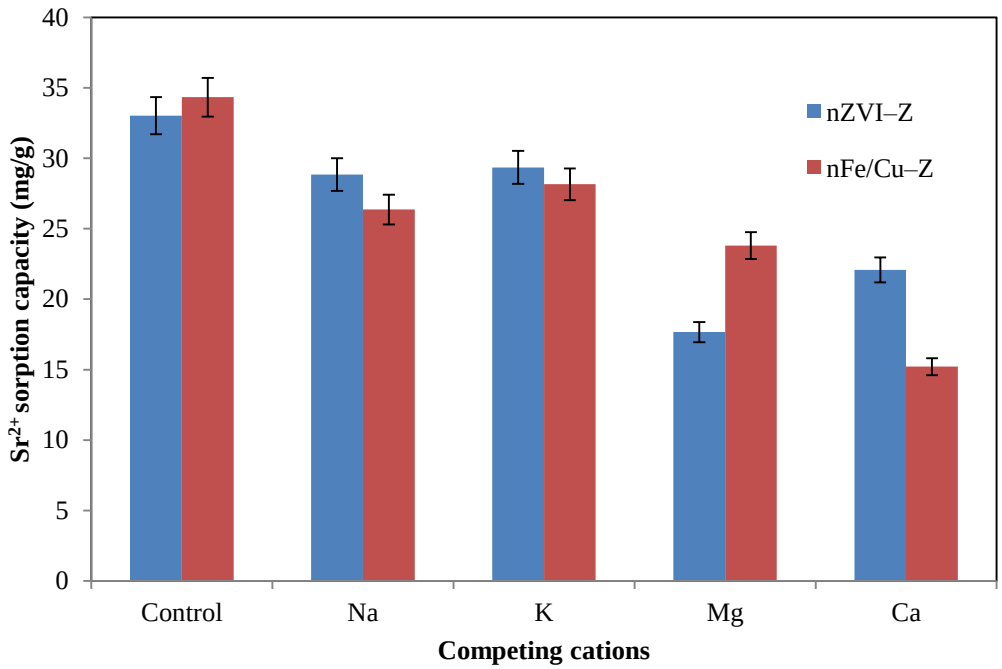

Fig. 6.9. Effect of different competing cation ions on Sr^{2+} sorption by nZVI–Z and nFe/Cu–Z. (Initial conditions: pH = 6, dosage = 2 g/L, initial Sr^{2+} concentration = 100 mg/L, temperature = 298 K).

6.3.8. Sorption kinetics

To investigate the mechanism of Sr^{2+} sorption onto the nZVI–Z and nFe/Cu–Z composites, pseudo-first-order, pseudo-second-order, Elovich and intraparticle diffusion kinetic equations were applied to describe the possible sorption kinetics. The pseudo-first-order kinetic model can be referred by the following [200]:

$$\ln(q_e - q_t) = \ln q_e - k_1 t \tag{6.4}$$

where q_t and q_e are the amount of Sr^{2+} on the surface of the nanocomposites (mg/g) at time t and at equilibrium, respectively and k_1 is the rate constant of first-order sorption (min^{-1}). The slope of the straight line plot of $\ln(q_e - q_t)$ versus t for different initial Sr^{2+} concentrations gives the value of the rate constants (k_1) and are listed in Table 6.1.

The linear form of pseudo-second-order kinetic model [201] can be represented by the following Eq. (6.5):

$$t/q_t = 1/(k_2 q_e^2) + (1/q_e)\, t \tag{6.5}$$

where k_2 is the rate constant of pseudo-second-order sorption (g/mg/min). In addition, the initial sorption rate, h, can be defined as follows:

$$h = k_2 q_e^2 \tag{6.6}$$

The pseudo-second-order parameters such as q_e, k, h and R^2 can be calculated by plotting t/q_t against t and the results are presented in Table 6.1 for all initial Sr^{2+} concentrations.

Table 6.1: The calculated parameters of pseudo-first-order and pseudo-second-order kinetic models for Sr^{2+} sorption onto nZVI–Z and nFe/Cu–Z.

Sorbents	Initial concen. (mg/L)	$q_{e\ (exp.)}$ (mg/g)	Pseudo-first order model			Pseudo-second order model			
			k_1 (min^{-1})	$q_{e\ (theor.)}$ (mg/g)	R^2	k_2 (g/mg/min)	$q_{e\ (theor.)}$ (mg/g)	h (mg/g/min)	R^2
nZVI–Z	1	0.18	0.1729	0.169	0.7706	1.5061	0.19	0.05	0.9871
	5	0.94	0.1599	0.378	0.7887	1.3440	0.96	1.23	0.9993
	50	9.08	0.1438	1.303	0.7635	0.6261	9.10	51.86	0.9999
	100	17.83	0.1601	6.394	0.8040	0.0799	18.04	26.01	0.9995
	150	26.17	0.1640	10.436	0.8116	0.0392	26.63	27.81	0.9989
	200	32.83	0.1668	17.372	0.8066	0.0220	33.61	24.91	0.9981
nFe/Cu–Z	1	0.17	0.1715	0.046	0.6353	1.7224	0.18	0.06	0.9868
	5	0.91	0.1601	0.134	0.6398	1.5596	0.92	1.32	0.9993
	50	9.57	0.1439	0.599	0.6232	0.7203	9.60	66.42	0.9999
	100	17.96	0.1591	2.546	0.6387	0.0856	18.18	28.30	0.9994
	150	26.50	0.1662	5.426	0.6363	0.0246	27.25	18.29	0.9964
	200	33.95	0.1655	6.651	0.6379	0.0219	34.81	26.53	0.9975

The Elovich equation can be simplified as [202]:

$$q_t = \ln(\alpha\beta)/\beta + \ln t/\beta \tag{6.7}$$

where α is the initial sorption rate (mg/g/min) and β is related to the number of sites available for sorption (g/mg). The equation constants can be determined from the slope and the intercept of the plot of q_t against $\ln t$ and the results are given in Table 6.2.

The intraparticle diffusion kinetic model utilized here attributes to the theory suggested by Weber and Morris [203] and its equation can be expressed as:

$$q_t = K_{\text{diff}} t^{1/2} + C \tag{6.8}$$

where K_{diff} and C are constants related to reaction rate and thickness of the boundary layer, respectively. The constants for intraparticle diffusion model at various initial Sr^{2+}

concentrations were calculated from the slope and the intercept obtained from the linear plot of q_t versus $t^{1/2}$. The results are illustrated in Table 6.2.

Table 6.2: The calculated parameters of Elovich and intraparticle diffusion kinetic models for Sr^{2+} sorption onto nZVI–Z and nFe/Cu–Z.

Sorbents	Initial concen. (mg/L)	Elovich model			Intraparticle diffusion model		
		α (mg/g/min)	β (g/mg)	R^2	K_{diff} (mg/g/min)	C (mg/g)	R^2
nZVI–Z	1	0.059	22.514	0.9568	0.023	0.03	0.8637
	5	0.572	4.530	0.7719	0.107	0.33	0.6206
	50	6.864	0.483	0.6825	0.984	3.66	0.5240
	100	10.696	0.238	0.7777	2.042	6.16	0.6235
	150	13.708	0.157	0.8330	3.112	8.16	0.6798
	200	15.532	0.124	0.8694	3.990	9.28	0.7245
nFe/Cu–Z	1	0.055	21.340	0.9410	0.024	0.03	0.8246
	5	0.512	4.580	0.8047	0.106	0.30	0.6463
	50	6.974	0.452	0.7001	1.051	3.80	0.5375
	100	10.517	0.233	0.7889	2.080	6.13	0.6315
	150	11.886	0.151	0.8797	3.284	7.10	0.7385
	200	15.650	0.118	0.8755	4.185	9.40	0.7284

Based on correlation coefficient R^2 values given in Tables 6.1 and 6.2, it can be concluded that the kinetic process for the sorption of Sr^{2+} ions by nZVI–Z and nFe/Cu–Z was perfectly fitted by the pseudo-second-order reaction model ($R^2 \approx 1$) for all initial concentrations. Moreover, it can be seen from Table 6.1 that the experimental sorption capacities, $q_{e\,(\text{exp.})}$ were in good agreement with the theoretical sorption capacities $q_{e\,(\text{theor.})}$ obtained by pseudo second order Eq. (6.5). This finding suggested that Sr^{2+} sorption rate was predominated through a chemical sorption reaction. These results are consistent with previous studies [197, 198]. It is clear that the values of the pseudo-second-order sorption rate constants, k_2, decreased with the increase in the initial Sr^{2+} concentrations from 1 to 200 mg/L. This indicated that Sr^{2+} sorption progressed faster for a lower Sr concentration in the liquid media. Chegrouche et al. [204] observed similar phenomena in sorption of Sr^{2+} on activated carbon. We can also notice that the k_2 values of Sr^{2+} onto the nFe/Cu–Z composite was slightly higher than that of nZVI–Z, indicating the nFe/Cu–Z composite have a higher sorption rate for Sr^{2+} than that on nZVI–Z.

6.3.9. Sorption isotherms

To evaluate the maximum sorption capacity and to gain a better explanation of Sr sorption mechanism, the Sr sorption isotherm experiments over a wide initial concentration range (1–1000 mg/L) were performed. Fig. 6.10 shows the sorption isotherm of Sr^{2+} onto nZVI–Z and nFe/Cu–Z. The Sr^{2+} sorption on both nanocomposites increased with increasing initial concentration. This can be ascribed to the increase in the driving force as the initial concentration increases (i.e., higher concentration difference at higher initial concentration) [178]. Two theoretical isotherm models, Langmuir and Freundlich, were employed to simulate the equilibrium data. The Langmuir isotherm model represents the monolayer sorption that takes place on a surface with homogenous binding sites and assumes no interaction between sorbates in the plane of the surface [14]. This model can be expressed as follows:

$$1/q_e = 1/q_{max} + 1/(q_{max} b C_e) \quad (6.9)$$

where q_e is the amount of Sr^{2+} sorbed at equilibrium concentration (mg/g), C_e is the equilibrium concentration of Sr^{2+} in solution (mg/L), b is the Langmuir constant related to the heat of sorption (L/mg) and q_{max} is the maximum monolayer sorption capacity (mg/g).

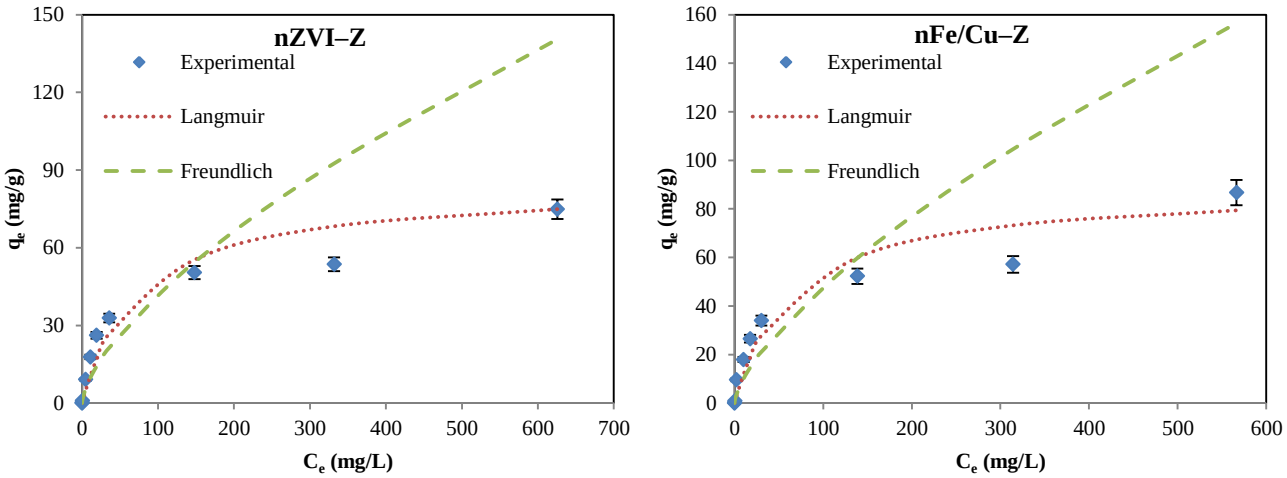

Fig. 6.10. Sorption isotherms of Sr^{2+} onto nZVI–Z and nFe/Cu–Z. (Initial conditions: pH = 6, dosage = 5 g/L, temperature = 298 K).

The Freundlich isotherm is an empirical model that considers the heterogeneity of sorbent surface [205]. The linear form of the Freundlich model can be given by the following equation:

$$\ln q_e = \ln K_f + 1/n \ \ln C_e \tag{6.10}$$

where K_f and n are Freundlich constants related to capacity and intensity of sorption, respectively. The constant n depends on the heterogeneity of the material. When n values are in the range $1 < n < 10$, the adsorption process is favourable.

The linear plots of Langmuir and Freundlich isotherms for the sorption data of Sr^{2+} onto nZVI–Z and nFe/Cu–Z are shown in Figs. AIV (3) and (4). The related parameters of the two models are summarized in Table 6.3. According to the correlation coefficient R^2, the Langmuir model gives a better fit of the experimental data ($R^2 = 0.9564$ and 0.9915 for nZVI–Z and nFe/Cu–Z, respectively) than the Freundlich model for both nanocomposites. These results suggested that the sorption of Sr^{2+} was achieved with monolayer coverage. Thus, the entire surface is energetically homogeneous and the adsorbed species are independent of each other. Ryu et al. [15] reported consistent results. Ryu applied titanate nanotubes to adsorb Sr^{2+} ions and the sorption isotherm were fit well with the Langmuir model. The maximum sorption capacity of Sr^{2+} on nZVI–Z and nFe/Cu–Z was calculated to be 84.12 and 88.74 mg/g, respectively, which is very close to the experimental results. The higher Langmuir sorption capacity of nFe/Cu–Z compared to nZVI–Z may be explained by the enhancement in specific surface area and metallic affinity in the presence of Cu [61, 131].

Table 6.3: Sorption isotherm parameters for Sr^{2+} sorption onto nZVI–Z and nFe/Cu–Z.

Isotherm	Sorbents	Model parameters			
		q_{max} (mg/g)	$b \times 10^3$ (L/mg)	R_L	R^2
Langmuir	nZVI–Z	84.12	13	0.071	0.9564
	nFe/Cu–Z	88.74	15	0.063	0.9915
Freundelich		n	K_f (mg/g)		R^2
	nZVI–Z	1.52	2.03		0.9156
	nFe/Cu–Z	1.46	2.05		0.8877

One of the essential characteristics of the Langmuir isotherm is the dimensionless constant separation factor (R_L) and can be defined by [174]:

$$R_L = 1/(1 + bC_0) \quad (6.11)$$

where C_0 is the initial Sr^{2+} concentration (mg/L). The parameter R_L indicates the type of isotherm which is determined by the sorption characteristics. The R_L value between 0 and 1 indicates favorable sorption (see Table 6.4). The R_L values presented in Table 6.3 are in the range of 0–1, which suggest favorable sorption of Sr^{2+} ions on the nanocomposites.

The Sr^{2+} sorption capacities of nZVI–Z and nFe/Cu–Z were compared with different reported sorbents for Sr^{2+} removal [16, 153, 177-179, 197, 198, 204, 206-209] and are shown in Table 6.5. Clearly, among the presented sorbents, the nZVI–Z and nFe/Cu–Z composites exhibit the highest maximum sorption capacity. In addition, nZVI–Z and nFe/Cu–Z could be easily separated from the end water magnetically.

Table 6.4: Types of isotherms for different values of R_L.

R_L value	Type of isotherm
$R_L > 1$	Unfavorable
$R_L = 1$	Linear
$0 < R_L < 1$	Favorable
$R_L = 0$	Irreversible

Table 6.5: Comparison of sorption capacities for Sr^{2+} between different sorbents.

Sorbents	Capacity (mg/g)	References
TiO_2-SiO_2 gel	48.77	[206]
Antimony silicate	60	[207]
Clinoptilolite	6.69	[179]
Na-montmorillonite	10.93	[16]
Activated carbon	44.4	[204]
Magnetic zeolite composite	83.68	[153]
Phosphate modified montmorillonite	12.53	[178]
Sericite	21.41	[197]
Fe_3O_4	12.6	[208]
FeOOH BT1	38.46	[198]
Marble	2.094	[177]
Hydroxyl apatite	12.84	[209]
nZVI–Zeolite	84.12	Present study
nano-Fe/Cu–Zeolite	88.74	Present study

6.3.10. Thermodynamic parameters

The thermodynamic parameters (Gibbs free energy change ($\Delta G°$), entropy change ($\Delta S°$) and enthalpy change ($\Delta H°$)) for Sr^{2+} sorption onto nZVI–Z and nFe/Cu–Z can be calculated using the equations [204]:

$$\Delta G° = -RT \ln K_d = \Delta H° - T\Delta S° \quad (6.12)$$

$$\ln K_d = (\Delta S°/R) - (\Delta H°/RT) \quad (6.13)$$

where R is the ideal gas constant (8.314 J/mol/K), T is the temperature in Kelvin and K_d is the distribution coefficient (mL/g). Therefore, the slope and intercept of the linear plot of $\ln K_d$ versus $1/T$ (Fig. AIV (5)) give the values of $\Delta H°$ and $\Delta S°$, respectively. The thermodynamic parameters are presented in Table 6.6 in detail. The positive values of $\Delta H°$ (4.20 kJ/mol for nZVI–Z and 2.55 kJ/mol for nFe/Cu–Z) indicated that the sorption of Sr^{2+} on the nanocomposites is an endothermic process, which was also supported by the increase in K_d with temperature. One possible explanation of this positive enthalpy is that the Sr^{2+} sorption has to overcome an activation barrier before its sorption onto the nanocomposites [178]. Thus this process needs energy and increasing temperature favors this reaction. The assumption revealed that the endothermic energy of dehydration process is higher than the exothermic energy of the ions attaching to the nanocomposite surface [197]. The changes in entropy ($\Delta S°$) for nZVI–Z and nFe/Cu–Z were 0.0711 and 0.0667 kJ/mol/K, respectively. The positive value of $\Delta S°$ suggested the affinity of nZVI–Z and nFe/Cu–Z toward Sr^{2+} ions in aqueous solutions and the sorption process was accompanied with some structural changes of the nanocomposites [204]. Unuabonah et al. [210] reported that the positive $\Delta S°$ shows the enhanced degree of randomness at the solid–liquid interface during the sorption of Sr^{2+}. The changes of free energy ($\Delta G°$) were negative denoting that the sorption of Sr^{2+} onto nZVI–Z and nFe/Cu–Z is spontaneous in nature. The value of $\Delta G°$ became more negative with increasing temperature suggesting more efficient sorption at high temperature. Similar results were reported by Kaçan and Kütahyalı [205]. They found that sorption of Sr^{2+} onto activated carbon prepared from textile sewage sludge was a spontaneous process and preferable at high temperature. The results demonstrated that the sorption of Sr^{2+} by nZVI–Z and nFe/Cu–Z is a spontaneous and endothermic process.

Table 6.6: Thermodynamic parameters for Sr^{2+} sorption onto nZVI–Z and nFe/Cu–Z.

Sorbents	$\Delta H°$ (kJ/mol)	$\Delta S° \times 10^2$ (kJ/mol/K)	$\Delta G°$ (kJ/mol)			
			298 K	313 K	328 K	343 K
nZVI–Z	4.20	7.11	−16.98	−18.05	−19.12	−20.18
nFe/Cu–Z	2.55	6.67	−17.32	−18.32	−19.32	−20.32

6.3.11. Removal of Sr^{2+} from a real seawater medium

From a practical point of view, the Sr^{2+} sorption performance of nZVI–Z and nFe/Cu–Z composites in the real seawater medium was tested to demonstrate the feasibility and investigate the sorption behavior of the nanocomposites in real seawater conditions. Table 7 shows the Sr^{2+} uptake of the nanocomposites in the 100 mg/L Sr spiked seawater. The Sr^{2+} sorption capacity in seawater was influenced compared with that in deionized water. Seawater contains a tremendous number of mineral ions, including Na^+ (10000 mg/L), K^+ (400 mg/L), Mg^{2+} (1200 mg/L) and Ca^{2+} (400 mg/L). These extremely high concentrations of cations can interfere and affect the Sr^{2+} sorption properties of nZVI–Z and nFe/Cu–Z, thereby decreasing the sorption capacity [14]. From Table 6.7, it could be drawn that the Sr^{2+} uptake decreased in seawater as the other cation ions abundantly co-existed in the solution; in particular, Ca^{2+} had the highest inhibition effect on Sr^{2+} sorption.

Table 6.7: Sr^{2+} uptake on nZVI–Z and nFe/Cu–Z in seawater medium. Initial conditions: pH = 6, initial Sr^{2+} concentration = 100 mg/L, temperature = 298 K.

Condition	Dosage (g/L)	nZVI–Z			nFe/Cu–Z		
		K_d (mL/g)	RE (%)	q_e (mg/g)	K_d (mL/g)	RE (%)	q_e (mg/g)
Control	2	972.72	66.05	33.02	1095.77	68.67	34.33
Na^+ (10000 mg/L)	2	240.57	32.48	16.24	122.01	19.61	9.81
K^+ (400 mg/L)	2	512.79	50.63	25.32	450.26	47.38	23.69
Mg^{2+} (1200 mg/L)	2	145.89	22.59	11.29	103.93	17.21	8.60
Ca^{2+} (400 mg/L)	2	106.16	17.51	8.76	111.08	18.18	9.09
Seawater	2	78.10	13.51	6.40	87.51	14.90	6.95
	5	61.41	23.49	4.45	56.96	22.17	4.14
	10	61.07	37.92	3.54	51.08	33.81	3.16

However, in the real Sr contaminated solutions such as seawater, the Sr concentration is not so high compared with the other competing cations. Accordingly, the selectively of nZVI–Z and nFe/Cu–Z toward Sr^{2+} ions will be greatly offset in a seawater medium. In addition, the Sr^{2+} uptake was improved when the dosage of the nanocomposites was increased to 5 and 10 g/L, as summarized in Table 6.7. The strategy of increasing the

dosage of the nanocomposites can be an effective method to enhance the removal efficiency of Sr^{2+} from seawater. From this result, it can be concluded that nZVI–Z and nFe/Cu–Z are promising materials for removal and recovery of Sr from seawater.

6.3.12. Analysis of the nanocomposites after Sr^{2+} sorption

The XRD patterns of the final solid samples were investigated after reaction with Sr^{2+} solution (Fig. 6.11). nZVI–Z and nFe/Cu–Z showed a very poor crystal structure after exposure to Sr^{2+} solution (Fig. 6.11a and b). Diminished diffraction peaks of Fe^0 located at 2θ = 44.60°, 64.68° and 82.35° were observed in the XRD spectra of the composites [166]. Lepidocrocite (γ-FeOOH), goethite (α-FeOOH), hematite (Fe_2O_3) and magnetite (Fe_3O_4) were all present after nZVI–Z and nFe/Cu–Z were used to remove Sr^{2+} [71]. This indicated that the composites were oxidized during the removal of Sr^{2+} ions. Besides, Cu (2θ = 43.47°, 50.67° and 74.68°) and CuO (2θ = 10.71°, 32.41°, 35.60°, 39.13°, 49.21°, 61.80° and 68.42°) can also be detected in the case of nFe/Cu–Z [112, 192, 194]. Meanwhile, new diffraction peaks (2θ = 22.04°, 23.02°, 32.38°, 35.92°, 36.39°, 41.01°, 42.95° and 65.50°) were found in the XRD patterns after the exposure of the nanocomposites to Sr^{2+} (Fig. 6.11a and b), which belong to $SrCl_2$ [211]. This result confirmed sorption of Sr^{2+} on nZVI–Z and nFe/Cu–Z composites.

Fig. AIV (6) shows the morphological changes in zeolite, nZVI–Z and nFe/Cu–Z after Sr^{2+} removal characterized by SEM microscopy. The porous and homogeneous structure of zeolite still existed (Fig. AIV (6a and b)). The SEM images of nZVI–Z and nFe/Cu–Z (Fig. AIV (6c-f)) showed that the irregularly shaped particles were still dominant but also indicated the presence of some larger aggregates after Sr^{2+} sorption, stemming possibly from the formation of iron oxide/hydroxide compounds. This observation is analogous to the result reported by Arancibia-Miranda et al. [165].

The EDS spectra was also recorded for zeolite, nZVI–Z and nFe/Cu–Z samples after Sr^{2+} sorption, as illustrated in Fig. AIV (7a-c). New peaks were detected in the EDS analyses, which were attributed to Sr element. Therefore, the strong peaks at 1.81 and 1.87 keV in the EDS spectra provided an important evidence for Sr^{2+} sorption on the samples [178]. These results confirmed that Sr^{2+} was sorbed onto the surface of nZVI–Z and

nFe/Cu–Z efficiently. The EDS quantitative analyses revealed the weight percentages of Sr on nZVI–Z and nFe/Cu–Z were 5.60% and 4.58%, respectively.

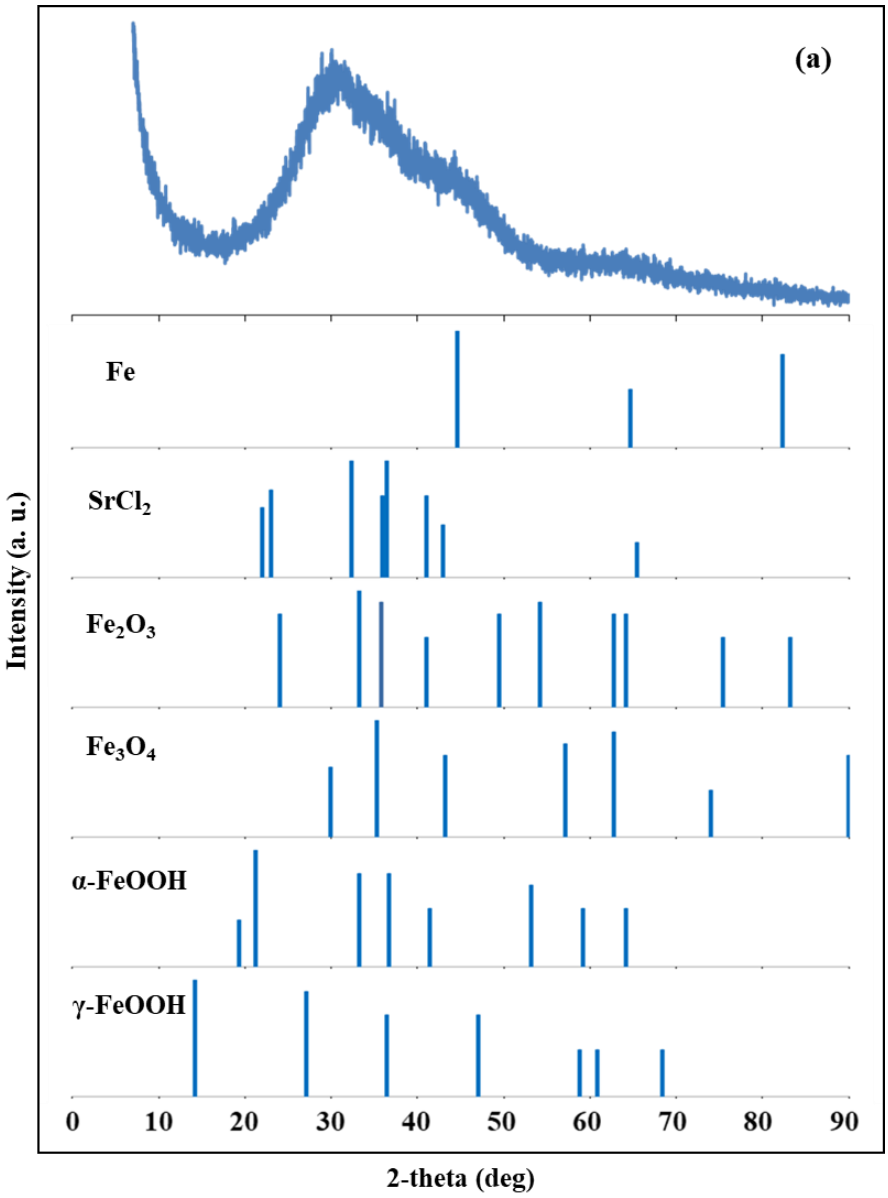

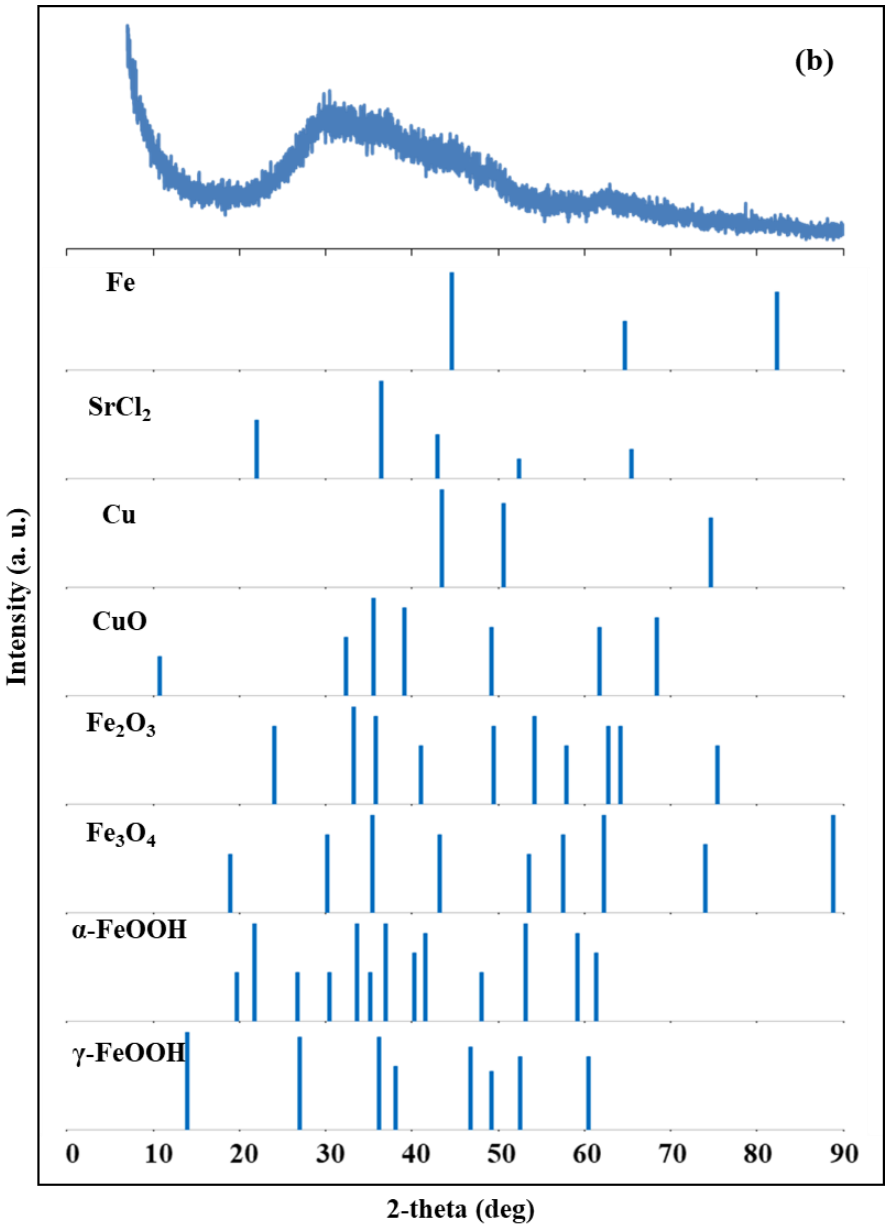

Fig. 6.11. XRD spectra of (a) zeolite, (b) nZVI–Z and (c) nFe/Cu–Z acquired at the end of experiments after Sr^{2+} sorption.

6.4. Conclusion

In this chapter, nanocomposites nZVI–Z and nFe/Cu–Z were prepared by a simple liquid-phase reduction strategy and their sorption behaviors toward Sr^{2+} were investigated for the first time. Both nanocomposites showed increase in Sr^{2+} sorption when pH was raised from 3 to 12. Increasing the temperature increased the Sr^{2+} sorption capacity. It was found that the efficiency of Sr^{2+} removal was enhanced with the increase in nanocomposite

dosage and decreased with the initial Sr^{+2} concentrations. In the presence of coexistent cations, e.g., Na^{+}, K^{+}, Mg^{2+} and Ca^{2+}, it was resulted that the Sr^{2+} sorption capacity of nZVI–Z and nFe/Cu–Z was affected. The kinetic studies proved that the sorption process closely followed the pseudo-second-order kinetic model indicating that the chemisorption was the rate-limiting step. The equilibrium isotherm analysis revealed that the Langmuir model showed a better fit than the Freundlich model indicating the applicability of monolayer coverage of Sr^{2+} on the nanocomposites surfaces. The maximum sorption capacities of Sr^{2+} on nZVI–Z and nFe/Cu–Z calculated from the Langmuir model were 84.12 mg/g and 88.74 mg/g, respectively which were higher than that for many previously reported sorbents. The thermodynamic analysis obtained from temperature dependent sorption experiments confirmed that the Sr^{2+} sorption process was endothermic and spontaneous in nature. The nanocomposites demonstrated desirable performance for Sr^{2+} removal in complex media such as seawater. Due to the magnetic properties of the nanocomposites, a fast and efficient separation process can be easily applied using a magnetic field to separate the nanocomposites entirely from the treated solutions after sorption. It can be concluded that nZVI–Z and nFe/Cu–Z have the potential application for treating Sr^{2+} contaminated water sources thanks to their high uptake capability and magnetic separation property.

CHAPTER 7

CONCLUSIONS AND RECOMMENDATIONS

CHAPETR 7- Conclusions and Recommendations

7.1. Conclusions

The main objective of this research work was to investigate the effectiveness of using nZVI, bimetallic nano-Fe/Cu particles and their composites with zeolite in the clean-up of nitrate and radionuclides contaminated waters. Therefore, this work introduces a new technology for the purpose of nuclear waste management, sustainable development of drinking water resources and alleviating the environmental pollution stress. The major findings of this project are concluded as follows:

- The best condition to remove nitrate among nZVI/sand columns was observed when using a single 10-cm high layer of nZVI/sand and more than 97% of influent nitrate was removed. Whereas in (nano-Fe/Cu)/sand columns, the optimum performance was noted when using double 5-cm high layers of (nano-Fe/Cu)/sand and a complete removal was attained (100%). The nano-Fe/Cu particles exhibited more efficient and rapid nitrate removal than nZVI when the feed solution was simulated groundwater.
- Nitrate removal in porous media could be enhanced effectively by using nZVI on the full length of porous media or using nano-Fe/Cu in multilayer porous media.
- A minimum removal efficiency of 99% was reached for nZVI and nano-Fe/Cu particles at initial cesium concentration of 1 mg/L and a dosage of 1 g-nanoparticles/L. The cesium sorption rate of nano-Fe/Cu particles was much faster than that of nZVI. Therefore, nano-Fe/Cu particles offer a much faster way in the treatment of radioactive cesium wastes in emergencies after an incident at a nuclear power plant. Also the sorption capacity of the nano-Fe/Cu particles was higher than of nZVI.
- nZVI and nano-Fe/Cu partilces selectively sorbed cesium in the presence of competing cation ions (Na^+, K^+, Mg^{2+} and Ca^{2+}) in the simulated contaminated water after Fukushima accident.
- Both nZVI–zeolite and nano-Fe/Cu–zeolite composites demonstrated effective performance for cesium removal from contaminated water.

- The maximum adsorption capacity of nano-Fe/Cu–zeolite (77.51 mg/g) was found to be higher than that for nZVI–zeolite (71.12 mg/g). In addition, the rate constant values for adsorption by nano-Fe/Cu–zeolite were greater than the values obtained for nZVI–zeolite, meaning that nano-Fe/Cu–zeolite had faster adsorption kinetics towards cesium solutions.
- Separation of the nZVI–zeolite and nano-Fe/Cu–zeolite composites from solution after cesium adsorption was rapidly achieved via applying an external magnet.
- Initial pH and temperature were significant for strontium sorption on nZVI–zeolite and nano-Fe/Cu–zeolite composites. Both nanocomposites showed increase in strontium sorption when pH was raised from 3 to 12. Increasing the temperature increased the strontium sorption capacity. It was also found the strontium sorption efficiency increases with the increase in nanocomposite dosage and decreases with the strontium concentration.
- Although the sorption of strontium was decreased by the presence of coexisting cations, e.g., Na^{+}, K^{+}, Mg^{2+} and Ca^{2+}, the nanocomposites still exhibited high uptake capacity of strontium ions.
- The maximum sorption capacities of strontium on nZVI–zeolite and nano-Fe/Cu–zeolite composites calculated from the Langmuir model were 84.12 mg/g and 88.74 mg/g, respectively which were higher than that for many previously reported sorbents. In addition to the high sorption capacity, the nanocomposites could be easily separated from aqueous media after strontium sorption using an external magnetic field.
- The nZVI–zeolite and nano-Fe/Cu–zeolite composites demonstrated desirable performance for strontium removal in complicated medium such as seawater.

7.2. Recommendations

Based on the research work outcomes, here are some suggestions and recommendations:

- Further studies are necessary to investigate the performance of effective parameters like initial nitrate concentration, nanoparticles concentration and flow rate (retention

time) through the packed column on nitrate reduction rate before the application of multilayer technique on large-scale remediation.

- nZVI and nano-Fe/Cu particles could be used as efficient materials for cesium removal from the contaminated solutions.
- The potential use of nZVI–zeolite and nano-Fe/Cu–zeolite composites for treating cesium contaminated water sources.
- nZVI–zeolite and nano-Fe/Cu–zeolite composites could be employed as promising methods for the removal of strontium from wastewater streams.
- The application of nZVI, nano-Fe/Cu particles and their composites with zeolite for cesium and strontium removal from radioactive liquid waste should be investigated under real contaminated conditions.
- Treatment of radioactive liquid waste by iron based nanoparticles and nanocomposites should be evaluated under continuous flow conditions such as column studies, etc.
- The regeneration and reuse of iron based nanoparticles and nanocomposites after treatment of radioactive wastewaters should be confirmed.

REFERENCES

References

[1] F. Fu, D.D. Dionysiou, H. Liu, The use of zero-valent iron for groundwater remediation and wastewater treatment: a review, J. Hazard. Mater. 267 (2014) 194-205.
[2] S. Kumar, P. Gopinath, Nano-bioremediation, applications of nanotechnology for bioremediation, Remediation of heavy metals in the environment (2016) 46-58.
[3] B. Karn, T. Kuiken, M. Otto, Nanotechnology and in situ remediation: a review of the benefits and potential risks, Environ. Health Perspect. 117 (2009) 1813-1831.
[4] J. Qu, M. Fan, The current state of water quality and technology development for water pollution control in China, Critical Reviews in Environmental Science and Technology 40 (2010) 519-560.
[5] Y. Sekine, R. Motokawa, N. Kozai, T. Ohnuki, D. Matsumura, T. Tsuji, R. Kawasaki, K. Akiyoshi, Calcium-deficient hydroxyapatite as a potential sorbent for strontium, Scientific reports 7 (2017) 2064.
[6] A.S. Adeleye, J.R. Conway, K. Garner, Y. Huang, Y. Su, A.A. Keller, Engineered nanomaterials for water treatment and remediation: costs, benefits, and applicability, Chem. Eng. J. 286 (2016) 640-662.
[7] S.M. Hosseini, B. Ataie-Ashtiani, M. Kholghi, Bench-Scaled Nano-Fe0 Permeable Reactive Barrier for Nitrate Removal, Ground Water Monit. Rem. 31 (2011) 82-94.
[8] T. Shubair, O. Eljamal, A.M. Khalil, N. Matsunaga, Multilayer system of nanoscale zero valent iron and Nano-Fe/Cu particles for nitrate removal in porous media, Sep. Purif. Technol. 193 (2018) 242-254.
[9] S.M. Hosseini, B. Ataie-Ashtiani, M. Kholghi, Nitrate reduction by nano-Fe/Cu particles in packed column, Desalination 276 (2011) 214-221.
[10] Y. Koma, A. Shibata, T. Ashida, Radioactive contamination of several materials following the Fukushima Daiichi Nuclear Power Station accident, Nucl. Mater. Energy 10 (2017) 35-41.
[11] F. Daiichi, ANS Committee Report, A Report by The American Nuclear Society Special Committee on Fukushima (2012).
[12] M. López, M. Martín, Medical management of the acute radiation syndrome, Reports of Practical Oncology & Radiotherapy 16 (2011) 138-146.
[13] N. Evangeliou, Y. Balkanski, A. Cozic, A.P. Møller, Global and local cancer risks after the Fukushima Nuclear Power Plant accident as seen from Chernobyl: A modeling study for radiocaesium (134 Cs & 137 Cs), Environment international 64 (2014) 17-27.
[14] H.-J. Hong, J. Ryu, I.-S. Park, T. Ryu, K.-S. Chung, B.-G. Kim, Investigation of the strontium (Sr (II)) adsorption of an alginate microsphere as a low-cost adsorbent for removal and recovery from seawater, Journal of environmental management 165 (2016) 263-270.

[15] J. Ryu, S. Kim, H.-J. Hong, J. Hong, M. Kim, T. Ryu, I.-S. Park, K.-S. Chung, J.S. Jang, B.-G. Kim, Strontium ion (Sr2+) separation from seawater by hydrothermally structured titanate nanotubes: Removal vs. recovery, Chem. Eng. J. 304 (2016) 503-510.
[16] S. Yu, H. Mei, X. Chen, X. Tan, B. Ahmad, A. Alsaedi, T. Hayat, X. Wang, Impact of environmental conditions on the sorption behavior of radionuclide 90Sr (II) on Na-montmorillonite, J. Mol. Liq. 203 (2015) 39-46.
[17] J. Jortner, C. Rao, Nanostructured advanced materials. Perspectives and directions, Pure Appl. Chem. 74 (2002) 1491-1506.
[18] R. Crane, T. Scott, Nanoscale zero-valent iron: future prospects for an emerging water treatment technology, J. Hazard. Mater. 211 (2012) 112-125.
[19] Y. Zou, X. Wang, A. Khan, P. Wang, Y. Liu, A. Alsaedi, T. Hayat, X. Wang, Environmental remediation and application of nanoscale zero-valent iron and its composites for the removal of heavy metal ions: a review, Environ. Sci. Technol. 50 (2016) 7290-7304.
[20] M. Stefaniuk, P. Oleszczuk, Y.S. Ok, Review on nano zerovalent iron (nZVI): from synthesis to environmental applications, Chem. Eng. J. 287 (2016) 618-632.
[21] D. O'Carroll, B. Sleep, M. Krol, H. Boparai, C. Kocur, Nanoscale zero valent iron and bimetallic particles for contaminated site remediation, Adv. Water Res. 51 (2013) 104-122.
[22] E. Lefevre, N. Bossa, M.R. Wiesner, C.K. Gunsch, A review of the environmental implications of in situ remediation by nanoscale zero valent iron (nZVI): behavior, transport and impacts on microbial communities, Sci. Total Environ. 565 (2016) 889-901.
[23] C.-B. Wang, W.-X. Zhang, Synthesizing nanoscale iron particles for rapid and complete dechlorination of TCE and PCBs, Environ. Sci. Technol. 31 (1997) 2154-2156.
[24] R. Miehr, P.G. Tratnyek, J.Z. Bandstra, M.M. Scherer, M.J. Alowitz, E.J. Bylaska, Diversity of contaminant reduction reactions by zerovalent iron: Role of the reductate, Environ. Sci. Technol. 38 (2004) 139-147.
[25] B.-W. Zhu, T.-T. Lim, Catalytic reduction of chlorobenzenes with Pd/Fe nanoparticles: reactive sites, catalyst stability, particle aging, and regeneration, Environ. Sci. Technol. 41 (2007) 7523-7529.
[26] Y.-H. Tee, E. Grulke, D. Bhattacharyya, Role of Ni/Fe nanoparticle composition on the degradation of trichloroethylene from water, Industrial & engineering chemistry research 44 (2005) 7062-7070.
[27] B. Schrick, J.L. Blough, A.D. Jones, T.E. Mallouk, Hydrodechlorination of trichloroethylene to hydrocarbons using bimetallic nickel− iron nanoparticles, Chem. Mater. 14 (2002) 5140-5147.
[28] J. Quinn, C. Geiger, C. Clausen, K. Brooks, C. Coon, S. O'Hara, T. Krug, D. Major, W.-S. Yoon, A. Gavaskar, Field demonstration of DNAPL dehalogenation using emulsified zero-valent iron, Environ. Sci. Technol. 39 (2005) 1309-1318.
[29] N.D. Berge, C.A. Ramsburg, Oil-in-water emulsions for encapsulated delivery of reactive iron particles, Environ. Sci. Technol. 43 (2009) 5060-5066.

[30] J. WooáLee, S. BináKim, Enhanced Cr (VI) removal using iron nanoparticle decorated graphene, Nanoscale 3 (2011) 3583-3585.
[31] X. Li, L. Ai, J. Jiang, Nanoscale zerovalent iron decorated on graphene nanosheets for Cr (VI) removal from aqueous solution: surface corrosion retard induced the enhanced performance, Chem. Eng. J. 288 (2016) 789-797.
[32] Z.-J. Li, L. Wang, L.-Y. Yuan, C.-L. Xiao, L. Mei, L.-R. Zheng, J. Zhang, J.-H. Yang, Y.-L. Zhao, Z.-T. Zhu, Efficient removal of uranium from aqueous solution by zero-valent iron nanoparticle and its graphene composite, J. Hazard. Mater. 290 (2015) 26-33.
[33] X.-q. Li, J. Cao, W.-x. Zhang, Stoichiometry of Cr (VI) immobilization using nanoscale zerovalent iron (nZVI): a study with high-resolution X-ray photoelectron spectroscopy (HR-XPS), Industrial & Engineering Chemistry Research 47 (2008) 2131-2139.
[34] X.-q. Li, W.-x. Zhang, Sequestration of metal cations with zerovalent iron nanoparticles a study with high resolution X-ray photoelectron spectroscopy (HR-XPS), The Journal of Physical Chemistry C 111 (2007) 6939-6946.
[35] Ç. Üzüm, T. Shahwan, A.E. Eroğlu, I. Lieberwirth, T.B. Scott, K.R. Hallam, Application of zero-valent iron nanoparticles for the removal of aqueous Co2+ ions under various experimental conditions, Chem. Eng. J. 144 (2008) 213-220.
[36] J. Li, C. Chen, K. Zhu, X. Wang, Nanoscale zero-valent iron particles modified on reduced graphene oxides using a plasma technique for Cd (II) removal, Journal of the Taiwan Institute of Chemical Engineers 59 (2016) 389-394.
[37] Z. Zhou, C. Dai, X. Zhou, J. Zhao, Y. Zhang, The removal of antimony by novel NZVI-zeolite: the role of iron transformation, Water, Air, & Soil Pollution 226 (2015) 76.
[38] Y.-P. Sun, X.-q. Li, J. Cao, W.-x. Zhang, H.P. Wang, Characterization of zero-valent iron nanoparticles, Adv. Colloid Interface Sci. 120 (2006) 47-56.
[39] M.A. Ramos, W. Yan, X.-q. Li, B.E. Koel, W.-x. Zhang, Simultaneous oxidation and reduction of arsenic by zero-valent iron nanoparticles: understanding the significance of the core− shell structure, The Journal of Physical Chemistry C 113 (2009) 14591-14594.
[40] M. Biterna, L. Antonoglou, E. Lazou, D. Voutsa, Arsenite removal from waters by zero valent iron: batch and column tests, Chemosphere 78 (2010) 7-12.
[41] M. Dickinson, T.B. Scott, The application of zero-valent iron nanoparticles for the remediation of a uranium-contaminated waste effluent, J. Hazard. Mater. 178 (2010) 171-179.
[42] C. Jing, Y. Li, S. Landsberger, Review of soluble uranium removal by nanoscale zero valent iron, Journal of Environmental radioactivity 164 (2016) 65-72.
[43] R.A. Crane, T.B. Scott, The removal of uranium onto nanoscale zero-valent iron particles in anoxic batch systems, Journal of Nanomaterials 2014 (2014) 12.
[44] Y.-T. Wei, S.-C. Wu, C.-M. Chou, C.-H. Che, S.-M. Tsai, H.-L. Lien, Influence of nanoscale zero-valent iron on geochemical properties of groundwater and vinyl chloride degradation: A field case study, Water Res. 44 (2010) 131-140.

[45] D.W. Elliott, W.-X. Zhang, Field assessment of nanoscale bimetallic particles for groundwater treatment, Environ. Sci. Technol. 35 (2001) 4922-4926.
[46] N.C. Mueller, J. Braun, J. Bruns, M. Černík, P. Rissing, D. Rickerby, B. Nowack, Application of nanoscale zero valent iron (NZVI) for groundwater remediation in Europe, Environmental Science and Pollution Research 19 (2012) 550-558.
[47] R. Araujo, A.C.M. Castro, J.S. Baptista, A. Fiuza, Nanosized iron based permeable reactive barriers for nitrate removal–Systematic review, Physics and Chemistry of the Earth, Parts A/B/C 94 (2016) 29-34.
[48] R.T. Wilkin, S.D. Acree, R.R. Ross, R.W. Puls, T.R. Lee, L.L. Woods, Fifteen-year assessment of a permeable reactive barrier for treatment of chromate and trichloroethylene in groundwater, Sci. Total Environ. 468 (2014) 186-194.
[49] A. Neumann, R. Kaegi, A. Voegelin, A. Hussam, A.K. Munir, S.J. Hug, Arsenic removal with composite iron matrix filters in Bangladesh: a field and laboratory study, Environ. Sci. Technol. 47 (2013) 4544-4554.
[50] S.-J. Liu, Z.-Y. Zhao, J. Li, J. Wang, Y. Qi, An anaerobic two-layer permeable reactive biobarrier for the remediation of nitrate-contaminated groundwater, Water Res. 47 (2013) 5977-5985.
[51] A. Nel, T. Xia, L. Mädler, N. Li, Toxic potential of materials at the nanolevel, science 311 (2006) 622-627.
[52] Z.-m. Xiu, Z.-h. Jin, T.-l. Li, S. Mahendra, G.V. Lowry, P.J. Alvarez, Effects of nano-scale zero-valent iron particles on a mixed culture dechlorinating trichloroethylene, Bioresour. Technol. 101 (2010) 1141-1146.
[53] P.-J. Chen, C.-H. Su, C.-Y. Tseng, S.-W. Tan, C.-H. Cheng, Toxicity assessments of nanoscale zerovalent iron and its oxidation products in medaka (Oryzias latipes) fish, Marine pollution bulletin 63 (2011) 339-346.
[54] Y.S. El-Temsah, E.J. Joner, Effects of nano-sized zero-valent iron (nZVI) on DDT degradation in soil and its toxicity to collembola and ostracods, Chemosphere 92 (2013) 131-137.
[55] Y.S. El-Temsah, E.J. Joner, Ecotoxicological effects on earthworms of fresh and aged nano-sized zero-valent iron (nZVI) in soil, Chemosphere 89 (2012) 76-82.
[56] Y.S. El-Temsah, E.J. Joner, Impact of Fe and Ag nanoparticles on seed germination and differences in bioavailability during exposure in aqueous suspension and soil, Environmental toxicology 27 (2012) 42-49.
[57] X. Ma, A. Gurung, Y. Deng, Phytotoxicity and uptake of nanoscale zero-valent iron (nZVI) by two plant species, Sci. Total Environ. 443 (2013) 844-849.
[58] T. Phenrat, T.C. Long, G.V. Lowry, B. Veronesi, Partial oxidation ("aging") and surface modification decrease the toxicity of nanosized zerovalent iron, Environ. Sci. Technol. 43 (2008) 195-200.
[59] Z. Tong, M. Bischoff, L. Nies, B. Applegate, R.F. Turco, Impact of fullerene (C60) on a soil microbial community, Environ. Sci. Technol. 41 (2007) 2985-2991.

[60] J. Němeček, O. Lhotský, T. Cajthaml, Nanoscale zero-valent iron application for in situ reduction of hexavalent chromium and its effects on indigenous microorganism populations, Sci. Total Environ. 485 (2014) 739-747.
[61] A.M. Khalil, O. Eljamal, S. Jribi, N. Matsunaga, Promoting nitrate reduction kinetics by nanoscale zero valent iron in water via copper salt addition, Chem. Eng. J. 287 (2016) 367-380.
[62] R. Eljamal, O. Eljamal, A.M. Khalil, B.B. Saha, N. Matsunaga, Improvement of the chemical synthesis efficiency of nano-scale zero-valent iron particles, J. Environ. Chem. Eng. 6 (2018) 4727-4735.
[63] W. Wang, M. Zhou, Q. Mao, J. Yue, X. Wang, Novel NaY zeolite-supported nanoscale zero-valent iron as an efficient heterogeneous Fenton catalyst, Catal. Commun. 11 (2010) 937-941.
[64] R.A. Crane, M. Dickinson, T.B. Scott, Nanoscale zero-valent iron particles for the remediation of plutonium and uranium contaminated solutions, Chem. Eng. J. 262 (2015) 319-325.
[65] S.K. Sharma, R.C. Sobti, Nitrate removal from ground water: a review, J. Chem. 9 (2012) 1667-1675.
[66] S. Gandhi, B.-T. Oh, J.L. Schnoor, P.J. Alvarez, Degradation of TCE, Cr (VI), sulfate, and nitrate mixtures by granular iron in flow-through columns under different microbial conditions, Water Res. 36 (2002) 1973-1982.
[67] C. Ruangchainikom, C.-H. Liao, J. Anotai, M.-T. Lee, Effects of water characteristics on nitrate reduction by the Fe 0/CO 2 process, Chemosphere 63 (2006) 335-343.
[68] M. Biterna, A. Arditsoglou, E. Tsikouras, D. Voutsa, Arsenate removal by zero valent iron: batch and column tests, J. Hazard. Mater. 149 (2007) 548-552.
[69] E. Petala, K. Dimos, A. Douvalis, T. Bakas, J. Tucek, R. Zbořil, M.A. Karakassides, Nanoscale zero-valent iron supported on mesoporous silica: characterization and reactivity for Cr (VI) removal from aqueous solution, J. Hazard. Mater. 261 (2013) 295-306.
[70] A.M. Azzam, S.T. El-Wakeel, B.B. Mostafa, M. El-Shahat, Removal of Pb, Cd, Cu and Ni from aqueous solution using nano scale zero valent iron particles, J. Environ. Chem. Eng. 4 (2016) 2196-2206.
[71] H. Pullin, R. Crane, D. Morgan, T. Scott, The effect of common groundwater anions on the aqueous corrosion of zero-valent iron nanoparticles and associated removal of aqueous copper and zinc, J. Environ. Chem. Eng. 5 (2017) 1166-1173.
[72] O. Eljamal, A.M. Khalil, Y. Sugihara, N. Matsunaga, Phosphorus removal from aqueous solution by nanoscale zero valent iron in the presence of copper chloride, Chem. Eng. J. 293 (2016) 225-231.
[73] A.M. Khalil, O. Eljamal, T.W. Amen, Y. Sugihara, N. Matsunaga, Optimized nano-scale zero-valent iron supported on treated activated carbon for enhanced nitrate and phosphate removal from water, Chem. Eng. J. 309 (2017) 349-365.

[74] L. Hu, C. Zhang, G. Zeng, G. Chen, J. Wan, Z. Guo, H. Wu, Z. Yu, Y. Zhou, J. Liu, Metal-based quantum dots: synthesis, surface modification, transport and fate in aquatic environments and toxicity to microorganisms, RSC Advances 6 (2016) 78595-78610.
[75] G. Zeng, J. Wan, D. Huang, L. Hu, C. Huang, M. Cheng, W. Xue, X. Gong, R. Wang, D. Jiang, Precipitation, adsorption and rhizosphere effect: The mechanisms for Phosphate-induced Pb immobilization in soils—A review, J. Hazard. Mater. 339 (2017) 354-367.
[76] Q. Huang, W. Liu, P.a. Peng, W. Huang, Reductive dechlorination of tetrachlorobisphenol A by Pd/Fe bimetallic catalysts, J. Hazard. Mater. 262 (2013) 634-641.
[77] H. Choi, S.R. Al-Abed, S. Agarwal, Effects of aging and oxidation of palladized iron embedded in activated carbon on the dechlorination of 2-chlorobiphenyl, Environ. Sci. Technol. 43 (2009) 4137-4142.
[78] P.G. Tratnyek, M.M. Scherer, T.L. Johnson, L.J. Matheson, Permeable reactive barriers of iron and other zero-valent metals, Environ. Sci. Pollut. control Ser. (2003) 371-422.
[79] P.G. Tratnyek, R.L. Johnson, Nanotechnologies for environmental cleanup, Nano today 1 (2006) 44-48.
[80] G. Huang, Y. Huang, H. Hu, F. Liu, Y. Zhang, R. Deng, Remediation of nitrate–nitrogen contaminated groundwater using a pilot-scale two-layer heterotrophic–autotrophic denitrification permeable reactive barrier with spongy iron/pine bark, Chemosphere 130 (2015) 8-16.
[81] C. Tang, Z. Zhang, X. Sun, Effect of common ions on nitrate removal by zero-valent iron from alkaline soil, J. Hazard. Mater. 231 (2012) 114-119.
[82] M.R.F. Tehrani, M. Vossoughi, A. Shamsai, In-situ nitrate remediation using nano iron/nickel particles, Environ. Prot. Eng. 40 (2014) 75--86.
[83] Y.H. Huang, T.C. Zhang, Enhancement of nitrate reduction in Fe 0-packed columns by selected cations, J. Environ. Eng. 131 (2005) 603-611.
[84] J.-Y. Jeong, H.-K. Kim, J.-H. Kim, J.-Y. Park, Electrochemical removal of nitrate using ZVI packed bed bipolar electrolytic cell, Chemosphere 89 (2012) 172-178.
[85] S.M. Hosseini, T. Tosco, Integrating NZVI and carbon substrates in a non-pumping reactive wells array for the remediation of a nitrate contaminated aquifer, J. Contam. Hydrol. 179 (2015) 182-195.
[86] R. Araújo, A.C.M. Castro, J.S. Baptista, A. Fiúza, Nanosized iron based permeable reactive barriers for nitrate removal–Systematic review, Physics and Chemistry of the Earth, Parts A/B/C 94 (2016) 29-34.
[87] Y.H. Liou, S.-L. Lo, W.H. Kuan, C.-J. Lin, S.C. Weng, Effect of precursor concentration on the characteristics of nanoscale zerovalent iron and its reactivity of nitrate, Water Res. 40 (2006) 2485-2492.
[88] G.C. Yang, H.-L. Lee, Chemical reduction of nitrate by nanosized iron: kinetics and pathways, Water Res. 39 (2005) 884-894.

[89] Y.H. Liou, S.-L. Lo, C.-J. Lin, W.H. Kuan, S.C. Weng, Chemical reduction of an unbuffered nitrate solution using catalyzed and uncatalyzed nanoscale iron particles, J. Hazard. Mater. 127 (2005) 102-110.
[90] P. Westerhoff, J. James, Nitrate removal in zero-valent iron packed columns, Water Res. 37 (2003) 1818-1830.
[91] S.M. Hosseini, B. Ataie-Ashtiani, M. Kholghi, Nitrate reduction by nano-Fe/Cu particles in packed column, Desalination 276 (2011) 214-221.
[92] K.-Y. Lee, K.-W. Kim, M. Park, J. Kim, M. Oh, E.-H. Lee, D.-Y. Chung, J.-K. Moon, Novel application of nanozeolite for radioactive cesium removal from high-salt wastewater, Water Res. 95 (2016) 134-141.
[93] G.-R. Chen, Y.-R. Chang, X. Liu, T. Kawamoto, H. Tanaka, D. Parajuli, M.-L. Chen, Y.-K. Lo, Z. Lei, D.-J. Lee, Prussian blue non-woven filter for cesium removal from drinking water, Sep. Purif. Technol. 153 (2015) 37-42.
[94] D. Cuc, S. Bouguet-Bonnet, N. Morel-Desrosiers, J.-P. Morel, P. Mutzenhardt, D. Canet, Behavior of cesium and thallium cations inside a calixarene cavity as probed by nuclear spin relaxation. evidence of cation− π interactions in water, J. Phys. Chem. B 113 (2009) 10800-10807.
[95] S. Bayülken, E. Başçetin, K. Güçlü, R. Apak, Investigation and modeling of cesium (I) adsorption by Turkish clays: bentonite, zeolite, sepiolite, and kaolinite, Environ. Prog. Sustain. Energy 30 (2011) 70-80.
[96] A. Dyer, N. James, N. Terrill, Uptake of cesium and strontium radioisotopes onto pillared clays, J. Radioanal. Nucl. Chem. 240 (1999) 589-592.
[97] J.-O. Kim, S.-M. Lee, C. Jeon, Adsorption characteristics of sericite for cesium ions from an aqueous solution, Chem. Eng. Res. Des. 92 (2014) 368-374.
[98] S. Gaur, Determination of Cs-137 in environmental water by ion-exchange chromatography, J. Chromatogr. A 733 (1996) 57-71.
[99] Q. He, Y. Tian, Y. Cui, H. Möhwald, J. Li, Layer-by-layer assembly of magnetic polypeptide nanotubes as a DNA carrier, J. Mater. Chem. 18 (2008) 748-754.
[100] T. Shubair, O. Eljamal, A.M. Khalil, N. Matsunaga, Multilayer system of nanoscale zero valent iron and Nano-Fe/Cu particles for nitrate removal in porous media, Sep. Purif. Technol. (2017).
[101] S.C. Tang, I.M. Lo, Magnetic nanoparticles: essential factors for sustainable environmental applications, Water Res. 47 (2013) 2613-2632.
[102] O.A. Moamen, H. Ibrahim, N. Abdelmonem, I. Ismail, Thermodynamic analysis for the sorptive removal of cesium and strontium ions onto synthesized magnetic nano zeolite, Microporous Mesoporous Mater. 223 (2016) 187-195.
[103] W. Yang, A.T. Kan, W. Chen, M.B. Tomson, pH-dependent effect of zinc on arsenic adsorption to magnetite nanoparticles, Water Res. 44 (2010) 5693-5701.
[104] J. Hu, G. Chen, I.M. Lo, Removal and recovery of Cr (VI) from wastewater by maghemite nanoparticles, Water Res. 39 (2005) 4528-4536.

[105] P. Tang, J. Shen, Z. Hu, G. Bai, M. Wang, B. Peng, R. Shen, W. Linghu, High-efficient scavenging of U (VI) by magnetic Fe 3 O 4@ gelatin composite, J. Mol. Liq. 221 (2016) 497-506.
[106] M.A. Farghali, T.A.S. El-Din, A.M. Al-Enizi, R.M. El Bahnasawy, Graphene/magnetite nanocomposite for potential environmental application, Int. J. Electrochem. Sci 10 (2015) 529-537.
[107] J.-f. Liu, Z.-s. Zhao, G.-b. Jiang, Coating Fe3O4 magnetic nanoparticles with humic acid for high efficient removal of heavy metals in water, Environ. Sci. Technol. 42 (2008) 6949-6954.
[108] K.S. Hwang, C.W. Park, K.-W. Lee, S.-J. Park, H.-M. Yang, Highly efficient removal of radioactive cesium by sodium-copper hexacyanoferrate-modified magnetic nanoparticles, Colloids Surf. A Physicochem. Eng. Asp. 516 (2017) 375-382.
[109] H.-M. Yang, S.-C. Jang, S.B. Hong, K.-W. Lee, C. Roh, Y.S. Huh, B.-K. Seo, Prussian blue-functionalized magnetic nanoclusters for the removal of radioactive cesium from water, J. Alloys Compd. 657 (2016) 387-393.
[110] H. Faghihian, M. Moayed, A. Firooz, M. Iravani, Evaluation of a new magnetic zeolite composite for removal of Cs+ and Sr 2+ from aqueous solutions: Kinetic, equilibrium and thermodynamic studies, C. R. Chim. 17 (2014) 108-117.
[111] Y. Liu, S.A. Majetich, R.D. Tilton, D.S. Sholl, G.V. Lowry, TCE dechlorination rates, pathways, and efficiency of nanoscale iron particles with different properties, Environ. Sci. Technol. 39 (2005) 1338-1345.
[112] W. Han, F. Fu, Z. Cheng, B. Tang, S. Wu, Studies on the optimum conditions using acid-washed zero-valent iron/aluminum mixtures in permeable reactive barriers for the removal of different heavy metal ions from wastewater, J. Hazard. Mater. 302 (2016) 437-446.
[113] Ç. Üzüm, T. Shahwan, A.E. Eroğlu, I. Lieberwirth, T.B. Scott, K.R. Hallam, Application of zero-valent iron nanoparticles for the removal of aqueous Co 2+ ions under various experimental conditions, Chem. Eng. J. 144 (2008) 213-220.
[114] T. Scott, I. Popescu, R. Crane, C. Noubactep, Nano-scale metallic iron for the treatment of solutions containing multiple inorganic contaminants, J. Hazard. Mater. 186 (2011) 280-287.
[115] X.-q. Li, W.-x. Zhang, Sequestration of metal cations with zerovalent iron nanoparticles a study with high resolution X-ray photoelectron spectroscopy (HR-XPS), J. Phys. Chem. C 111 (2007) 6939-6946.
[116] S. Klimkova, M. Cernik, L. Lacinova, J. Filip, D. Jancik, R. Zboril, Zero-valent iron nanoparticles in treatment of acid mine water from in situ uranium leaching, Chemosphere 82 (2011) 1178-1184.
[117] S. Simon, A. Courtin-Nomade, A. Vasiliu, N. Sleiman, V. Deluchat, Long-term influence of aeration on arsenic trapping in a ZVI/sand bed reactor, RSC Advances 6 (2016) 54479-54485.

[118] J. Wan, J. Pressigout, S. Simon, V. Deluchat, Distribution of As trapping along a ZVI/sand bed reactor, Chem. Eng. J. 246 (2014) 322-327.
[119] J.T. Olegario, N. Yee, M. Miller, J. Sczepaniak, B. Manning, Reduction of Se (VI) to Se (-II) by zerovalent iron nanoparticle suspensions, J. Nanopart. Res. 12 (2010) 2057-2068.
[120] O. Celebi, Ç. Üzüm, T. Shahwan, H.N. Erten, A radiotracer study of the adsorption behavior of aqueous Ba 2+ ions on nanoparticles of zero-valent iron, J. Hazard. Mater. 148 (2007) 761-767.
[121] M. Dickinson, T.B. Scott, The application of zero-valent iron nanoparticles for the remediation of a uranium-contaminated waste effluent, J. Hazard. Mater. 178 (2010) 171-179.
[122] J.G. Darab, A.B. Amonette, D.S. Burke, R.D. Orr, S.M. Ponder, B. Schrick, T.E. Mallouk, W.W. Lukens, D.L. Caulder, D.K. Shuh, Removal of pertechnetate from simulated nuclear waste streams using supported zerovalent iron, Chem. Mater. 19 (2007) 5703-5713.
[123] A. Tiraferri, R. Sethi, Enhanced transport of zerovalent iron nanoparticles in saturated porous media by guar gum, J. Nanopart. Res. 11 (2009) 635.
[124] F. He, D. Zhao, C. Paul, Field assessment of carboxymethyl cellulose stabilized iron nanoparticles for in situ destruction of chlorinated solvents in source zones, Water Res. 44 (2010) 2360-2370.
[125] F. He, D. Zhao, Preparation and characterization of a new class of starch-stabilized bimetallic nanoparticles for degradation of chlorinated hydrocarbons in water, Environ. Sci. Technol. 39 (2005) 3314-3320.
[126] X. Zhao, W. Liu, Z. Cai, B. Han, T. Qian, D. Zhao, An overview of preparation and applications of stabilized zero-valent iron nanoparticles for soil and groundwater remediation, Water Res. 100 (2016) 245-266.
[127] T.W. Amen, O. Eljamal, A.M. Khalil, N. Matsunaga, Wastewater degradation by iron/copper nanoparticles and the microorganism growth rate, Journal of Environmental Sciences (2018).
[128] Y. Zeng, H. Walker, Q. Zhu, Reduction of nitrate by NaY zeolite supported Fe, Cu/Fe and Mn/Fe nanoparticles, J. Hazard. Mater. 324 (2017) 605-616.
[129] K.S. Hwang, C.W. Park, K.-W. Lee, S.-J. Park, H.-M. Yang, Highly efficient removal of radioactive cesium by sodium-copper hexacyanoferrate-modified magnetic nanoparticles, Colloids and Surfaces A: Physicochemical and Engineering Aspects 516 (2017) 375-382.
[130] E. Borai, R. Harjula, A. Paajanen, Efficient removal of cesium from low-level radioactive liquid waste using natural and impregnated zeolite minerals, J. Hazard. Mater. 172 (2009) 416-422.
[131] B. Hu, F. Ye, C. Jin, X. Ma, C. Huang, G. Sheng, J. Ma, X. Wang, Y. Huang, The enhancement roles of layered double hydroxide on the reductive immobilization of selenate

by nanoscale zero valent iron: Macroscopic and microscopic approaches, Chemosphere (2017).
[132] T. Shahwan, H. Erten, Thermodynamic parameters of Cs+ sorption on natural clays, J. Radioanal. Nucl. Chem. 253 (2002) 115-120.
[133] Y.-S. Ho, G. McKay, Pseudo-second order model for sorption processes, Process Biochem. 34 (1999) 451-465.
[134] A. Sheikhhosseini, M. Shirvani, H. Shariatmadari, F. Zvomuya, B. Najafic, Kinetics and thermodynamics of nickel sorption to calcium–palygorskite and calcium–sepiolite: a batch study, Geoderma 217 (2014) 111-117.
[135] T. Shahwan, H.N. Erten, S. Unugur, A characterization study of some aspects of the adsorption of aqueous Co2+ ions on a natural bentonite clay, J. Colloid Interface Sci. 300 (2006) 447-452.
[136] P. Sylvester, T. Milner, J. Jensen, Radioactive liquid waste treatment at Fukushima Daiichi, J. Chem. Technol. Biotechnol. 88 (2013) 1592-1596.
[137] Y.-M. Hao, C. Man, Z.-B. Hu, Effective removal of Cu (II) ions from aqueous solution by amino-functionalized magnetic nanoparticles, J. Hazard. Mater. 184 (2010) 392-399.
[138] T.W. Amen, O. Eljamal, A.M. Khalil, N. Matsunaga, Biochemical methane potential enhancement of domestic sludge digestion by adding pristine iron nanoparticles and iron nanoparticles coated zeolite compositions, J. Environ. Chem. Eng. 5 (2017) 5002-5013.
[139] S. Naamen, N. Jâafar, H.B. Rhaiem, A.B.H. Amara, A. Plançon, F. Muller, XRD investigation of the intercalation of nacrite with cesium chloride, Clay Minerals 51 (2016) 29-38.
[140] J. Zhu, D. Li, H. Chen, X. Yang, L. Lu, X. Wang, Highly dispersed CuO nanoparticles prepared by a novel quick-precipitation method, Mater. Lett. 58 (2004) 3324-3327.
[141] T.M.D. Dang, T.T.T. Le, E. Fribourg-Blanc, M.C. Dang, The influence of solvents and surfactants on the preparation of copper nanoparticles by a chemical reduction method, Advances in Natural Sciences: Nanoscience and Nanotechnology 2 (2011) 025004.
[142] N. Jaafar, H.B. Rhaiem, A.B.H. Amara, Impact of low normality of cesium chloride (n= 0.3 N) on the electrical features of nacrite-[(CsCl) n] nanohybrid subjected to excitation of frequency under controlled temperature, Applied Clay Science 151 (2018) 157-163.
[143] N. Sleiman, V. Deluchat, M. Wazne, M. Mallet, A. Courtin-Nomade, V. Kazpard, M. Baudu, Phosphate removal from aqueous solution using ZVI/sand bed reactor: Behavior and mechanism, Water Res. 99 (2016) 56-65.
[144] A.K. Vipin, S. Ling, B. Fugetsu, Removal of Cs+ and Sr2+ from water using MWCNT reinforced Zeolite-A beads, Microporous Mesoporous Mater. 224 (2016) 84-88.
[145] A. El-Kamash, Evaluation of zeolite A for the sorptive removal of Cs+ and Sr2+ ions from aqueous solutions using batch and fixed bed column operations, J. Hazard. Mater. 151 (2008) 432-445.

[146] F. Ji, C. Li, B. Tang, J. Xu, G. Lu, P. Liu, Preparation of cellulose acetate/zeolite composite fiber and its adsorption behavior for heavy metal ions in aqueous solution, Chem. Eng. J. 209 (2012) 325-333.
[147] S. Bayülken, E. Başçetin, K. Güçlü, R. Apak, Investigation and modeling of cesium (I) adsorption by Turkish clays: bentonite, zeolite, sepiolite, and kaolinite, Environmental Progress & Sustainable Energy 30 (2011) 70-80.
[148] S. Wang, Y. Peng, Natural zeolites as effective adsorbents in water and wastewater treatment, Chem. Eng. J. 156 (2010) 11-24.
[149] E.I. Basaldella, P.G. Vázquez, F. Iucolano, D. Caputo, Chromium removal from water using LTA zeolites: Effect of pH, J. Colloid Interface Sci. 313 (2007) 574-578.
[150] V. Inglezakis, M. Fyrillas, M. Stylianou, Two-phase homogeneous diffusion model for the fixed bed sorption of heavy metals on natural zeolites, Microporous Mesoporous Mater. (2018).
[151] P. Tang, J. Shen, Z. Hu, G. Bai, M. Wang, B. Peng, R. Shen, W. Linghu, High-efficient scavenging of U (VI) by magnetic Fe3O4@ gelatin composite, J. Mol. Liq. 221 (2016) 497-506.
[152] D. Yamaguchi, K. Furukawa, M. Takasuga, K. Watanabe, A magnetic carbon sorbent for radioactive material from the Fukushima nuclear accident, Scientific reports 4 (2014) 6053.
[153] H. Faghihian, M. Moayed, A. Firooz, M. Iravani, Evaluation of a new magnetic zeolite composite for removal of Cs+ and Sr2+ from aqueous solutions: kinetic, equilibrium and thermodynamic studies, Comptes rendus chimie 17 (2014) 108-117.
[154] L.C. Oliveira, D.I. Petkowicz, A. Smaniotto, S.B. Pergher, Magnetic zeolites: a new adsorbent for removal of metallic contaminants from water, Water Res. 38 (2004) 3699-3704.
[155] H.-J. Hong, H.S. Jeong, B.-G. Kim, J. Hong, I.-S. Park, T. Ryu, K.-S. Chung, H. Kim, J. Ryu, Highly stable and magnetically separable alginate/Fe3O4 composite for the removal of strontium (Sr) from seawater, Chemosphere 165 (2016) 231-238.
[156] B. Hu, F. Ye, C. Jin, X. Ma, C. Huang, G. Sheng, J. Ma, X. Wang, Y. Huang, The enhancement roles of layered double hydroxide on the reductive immobilization of selenate by nanoscale zero valent iron: Macroscopic and microscopic approaches, Chemosphere 184 (2017) 408-416.
[157] M. Arafa, M. Alqedra, T. Shubair, Quantifying the Effect of Ammonium Nitrate Attack on Mechanical and Physical Properties of Cement Mortars, J. Sci. Res. Rep (2015) 137-145.
[158] T. Shubair, M. Arafa, M. Alqedra, Investigate the Mechanical and Durability Properties of Cement Mortars being Exposed to Ammonium Nitrate Solutions, Proc. Int. Exch. Innov. Conf. Eng. Sci. (IEICES) (2016) 15-18.

[159] T. Shubair, O. Eljamal, A. Khalil, N. Matsunaga, Nitrate Removal in Porous Media Using Nanoscale Zero Valent Iron: Column Experiment, Proc. Int. Exch. Innov. Conf. Eng. Sci. (IEICES) 3 (2017) 145-148.
[160] O. Celebi, Ç. Üzüm, T. Shahwan, H.N. Erten, A radiotracer study of the adsorption behavior of aqueous Ba2+ ions on nanoparticles of zero-valent iron, J. Hazard. Mater. 148 (2007) 761-767.
[161] T. Shubair, O. Eljamal, M. AhmedKhalil, A. Tahara, N. Matsunaga, Novel application of nanoscale zero valent iron and bimetallic nano-Fe/Cu particles for the treatment of cesium contaminated water, J. Environ. Chem. Eng. (2018).
[162] T. Shubair, O. Eljamal, N. Matsunaga, Evaluation of nanoscale zero valent iron particles for the removal of cesium from aqueous solutions, IOP Conference Series: Materials Science and Engineering, IOP Publishing, 2018, pp. 012104.
[163] I. Maamoun, O. Eljamal, T. Shubair, H. Noutsuka, B.B. Saha, N. Matsunaga, Integrating nano-scale zero valent iron (nZVI) in phosphorus removal from aqueous solution through porous media: packed-column experiment, Proc. Int. Exch. Innov. Conf. Eng. Sci. (IEICES) 3 (2017) 25–30.
[164] T. Shubair, O. Eljamal, N. Matsunaga, Nano-Fe/Cu particles for the remediation of cesium contaminated solutions, (2018).
[165] N. Arancibia-Miranda, S.E. Baltazar, A. García, D. Munoz-Lira, P. Sepúlveda, M.A. Rubio, D. Altbir, Nanoscale zero valent supported by zeolite and montmorillonite: template effect of the removal of lead ion from an aqueous solution, J. Hazard. Mater. 301 (2016) 371-380.
[166] S.A. Kim, S. Kamala-Kannan, K.-J. Lee, Y.-J. Park, P.J. Shea, W.-H. Lee, H.-M. Kim, B.-T. Oh, Removal of Pb (II) from aqueous solution by a zeolite–nanoscale zero-valent iron composite, Chem. Eng. J. 217 (2013) 54-60.
[167] Y. Zhang, Y. Li, J. Li, L. Hu, X. Zheng, Enhanced removal of nitrate by a novel composite: nanoscale zero valent iron supported on pillared clay, Chem. Eng. J. 171 (2011) 526-531.
[168] D. Sparis, C. Mystrioti, A. Xenidis, N. Papassiopi, Reduction of nitrate by copper-coated ZVI nanoparticles, Desalin. Water Treat. 51 (2013) 2926-2933.
[169] Y. Wu, Q. Yue, Y. Gao, Z. Ren, B. Gao, Performance of bimetallic nanoscale zero-valent iron particles for removal of oxytetracycline, Journal of Environmental Sciences (2017).
[170] H. Akaike, A new look at the statistical model identification, IEEE transactions on automatic control 19 (1974) 716-723.
[171] M.I. El-Khaiary, G.F. Malash, Common data analysis errors in batch adsorption studies, Hydrometallurgy 105 (2011) 314-320.
[172] H.K. Boparai, M. Joseph, D.M. O'Carroll, Kinetics and thermodynamics of cadmium ion removal by adsorption onto nano zerovalent iron particles, J. Hazard. Mater. 186 (2011) 458-465.

[173] K.G. Scheckel, D.L. Sparks, Temperature effects on nickel sorption kinetics at the mineral–water interface, Soil Science Society of America Journal 65 (2001) 719-728.
[174] A. Ahmadpour, M. Zabihi, M. Tahmasbi, T.R. Bastami, Effect of adsorbents and chemical treatments on the removal of strontium from aqueous solutions, J. Hazard. Mater. 182 (2010) 552-556.
[175] X. Zhang, S. Lin, Z. Chen, M. Megharaj, R. Naidu, Kaolinite-supported nanoscale zero-valent iron for removal of Pb2+ from aqueous solution: reactivity, characterization and mechanism, Water Res. 45 (2011) 3481-3488.
[176] K.-Y. Lee, M. Park, J. Kim, M. Oh, E.-H. Lee, K.-W. Kim, D.-Y. Chung, J.-K. Moon, Equilibrium, kinetic and thermodynamic study of cesium adsorption onto nanocrystalline mordenite from high-salt solution, Chemosphere 150 (2016) 765-771.
[177] M.M. Hamed, M. Aly, A. Nayl, Kinetics and thermodynamics studies of cobalt, strontium and caesium sorption on marble from aqueous solution, Chemistry and Ecology 32 (2016) 68-87.
[178] B. Ma, S. Oh, W.S. Shin, S.-J. Choi, Removal of Co2+, Sr2+ and Cs+ from aqueous solution by phosphate-modified montmorillonite (PMM), Desalination 276 (2011) 336-346.
[179] I. Smičiklas, S. Dimović, I. Plećaš, Removal of Cs1+, Sr2+ and Co2+ from aqueous solutions by adsorption on natural clinoptilolite, Applied Clay Science 35 (2007) 139-144.
[180] T. Sasaki, S. Tanaka, Magnetic separation of cesium ion using Prussian blue modified magnetite, Chem. Lett. 41 (2011) 32-34.
[181] R. Sheha, E. Metwally, Equilibrium isotherm modeling of cesium adsorption onto magnetic materials, J. Hazard. Mater. 143 (2007) 354-361.
[182] Y.-W. Chen, J.-L. Wang, Removal of cesium from radioactive wastewater using magnetic chitosan beads cross-linked with glutaraldehyde, Nuclear Science and Techniques 27 (2016) 43.
[183] H. Yang, L. Sun, J. Zhai, H. Li, Y. Zhao, H. Yu, In situ controllable synthesis of magnetic Prussian blue/graphene oxide nanocomposites for removal of radioactive cesium in water, Journal of Materials Chemistry A 2 (2014) 326-332.
[184] Y. Lin, G.E. Fryxell, H. Wu, M. Engelhard, Selective sorption of cesium using self-assembled monolayers on mesoporous supports, Environ. Sci. Technol. 35 (2001) 3962-3966.
[185] D.N. Thanh, P. Novák, J. Vejpravova, H.N. Vu, J. Lederer, T. Munshi, Removal of copper and nickel from water using nanocomposite of magnetic hydroxyapatite nanorods, J. Magn. Magn. Mater. 456 (2018) 451-460.
[186] S. Periyasamy, V. Gopalakannan, N. Viswanathan, Hydrothermal assisted magnetic nano-hydroxyapatite encapsulated alginate beads for efficient Cr (VI) uptake from water, J. Environ. Chem. Eng. 6 (2018) 1443-1454.
[187] H. Niu, D. Zhang, S. Zhang, X. Zhang, Z. Meng, Y. Cai, Humic acid coated Fe3O4 magnetic nanoparticles as highly efficient Fenton-like catalyst for complete mineralization of sulfathiazole, J. Hazard. Mater. 190 (2011) 559-565.

[188] S.S. Banerjee, D.-H. Chen, Fast removal of copper ions by gum arabic modified magnetic nano-adsorbent, J. Hazard. Mater. 147 (2007) 792-799.
[189] T. Shubair, O. Eljamal, A. Khalil, N. Matsunaga, Nitrate Removal in Porous Media Using Nanoscale Zero Valent Iron: Column Experiment, (2017).
[190] T. Shubair, M. Arafa, M. Alqedra, Investigate the Mechanical and Durability Properties of Cement Mortars being Exposed to Ammonium Nitrate Solutions, (2016).
[191] H. Zhu, Y. Jia, X. Wu, H. Wang, Removal of arsenic from water by supported nano zero-valent iron on activated carbon, J. Hazard. Mater. 172 (2009) 1591-1596.
[192] F. Zhu, L. Li, S. Ma, Z. Shang, Effect factors, kinetics and thermodynamics of remediation in the chromium contaminated soils by nanoscale zero valent Fe/Cu bimetallic particles, Chem. Eng. J. 302 (2016) 663-669.
[193] S.M. Ponder, J.G. Darab, J. Bucher, D. Caulder, I. Craig, L. Davis, N. Edelstein, W. Lukens, H. Nitsche, L. Rao, Surface chemistry and electrochemistry of supported zerovalent iron nanoparticles in the remediation of aqueous metal contaminants, Chem. Mater. 13 (2001) 479-486.
[194] O. Eljamal, T. Shubair, A. Tahara, Y. Sugihara, N. Matsunaga, Iron based nanoparticles-zeolite composites for the removal of cesium from aqueous solutions, J. Mol. Liq. (2018).
[195] Y. Sun, X. Wang, C. Ding, W. Cheng, C. Chen, T. Hayat, A. Alsaedi, J. Hu, X. Wang, Direct synthesis of bacteria-derived carbonaceous nanofibers as a highly efficient material for radionuclides elimination, ACS Sustainable Chemistry & Engineering 4 (2016) 4608-4616.
[196] H. Faghihian, M. Iravani, M. Moayed, M. Ghannadi-Maragheh, Preparation of a novel PAN–zeolite nanocomposite for removal of Cs+ and Sr2+ from aqueous solutions: Kinetic, equilibrium, and thermodynamic studies, Chem. Eng. J. 222 (2013) 41-48.
[197] B. Hu, Q. Hu, D. Xu, C. Chen, Macroscopic and microscopic investigation on adsorption of Sr (II) on sericite, J. Mol. Liq. 225 (2017) 563-568.
[198] C.-H. Liu, Y.-J. Shih, Y.-H. Huang, C.-P. Huang, Kinetic and thermodynamic studies for adsorptive removal of Sr2+ using waste iron oxide, Journal of the Taiwan Institute of Chemical Engineers 45 (2014) 914-920.
[199] K.G. Bhattacharyya, S.S. Gupta, Adsorption of Fe (III), Co (II) and Ni (II) on ZrO–kaolinite and ZrO–montmorillonite surfaces in aqueous medium, Colloids and surfaces A: Physicochemical and engineering aspects 317 (2008) 71-79.
[200] N. Viswanathan, S. Meenakshi, Role of metal ion incorporation in ion exchange resin on the selectivity of fluoride, J. Hazard. Mater. 162 (2009) 920-930.
[201] L. Dong, Z. Zhu, Y. Qiu, J. Zhao, Removal of lead from aqueous solution by hydroxyapatite/magnetite composite adsorbent, Chem. Eng. J. 165 (2010) 827-834.
[202] A. Günay, E. Arslankaya, I. Tosun, Lead removal from aqueous solution by natural and pretreated clinoptilolite: adsorption equilibrium and kinetics, J. Hazard. Mater. 146 (2007) 362-371.

[203] W.J. Weber, J.C. Morris, Equilibria and capacities for adsorption on carbon, Journal of the Sanitary Engineering Division 90 (1964) 79-108.
[204] S. Chegrouche, A. Mellah, M. Barkat, Removal of strontium from aqueous solutions by adsorption onto activated carbon: kinetic and thermodynamic studies, Desalination 235 (2009) 306-318.
[205] E. Kaçan, C. Kütahyalı, Adsorption of strontium from aqueous solution using activated carbon produced from textile sewage sludges, J. Anal. Appl. Pyrolysis 97 (2012) 149-157.
[206] G. Gürboğa, H. Tel, Preparation of TiO2–SiO2 mixed gel spheres for strontium adsorption, J. Hazard. Mater. 120 (2005) 135-142.
[207] L. Zhang, J. Wei, X. Zhao, F. Li, F. Jiang, Adsorption characteristics of strontium on synthesized antimony silicate, Chem. Eng. J. 277 (2015) 378-387.
[208] Z. Cheng, Z. Gao, W. Ma, Q. Sun, B. Wang, X. Wang, Preparation of magnetic Fe3O4 particles modified sawdust as the adsorbent to remove strontium ions, Chem. Eng. J. 209 (2012) 451-457.
[209] S.S. Metwally, I.M. Ahmed, H.E. Rizk, Modification of hydroxyapatite for removal of cesium and strontium ions from aqueous solution, J. Alloys Compd. 709 (2017) 438-444.
[210] E. Unuabonah, K. Adebowale, B. Olu-Owolabi, Kinetic and thermodynamic studies of the adsorption of lead (II) ions onto phosphate-modified kaolinite clay, J. Hazard. Mater. 144 (2007) 386-395.
[211] M.H. Alkhraisat, C. Rueda, E. López Cabarcos, Strontium ions substitution in brushite crystals: the role of strontium chloride, Journal of functional biomaterials 2 (2011) 31-38.

APPENDICES

AI. Multilayer System of nZVI and Fe/Cu Nanoparticles for Nitrate Removal in Porous Media

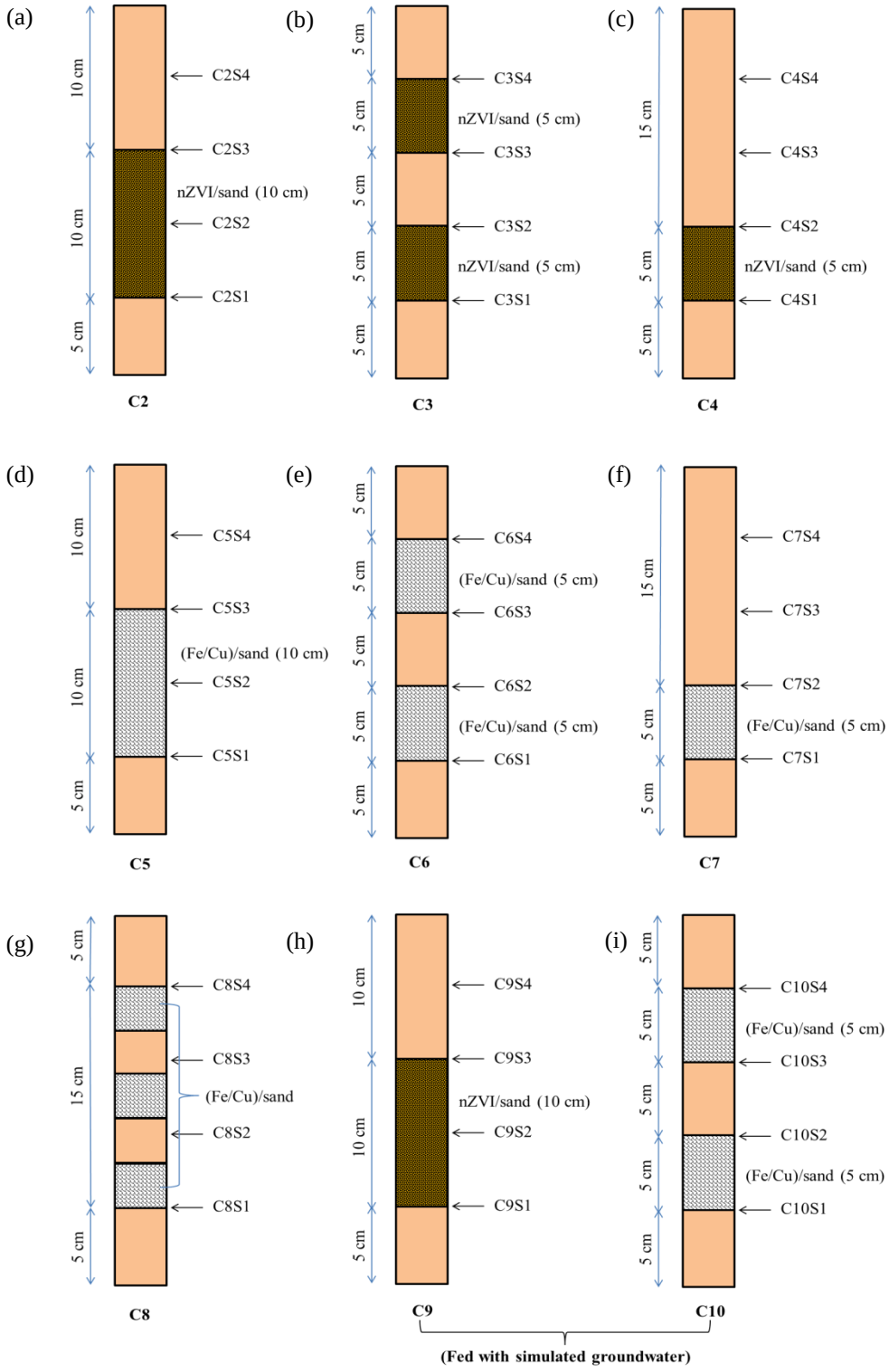

Fig. AI1. Schematic of the column experiments C2–C10 layers.

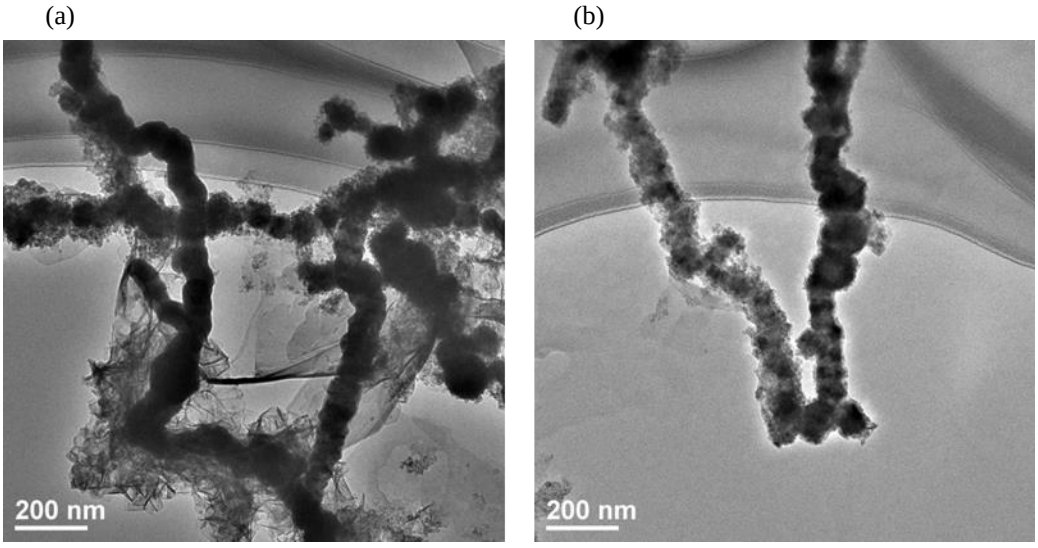

Fig. AI2. TEM images of synthesized (a) nZVI and (b) nano-Fe/Cu particles.

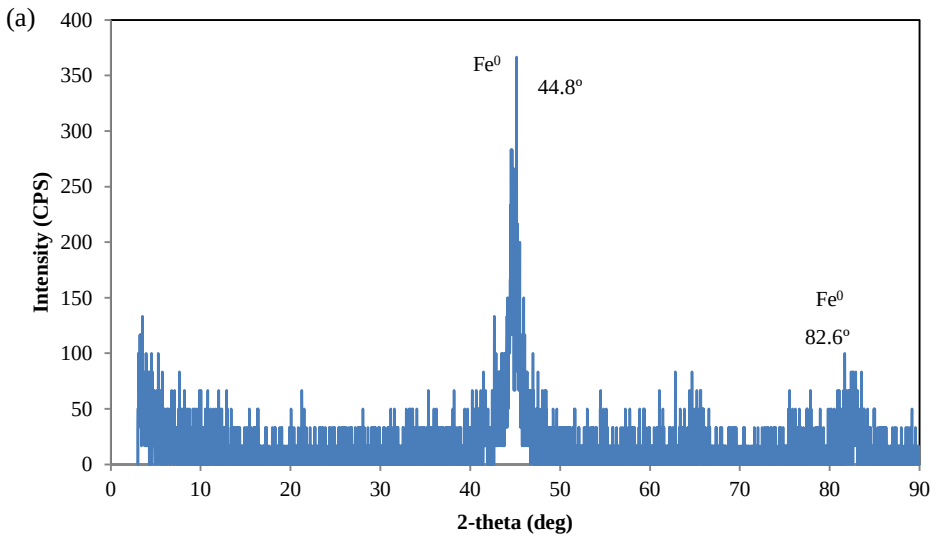

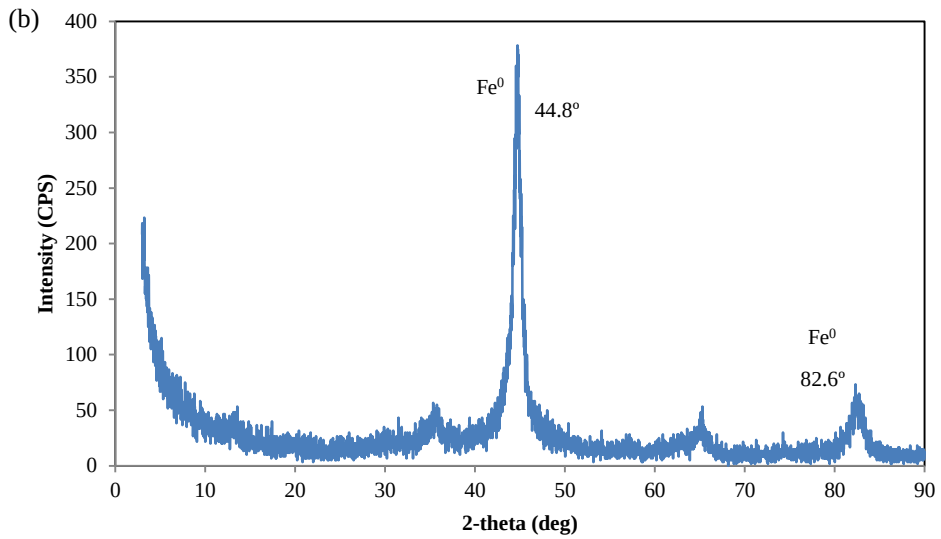

Fig. AI3. XRD patterns of synthesized (a) nZVI and (b) nano-Fe/Cu particles.

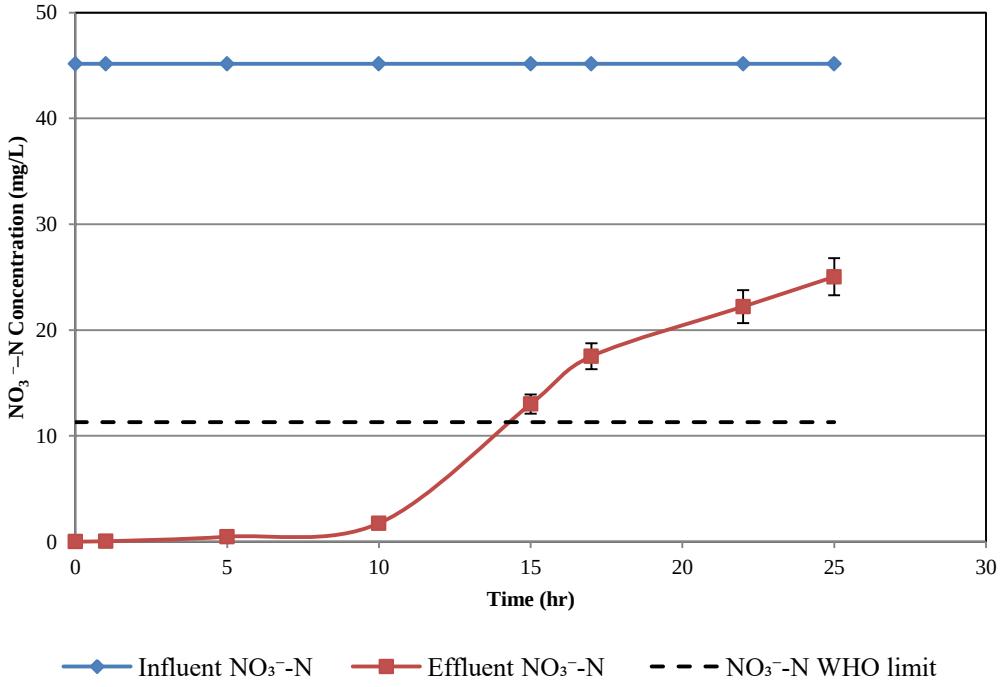

Fig. AI4. Changes in NO_3^-–N concentration over time in C8 with 3 layers of (nano-Fe/Cu)/sand.

(a)

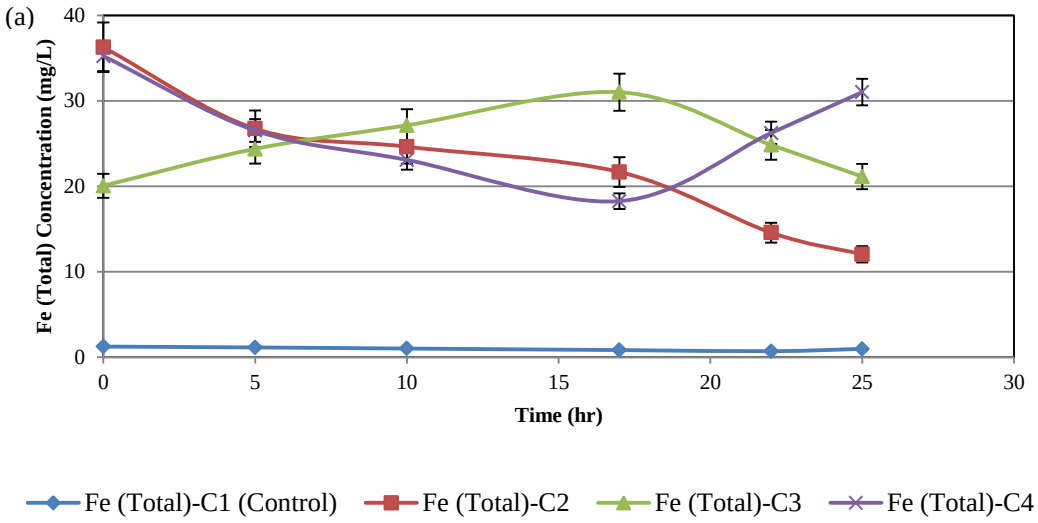
Fe (Total) Concentration (mg/L)
40
30
20
10
0
0
5
10
15
20
25
30
Time (hr)
Fe (Total)-C1 (Control)
Fe (Total)-C2
Fe (Total)-C3
Fe (Total)-C4

(b)

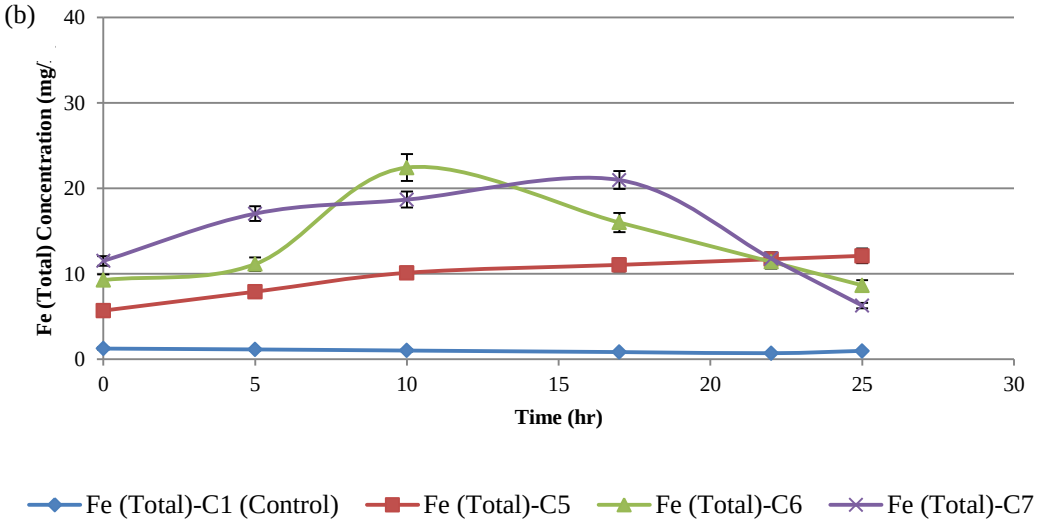
Fe (Total) Concentration (mg/
40
30
20
10
0
0
5
10
15
20
25
30
Time (hr)
Fe (Total)-C1 (Control)
Fe (Total)-C5
Fe (Total)-C6
Fe (Total)-C7

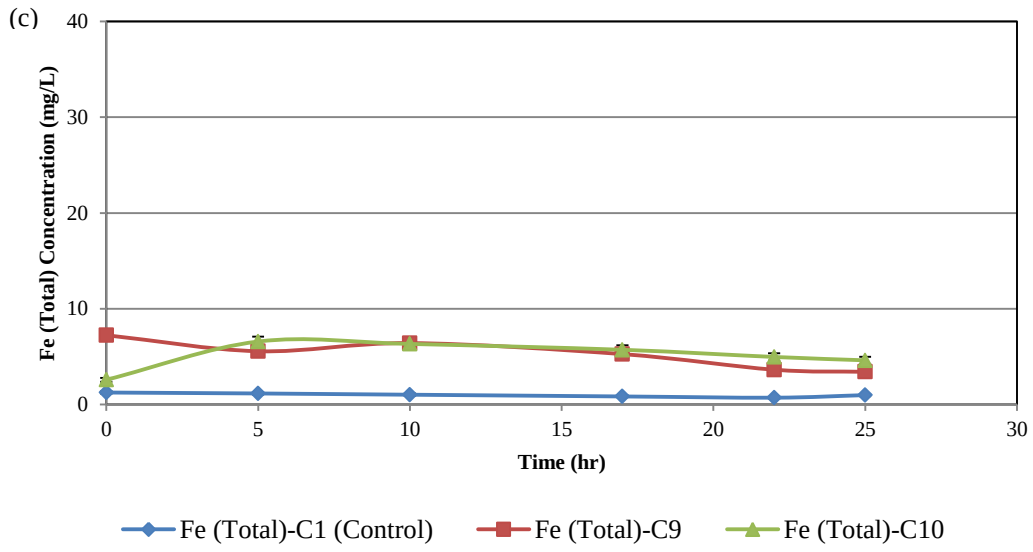

Fig. AI5. Changes in total Fe concentrations over time in (a) nZVI/sand columns (C2–C4), (b) (nano-Fe/Cu)/sand columns (C5–C7) and (c) when nitrate in simulated groundwater (C9–C10).

(a)

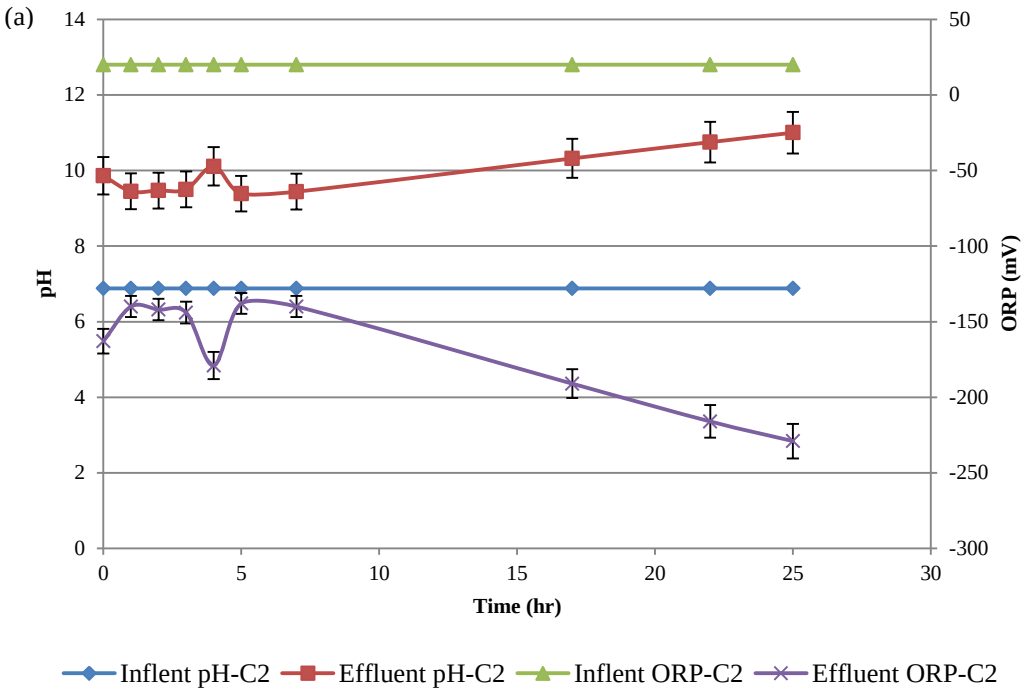
14
12
10
8
6
4
2
0
50
0
-50
-100
-150
-200
-250
-300
pH
ORP (mV)
0
5
10
15
20
25
30
Time (hr)
Inflent pH-C2
Effluent pH-C2
Inflent ORP-C2
Effluent ORP-C2

(b)

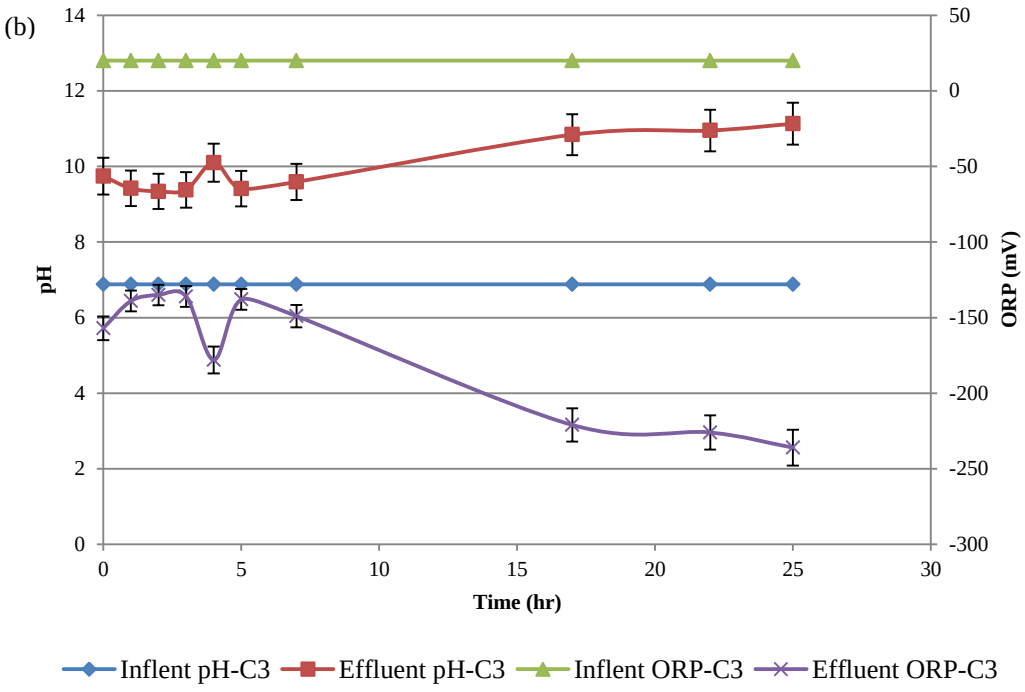
14
12
10
8
6
4
2
0
50
0
-50
-100
-150
-200
-250
-300
pH
ORP (mV)
0
5
10
15
20
25
30
Time (hr)
Inflent pH-C3
Effluent pH-C3
Inflent ORP-C3
Effluent ORP-C3

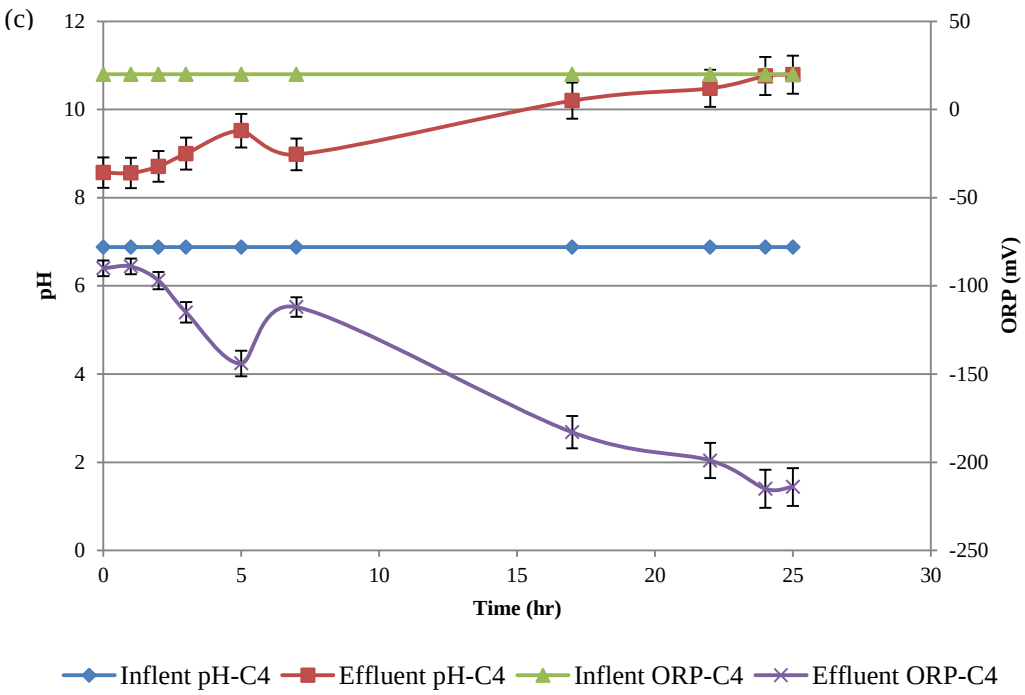

Fig. AI6. Changes in pH and ORP in nZVI/sand columns over time in (a) C2, (b) C3 and (c) C4.

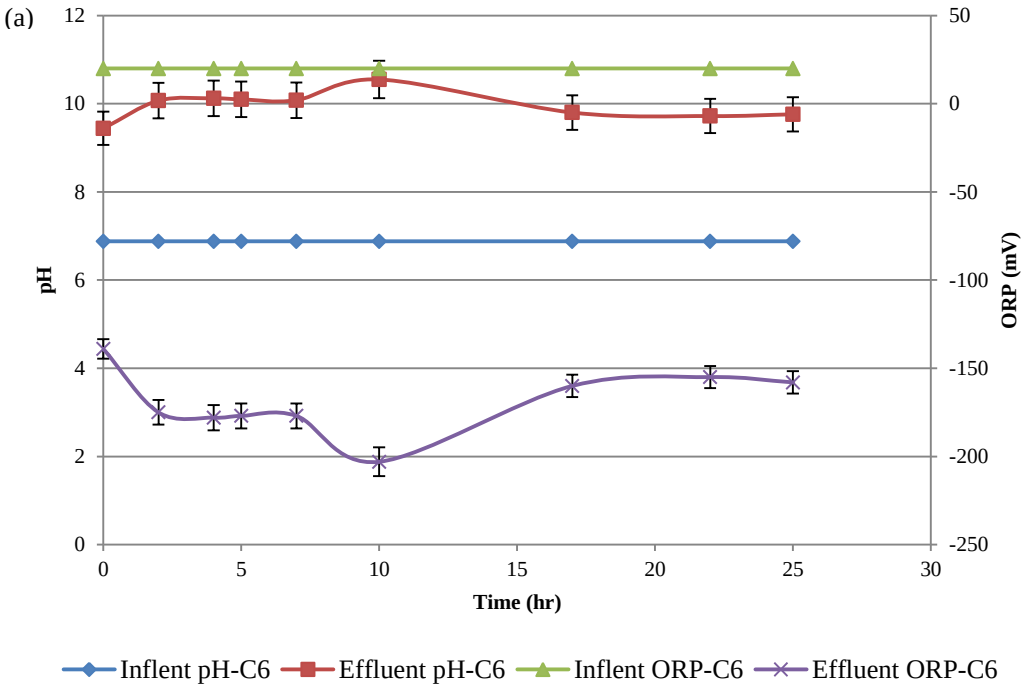

(b)

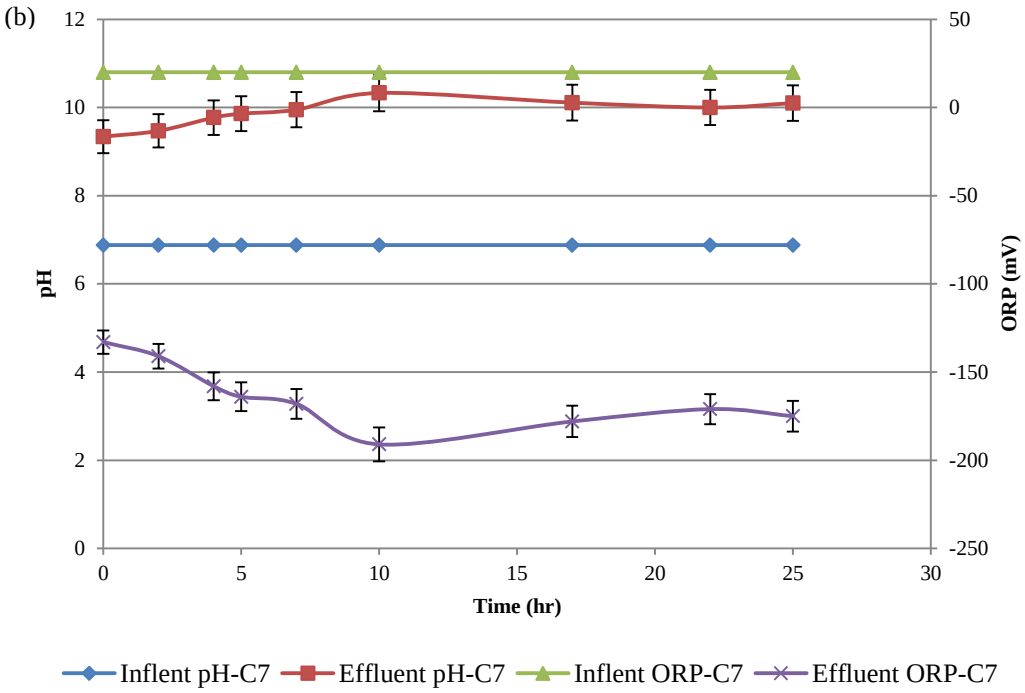
12
10
8
6
4
2
0
pH
50
0
-50
-100
-150
-200
-250
ORP (mV)
0
5
10
15
20
25
30
Time (hr)
Inflent pH-C7
Effluent pH-C7
Inflent ORP-C7
Effluent ORP-C7

(c)

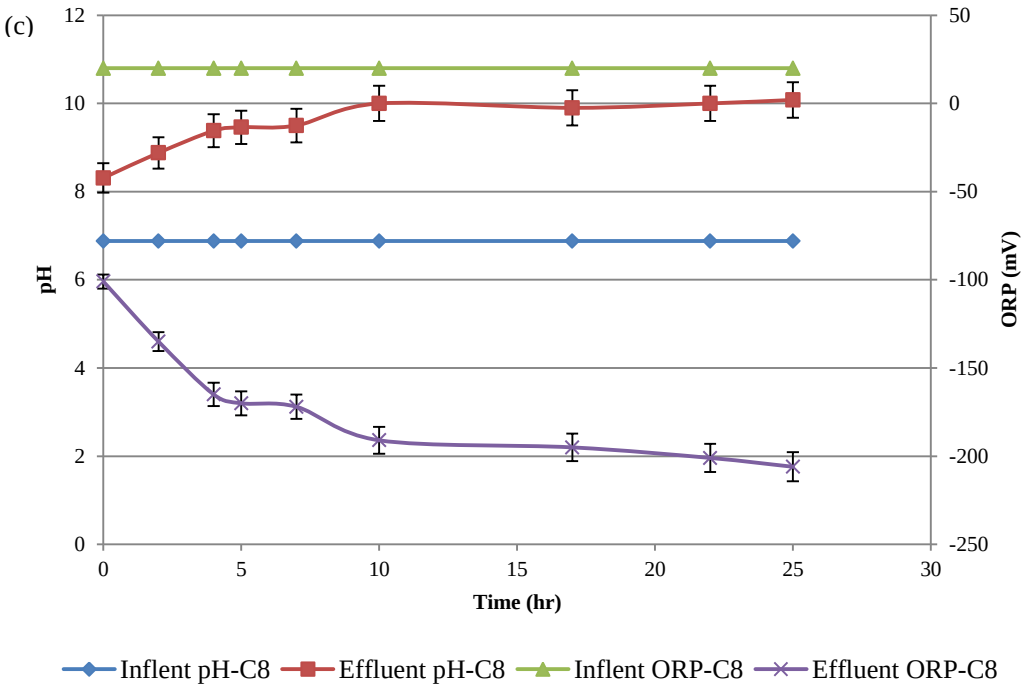
12
10
8
6
4
2
0
pH
50
0
-50
-100
-150
-200
-250
ORP (mV)
0
5
10
15
20
25
30
Time (hr)
Inflent pH-C8
Effluent pH-C8
Inflent ORP-C8
Effluent ORP-C8

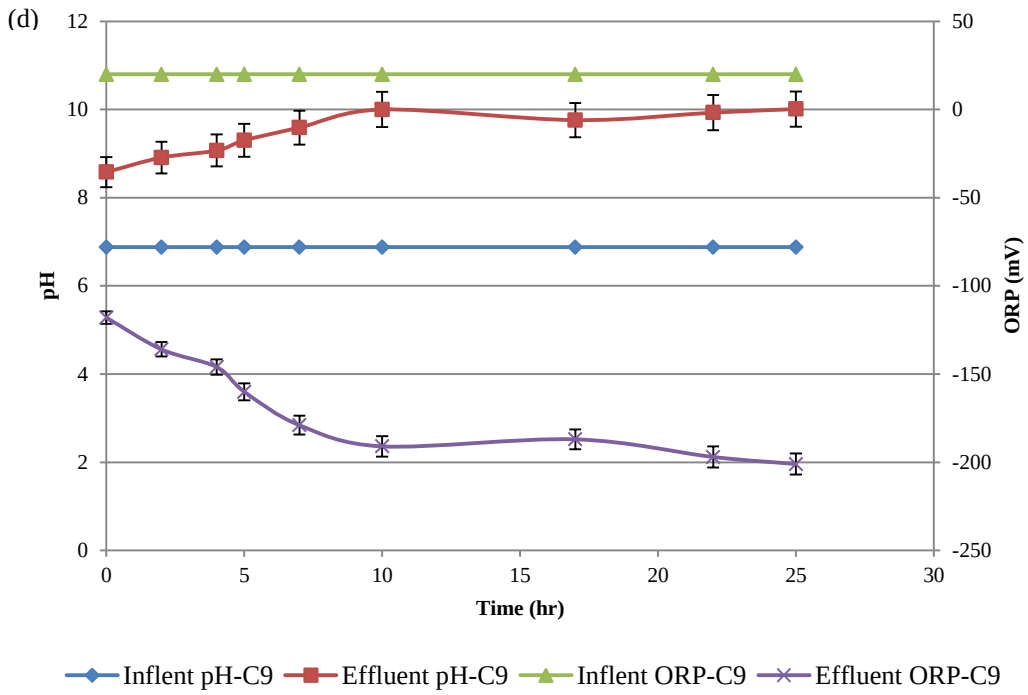

Fig. AI7. Changes in pH and ORP in nano-Fe/Cu/sand columns over time in (a) C5, (b) C6, (c) C7 and (d) C8.

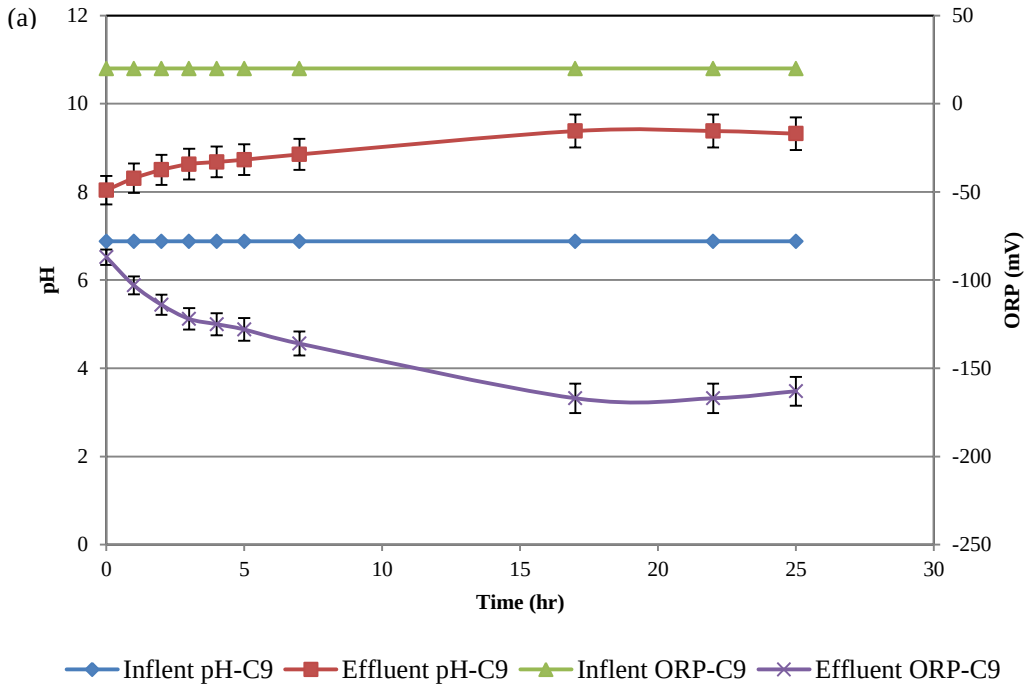

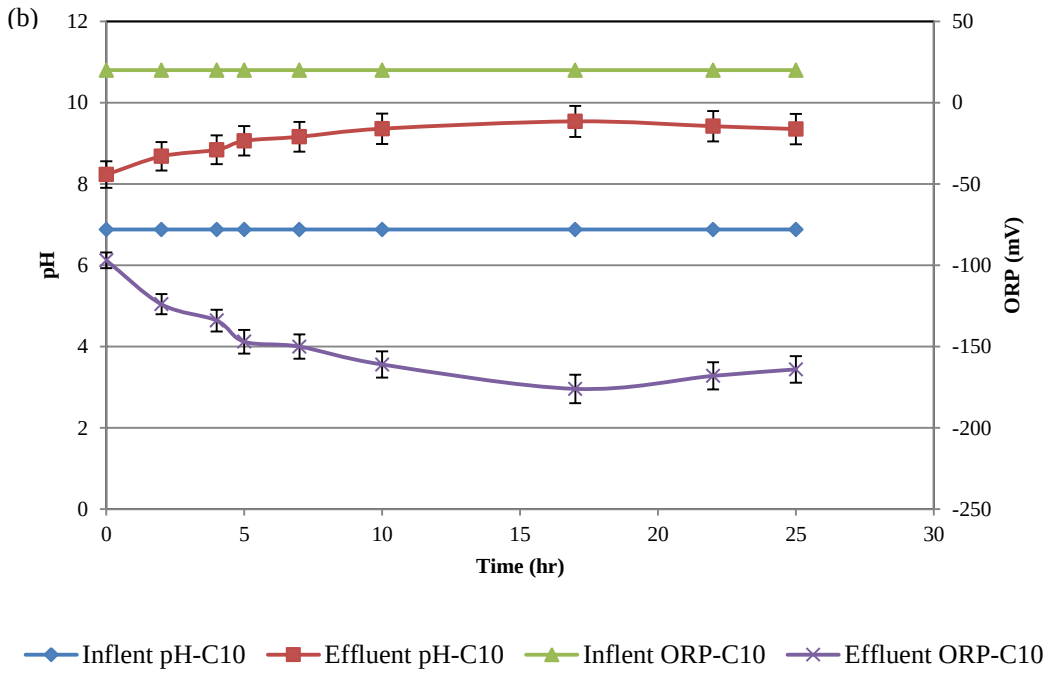

Fig. AI8. Changes in pH and ORP in (a) C9 and (b) C10 over time when nitrate in simulated groundwater.

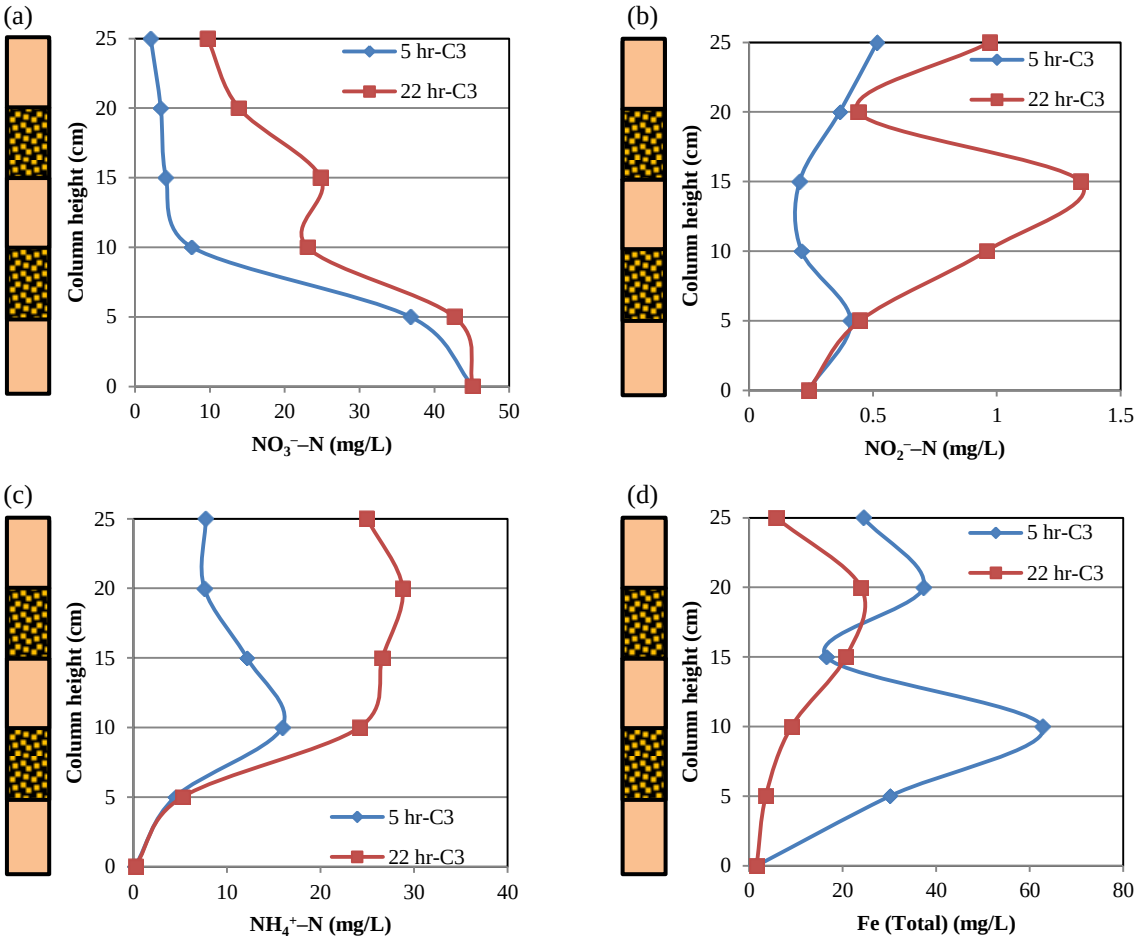

Fig. AI9. Sample profiles of NO_3^-–N, NO_2^-–N, NH_4^+–N and total Fe concentrations along C3 after 5 and 22 hr feeding with 45 mg NO_3^-–N /L.

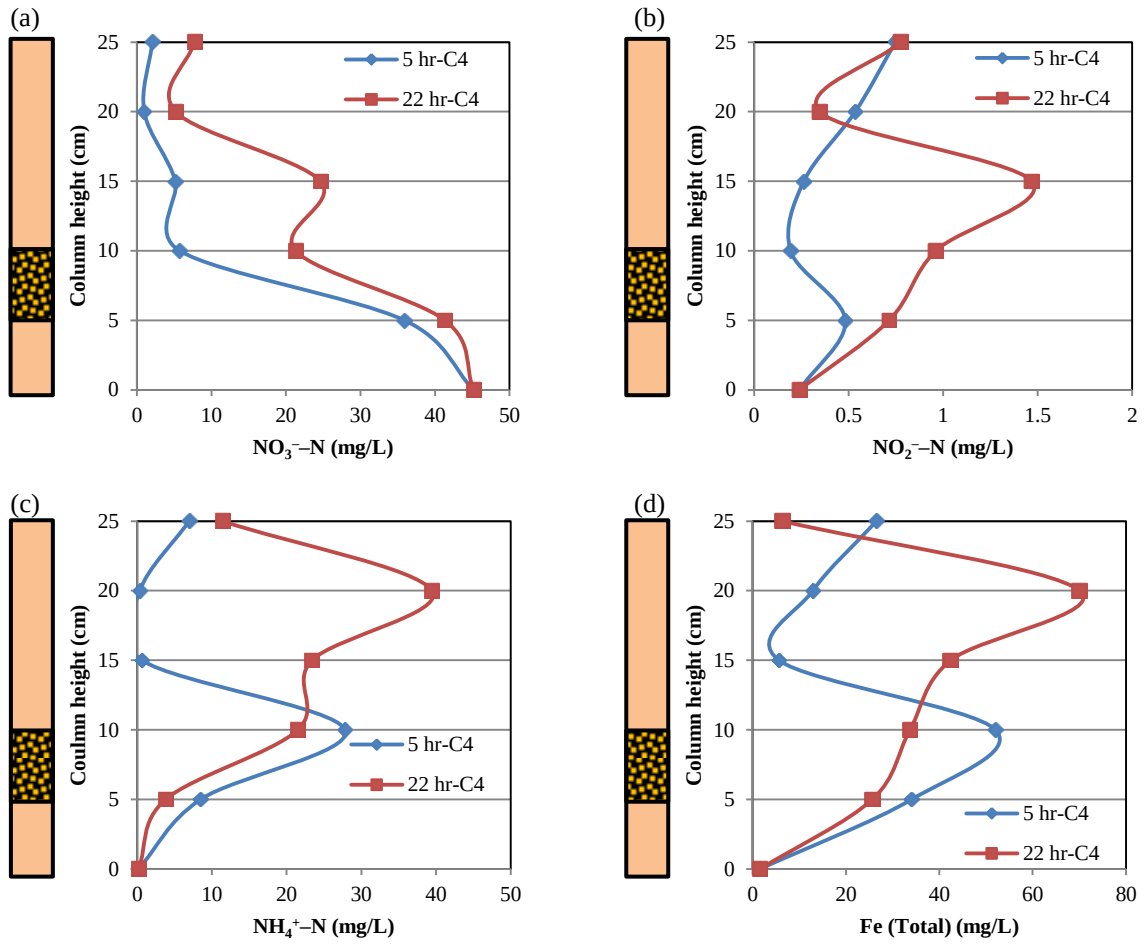

Fig. AI10. Sample profiles of NO_3^-–N, NO_2^-–N, NH_4^+–N and total Fe concentrations along C4 after 5 and 22 hr feeding with 45 mg NO_3^-–N /L.

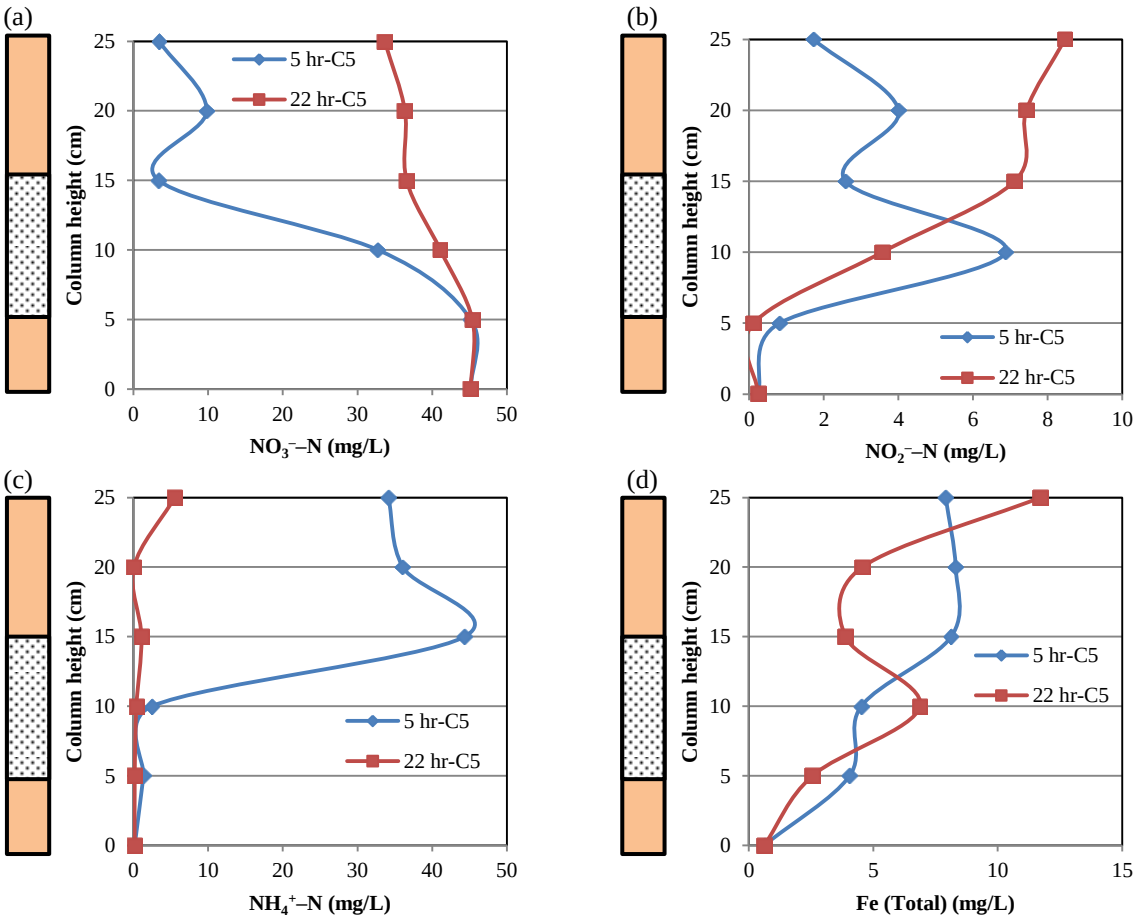

Fig. AI11. Sample profiles of NO_3^-–N, NO_2^-–N, NH_4^+–N and total Fe concentrations along C5 after 5 and 22 hr feeding with 45 mg NO_3^-–N /L.

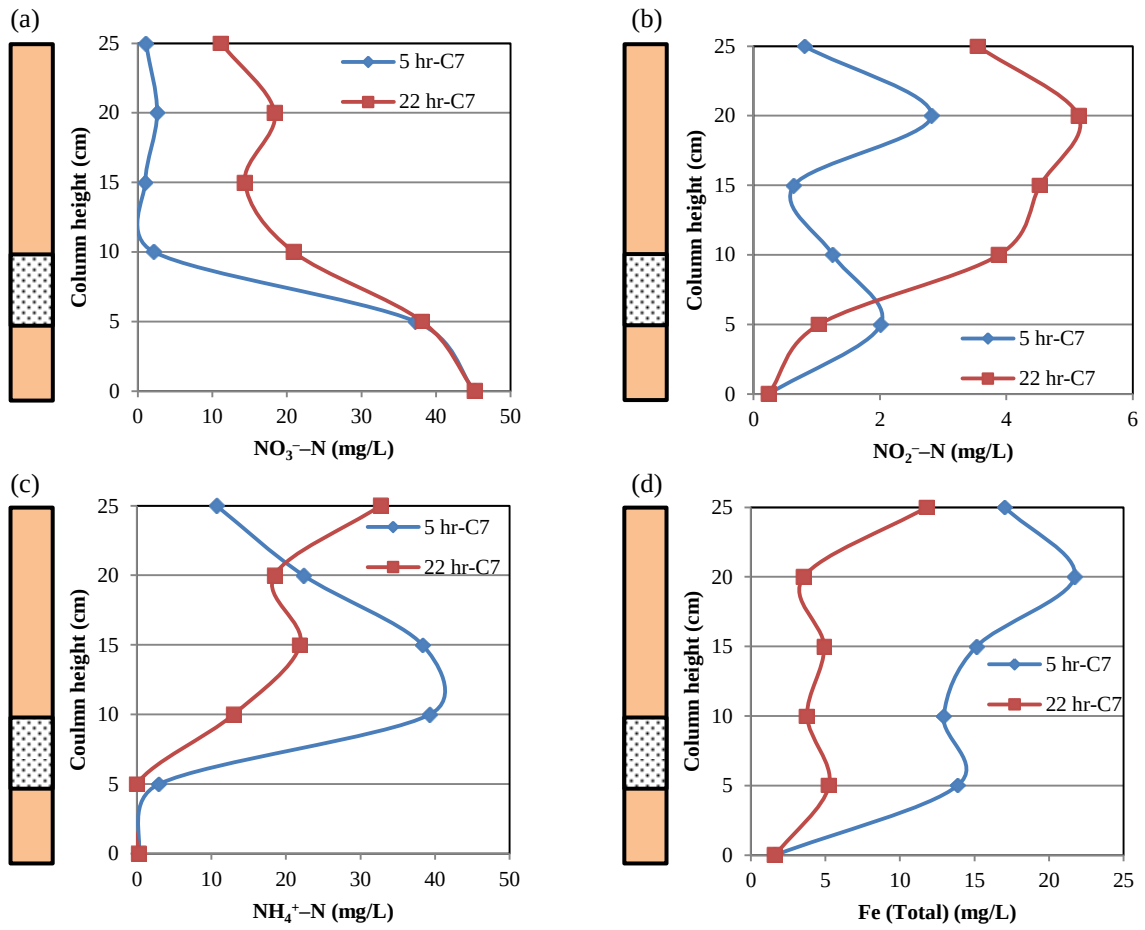

Fig. AI12. Sample profiles of NO_3^-–N, NO_2^-–N, NH_4^+–N and total Fe concentrations along C7 after 5 and 22 hr feeding with 45 mg NO_3^-–N /L.

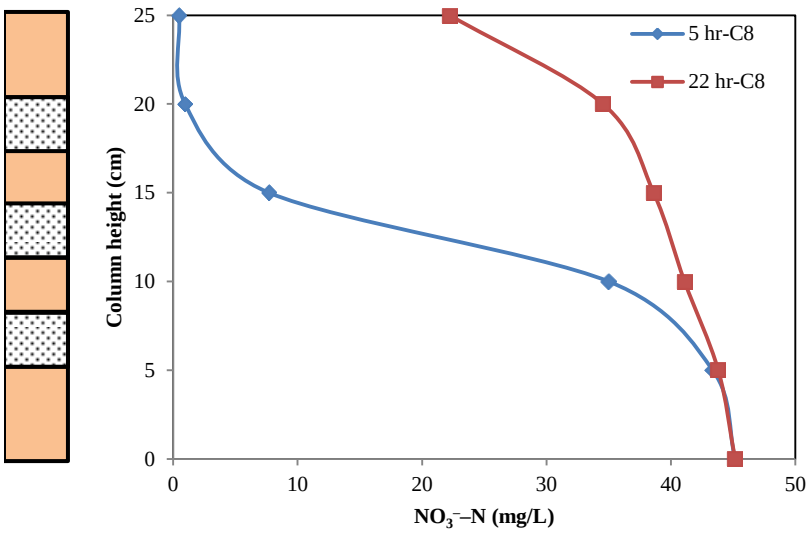

Fig. AI13. Sample profiles of NO_3^-–N concentration along C8 after 5 and 22 hr feeding with 45 mg NO_3^-–N /L.

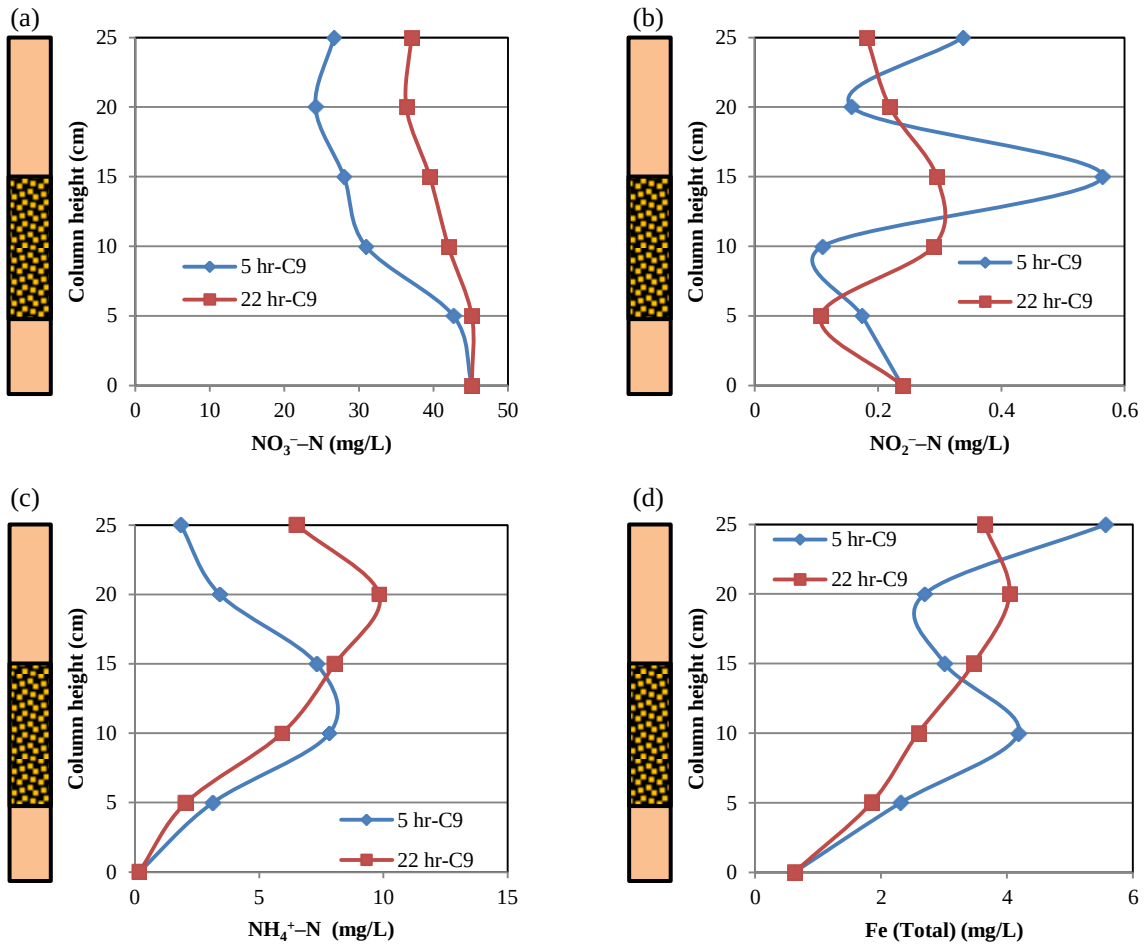

Fig. AI14. Sample profiles of NO_3^-–N, NO_2^-–N, NH_4^+–N and total Fe concentrations along C9 after 5 and 22 hr feeding with simulated groundwater containing 45 mg NO_3^-–N /L.

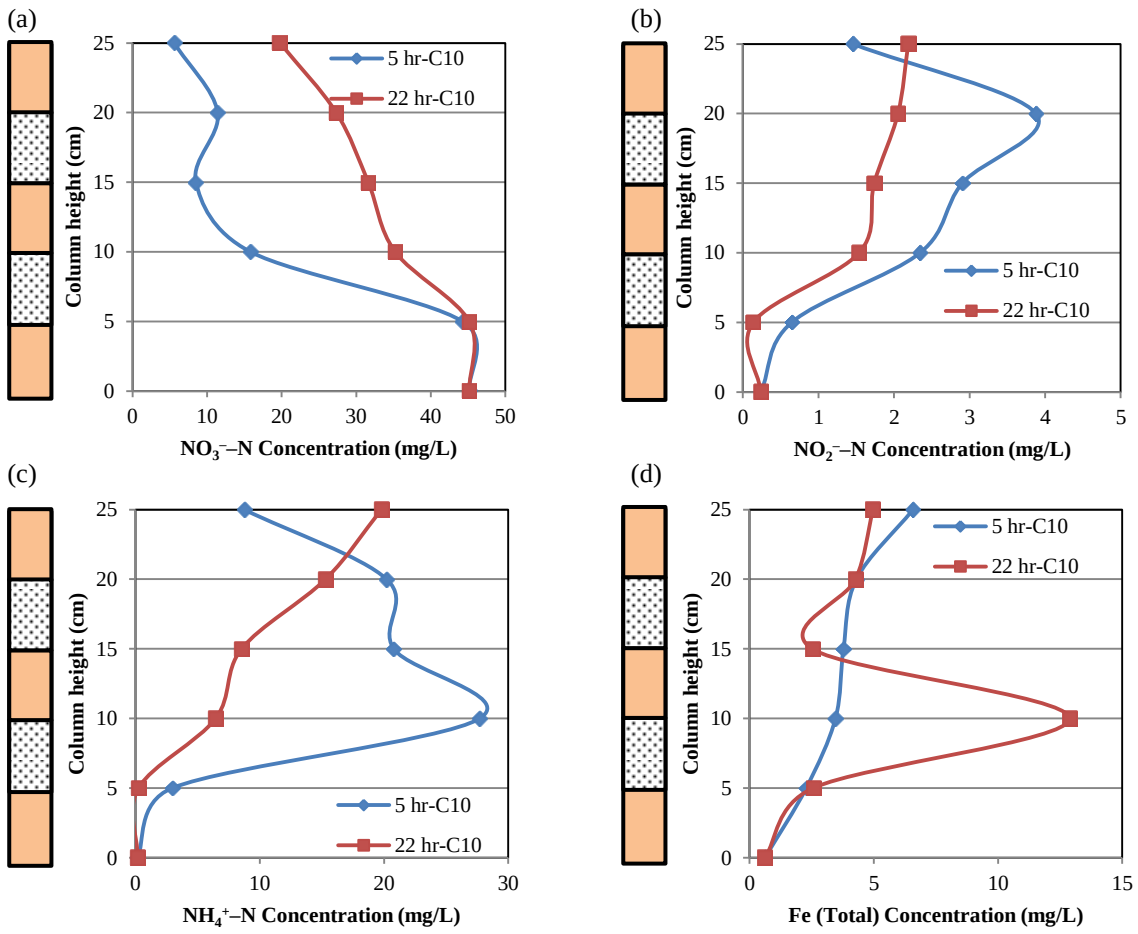

Fig. AI15. Sample profiles of NO_3^-–N, NO_2^-–N, NH_4^+–N and total Fe concentrations along C10 after 5 and 22 hr feeding with simulated groundwater containing 45 mg NO_3^-–N /L.

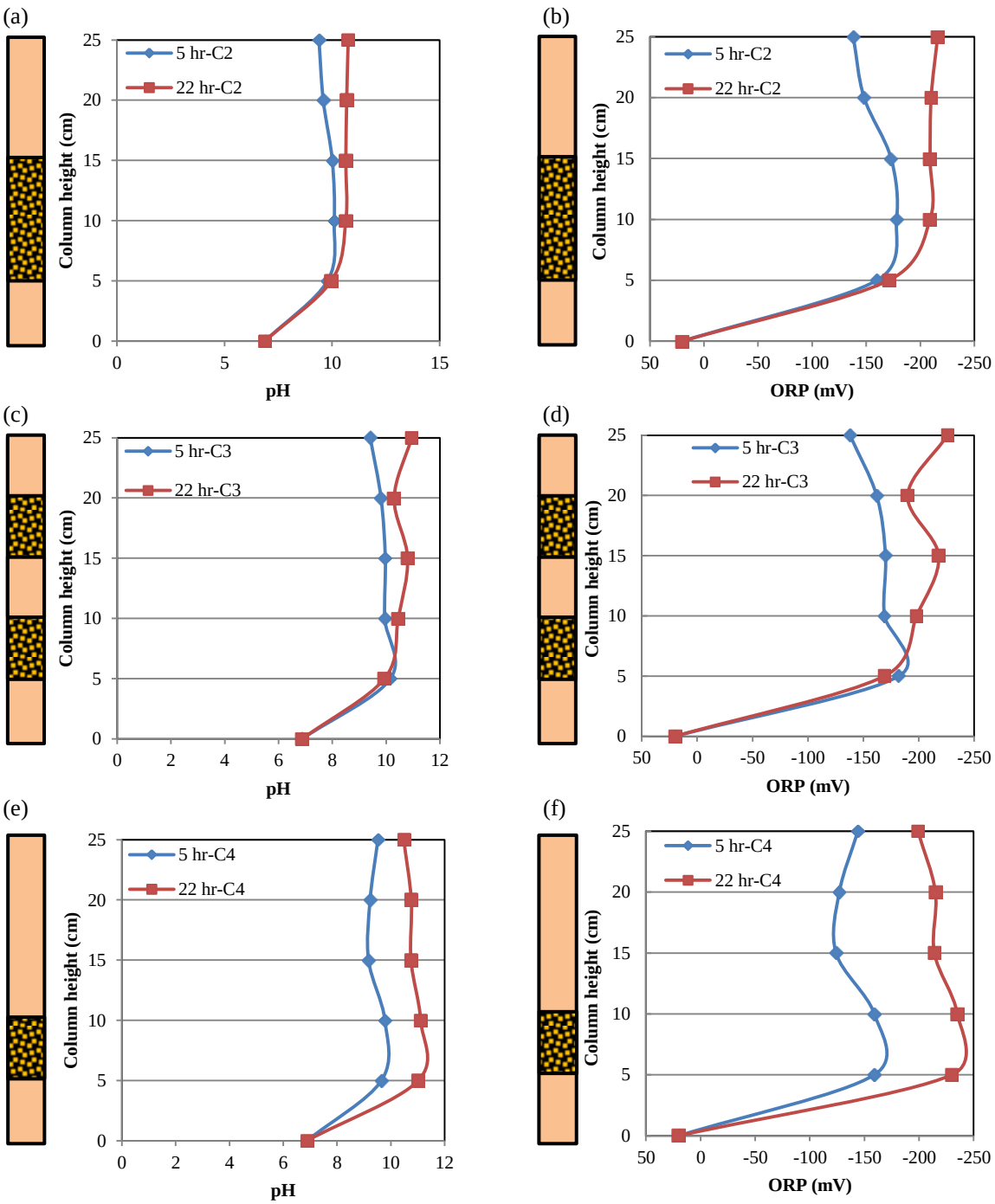

Fig. AI16. Sample profiles of pH and ORP along nZVI/sand columns (C2–C4) after 5 and 22 hr feeding with 45 mg NO_3^-–N /L.

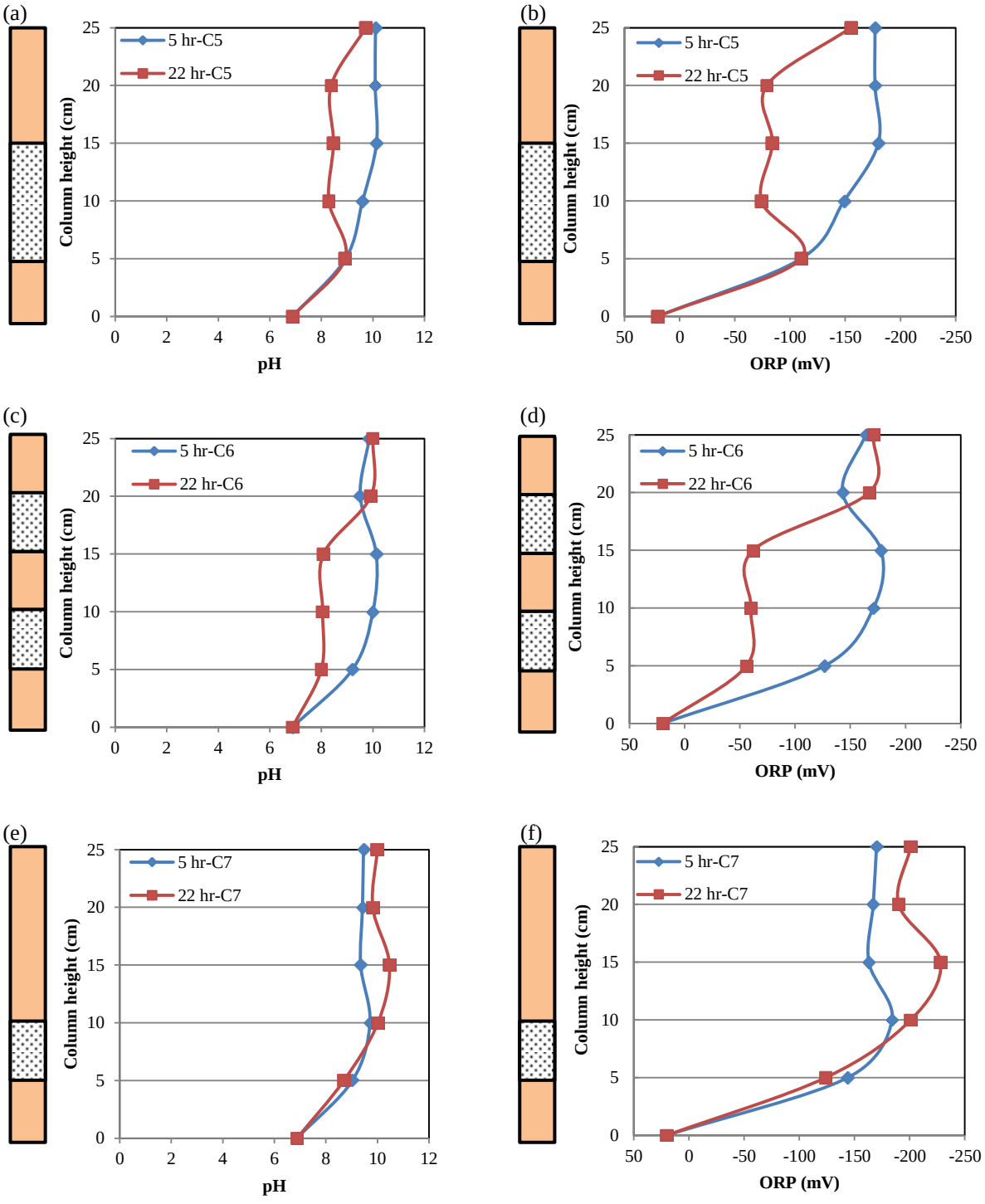
(a)
5 hr-C5
22 hr-C5
Column height (cm)
pH
(b)
5 hr-C5
22 hr-C5
Column height (cm)
ORP (mV)
(c)
5 hr-C6
22 hr-C6
Column height (cm)
pH
(d)
5 hr-C6
22 hr-C6
Column height (cm)
ORP (mV)
(e)
5 hr-C7
22 hr-C7
Column height (cm)
pH
(f)
5 hr-C7
22 hr-C7
Column height (cm)
ORP (mV)

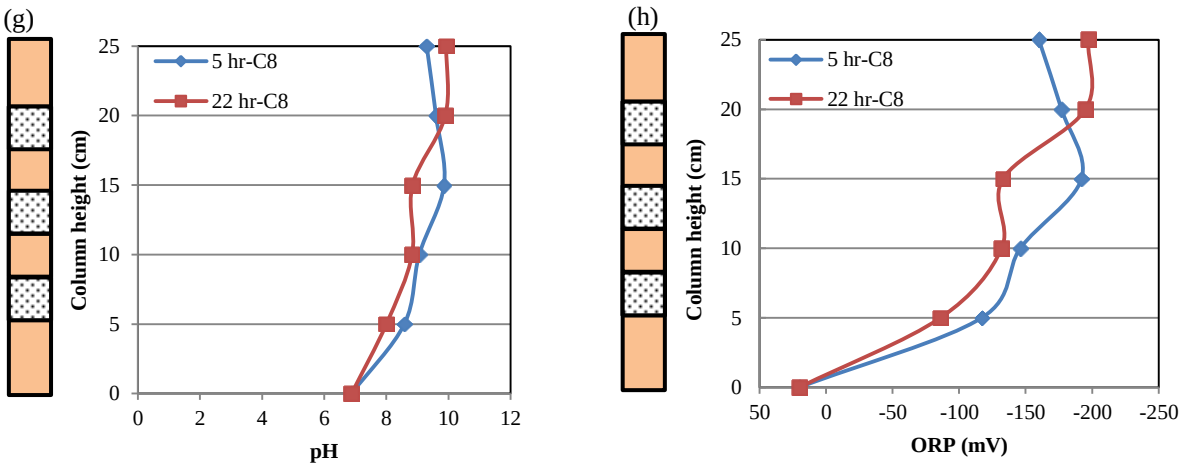

Fig. AI17. Sample profiles of pH and ORP along (nano-Fe/Cu)/sand columns (C5–C8) after 5 and 22 hr feeding with 45 mg NO_3^-–N /L.

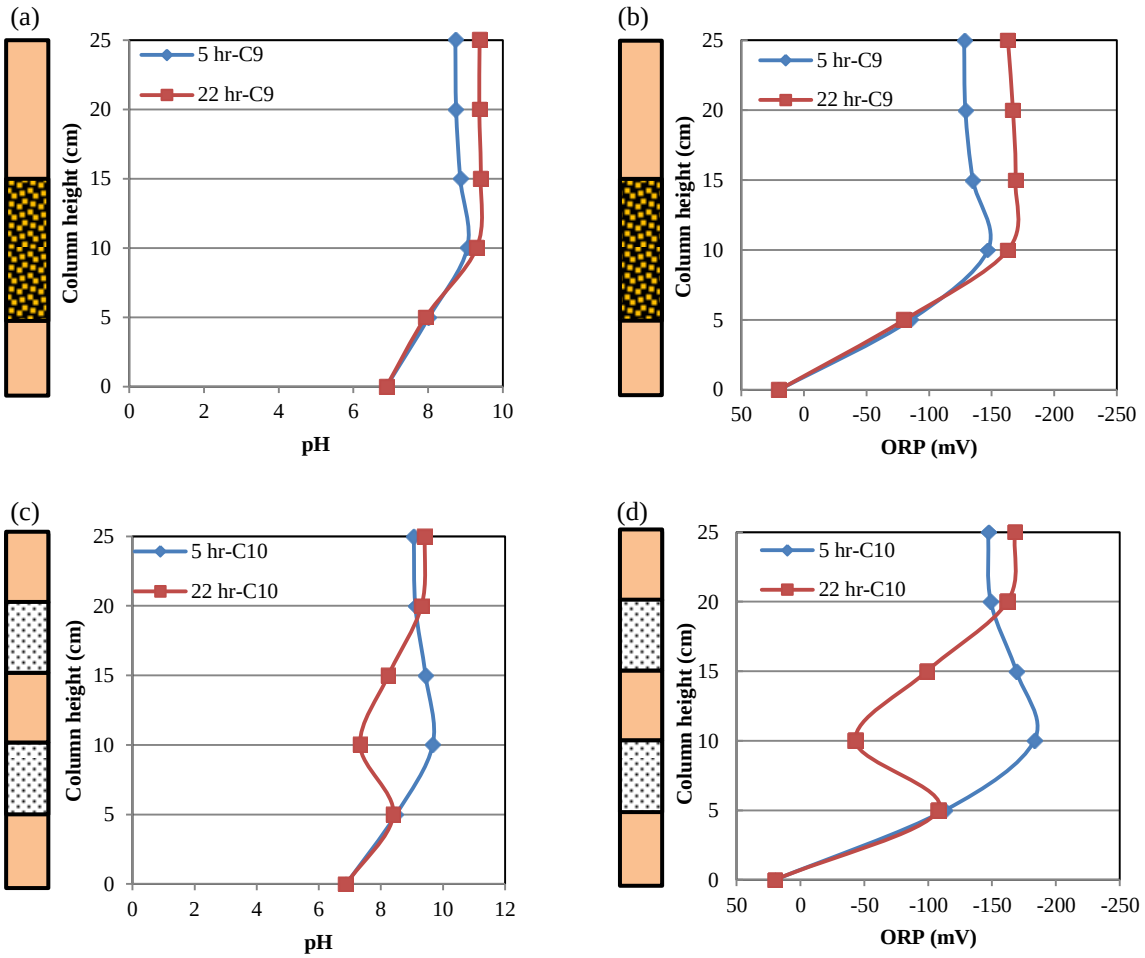

Fig. AI18. Sample profiles of pH and ORP along C9 and C10 after 5 and 22 hr feeding with simulated groundwater containing 45 mg NO_3^-–N /L.

AII. Treatment of Cesium Contaminated Water by nZVI and Fe/Cu Nanoparticles

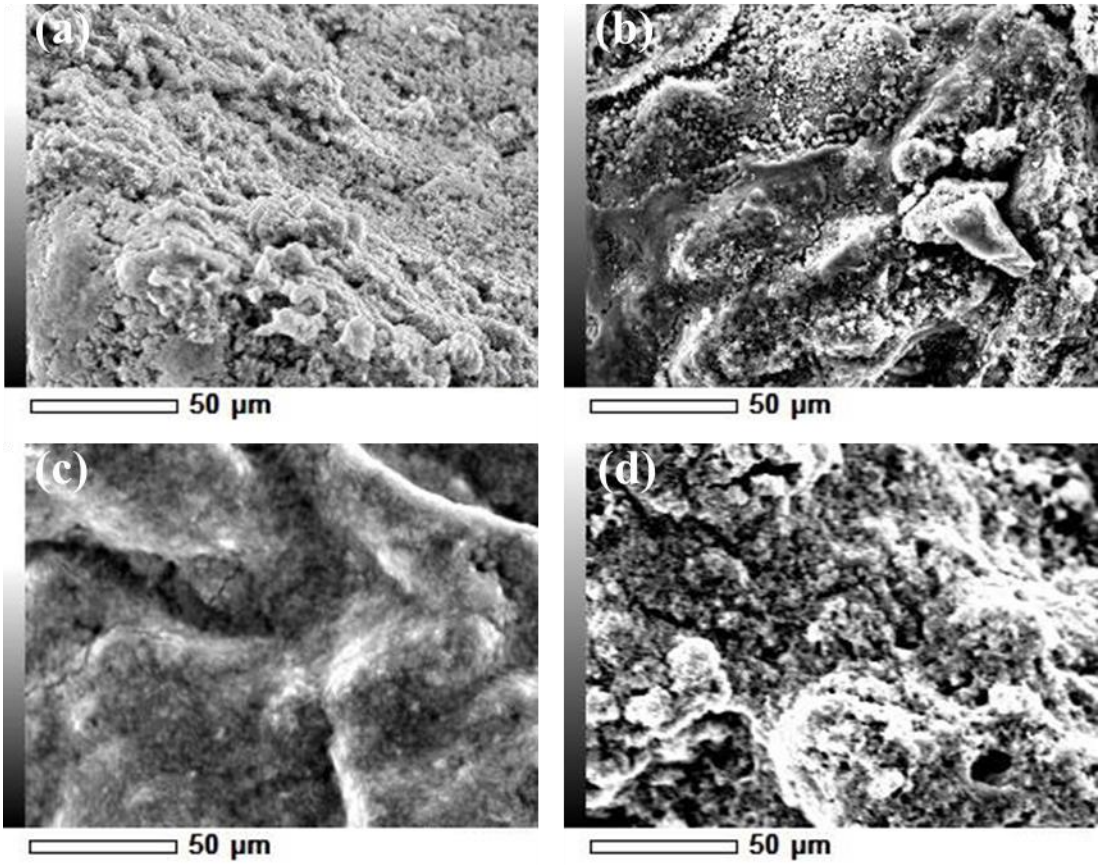

Fig. AII1. SEM images of synthesized (a) nZVI; (b) nano-Fe/Cu particles and the reacted nanoparticle solids acquired at the end of experiments (c) nZVI; (d) nano-Fe/Cu particles.

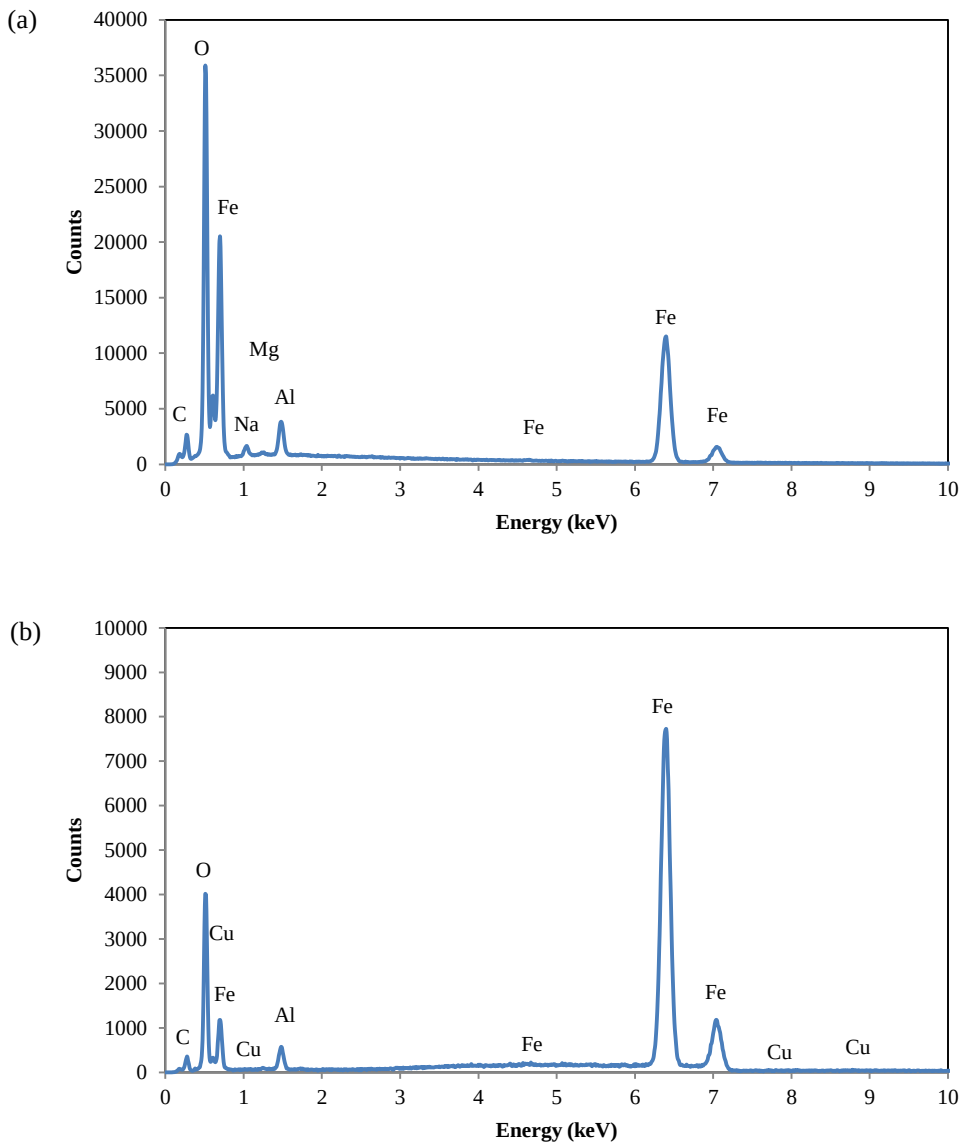

Fig. AII2. EDS spectrums of synthesized (a) nZVI and (b) nano-Fe/Cu particles.

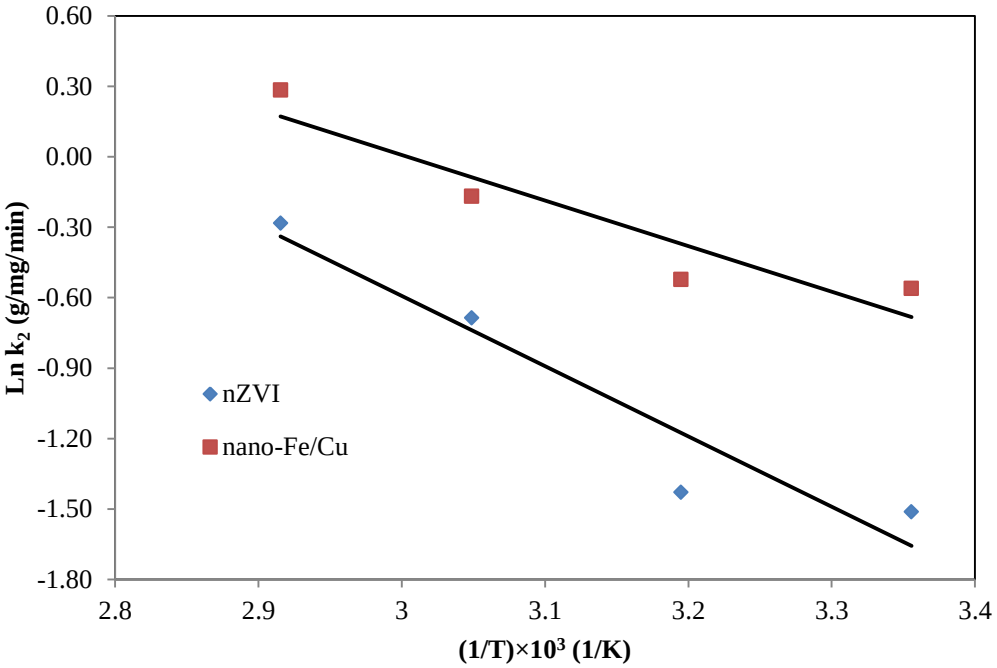

Fig. AII3. Arrhenius plot for calculating the activation energy of nZVI and nano-Fe/Cu particles (E_a) for cesium sorption.

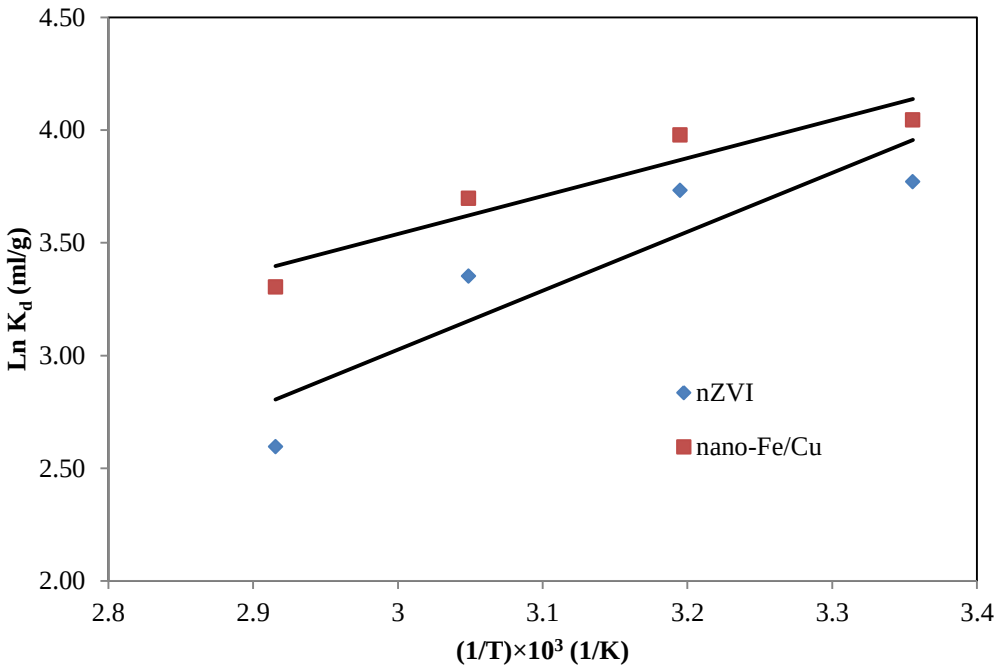

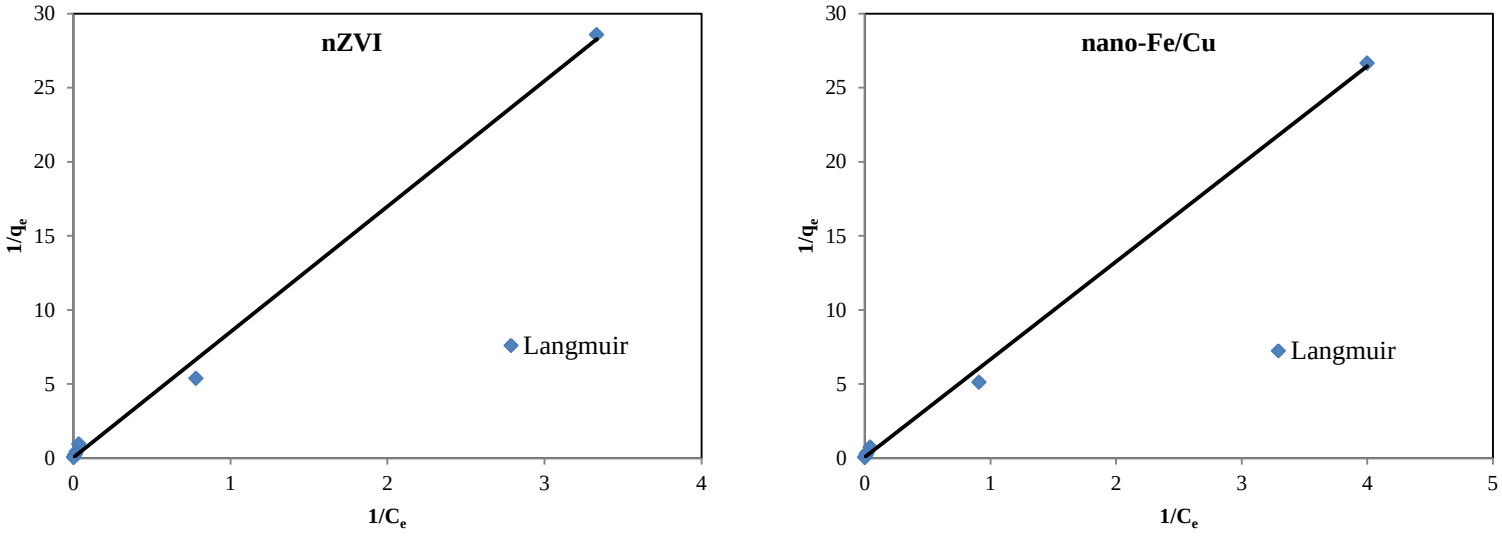

Fig. AII4. Van't Hoff plot for cesium sorption onto nZVI and nano-Fe/Cu particles.

Fig. AII5. Langmuir isotherm plots for cesium sorption onto nZVI and nano-Fe/Cu particles.

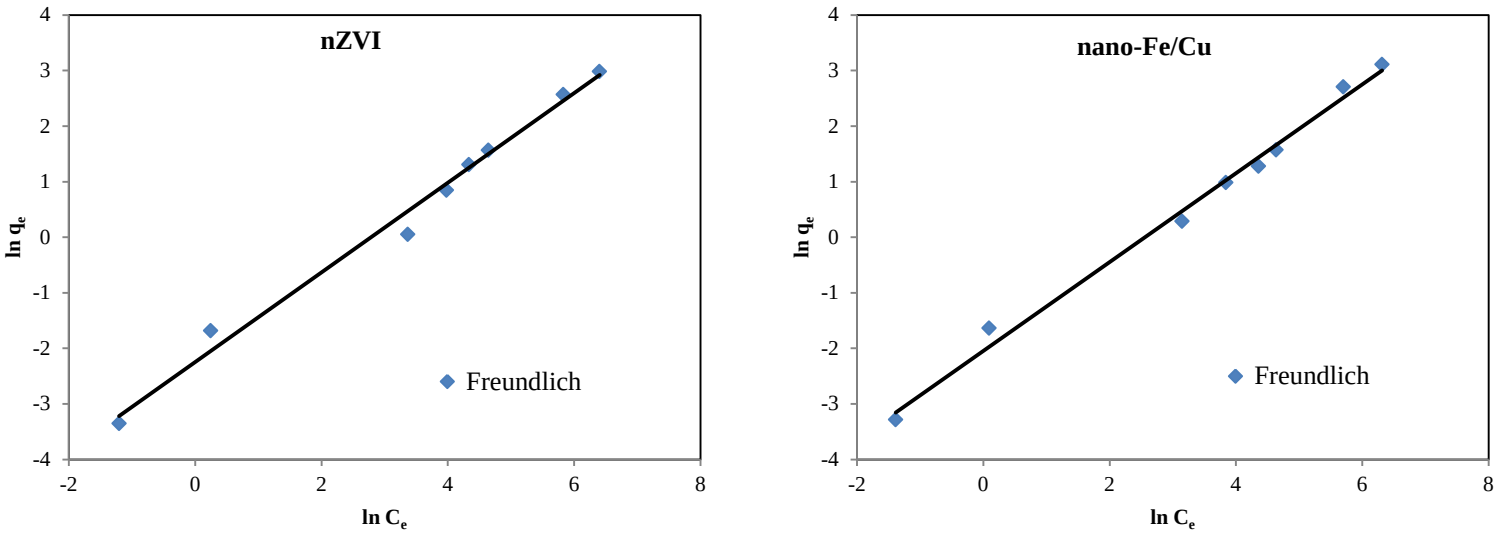

Fig. AII6. Freundlich isotherm plots for cesium sorption onto nZVI and nano-Fe/Cu particles.

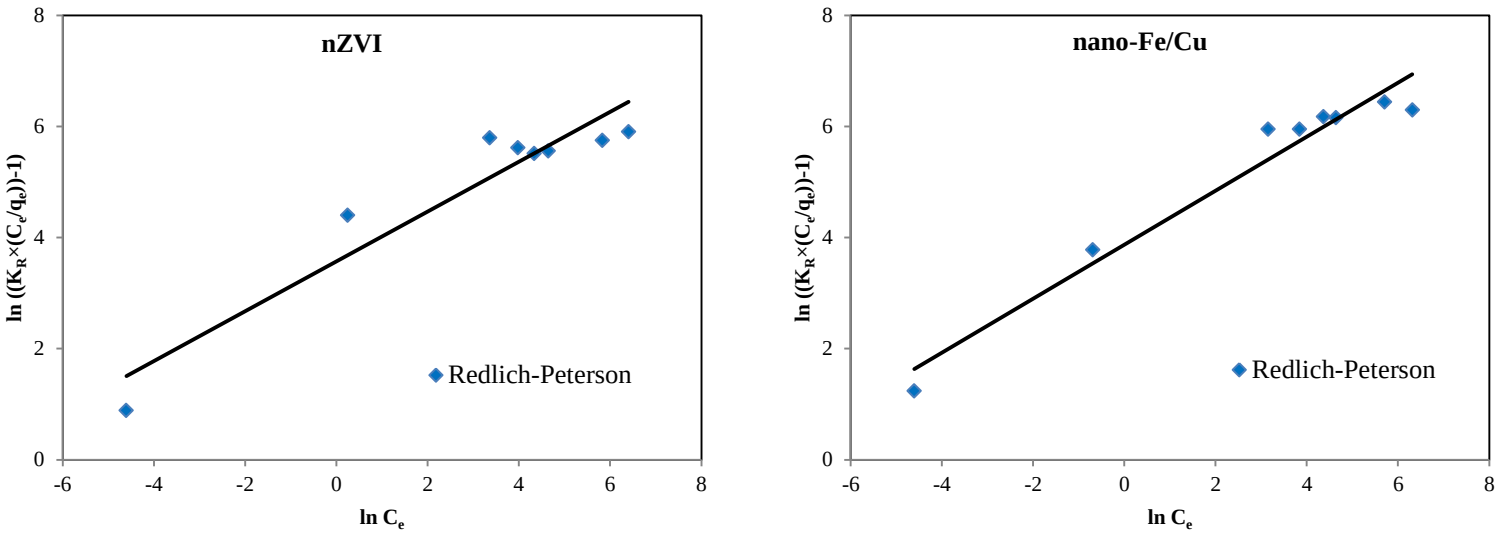

Fig. AII7. Redlich-Peterson isotherm plots for cesium sorption onto nZVI and nano-Fe/Cu particles.

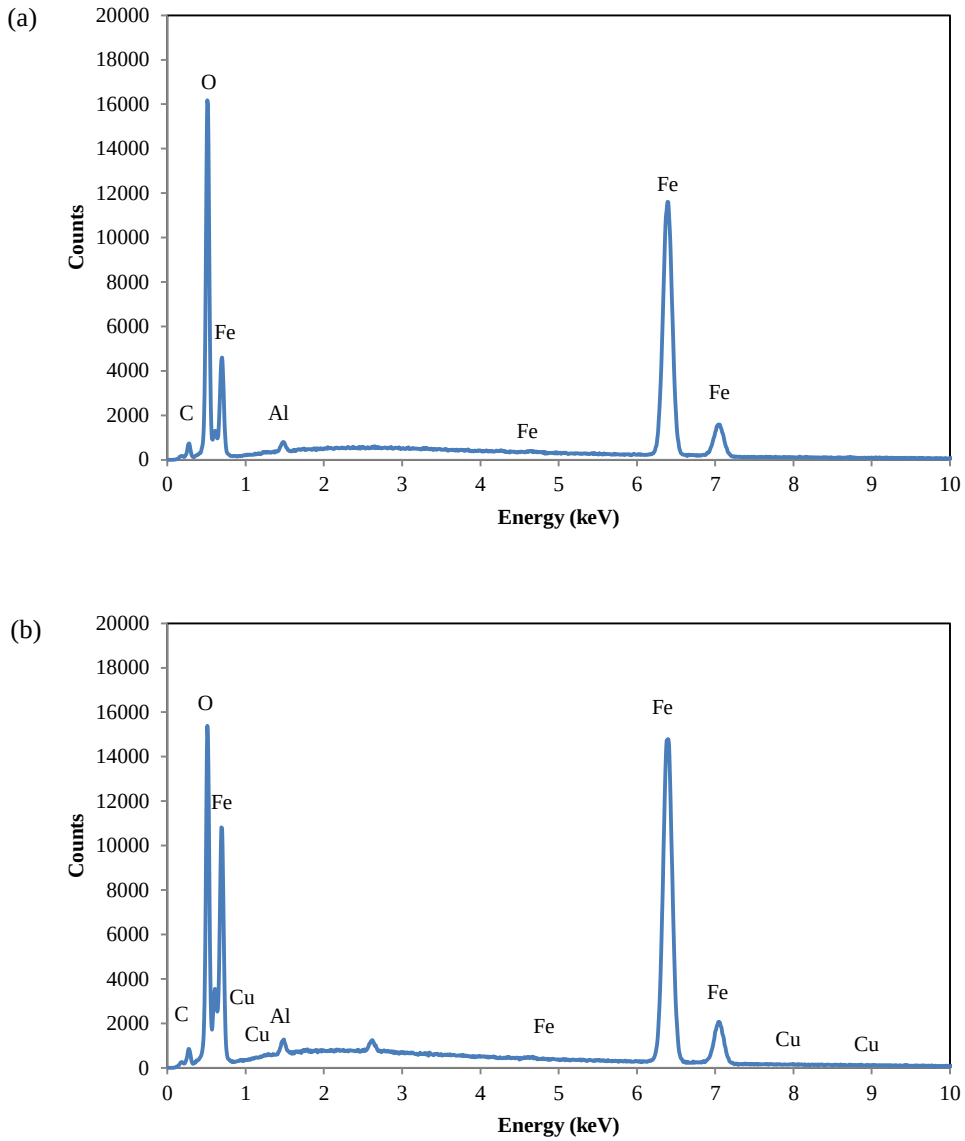

Fig. AII8. EDS spectrums acquired from the reacted nanoparticle solids at the end of experiments; (a) nZVI and (b) nano-Fe/Cu particles.

AIII. Removal of Cesium by Iron Based Nanoparticles–Zeolite Composites

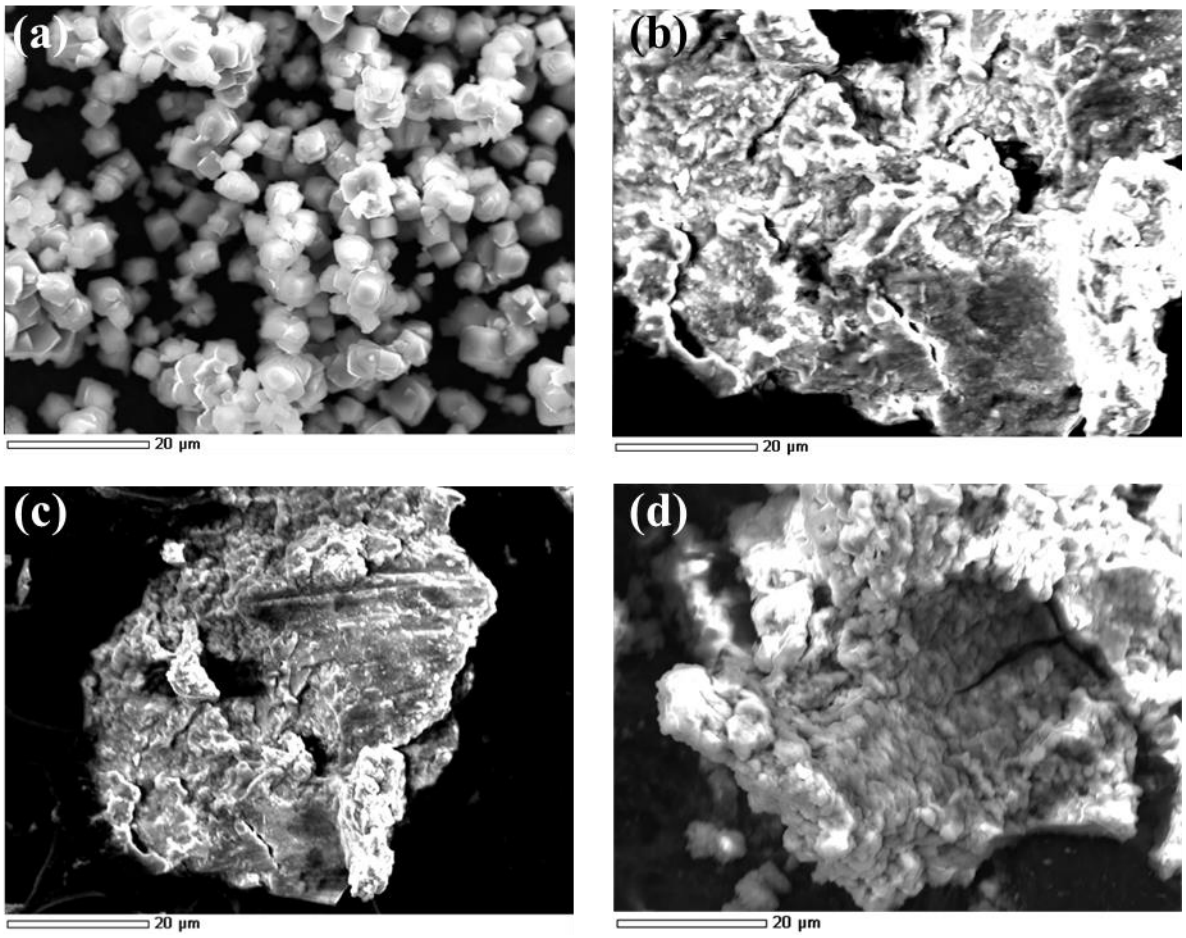

Fig. AIII9. SEM images of (a) zeolite, (b,c) nZVI–Z composite and (d) nFe/Cu–Z composite.

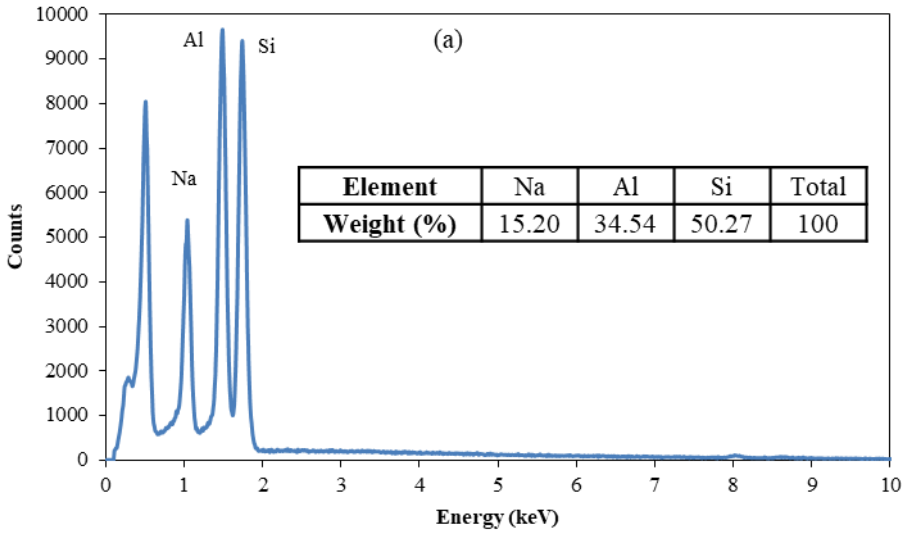

Element	Na	Al	Si	Total
Weight (%)	15.20	34.54	50.27	100

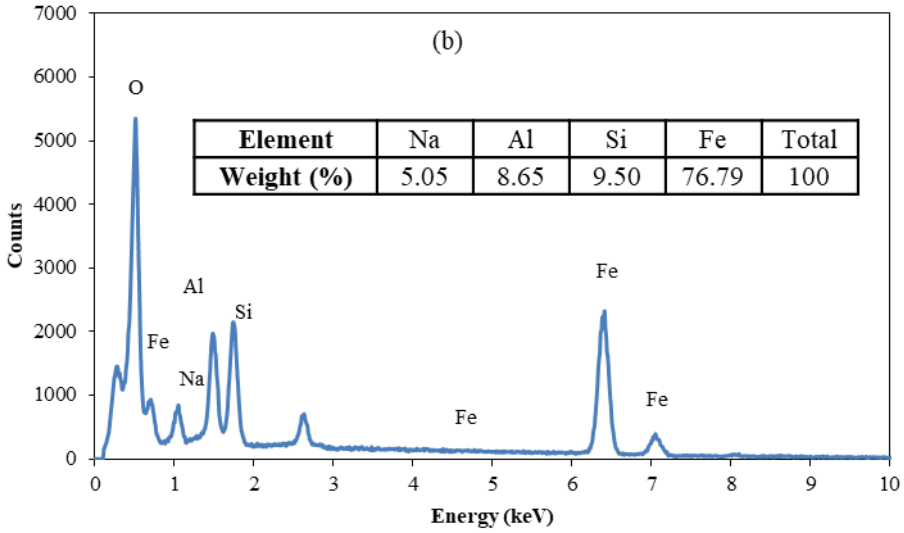

Element	Na	Al	Si	Fe	Total
Weight (%)	5.05	8.65	9.50	76.79	100

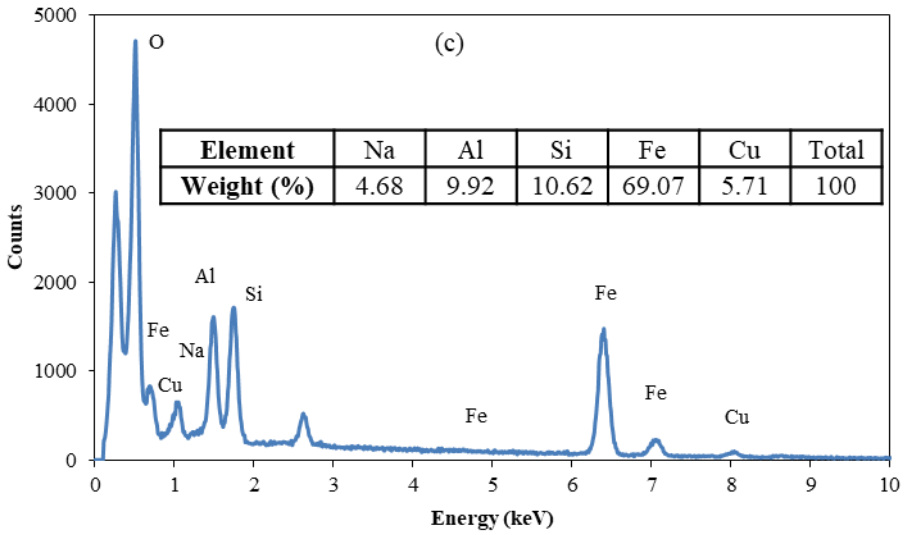

Element	Na	Al	Si	Fe	Cu	Total
Weight (%)	4.68	9.92	10.62	69.07	5.71	100

Fig. AIII10. EDS spectrums of (a) zeolite, (b) nZVI–Z composite and (c) nFe/Cu–Z composite.

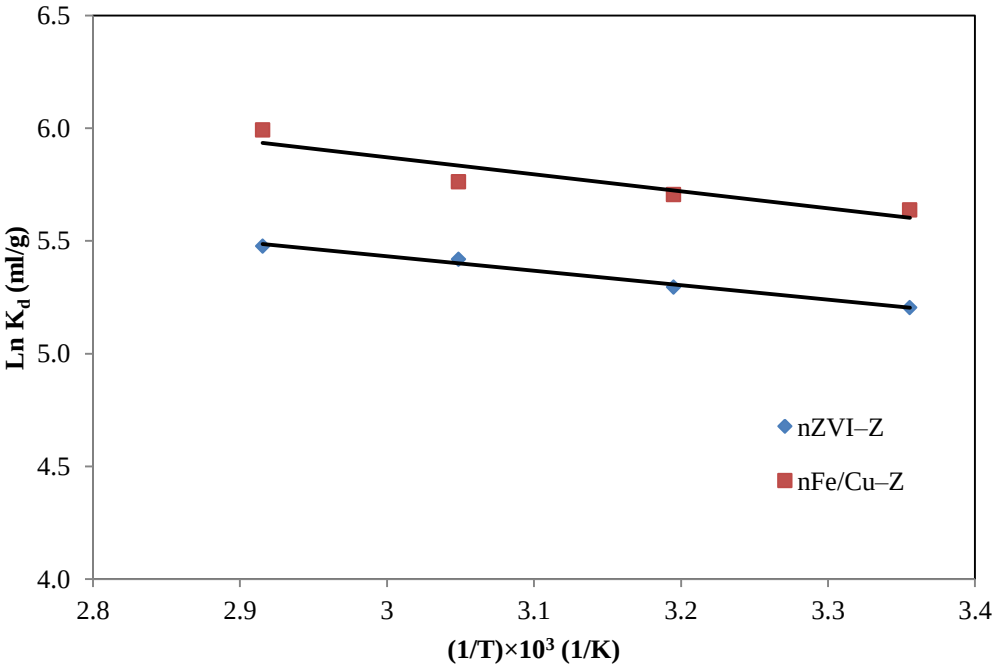

Fig. AIII11. Van't Hoff plot for cesium adsorption onto nZVI–Z and nFe/Cu–Z.

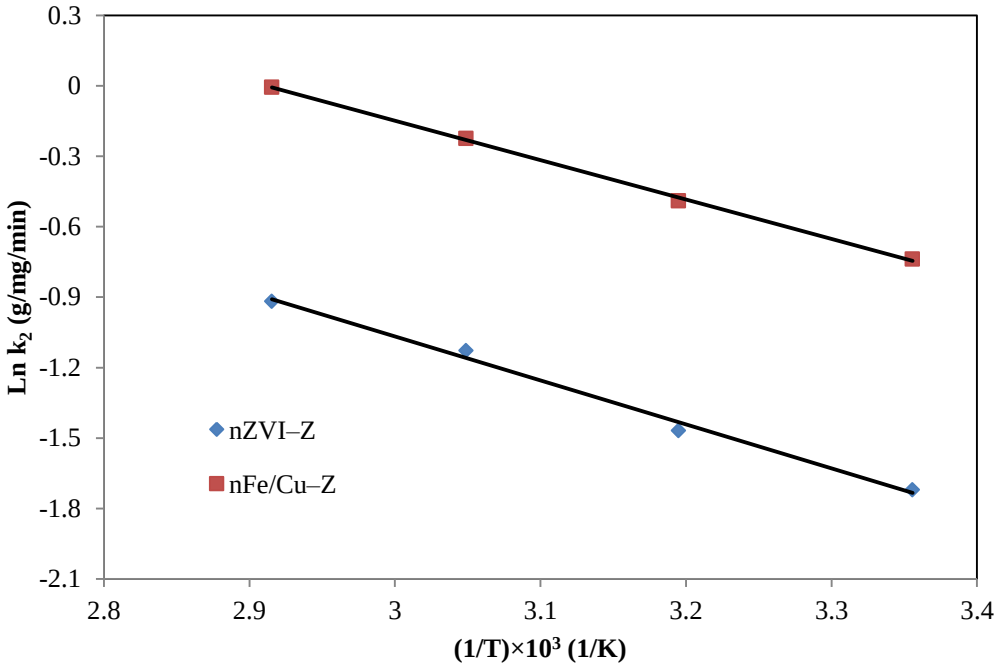

Fig. AIII12. Arrhenius plot for calculating the activation energy of nZVI–Z and nFe/Cu–Z (E_a) for cesium adsorption.

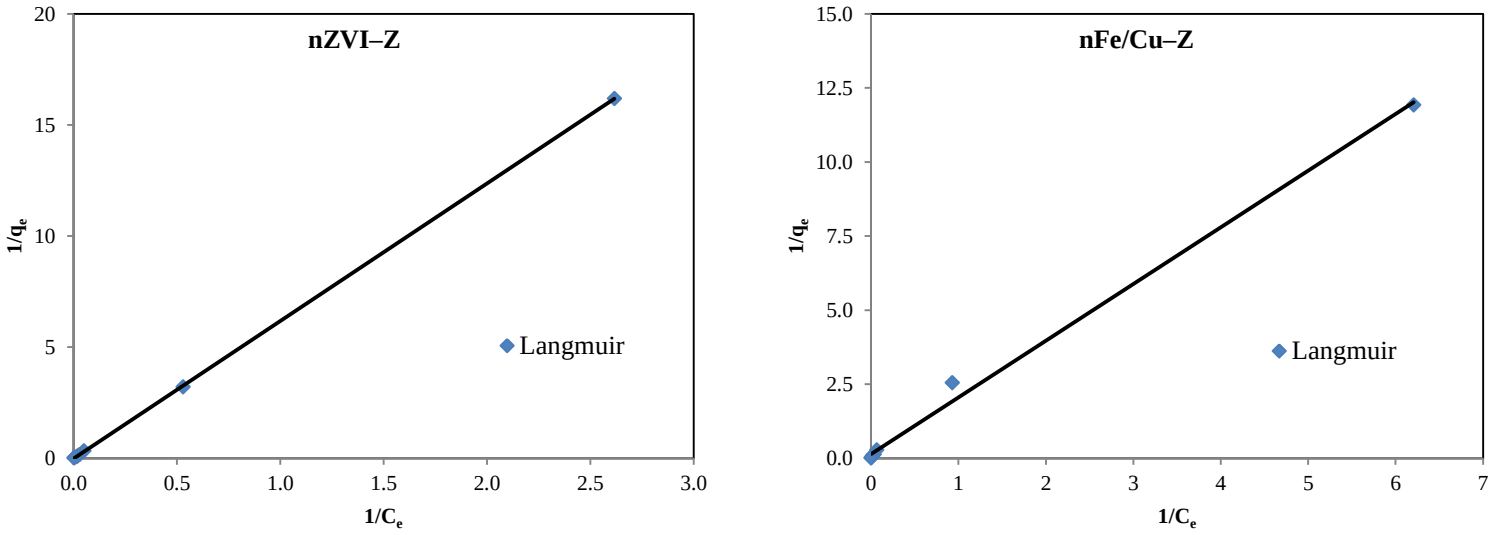

Fig. AIII13. Langmuir isotherm plots for cesium adsorption onto nZVI–Z and nFe/Cu–Z.

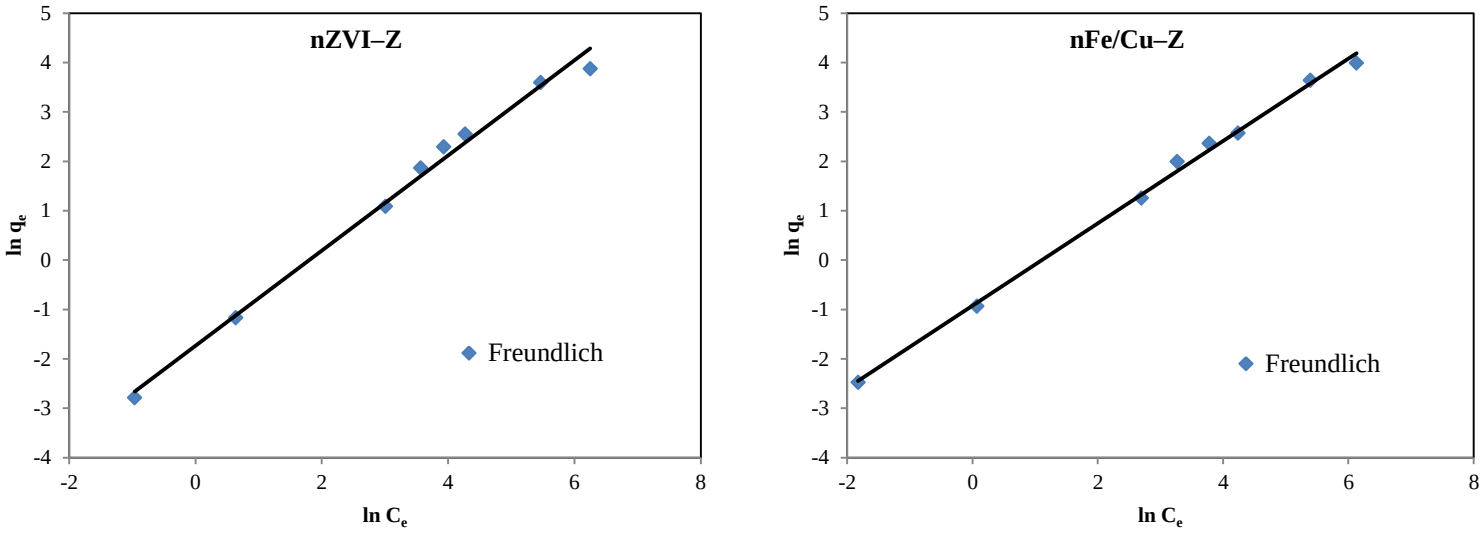

Fig. AIII14. Freundlich isotherm plots for cesium adsorption onto nZVI–Z and nFe/Cu–Z.

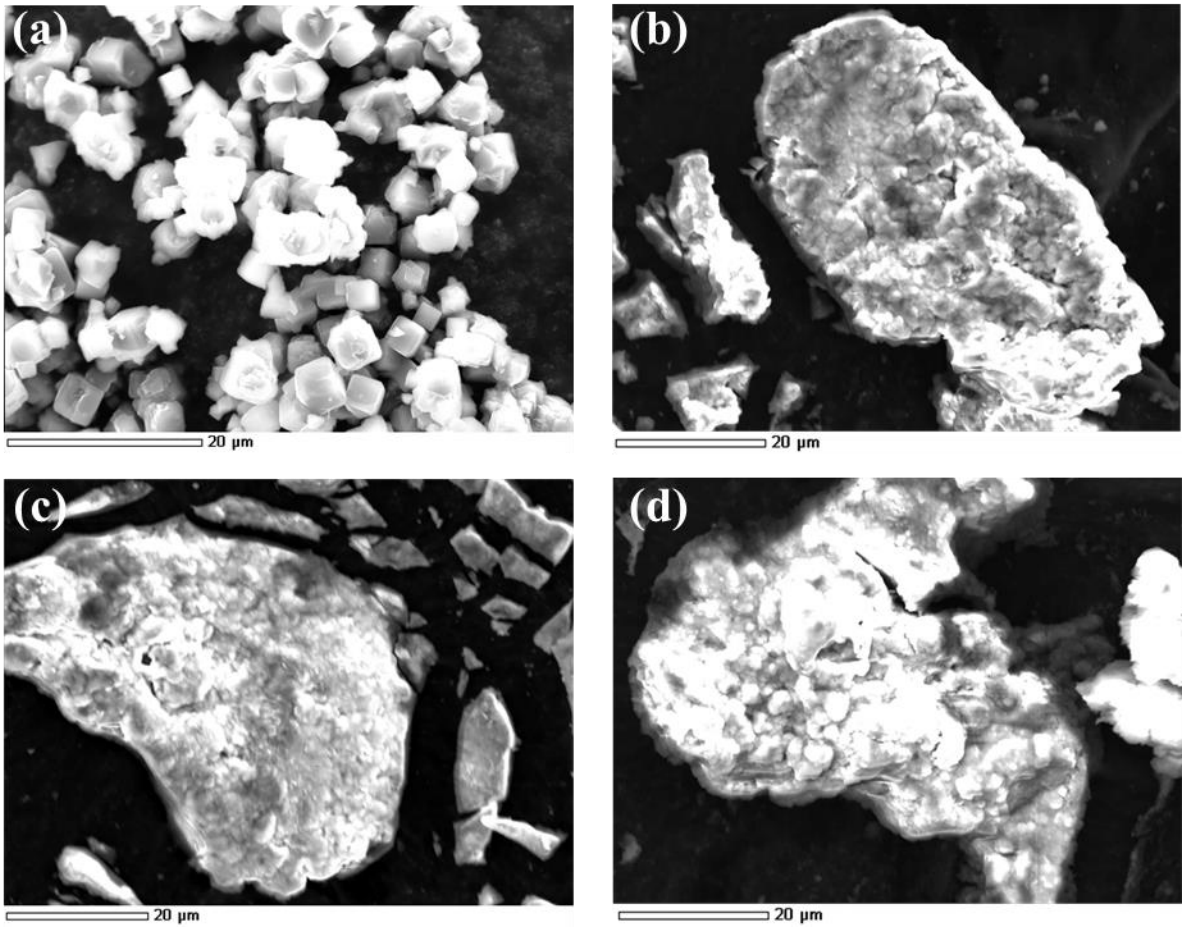

Fig. AIII15. SEM images of (a) zeolite, (b,c) nZVI–Z composite and (d) nFe/Cu–Z composite acquired at the end of experiments after Cs^+ adsorption.

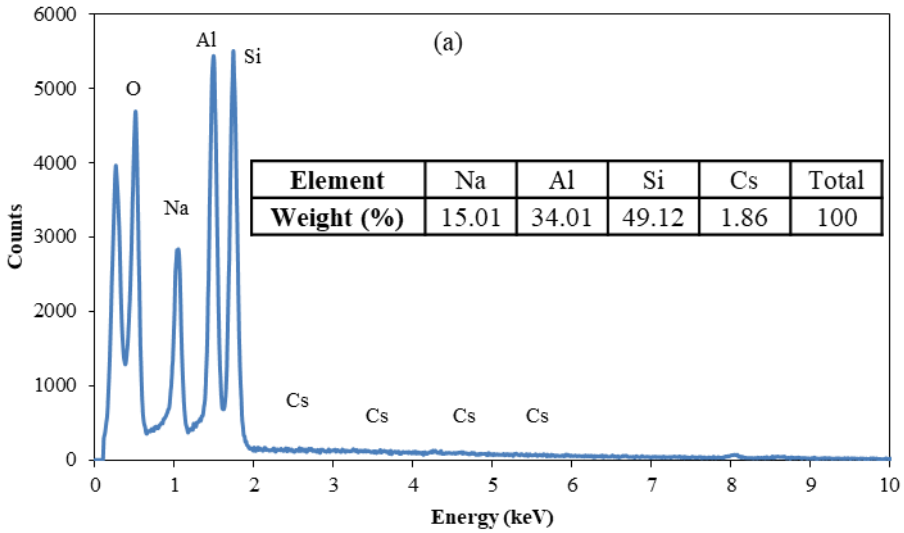

Element	Na	Al	Si	Cs	Total
Weight (%)	15.01	34.01	49.12	1.86	100

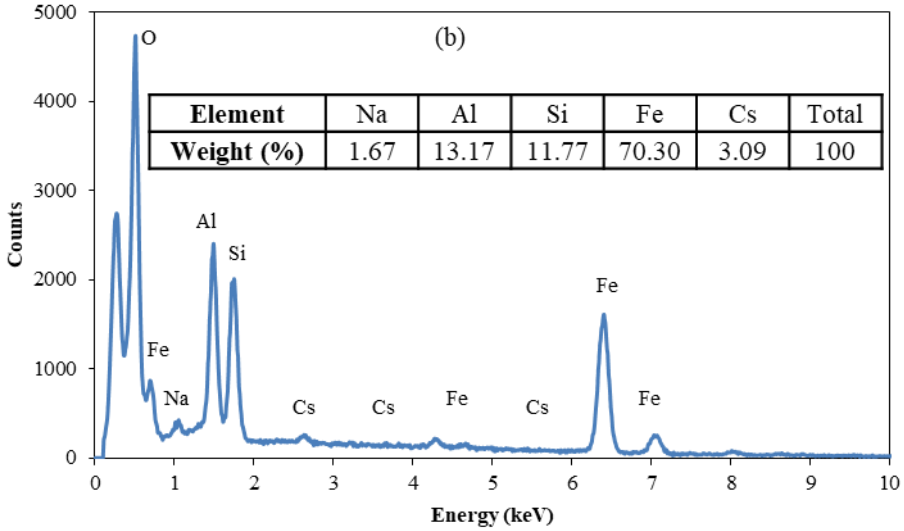

Element	Na	Al	Si	Fe	Cs	Total
Weight (%)	1.67	13.17	11.77	70.30	3.09	100

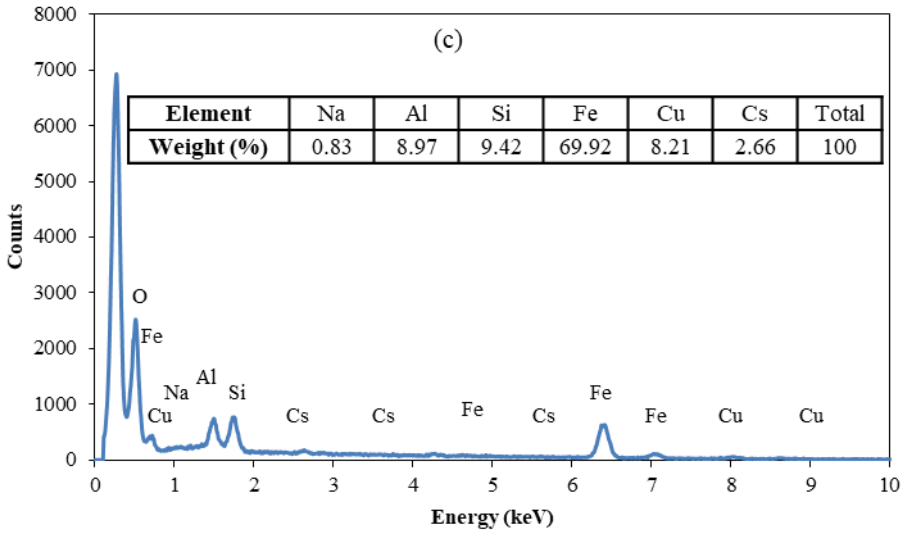

Fig. AIII16. EDS spectrums of (a) zeolite, (b) nZVI–Z composite and (c) nFe/Cu–Z composite acquired at the end of experiments after Cs^+ adsorption.

AIV. Removal of Strontium Using Magnetic Zeolite Nanocomposites

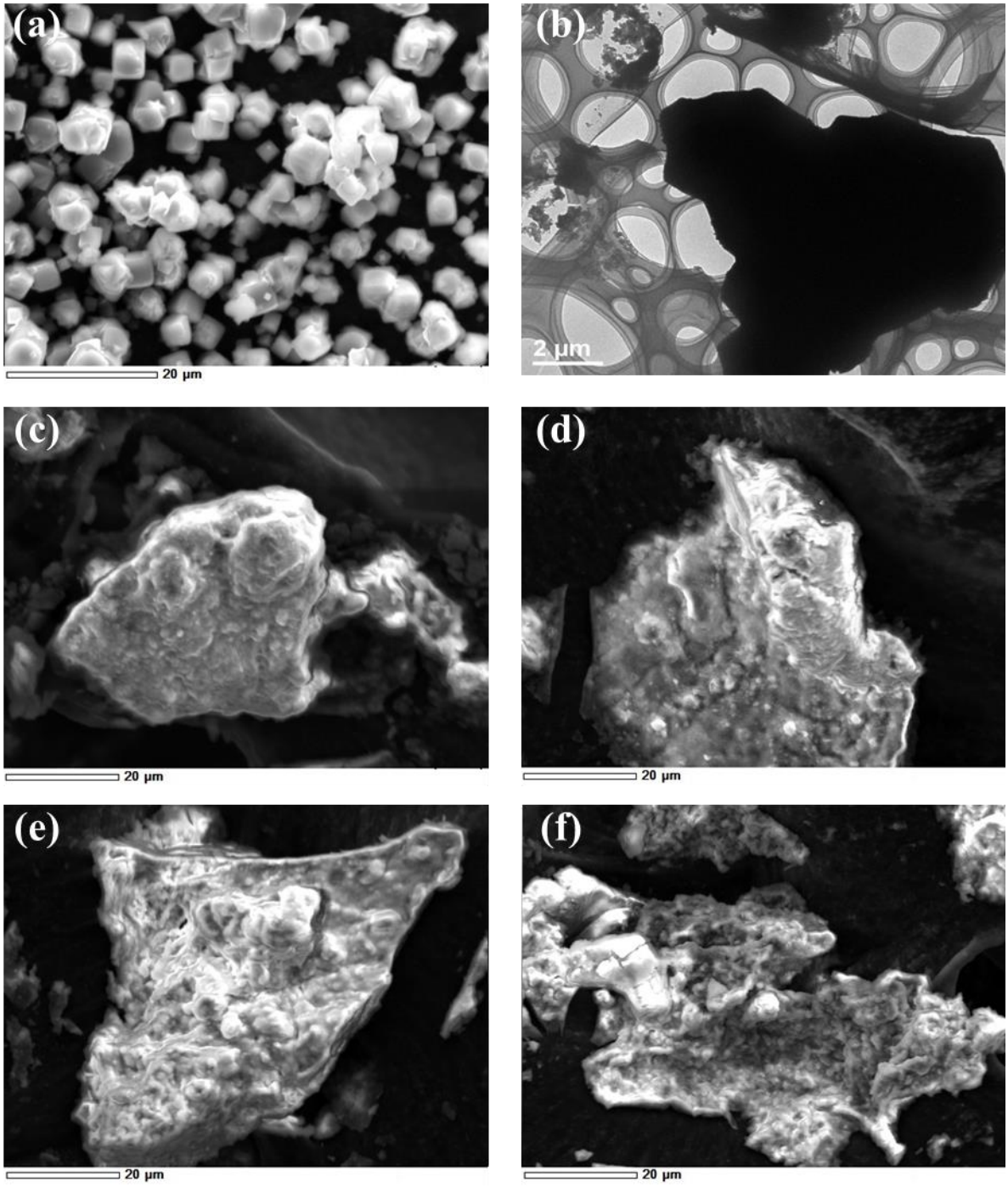

Fig. AIV17. SEM image of (a) zeolite; TEM image of (b) nZVI–Z; SEM images of (c, d) nZVI–Z and (e, f) nFe/Cu–Z.

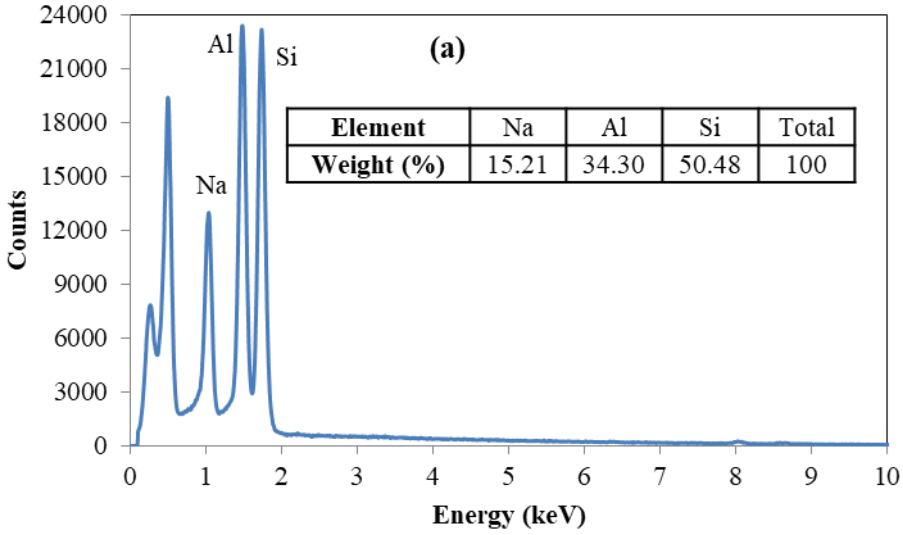

Element	Na	Al	Si	Total
Weight (%)	15.21	34.30	50.48	100

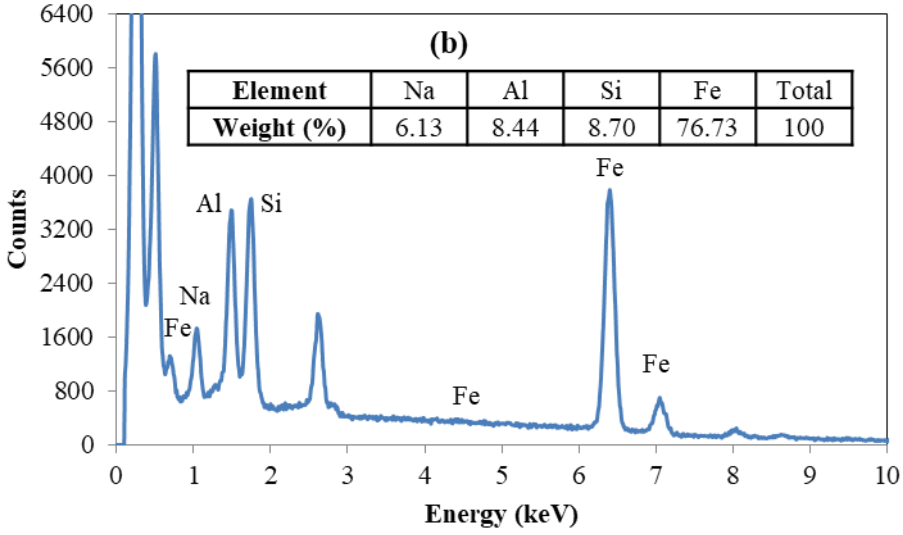

Element	Na	Al	Si	Fe	Total
Weight (%)	6.13	8.44	8.70	76.73	100

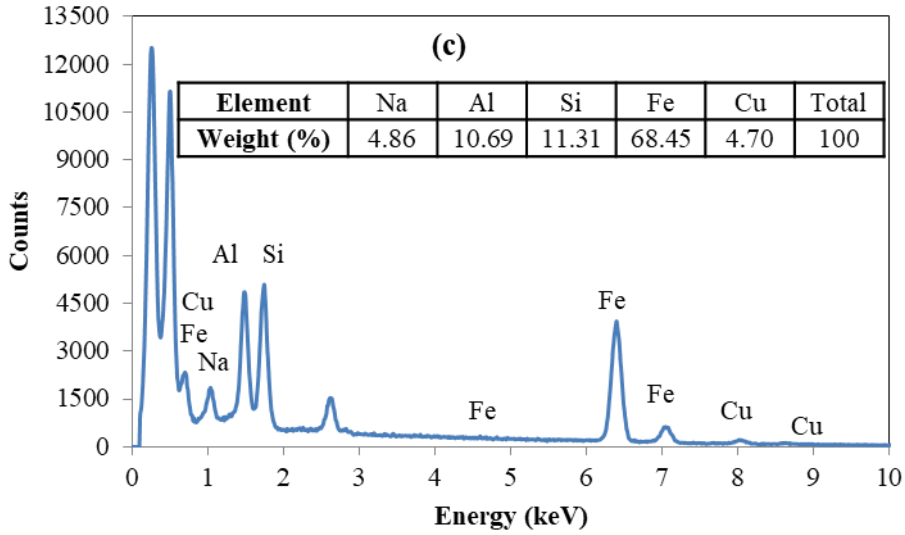

Fig. AIV18. EDS spectra of (a) zeolite, (b) nZVI–Z and (c) nFe/Cu–Z.

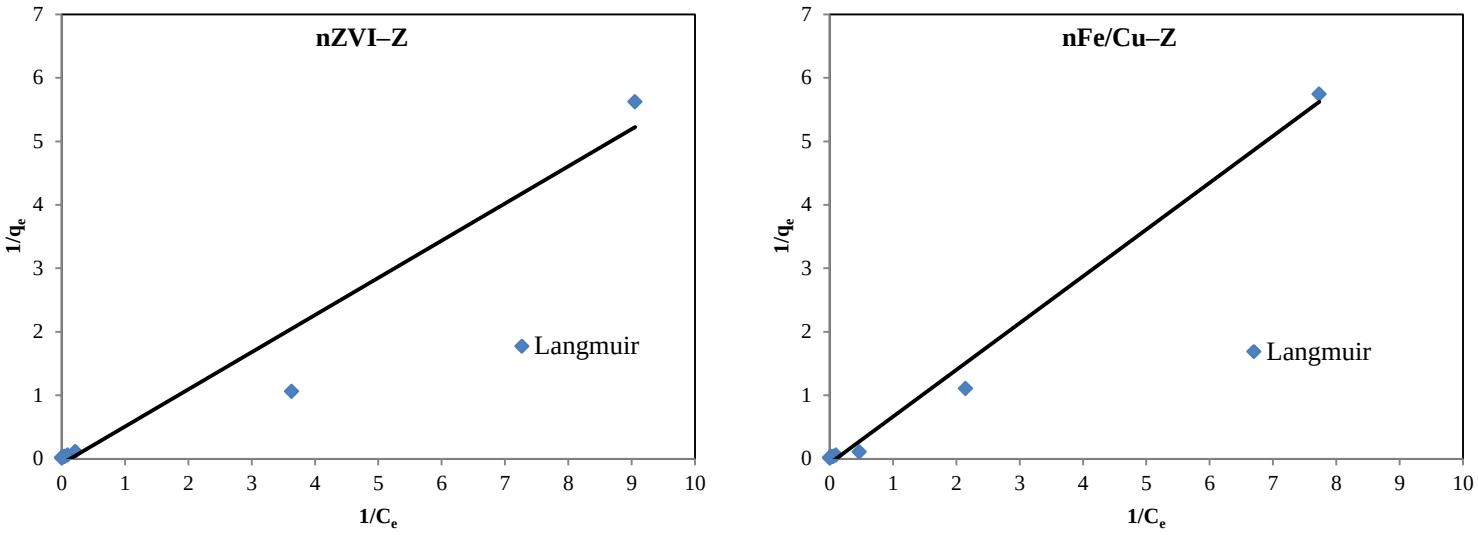

Fig. AIV19. Langmuir isotherm plots for Sr^{2+} sorption onto nZVI–Z and nFe/Cu–Z.

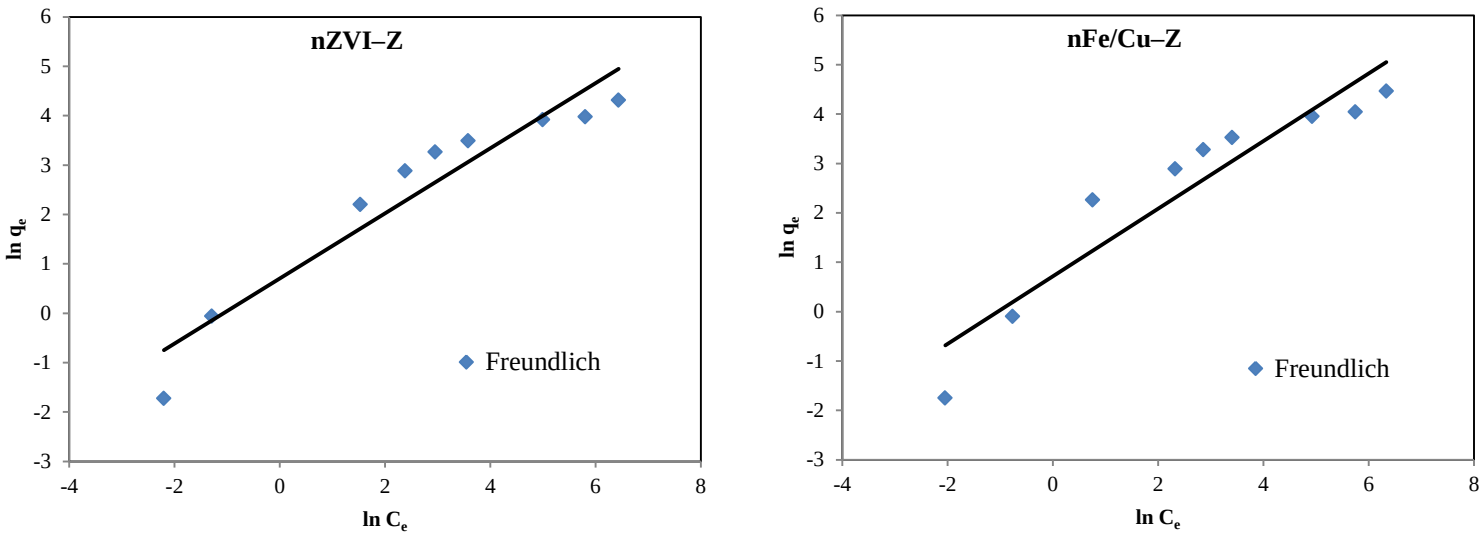

Fig. AIV20. Freundlich isotherm plots for Sr^{2+} sorption onto nZVI–Z and nFe/Cu–Z.

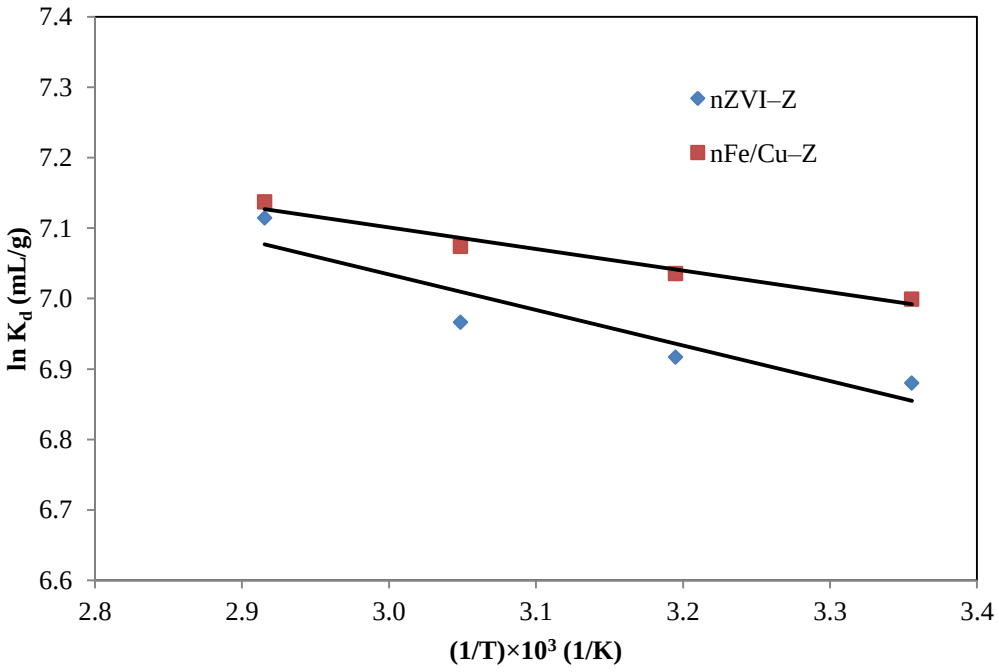

Fig. AIV21. Plot of $\ln K_d$ vs. $1/T$ for Sr^{2+} sorption onto nZVI–Z and nFe/Cu–Z.

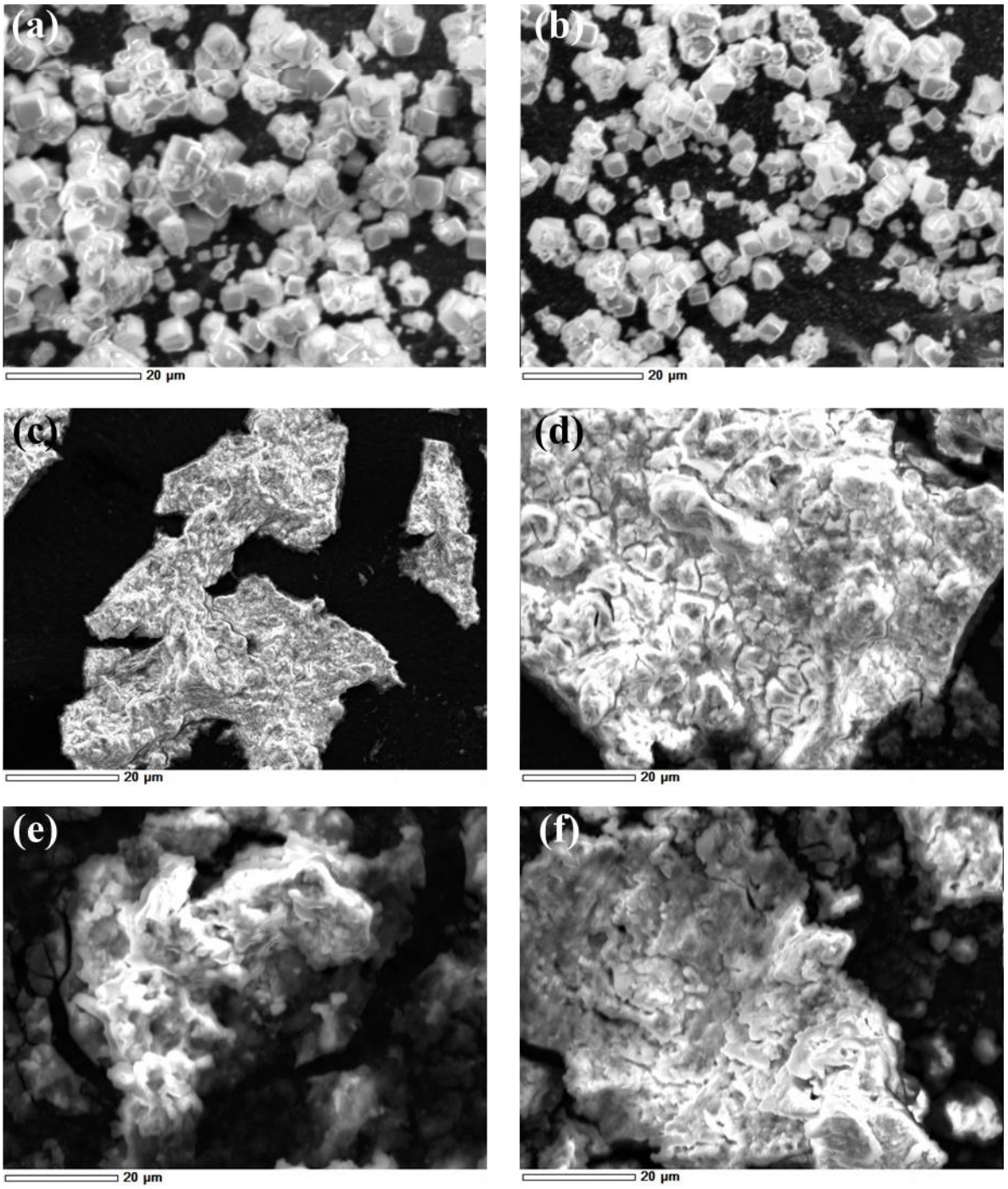

Fig. AIV22. SEM images of (a, b) zeolite, (c, d) nZVI–Z and (e, f) nFe/Cu–Z acquired at the end of experiments after Sr^{2+} sorption.

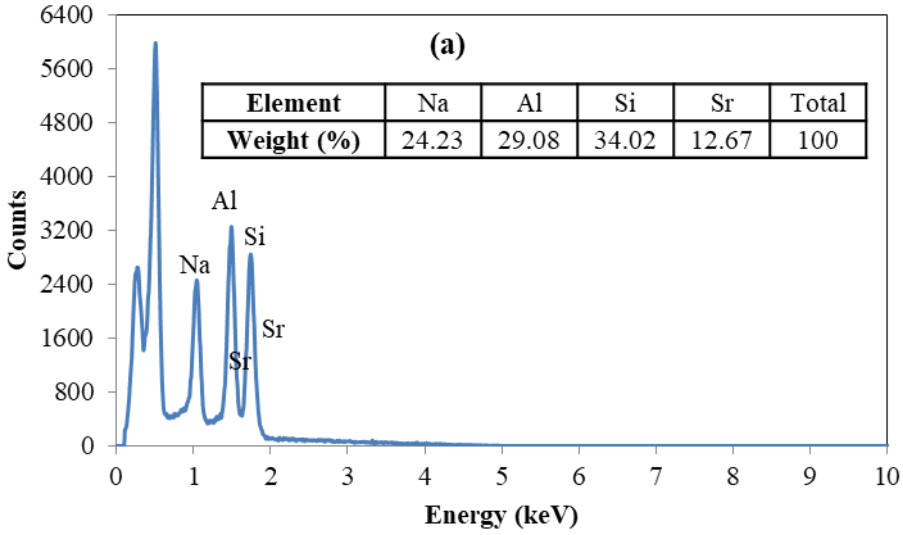
(a)
Element | Na | Al | Si | Sr | Total
Weight (%) | 24.23 | 29.08 | 34.02 | 12.67 | 100
Counts
Energy (keV)
Na
Al
Si
Sr
Sr

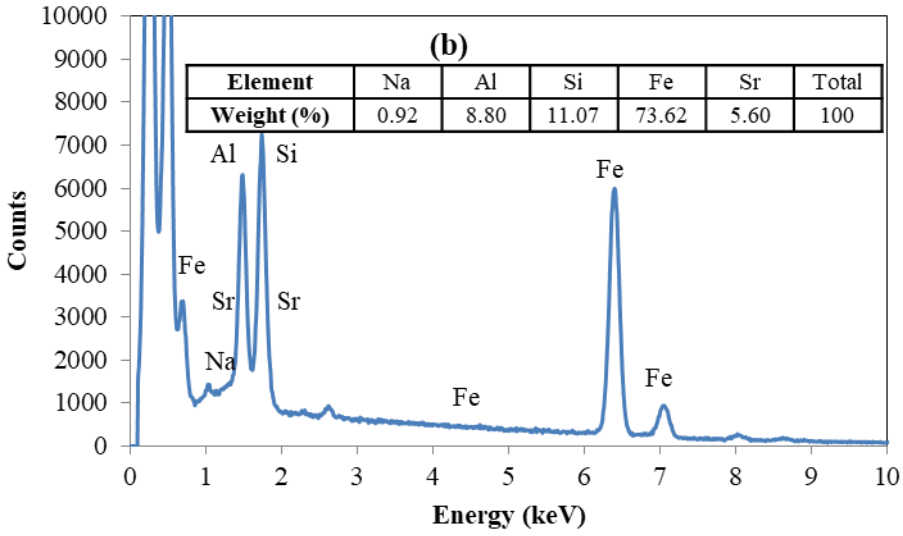
(b)
Element | Na | Al | Si | Fe | Sr | Total
Weight (%) | 0.92 | 8.80 | 11.07 | 73.62 | 5.60 | 100
Counts
Energy (keV)
Al
Si
Fe
Sr
Sr
Na
Fe
Fe
Fe

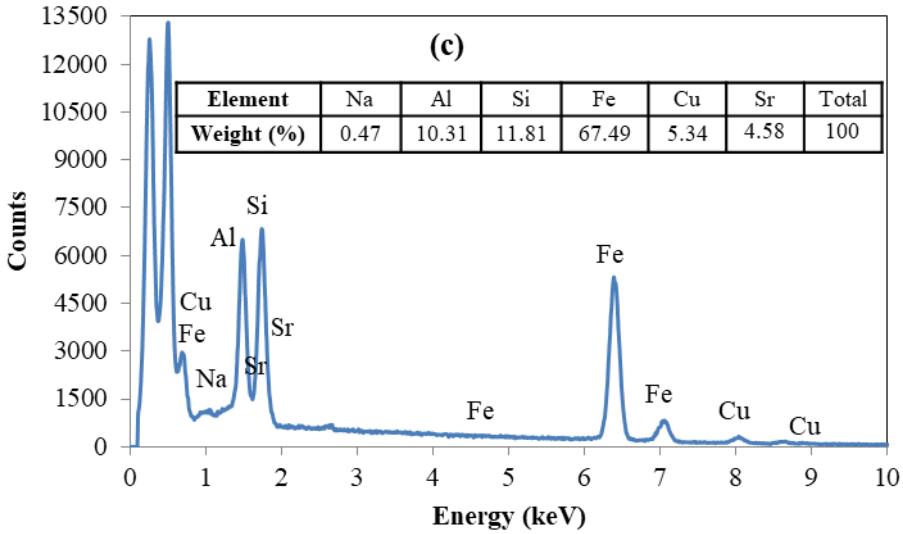

Fig. AIV23. EDS spectra of (a) zeolite, (b) nZVI–Z and (c) nFe/Cu–Z acquired at the end of experiments after Sr^{2+} sorption.